

Unique Dynamic Behaviors of Ice Divides:
Siple Dome and the Rheological Properties of Ice

Erin C. Pettit

A dissertation submitted in partial fulfillment of
the requirements for the degree of

Doctor of Philosophy

University of Washington

2003

Program Authorized to Offer Degree: Earth and Space Sciences

UMI Number: 3111116

INFORMATION TO USERS

The quality of this reproduction is dependent upon the quality of the copy submitted. Broken or indistinct print, colored or poor quality illustrations and photographs, print bleed-through, substandard margins, and improper alignment can adversely affect reproduction.

In the unlikely event that the author did not send a complete manuscript and there are missing pages, these will be noted. Also, if unauthorized copyright material had to be removed, a note will indicate the deletion.

UMI[®]

UMI Microform 3111116

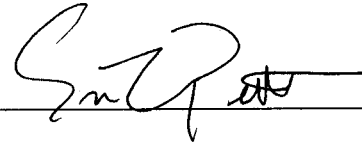
Copyright 2004 by ProQuest Information and Learning Company.

All rights reserved. This microform edition is protected against unauthorized copying under Title 17, United States Code.

ProQuest Information and Learning Company
300 North Zeeb Road
P.O. Box 1346
Ann Arbor, MI 48106-1346

In presenting this dissertation in partial fulfillment of the requirements for the Doctorial degree at the University of Washington, I agree that the Library shall make its copies freely available for inspection. I further agree that extensive copying of this thesis is allowable only for scholarly purposes, consistent with "fair use" as prescribed in the U.S. Copyright Law. Requests for copying or reproduction of this dissertation may be referred to University Microfilms, 1490 Eisenhower Place, P.O. Box 975, Ann Arbor, MI 48106, to whom the author has granted "the right to reproduce and sell (a) copies of the manuscript in microform and/or (b) printed copies of the manuscript made from microform."

Signature _____

A handwritten signature in black ink, appearing to be 'S. P. [unclear]', written over a horizontal line.

Date _____

Dec 5 2003

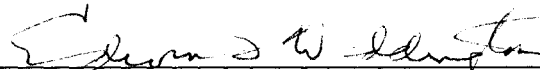
University of Washington
Graduate School

This is to certify that I have examined this copy of a doctoral dissertation by

Erin C. Pettit

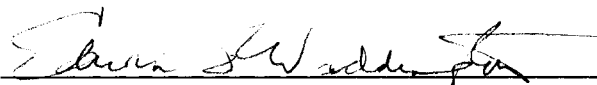
and have found that it is complete and satisfactory in all respects,
and that any and all revisions required by the final
examining committee have been made.

Chair of Supervisory Committee:

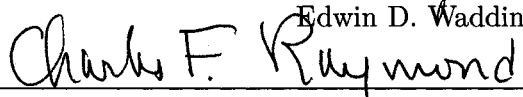


Edwin D. Waddington

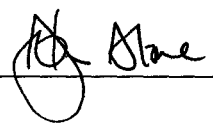
Reading Committee:



Edwin D. Waddington



Charles F. Raymond



John O. Stone

Date: Dec 5 2003

University of Washington

Abstract

Unique Dynamic Behaviors of Ice Divides:
Siple Dome and the Rheological Properties of Ice

Erin C. Pettit

Chair of Supervisory Committee
Professor Edwin D. Waddington
Earth and Space Sciences

The constitutive relationship between applied stress and deformation rate of ice controls the dynamic behavior of the divide regions of ice sheets. I use finite-element modelling to explore three aspects of flow near a divide: (1) the increased relative activity of linear creep mechanisms at low stress, (2) the impact of sliding on stratigraphy, and (3) the role of crystal fabric in deformation.

Raymond (1983) showed that a special flow pattern emerges near an ice divide when ice is modelled using Glen's flow law. I show that the dominance of linear creep mechanisms at low stress tends to decrease the prominence of the special divide flow pattern. No Raymond bump forms in the isochrones, and younger ice appears deeper in the ice column, when compared to a more conventional Glen divide. When nonlinear rheological properties are coupled with a strongly anisotropic fabric, the special divide flow pattern is enhanced. Crystal fabric has little effect when the linear term dominates deformation rate. Finally, my model results show that basal sliding tends to redistribute the longitudinal stresses within the ice such that the special divide flow pattern is suppressed.

I use these results and available data to study Siple Dome, West Antarctica. The divide region of Siple Dome is presently in steady state, it has thinned at most 40 meters in the last 2000 years, and has been an elevated dome-like feature for much of Holocene. This contrasts with other sites around the Ross Sea Embayment with show modern thinning.

Using unique measurements of vertical strain throughout the depth of Siple Dome together with a finite-element flow model, I assess the relative importance of the linear term in the flow law compared to the effect crystal fabric. The linear term does contribute to flow at Siple Dome; the crossover stress is $k = 0.22$ bar. The band of strong crystal fabric around 750 m depth modifies the divide flow pattern, and, on the flanks, shear strain is concentrated within this layer, rather than in the deeper basal ice, creating a false-bed effect.

TABLE OF CONTENTS

List of Figures	iv
List of Tables	vi
Chapter 1: Introduction	1
1.1 Background	1
1.2 Motivation and Goals	2
1.2.1 Ice divide behavior	2
1.2.2 History of Siple Dome	5
1.3 Synopsis	5
1.4 Measurements and Analysis Techniques	7
1.4.1 Siple Dome data collection	7
1.4.2 Analysis techniques	8
Chapter 2: Ice Flow at Low Deviatoric Stress	10
2.1 Summary	10
2.2 Introduction	10
2.3 Glen's Isotropic Flow Law	12
2.4 Microphysical Processes at Low Deviatoric Stress	14
2.5 Modified Isotropic Flow Law	17
2.6 Divide Characteristic Stress	22
2.7 Finite-Element Ice-Flow Model	26
2.8 Results	27
2.8.1 Vertical velocity and depth-age scale	27
2.8.2 Isochrones and surface morphology	29
2.9 Conclusions	31
Chapter 3: Effects of basal sliding on isochrones and flow near an ice divide	36
3.1 Summary	36
3.2 Introduction	36
3.3 Finite-Element Ice-Flow Model	39
3.4 Results	43
3.5 Discussion	50

3.6	Conclusion	53
Chapter 4:	The Role of Anisotropy in Flow Near an Ice Divide	56
4.1	Summary	56
4.2	Introduction and Background	56
4.3	An Anisotropic Constitutive Law for Ice	59
4.4	Measurements of Anisotropy	62
4.5	Anisotropic Flow near an Ice Divide	62
4.6	Finite-Element Ice-Flow Model	65
4.7	Model Results and Discussion	69
4.8	Conclusions and Implications	71
Chapter 5:	Mass Balance and Behavior of Siple Dome, West Antarctica	78
5.1	Summary	78
5.2	Introduction	79
5.3	Mass Balance of a Polar Ice Sheet	81
5.3.1	Balance of processes	81
5.3.2	Measurements of accumulation rate	82
5.3.3	Measurements of surface vertical velocity	87
5.3.4	Slope correction term	98
5.3.5	Net ice-sheet thinning rate	98
5.4	Implications for Siple Dome	98
5.4.1	History of Siple Dome	100
5.4.2	Siple Coast dynamics	101
5.4.3	Deglaciation of the Ross Sea Embayment	105
5.5	Conclusions	108
Chapter 6:	The Crossover Stress, Anisotropy, and the Flow Law at Siple Dome	110
6.1	Summary	110
6.2	Introduction and Background	111
6.3	Case Study of Siple Dome	113
6.4	The Constitutive Law for Ice	116
6.4.1	A two-term isotropic flow law	116
6.4.2	An anisotropic modification to flow	117
6.5	Finite-Element Ice-Flow Model	119
6.6	Field Site: Siple Dome, West Antarctica (81.65° S and 148.81° W).	121
6.6.1	Model inputs	121
6.6.2	Data used to constrain model outputs	128

6.7	The Inverse Problem	133
6.8	Results and Discussion	135
6.9	Conclusions and Implications for Other Ice Divides	142
6.9.1	Linear creep mechanisms	142
6.9.2	Crystal fabric	145
6.9.3	Other divides	146
Chapter 7: Conclusion		148
7.1	A Flow Law for Ice	149
7.2	Basal Boundary Conditions	150
7.3	Siple Dome, West Antarctica	151
Bibliography		153
Appendix A: Notation		164
Appendix B: Derivation of the Glen Flow Law		166
Appendix C: Borehole Deformation Correction		168
C.1	Isotropic Flow Correction	168
C.2	Anisotropic Flow Correction	169
C.3	Synthesis	172
Appendix D: Anisotropic Ice Flow		177
D.1	Background	177
D.2	Analytical Derivation	178

LIST OF FIGURES

1.1	Map of the Siple Coast of West Antarctica.	3
2.1	Pattern of effective deviatoric stress at an ice divide.	15
2.2	Strain rate versus deviatoric stress for the linear and cubic terms.	21
2.3	The natural range of divide characteristic stress on Earth.	24
2.4	Characterization of ice divides.	25
2.5	Modelled vertical-velocity profiles for divide flow (assuming a range of Ω_{char}) and for flank flow for the Small West Antarctic Ridge (SWAR).	30
2.6	Modelled steady-state isochrones for three idealized ice divides.	32
2.7	Modelled surface morphology for the three divides.	33
3.1	Finite-element model geometry.	40
3.2	Longitudinal profile of basal velocity and surface elevation for a range of till viscosities.	44
3.3	Vertical- and horizontal-velocity profiles for a range of till viscosities.	45
3.4	Isochrones and effective viscosities for a range of till viscosities.	48
3.5	Variation in amplitude of Raymond Bump (relative to the ice sheet thick- ness) with height above bed.	51
3.6	Raymond Bump amplitude versus till viscosity.	52
3.7	Depth-age scale at the ice divide for varying till viscosities.	55
4.1	Enhancement in vertical strain rate due to anisotropy for combined simple and pure shear.	64
4.2	Enhancement in vertical strain rate due to anisotropy for Siple Dome.	66
4.3	Finite element mesh for model of idealized divide.	68
4.4	Cone angle profiles, model results as vertical and horizontal velocities	72
4.5	Vertical and horizontal velocities for an ice sheet with Siple Dome's cone- angle profile.	74
4.6	Isochrones produced by anisotropic flow.	75
4.7	Arch height versus depth.	76
5.1	Map of Siple Coast and the Ross Sea Embayment, West Antarctica.	80
5.2	Radio Echo Sounding Image of a cross section of Siple Dome.	84
5.3	Accumulation rate pattern across Siple Dome.	85

5.4	Cartoon of Coffee-Can method.	90
5.5	Diagram of optical-fiber vertical-strain rate instrument.	92
5.6	Vertical velocity profile at the divide as measured by optical-fiber strain sensors and ice flow model.	95
5.7	Vertical velocity profile at the flank as measured by optical-fiber strain sensors and ice flow model.	95
5.8	Map view of GPS survey network at the divide site used for determining horizontal ice flux.	97
5.9	Map view of GPS survey network at the flank site used for determining horizontal ice flux.	97
5.10	Thinning rates plotted on a cross section of Siple Dome.	99
5.11	Satellite image of Siple Dome and surrounding ice streams.	103
5.12	Ross Ice Shelf deglaciation.	107
6.1	Map of Siple Coast and the Ross Sea Embayment, West Antarctica.	114
6.2	Radar image of divide region of Siple Dome.	115
6.3	Finite element model geometry and mesh for Siple Dome.	122
6.4	Temperature field model input.	125
6.5	Cone angle, grain size, and temperature with depth at the divide.	127
6.6	Horizontal surface velocities from GPS stake surveys.	129
6.7	Wire-resistance and fiber-optic strain gauge data.	131
6.8	Misfit index for models output covering the 4-D parameter space.	136
6.9	Strain-rate profile for best fitting parameter set.	138
6.10	Sensitivity of the models to model parameters.	140
6.11	Velocity fields for best fitting model with surface evolution.	143
6.12	Inferred isochrones overlaid on radar data.	144
C.1	Evolution of borehole with time.	169
C.2	Vertical strain rate correction due to horizontal shearing: fiber.	170
C.3	Vertical strain rate correction due to horizontal shearing: wire.	170
C.4	Horizontal velocity profile at flank with anisotropy.	172
C.5	Deformation of the borehole due to horizontal motion.	173
C.6	Correction for the fiber instruments.	175
C.7	Correction for the wire instruments.	175
C.8	Total strain accumulated over time in the wire-resistance gauges.	176
D.1	a through e as a function of cone angle.	179
D.2	Matrix elements as a function of cone angle.	182
D.3	Coefficients for u_{xx} , w_{zz} , u_{zz} , w_{xx}	187

LIST OF TABLES

2.1	Model input parameters for three divides.	28
3.1	Finite-Element model parameters.	42
5.1	Average accumulation rates based on measured depth-age scale from ice core	87
5.2	Ice sheet thinning results.	88

ACKNOWLEDGMENTS

I have many people to thank for their support and help during my Ph.D. My advisor, Ed Waddington, deserves the lion's share of my appreciation. He has spent many hours answering questions and challenging my thinking. I also must thank Howard Conway, Charlie Raymond, and John Stone for their support and useful discussions on this project. Of course, this work would not have been possible with the contributions from my co-authors: Will Harrison, John Morack, Dan Elsborg, Mark Zumberge, Eric Husmann, Gordon Hamilton, Gregg Lamorey, Throstur Throsteinsson, Paul Jacobson, and Nadine Nereson. Also, I owe a lot to the whole Siple Dome Deep Drilling Program.

I am fortunate to have completed my Ph.D. work at the University of Washington with its fantastic glaciology program. I have benefitted greatly over the years from discussions with Bernard Hallet, Al Rasmussen, Nadine Nereson, Tony Gades, Tom Neumann, Throstur Thorsteinsson, Bob Hawley, Ben Smith, Ginny Catania, Dale Weinbrenner, Steve Warren, Kurt Cuffey, and the rest of my fellow graduate students. Also, I learned so much from all the "Northwest" Glaciologists, thank you.

I would not have enjoyed these six years in Seattle as much without the friends I have made. They deserve a special thanks for always being there to help me. In particular I'd like to thank Megan, Tracie, Bob, Michele, and Megan (yes, two Megans) for helping me start and continue the Girls on Ice Program; Jen, Darlene, Dawn, Chuck, Julia, and Shaun for being awesome housemates as well as friends; Meredith, Chase, Aaron, Marianne, Keira, Steve, Maarten, Andrea as well as many others for being fantastic friends.

My family also deserves more thanks than I can ever give. It has been great living here and being close to all my relatives and my history. Thank you Mom, Dad, Scot, Ginny, Gram, Omah, Boppa, Tom, Carol, Jonnie, Vic and the rest of my family.

And I must not forget to thank my cats for keeping me warm at night.

This dissertation is dedicated to Katherine, because many years ago, when we were small children, she taught me how to be me.

Chapter 1

INTRODUCTION

1.1 Background

In recent decades, many scientists have collaborated to piece together a history of Earth's climate from information stored in the ice sheets of Antarctica and Greenland. While some of this climate information is stored directly as chemical, structural, isotopic, and gaseous signatures in the preserved annual layers of snow, researchers can also gather additional clues from ice sheet behavior. Because large ice sheets respond dynamically to climate changes, observations of present behavior and large scale structure reflect past geometry, behavior, and climate forcings. An ice sheet's dynamic history provides important constraints for interpretation of ice-core data, but it also influences our understanding of how the ice sheet will respond to future changes in climate.

Much of the West Antarctic Ice Sheet is grounded below sea level, which makes it different from Earth's other present-day large ice sheets. It is also unique in that over 90% of its inland ice drains to the ocean through fast-flowing ice streams [McIntyre, 1985]. Ice streams have the ability to respond rapidly and possibly unstably to changes in their boundary conditions [Retzlaff and Bentley, 1993; Anandakrishnan and Alley, 1997, e.g.]. For this reason, many scientists have put emphasis on understanding the dynamics of the West Antarctic ice-stream system [Alley and Bindschadler, 2001].

Siple Dome (81.65° S and 148.81° W, Figure 1.1) is a ridge of slow-moving ice between Kamb Ice Stream and Bindschadler Ice Stream (also referred to as Ice Streams C and D, respectively) on the Siple Coast of West Antarctica, which drains into the Ross Sea. It has been a cornerstone in connecting these two important glaciological questions: the stability and dynamics of the ice stream system and the interpretation of ice-core data for

climate history. In that role it is certainly offering many eye-opening puzzles into ice-sheet behavior [*Taylor et al.*, in prep, e.g.].

1.2 Motivation and Goals

In this work I have two primary goals. The first is to explore the unique behavior of ice divides, the boundaries that separate the drainage basins of ice sheets. The second is to examine the behavior of Siple Dome, as an example of an ice divide, not only for its reflection of the general divide dynamics, but also to assess its history, which is key to the deglaciation of the West Antarctic Ice Sheet and the interpretation of the recently drilled ice core.

1.2.1 Ice divide behavior

As the location where the surface slopes and shear stresses approach zero, an ice divide maintains a unique stress regime: the ice is essentially in pure shear with lower deviatoric stresses than elsewhere on the ice sheet. This stress regime poses an interesting challenge for ice dynamics modelling because the typical assumption that longitudinal stress is negligible does not hold. Yet, ice divides are desirable locations for ice cores because the stratigraphy may be relatively undisturbed and the ice source is local. Thus, modelling the flow of ice in this region is crucial for extracting information from ice cores and understanding the histories and possible futures of ice sheets.

Near a divide, the effective deviatoric stress is dominated by the longitudinal stress rather than by the shear stress. Also, the magnitudes of the deviatoric stresses (both longitudinal and shear) are small relative to those on the flanks of the ice sheet. According to Glen's flow law for ice, effective viscosity is inversely proportional to the square of the stress [*Nye*, 1953; *Glen*, 1958]. Thus, the region with the lowest stress (near the bed at the divide), is more resistant to deformation than surrounding areas. Deformation is concentrated in the softer ice nearer the surface; the ice flow is refracted by the increase in viscosity in the low stress zone, producing a special flow pattern. *Raymond* [1983] first described the details of this special divide flow pattern and noted that the internal stratig-

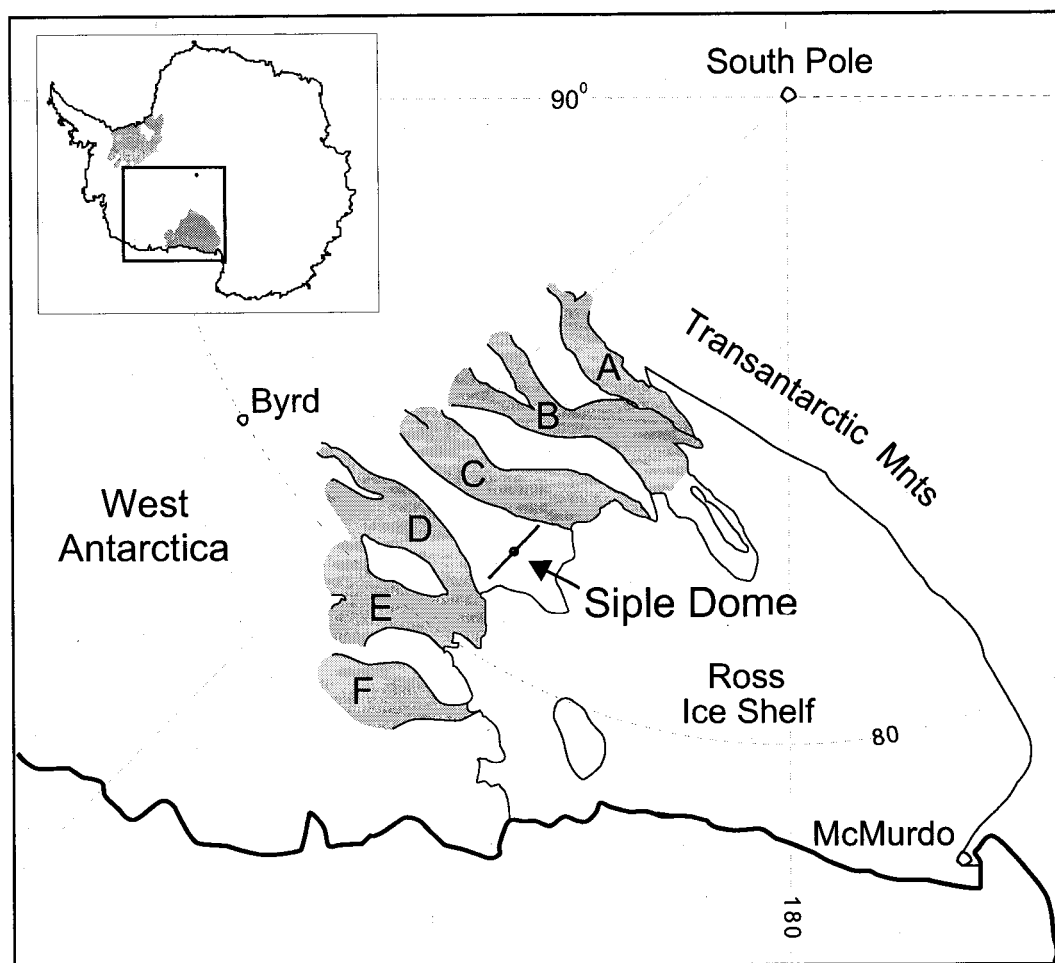


Figure 1.1: The Siple Coast and the Ross Sea Embayment, West Antarctica. Siple Dome (81.65° S and 148.81° W) is an inter-ice stream ridge on the Siple Coast of West Antarctica. Shaded regions represent fast flowing ice, including Mercer (A), Whillans (B), Kamb (C), Bindschadler (D), MacAyeal (E), and Echelmeyer (F) Ice Streams.

raphy at a steady-state divide would reflect this flow pattern, causing ice of a particular age to appear higher in the stratigraphic column at the divide than at the flank. Since the special divide flow pattern has a limited horizontal extent, blending into flank flow within one to two ice thicknesses from the divide, this flow pattern leads to an arch in the isochrones, commonly called a “Raymond bump”.

There are several reasons why a particular ice divide may not exhibit this “ideal” flow pattern. The first goal of this dissertation is to expand our understanding of this divide flow with respect to the ice-sheet boundary conditions and the rheological properties of ice.

The special divide flow pattern, and, therefore, the isochrone pattern that appears over time, is sensitive to different types of boundary conditions and to changes in these boundary conditions over time. *Nereson et al.* [1998a] explored the effects of changes in elevation of bounding ice streams (which can cause the divide to migrate). *Hvidberg* [1996] included realistic thermal boundary conditions, and *Nereson and Waddington* [2002] characterized isotherms more fully under migrating divides. I expand on these works by looking at the effect of basal sliding. Although Siple Dome is frozen to its bed, other divides may be warm enough at their base to slip at the ice–bedrock contact; Inland WAIS [*Morse et al.*, 2001], and Law Dome [*Budd et al.*, 1976] are examples.

In addition to boundary conditions, assumptions about the rheological properties of the ice can alter the predicted flow field. The deformation of ice may be affected by impurities [*Cuffey et al.*, 2000a; *Thorsteinsson et al.*, 1999, e.g.], grain size [*Cuffey et al.*, 2000b; *Goldsby and Kohlstedt*, 2001], and crystal anisotropy [*Azuma and Goto-Azuma*, 1996; *Castelnaud et al.*, 1996; *Thorsteinsson*, 2001, e.g.], especially because these properties vary with depth and horizontal position in an ice sheet. *Mangeney et al.* [1996] modelled the flow of anisotropic ice near an isothermal divide with a linear flow law for ice and found that the overall flow pattern differed minimally from that predicted using isotropic ice. Here, I use a model that combines the characteristics of anisotropic flow with a nonlinear constitutive relation to investigate how anisotropy perturbs the special divide flow pattern.

Finally, the degree to which ice behaves as a nonlinear fluid in the low-stress divide

region is still under debate. Conventionally, glaciologists have used Glen's Law, which describes ice as a power-law fluid with a cubic relation between stress and strain rate. It is possible that at low stresses the micro-scale mechanism driving ice flow shifts to a more linear creep mechanism [Langdon, 1996; Goldsby and Kohlstedt, 2001, e.g.]. My work with Ed Waddington (University of Washington) explores the effect of including a linear term in the flow law and the flow patterns that result from different combinations of linear and cubic flow laws.

1.2.2 History of Siple Dome

The summit of Siple Dome is a 1000 meter-thick ice divide; ice flows northeast about 60 km into Bindschadler Ice Stream and southwest a similar distance into Kamb Ice Stream. Because of its location on the active Siple Coast, its history may reflect the history of the region and provide clues to questions such as: Is the recent stoppage of Kamb Ice Stream [Retzlaff and Bentley, 1993] an anomalous event, or do ice streams frequently stop and start? Is the ice along the Siple Coast still responding to the warming at the end of the last ice age? What did the Ross Sea Embayment look like during the last ice age? The work that I present here will provide constraints on the answers to these and other questions.

Siple Dome is an ideal site for this investigation for several reasons. First, it has been the location of intensive field research over the last decade as the site of a U.S. Antarctic Program deep ice core. Second, its geometry lends itself to numerical modelling: as a linear, ridge-like feature it can be modelled in cross-section as 2-D plane-strain flow. Third, the layers that appear in low-frequency radar images suggest that it exhibits some degree of the special divide flow pattern [Nereson *et al.*, 1998b]. And finally, it is the most stable of the inter-ice-stream ridges, and therefore should hold the longest record.

1.3 Synopsis

This dissertation is composed of five stand-alone manuscripts that fall into two categories: theoretical studies of ice divides (Chapters 2 through 4) and dynamical analyses of Siple

Dome, West Antarctica (Chapters 5 and 6). Chapters 2 and 3 have been accepted for publication in the *Journal of Glaciology* and the *Annals of Glaciology*, respectively. The other three chapters are in preparation for publication. Since each chapter is a stand-alone manuscript, some of the introductory material in each chapter is repeated. Also, since other researchers contributed significantly to this work (as noted at the beginning of each chapter), I consistently use the pronoun ‘we’ instead of ‘I’.

In the first three chapters, I explore the effects on the flow at an idealized ice divide of including a linear term in Glen’s flow law, Glen’s Law (Chapter 2), of sliding at the ice–bedrock contact (Chapter 3), and of incorporating anisotropy in the flow law (Chapter 4). The first chapter follows from initial work by *Waddington et al.* [1996] to explore the effect of the linear term in the flow law on the divide flow pattern using the finite-element flow model originally developed by *Raymond* [1983].

In Chapter 2, I use a finite-element flow model developed by Paul Jacobson [*Jacobson*, 2001] to examine the effect of basal sliding on the flow at a divide. In the model, I vary the viscosity of a thin layer of linearly-viscous till at the ice–bedrock contact to simulate various amounts of sliding.

In Chapter 3, I look closely at the effect of a preferred crystal orientation in the ice. The preferred crystal orientation near an ice divide tends to be vertically oriented and can be described by an effective cone angle (the half angle of a vertical cone within which uniformly distributed c-axes produce deformation comparable to that from the real fabric; the method of determining effective cone angle depends on whether the fabric information is a sonic velocity or a Schmidt plot). I compare divides with different cone-angle profiles, including one based on the sonic log measured at Siple Dome.

Chapters 5 and 6 comprise the dynamical analyses of Siple Dome. In Chapter 5, I bring together the results of three independent studies of the mass balance of Siple Dome. These studies all agree that ice flow at Siple Dome is presently nearly in balance with the accumulation of snow on the surface. Then I examine the implications of this result for the larger scale questions regarding the past fluctuations of the adjacent ice streams and the deglaciation of the Ross Sea Embayment.

In Chapter 6, I compare finite-element models of Siple Dome to deformation measure-

ments, primarily the *in situ* vertical strain data, to investigate the dominant deformation processes affecting flow near an ice divide. Specifically, I examine the relative importance of deformation due to crystal anisotropy and due to near-linear creep mechanisms in the pattern of flow near the divide. This study provides insight into the general behavior of ice divides.

1.4 Measurements and Analysis Techniques

The bulk of this work relies on numerical modelling to interpret measurements of ice properties and deformation. As such, it builds on the work of many other scientists.

1.4.1 Siple Dome data collection

The data that I use were collected during more than 10 years of collaborative field work at Siple Dome. In 1994 and 1996, Charlie Raymond, Howard Conway, Nadine Nereson (University of Washington) and Ted Scambos (University of Colorado) set up and surveyed a stake network using Global Positioning System (GPS) receivers to study the surface flow of Siple Dome. During the same field seasons, Tony Gades (UW) and Bob Jacobel (St. Olaf College) collected low-frequency radar data. Nadine Nereson and Charlie Raymond collected a profile using ground-penetrating radar (high-frequency). John Morack (University of Alaska, Fairbanks) and I resurveyed the stake network in 1999.

In 1996, the United States Antarctic Program began a deep drilling project near the summit of Siple Dome. Although many researchers are involved in this project, I primarily rely on the layer-counting time-scale by Richard Alley (Pennsylvania State University) and Ken Taylor (Desert Research Institute), the preliminary grain-size data measured by Larry Wilen (University of Colorado), the density profile for the upper ice and firn (Joan Fitzpatrick) and the borehole sonic velocity log collected by Gregg Lamorey (Desert Research Institute). Independent temperature logs measured in the main borehole by Gary Clow (USGS), Bob Hawley (University of Washington) and Ed Waddington and in a summit borehole drilled with hot water by Hermann Englehardt (California Institute of Technology) provide constraints on the temperature field. The sonic log was converted

to cone angle for incorporation into the models by Throstur Thorsteinsson (University of Washington and University of Iceland). Many of these data sets are still unpublished and I use them here with permission from the researchers listed.

Numerous researchers have measured accumulation rate on Siple Dome. I use three of those data sets. Gordon Hamilton (University of Maine) measured modern accumulation rates across Siple Dome using Gross- β measurements on shallow cores [Hamilton, 2001]. Also, the University of Washington’s low-frequency radar and high-frequency radar images (interpreted by Nadine Nereson and me) provided relative accumulation patterns across the divide. Gordon Hamilton also measured the vertical velocity of the firn with the “coffee-can” technique, which uses markers buried in the firn and monitored by GPS [Hamilton, 2001].

The most essential data for this study are *in situ* vertical strain-rate measurements made in collaboration with the University of Alaska, Fairbanks (Will Harrison, Dan Elsberg, and John Morack) and the University of California, San Diego (Mark Zumberge and Eric Husmann). UA designed wire-resistance strain gauges in a Wheatstone bridge configuration to make continuous point measurements of deformation [Zumberge *et al.*, 2002; Elsberg *et al.*, in review]. UCSD developed fiber-optic position sensors, which measure annual strain rates averaged over a range of depth intervals from 174 to 800 meters.

1.4.2 Analysis techniques

Such a varied data set required the use of numerous analysis techniques. My goal was to understand the dynamics of ice flow near a divide; this study relies, therefore, on numerical modelling and inverse techniques. In some cases, simple kinematic models of ice flow were sufficient to describe the phenomena reflected in the observations; however, the bulk of my analysis required finite-element models.

We used two different finite-element ice-flow models. Both are two-dimensional plane-strain flow models that describe flow over a cross section of an ice divide. The first was developed by Charlie Raymond over twenty years ago. It has been modified and expanded since then by Ed Waddington, Christine Schøtt Hvidberg (University of Copenhagen), David Morse (University of Washington and University of Texas), and Nadine Nereson.

We used this model in Chapter 2.

Recently, a new thermo-mechanically coupled finite-element model was developed by Paul Jacobson (University of Washington) This model allows sliding at the bed (Chapter 3) and the incorporation of an anisotropic flow law (Chapters 4 and 6). Throstur Thorsteins-son developed the anisotropic model. The specific analytical description of anisotropy implemented in the Jacobson FEM is presently unpublished, I include the derivation used here as an appendix (Appendix D). The details of the relevant models and their imple-mentation are described in the relevant chapters.

Chapter 2

ICE FLOW AT LOW DEVIATORIC STRESS

This chapter is in press under the same title in *Journal of Glaciology*, with co-author E. D. Waddington from Earth and Space Sciences Department, University of Washington. Helpful review comments were provided by R. Greve, L. Tarasov, C. Raymond, T. Thorsteinsson, W. Harrison, and an anonymous reviewer.

2.1 Summary

The effective viscosity of ice depends upon many factors, including temperature, deviatoric stress, crystal orientation, and impurities. A flow law that includes these factors and is simple to implement is a requirement for numerically efficient ice-flow models. The dominant micro-scale flow mechanism changes as temperature, deviatoric stress, or grain size changes. For both anisotropic and isotropic constitutive relations, this shift in dominant flow mechanism is expressed as a change in the stress exponent. We study the effects of this shift in stress exponent on ice flow using a two-term flow law for isotropic ice. Our stress-strain-rate relationship does not explicitly describe the micro-scale processes of ice deformation; however, it encompasses a range of deformation behaviors with a simple law. In terrestrial ice, a flow-mechanism shift may occur in low-deviatoric-stress regions near ice divides, resulting in a near-linear constitutive relationship for ice flow. Compared to a nonlinear (Glen) divide, a divide dominated by a near-linear flow mechanism has vertical-velocity profiles that are similar at divide and flank sites, internal layers that do not develop a Raymond bump, and a steady-state surface profile that is more rounded near the divide.

2.2 Introduction

Information about the history of Earth's climate is preserved in annual layers in ice sheets. Our access to these annual layers, however, is limited to ice cores, boreholes, and ice-

penetrating radar. Full interpretation of these data in terms of climate and ice-sheet history requires an understanding of local ice flow through accurate ice-flow modelling.

By comparing paleoclimate ice-core records or radar images with predictions from ice flow models, scientists can infer constraints on the historical variations in accumulation rate, surface elevation, and surface temperature. For example, *Paterson and Waddington* [1984] deduced past accumulation rates on Devon Island from the thickness of stratigraphically-dated annual layers in ice cores. *Nereson et al.* [1998b] used a model of ice flow to infer recent flow history from radar internal reflections (isochrones) at Siple Dome, West Antarctica. *Hvidberg et al.* [1997] modelled the flow from the GRIP ice-core site to the GISP2 site in Greenland to aid in the interpretation of the cores. *Marshall and Cuffey* [2000] studied the effects of a wandering divide at Greenland’s summit on ice-core records. Large-scale models of present and paleo-ice-sheets relate geophysical and geologic evidence such as post-glacial uplift and glacial landforms to ice-core climate histories [e.g. *Marshall et al.*, 2000; *Peltier et al.*, 2000; *Greve*, 1997].

Most ice-sheet models use a constitutive relation for ice based on *Glen’s Law* [*Glen*, 1958]: $\dot{\epsilon}_{\text{eff}} = A\tau_{\text{eff}}^3$, where $\dot{\epsilon}_{\text{eff}}$ is the effective strain rate (the second invariant of the strain-rate tensor), τ_{eff} is the effective deviatoric stress (the second invariant of the stress tensor), and A is known as the *softness parameter*.¹ This relationship was generalized to a tensor form by *Nye* [1957]. Experiments and field observations show that Glen’s Law provides a good approximation to ice flow at many locations in glaciers and ice sheets, but its applicability is not universal. The deformation rate of ice is a function of many properties of the ice; impurity content, crystal orientation, and temperature are examples. Through detailed observations and modelling of ice sheets and glaciers, and through laboratory experiments on ice samples, deviations from Glen’s Law have become more evident. There is an increasing need to formulate a flow law that is more widely applicable and is also simple enough to be incorporated easily into current flow models.

There are multiple mechanisms at work in the deformation of ice, and different mechanisms dominate under different conditions. Glen’s Law [*Glen*, 1958], with an exponent

¹Appendix A is a table of the notation.

of 3, describes flow dominated by dislocation glide on the basal plane, rate-limited by dislocation climb [e.g. *Alley, 1992; Weertman, 1973*]. Another interpretation of Glen’s Law is that it expresses the transition region between dislocation creep with an exponent of 4 and a grain-size-sensitive process with an exponent of 1.8 [*Goldsby and Kohlstedt, 2001; Durham and Stern, 2001*]. In polycrystals, the dominant mechanisms shift as deviatoric stress decreases. At the lowest deviatoric stresses, Newtonian flow prevails, according to studies of polycrystalline metals [e.g. *Langdon, 1991, 1996*]. There is currently debate over which mechanisms dominate in various deviatoric-stress and temperature regimes within an ice sheet. We approach this discussion from an ice-sheet modelling point of view. A flow law that is non-mechanism-specific, but has the ability to encompass a wide range of behaviors would be useful for ice-sheet flow models. We formulate a phenomenological isotropic flow law, and incorporate it into a two-dimensional plane-strain steady-state finite-element model to explore how a shift in mechanism at low deviatoric stress expresses itself in ice sheets. Anisotropic flow laws [*Azuma, 1994; Azuma and Goto-Azuma, 1996; Castelnau et al., 1996; Thorsteinsson, 2001*] typically use a power law with a specified stress exponent, similar to Glen’s Law, to define deformation rate on the basal plane of individual crystals; thus, our results will apply to models of anisotropic ice as well.

2.3 Glen’s Isotropic Flow Law

Glen’s Law [*Glen, 1958*] relates deviatoric stress to strain rate, assuming that ice is an incompressible, isotropic polycrystal that obeys a power-law form similar to polycrystalline metals [*Glen, 1955; Nye, 1953*]. The most-widely-used expression of Glen’s Law is

$$\dot{\epsilon}_{ij} = EA_0 e^{-\frac{Q}{RT}} (\tau_{\text{eff}}^2)^{\frac{n-1}{2}} \tau_{ij}. \quad (2.1)$$

Appendix A contains a description of all the variables. In this equation, $\dot{\epsilon}_{ij}$ and τ_{ij} are the strain-rate and stress tensors, respectively, τ_{eff} is the effective shear stress, and n is a constant (usually equal to 3). A_0 (often called the *softness parameter*) is a constant that describes clean, isotropic, Holocene glacier ice, with units of $\text{Pa}^{-n}\text{s}^{-1}$. Strain rate is a function of temperature according to an Arrhenius relationship where Q is the thermal

activation energy for creep, R is the gas constant, and T is temperature. The coefficient E is the *enhancement factor*, a non-dimensional multiplier describing the increase or decrease in strain rate caused by variations in crystal size, impurity content, and crystal orientation. E is a function of position and, in the case of crystal orientation, local deformation field. The necessity of this correction factor is one indication of the need to refine Glen's Law. There is a slight dependence of strain rate on hydrostatic pressure [Paterson, 1994], but we follow standard practice and neglect it.

Laboratory and field studies have focused on empirically determining A_0 and n , assuming $E = 1$. Weertman [1973], Budd and Jacka [1989], Goldsby and Kohlstedt [2001], and Paterson [1994] provide reviews. Currently, most ice-sheet and glacier models use $n = 3$ and A_0 as given by Table 5.2 in Paterson [1994]. This formulation, however, is inadequate in some situations. For example, in strongly anisotropic ice, E is insufficient for expressing all but the simplest deformation fields. Equation (2.1) is inappropriate for ice with a strong crystal fabric [e.g. Azuma and Goto-Azuma, 1996; van der Veen and Whillans, 1994; Thorsteinsson, 2001].

In low-deviatoric-stress environments, particularly in the central regions of ice sheets, Glen's Law predicts unusually high viscosities. By rearranging Equation (2.1) to the standard form for a linear viscous fluid,

$$\tau_{ij} = 2\eta_{\text{eff}}\dot{\epsilon}_{ij}, \quad (2.2)$$

we define an effective viscosity, η_{eff} :

$$\eta_{\text{eff}} = [2EA_0e^{-\frac{Q}{RT}}(\tau_{\text{eff}}^2)^{\frac{n-1}{2}}]^{-1}. \quad (2.3)$$

For any n greater than 1, this viscosity goes to infinity as τ_{eff} goes to zero; this may result in a singularity in the viscosity at the base of the ice under a divide. In polycrystalline metals, however, the viscosity is bounded at low deviatoric stress by a transition to a linear regime [Langdon, 1991]. We can expect a similar transition to appear in flow mechanisms in ice.

The validity of Glen’s Law with $n = 3$ has been verified with some confidence in the laboratory and field down to $\tau_{\text{eff}} = 0.3$ bar (30 kPa) [Budd and Jacka, 1989]. However, Duval *et al.* [2000] suggest that $\tau_{\text{eff}} = 2$ bar is the lower limit to the validity of Glen’s Law with $n = 3$; at lower deviatoric stresses, $n < 2$. Since a deviatoric stress of less than 0.5 bar is not uncommon in divide regions of ice sheets, a constitutive relation for ice in ice-sheet models should incorporate behavior appropriate for low-deviatoric-stress flow regimes, especially those models that focus on near-divide regions.

Meier [1958] suggested adding a linear term to the flow law, explaining, “One should expect that the resultant flow of a polycrystalline mass would be the sum of contributions from at least two mechanisms.” The additional term implies that there is a shift in mechanism as the deviatoric stress decreases; but because Glen’s Law works most of the time, many researchers neglect the added complexity of an additional term. Also, at low deviatoric stresses and low temperatures, the laboratory experiments needed to determine the best flow-law parameters could take millennia to run. (For example, at deviatoric stresses and temperatures typical of Siple Dome, West Antarctica, 0.2 bar and -15° C, a sample could require ~ 1500 years to undergo 10% strain.) In the lower-deviatoric-stress regions of ice sheets (Figure 2.1), however, this change in behavior may be significant, particularly for interpreting ice-core or other data collected near an ice divide.

2.4 Microphysical Processes at Low Deviatoric Stress

Identifying the mechanisms at work in ice deformation is no easy chore, and we do not intend to do it here. Weertman [1973], Lliboutry [1987], Alley [1992], and Goldsby and Kohlstedt [2001] provide background information on the microphysical processes in ice. We do, however, want to highlight the processes that may make a multi-term flow law necessary at low deviatoric stresses.

At deviatoric stresses in the range 0.5 bar (50 kPa) to 1.5 bar (150 kPa), typical of ice in valley glaciers and in all but the central and near-surface regions of ice sheets, *dislocation glide* on the basal plane is thought to dominate deformation. During dislocation glide, dislocations move through the crystal along the basal plane. An applied stress causes

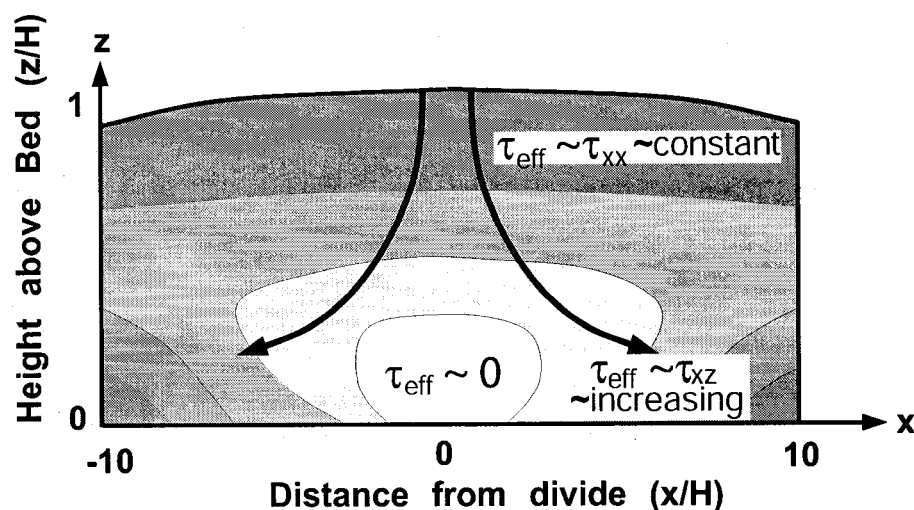


Figure 2.1: Cartoon showing the approximate pattern of effective deviatoric stress, τ_{eff} , for a typical ice divide. The arrows show approximate ice-flow trajectories. τ_{xx} is the longitudinal stress, which cannot be ignored in the region near an ice divide. It is largest near the surface and approaches zero near the bed [Raymond, 1983]. τ_{xz} is the horizontal shear stress. It is zero at the divide and increases with depth and with distance from the divide. The extent of the region of very low deviatoric stress (white) will vary with the thickness and the accumulation rate.

dislocations to multiply and get tangled up or stuck on obstacles (grain boundaries, solid impurities), thereby increasing strain energy in the crystal. Recovery processes work to decrease the strain energy. They include the creation and migration of grain and sub-grain boundaries (through polygonization or twinning), the diffusion of vacancies and interstitials, and the nucleation of new grains. In addition, crystals tend to rotate such that their c-axes move toward the principal compressive deviatoric stress. This rotation often requires a modification of grain shape through diffusion of vacancies, movement of dislocations along and within grain boundaries, and grain-boundary migration. In an ice sheet, all of these processes work to create characteristic grain sizes and crystal fabrics that depend on temperature and strain histories.

The third power of deviatoric stress in Glen's Law is an empirical result. Weertman [1973] discussed the dislocation-glide theory to support these results. According to Weertman [1973], Glen's Law can be derived from two assumptions. First, dislocations move

along the basal plane with a velocity proportional to the deviatoric stress. Second, balance between dislocation-multiplication and recovery processes determines the dislocation saturation density, which is proportional to the square of the stress deviator. This second assumption equates the average internal stress (due to the presence of dislocations) to the applied stress.

As deviatoric stress in the ice decreases, the dominant mechanism of flow changes. There are several processes that may be involved: *diffusion creep*, *Harper-Dorn creep*, and *grain boundary sliding* (superplasticity). In diffusion creep, a grain deforms by diffusion of vacancies from regions of low compressive stress to regions of high compressive stress through the crystal (*Nabarro-Herring creep*) and along boundaries (*Coble creep*). Likewise, interstitials move from regions of high compressive stress to regions of low compressive stress. Theoretically, this results in a linear stress-strain-rate relation [Lliboutry, 1987]. Because the high- and low-stress source and sink regions are most often along grain boundaries, this process depends on grain size. With the large grain sizes found in natural ice (1 mm to 10 cm), Lliboutry [1987] and many others consider diffusion creep to be negligible.

Harper-Dorn creep is similar to dislocation glide in that deformation is dominated by motion of dislocations along the basal plane; however, in this case, the dislocation density is independent of stress. This occurs when dislocation-multiplication processes proceed so slowly that the rate of recovery due to diffusion and grain-boundary migration dominates [Alley, 1992; Montagnat and Duval, 2000]; thus, dislocations disappear at the same rate as they are being created. According to this theory, $n \approx 1$ and the deformation rate has a negligible dependence on grain size.

Grain-boundary sliding is strongly dependent on grain size. In this superplastic deformation, almost all of the dislocations are on the grain boundaries. The deformation is primarily a result of dislocation climb and glide within the grain boundaries. Langdon [1991] and Langdon [1994] described this type of deformation and its relationship with other deformation mechanisms [see Langdon, 1991, Figure 7]. For grain-boundary sliding in metals, Langdon [1994] showed evidence that $n \sim 2$ for small grain sizes and $n \sim 3$ for larger grain sizes. Recently, Goldsby and Kohlstedt [1997] found evidence for grain-

boundary sliding in ice of small crystal size (3 to 200 μm) at moderate-to-high deviatoric stresses (relative to stresses found in existing ice sheets). They found $n = 1.8$ best fit their data. Whether this process dominates in natural ice (with much larger crystals and lower stresses) and what value of stress exponent is most applicable is still under debate. Grain size is not an independent parameter, and feed-backs between grain-growth processes and grain-size-sensitive deformation processes are not fully understood [Durham and Stern, 2001; Duval and Lliboutry, 1985]. Furthermore, larger crystals often have complex shapes and thus additional processes (for example, polygonization or grain-boundary migration) must be present to prevent cavities or overlapping grains, or to relieve stress concentrations. Even if grain-boundary sliding does become dominant at lower deviatoric stress, we expect that it must be superseded at still lower deviatoric stress by an $n = 1$ process by analogy with polycrystalline metals [Langdon, 1991].

2.5 Modified Isotropic Flow Law

Because ice in an ice sheet moves through regions of different deviatoric stress configurations, it is necessary to explore the assumption that strain rate depends only on the contemporary temperature and state of deviatoric stress. With this assumption, temperature and strain histories affect strain rate only through the grain size and crystal orientation that they produce. In other words, is ice moving through non-uniform deviatoric-stress fields slowly enough that its strain rate equilibrates with the local deviatoric-stress field, or are deviatoric-stress gradients also important? It is commonly assumed that ice “forgets” past stress conditions after the ice has undergone 10% total strain [defined as steady-state creep, Paterson, 1994, p.83]. The length-scale for significant changes in the deviatoric stress near an ice divide is one to several ice thicknesses [Raymond, 1983]. We express a characteristic length-scale, δ , over which ice acquires 10% total strain as:

$$\delta \approx 0.1 \frac{|\mathbf{u}|}{\dot{\epsilon}_{\text{char}}}, \quad (2.4)$$

where $|\mathbf{u}|$ is the velocity magnitude. A characteristic strain rate, $\dot{\epsilon}_{\text{char}}$, can be derived from the accumulation rate, \dot{b} , and the characteristic thickness, H ($\dot{\epsilon}_{\text{char}} \approx \dot{b}/H$). The speed, $|\mathbf{u}|$,

also scales with the accumulation rate. Thus, the characteristic length scale for 10% strain is $\delta \approx 0.1H$. Since $0.1H$ is much smaller than the scale of typical deviatoric-stress-field variations (except perhaps near bedrock bumps), we can assume that the strain-rate field near a divide is a function only of the contemporary deviatoric-stress field. This allows us to confidently write an ice-sheet-scale flow law that relates the strain rate to only the co-existing state of deviatoric stress in the ice and the co-existing ice properties.

Attention has recently focused on methods for relating deformation rate to anisotropic crystal fabric [e.g. *Azuma, 1994; Castelnau et al., 1996; Lliboutry, 1993; Thorsteinsson et al., 1999*]; impurities [e.g. *Cuffey, 1999; Paterson, 1991; Thorsteinsson et al., 1999*]; and grain size [e.g. *Cuffey et al., 2000b; Goldsby and Kohlstedt, 1997, 2001*]. In simple cases, these effects can be incorporated into the enhancement factor, E . In anisotropic flow laws for polycrystals, however, Glen’s Law is often abandoned in favor of one that details the strain rate of individual crystals within the polycrystalline aggregate, using a nonlinear constitutive relation for deformation along basal planes. For example, a flow law of this type worked well in separating crystal fabric and impurity effects on the shear strain rates measured in the Dye 3 borehole in Greenland [*Thorsteinsson et al., 1999; Thorsteinsson, 2000*].

These modifications to Glen’s Law, however, are incomplete. If the mechanism of deformation changes in low-deviatoric-stress regions of ice sheets, then a change in the enhancement factor, E , or implementation of a fully anisotropic flow law that maintains the $n = 3$ assumption cannot accurately describe the flow; a change in the exponent of the constitutive relation is also necessary.

There are two ways to combine creep rates of multiple mechanisms: *independently* and *sequentially* [*Langdon and Mohamed, 1977*]. In sequential processes [sometimes called dependent processes, *Durham and Stern, 2001*], the two mechanisms interact such that the slowest process is rate-limiting. The observed strain rate, $\dot{\epsilon}$ is determined through $1/\dot{\epsilon} = \sum_i 1/\dot{\epsilon}_i$, where $\dot{\epsilon}_i$ are the strain rates for individual mechanisms. If two mechanisms operate independently, then the fastest process dominates flow, and their strain rates sum: $\dot{\epsilon} = \sum_i \dot{\epsilon}_i$. In ice, most data [e.g. *Colbeck and Evans, 1973; Goldsby and Kohlstedt, 2001; Langdon, 1973; Durham et al., 2001*] show that the stress exponent in the flow law increases

with increasing deviatoric stress; this is a characteristic of independent processes. *Goldsby and Kohlstedt* [2001] did find sequential processes in some of their experiments, but only in their finest-grain samples ($3\mu\text{m}$); therefore, it is not likely to affect the flow of ice sheets. *Peltier et al.* [2000], *Goldsby and Kohlstedt* [2001], and *Durham et al.* [2001] suggest a flow law in which the total strain rate is an independent and sequential combination of four different mechanisms. This type of constitutive relation has also been found for polycrystalline metals [*Langdon*, 1991]. Such a relation is useful for studies of laboratory-scale ice deformation, but becomes less appealing at larger scales if it means we have to track particle size distributions as well as temperature and fabric.

While the debate over dominant mechanisms continues, we take a pragmatic approach to refining Glen’s Law for modelling ice sheets. We propose a multi-term flow law that can approximate the expected behavior from a combination of mechanisms. We expand Equation (2.1) to three terms and include a possible grain-size dependence. Our flow law is:

$$\dot{\epsilon}_{ij} = \sum_{m=1}^3 \frac{E_m A_{o_m}}{d^{p_m}} e^{-\frac{Q_m}{RT}} (\tau_{\text{eff}}^2)^{m-1} \tau_{ij}, \quad (2.5)$$

where A_o and E have the same meanings as in Equation (2.1), but may be different for each term. d is the average grain size, and p_m is a constant for each term.

For a given grain size, d , the three terms in this equation are equivalent to three versions of Equation (2.1) with $n = 1, 3$, or 5 . Laboratory and field studies have inferred exponents ranging from $n = 1$ to $n = 4.2$ [*Weertman*, 1973, Table 2]. For example, *Goldsby and Kohlstedt* [2001] fit $n = 1.8$ and $n = 2.4$ to their data in studies of grain-boundary sliding; *Wolff and Doake* [1986] argued that an $n = 1$ relation best predicts the borehole-deformation data from Devon Island and the depth-age profile at Camp Century. Many of these data can be fit (within their uncertainties) with our formulation in Equation (2.5) by selecting the appropriate softness parameter and enhancement factor for each term. For ice-sheet-scale modelling purposes, it is not always necessary to have a separate term for each suspected mechanism, as long as the form that is used approximates the correct behavior. Indeed, this formulation is not intended to individually describe the microphysics of each deformation mechanism, but to provide a simple empirical form to represent deformation

over a wider range of conditions than Glen's Law with $n = 3$.

Several other authors, in addition to *Meier* [1958], have found multi-term flow laws to be useful. *Lliboutry* [1969] used a three-term polynomial to accommodate the spread of existing laboratory and field data, as well as to achieve mathematical simplicity. *Colbeck and Evans* [1973] fit their data from Blue Glacier to a three-term flow law similar to Equation (2.5). *Hutter et al.* [1981] introduced a linear term to avoid the singularity in viscosity (Equation 2.3) in Glen's Law as the deviatoric stress goes to zero. *Smith and Morland* [1981] needed a polynomial flow law to express the stress-strain-rate relationship for the wide range of empirical data in the literature. *Waddington et al.* [1996] explored the effects of the linear term on ice divides. In this paper, we expand on *Waddington et al.* [1996] and show that a linear term can have a significant impact on some ice-sheet modelling applications.

To explore the effect of a shift in mechanism at low deviatoric stress, we focus on just the first two terms, representing linear and Glen ($n = 3$) stress-strain-rate dependencies:

$$\dot{\epsilon}_{ij} = \underbrace{\left[\frac{E_1 A_{o1}}{dp_1} e^{-\frac{Q_1}{RT}} \right]}_{\text{linear term}} + \underbrace{\left[\frac{E_2 A_{o2}}{dp_2} e^{-\frac{Q_2}{RT}} (\tau_{\text{eff}}^2) \right]}_{\text{Glen term}} \tau_{ij}. \quad (2.6)$$

By factoring out the coefficients of the second term, Equation (2.6) can be rewritten:

$$\dot{\epsilon}_{ij} = \Gamma [k^2 + \tau_{\text{eff}}^2] \tau_{ij}, \quad (2.7)$$

where

$$\Gamma = \frac{E_2 A_{o2}}{dp_2} e^{-\frac{Q_2}{RT}} \quad (2.8)$$

is the coefficient for normal Glen flow when $p_2 = 0$ (there is no crystal size dependency in Glen's Law) and

$$k = \left[\frac{E_1 A_{o1}}{E_2 A_{o2}} \frac{dp_2}{dp_1} e^{-\frac{Q_1 - Q_2}{RT}} \right]^{1/2}. \quad (2.9)$$

In this formulation, k , the *crossover stress*, is the effective deviatoric stress at which the linear and cubic terms contribute equally to the total strain rate (see Figure 2.2). k is the square root of the ratio of the coefficients of the two terms in Equation 2.6. The effective

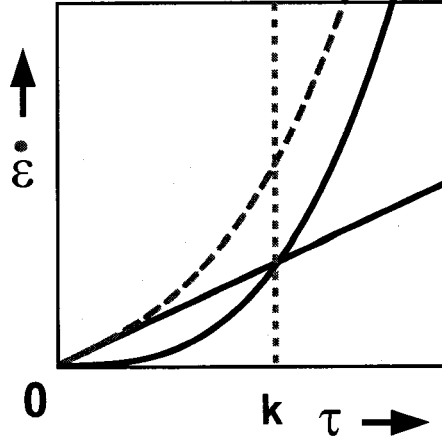


Figure 2.2: Strain rate versus deviatoric stress for the linear and cubic terms in Equation (2.7). The dashed curve shows the total strain rate (i.e. the sum of the two terms). k is the crossover stress at which the linear and cubic terms contribute equally to the total strain rate.

viscosity is now $\eta_{\text{eff}} = (2\Gamma[k^2 + \tau_{\text{eff}}^2])^{-1}$, which remains finite as $\tau_{\text{eff}} \rightarrow 0$ (compare with Equation (2.3)). The expression for k in Equation (2.9) highlights the sensitivity of the crossover stress to properties of the ice such as temperature, thermal activation energy, and grain size. For example, if the micro-scale flow mechanisms have different thermal activation energies, then k^2 will depend on temperature through a factor of $e^{-(Q_1 - Q_2)/RT}$. This effect can be large: a difference in activation energy of 10 kJ mol^{-1} will result in a difference of approximately one order of magnitude in k for typical ice sheet temperatures. *Langdon and Mohamed* [1977] have provided a detailed description of the effect of thermal activation energies for both sequentially and independently combined creep processes in metals.

As another example, two of the three mechanisms (diffusion creep and grain-boundary sliding) that may dominate at low deviatoric stress depend on grain size; therefore, we include a grain-size dependence in our flow law. Unless $p_1 = p_2$, the crossover stress will also depend on grain size. Creep rate is independent of instantaneous grain size for the normal Glen regime [*Paterson*, 1994], so probably $p_2 = 0$ in Equation (2.5). *Goldsby and*

Kohlstedt [1997] fit their data with a grain-size dependence of $p = 1.4$ for a flow law with an exponent of $n = 1.8$. To be represented by Equation (2.6), however, their data would have to be re-analyzed to find the best-fitting parameters.

Crossover stress may depend on other ice properties as well. For example, since the $n = 1$ Harper-Dorn creep mechanism is based on dislocation glide on the basal plane, it likely has the same crystal-orientation dependence as $n = 3$ dislocation creep. If these two mechanisms dominate, and crystal orientation is expressed approximately through enhancement factors, E_m , then $E_1 = E_2$ in Equation (2.9), and k is independent of crystal orientation. A diffusional process or grain-boundary sliding, however, may be independent of crystal orientation. If one of these processes dominates deformation rate at low deviatoric stress, then $E_1 \neq E_2$ and k depends on crystal orientation.

A useful parameter that can readily show which term (linear or Glen) is dominant anywhere in an ice sheet is:

$$\Omega = \left[\frac{\tau_{\text{eff}}^2}{k^2} \right]^{1/2}. \quad (2.10)$$

Ω is a non-dimensional stress that describes the relationship between the effective deviatoric stress and the crossover stress. The effective deviatoric stress is a function of a divide's geometry and climate, while the crossover stress is a material property independent of geometry and accumulation rate, but dependent upon other ice properties according to Equation (2.9). The flow law expressed in terms of Ω is:

$$\dot{\epsilon}_{ij} = \Gamma k^2 [1 + \Omega^2] \tau_{ij}. \quad (2.11)$$

2.6 Divide Characteristic Stress

The effect of the linear term in Equation (2.11) on an ice sheet depends on the distribution of deviatoric stress in the ice sheet and on the value of the crossover stress, k . The deviatoric-stress field in an ice sheet depends primarily on the geometry. Figure 2.1 shows the typical pattern of effective deviatoric stress, τ_{eff} , near an ice divide. The linear term in the flow law will be important if $\Omega = [\tau_{\text{eff}}^2/k^2]^{1/2} \leq 1$. Since Ω is a function of position, it is useful to define a characteristic stress (τ_{char}) to represent the large-scale behavior of a

particular divide. Equation (2.7) suggests the form:

$$\tau_{\text{char}} = \left[2\Gamma \frac{H}{\dot{b}} \right]^{-1/3}, \quad (2.12)$$

where $\dot{\epsilon}_{\text{char}} \approx \frac{\dot{b}}{H}$ is the characteristic strain rate. With this definition, τ_{char} is of the same order of magnitude as the average τ_{eff} in the vicinity of the divide, except for those divides strongly dominated by the linear term ($k^2 \gg \tau_{\text{eff}}^2$).

Similarly, we can define a non-dimensional characteristic stress using Ω :

$$\Omega_{\text{char}} = \left[\frac{\tau_{\text{char}}^2}{k_{\text{char}}^2} \right]^{1/2}, \quad (2.13)$$

where k_{char} is a characteristic value for k based on the properties of the ice at two-thirds depth under the divide (the region most sensitive to the presence of the linear term).

Figure 2.3 shows characteristic stresses for various divides, based on estimated ice thickness (H), average accumulation rate (\dot{b}), and temperature (T) in the lower half of the ice column. These numbers come from several sources, including a variety of scientific literature, web sites, and personal communications. While this is a crude representation of conditions under any particular divide, this graph shows the spread of possible characteristics. Even with estimates shown in Figure 2.3, we cannot determine which divides have $\Omega_{\text{char}} > 1$ (exhibiting primarily Glen rheology) or have $\Omega_{\text{char}} < 1$ (exhibiting primarily linear rheology) without knowing k_{char} . We can, however, use Figure 2.3 to guide selection of sites at which to make measurements to constrain k_{char} .

Figure 2.4 shows schematically the relationship between Ω_{char} and a divide's behavior. When Ω_{char} is large ($\tau_{\text{char}}^2 \gg k_{\text{char}}^2$), divide deformation is dominated by the Glen term in the flow law; we call this a *Glen divide*. When Ω_{char} is small ($\tau_{\text{char}}^2 \ll k_{\text{char}}^2$), we get a *linear divide*, where the linear term dominates right at the divide, while the Glen term is progressively more important with increasing distance from the divide. In a *transitional divide* ($0.5 < \Omega_{\text{char}} < 2$), both terms contribute significantly to the modelled deformation rate at the divide. Ice flow at linear and transitional divides is modelled inaccurately with the conventional Glen's Law.

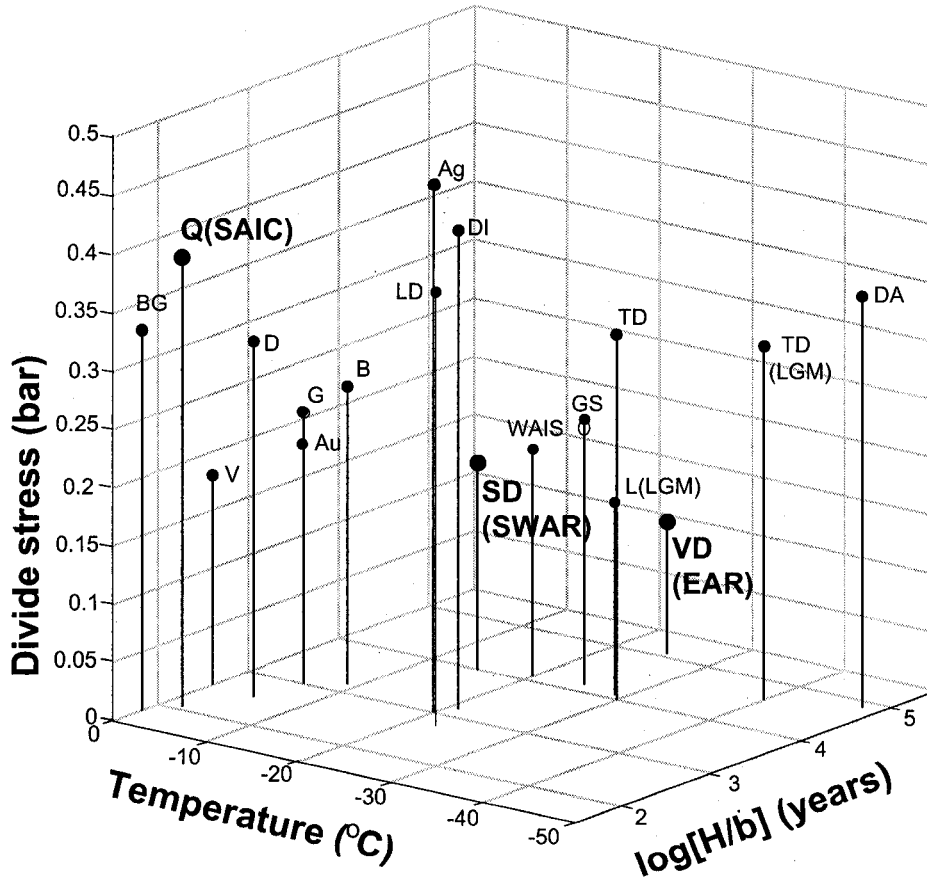


Figure 2.3: The natural range of divide characteristic stress on Earth, illustrated by applying Equation (2.12) to a wide range of ice divides worldwide. We estimated H , \dot{b} , and T from data available from a variety of sources, including scientific literature, web sites, atlases, and personal communications. The three divides shown in large type are studied in more detail in Figures 2.6 and 2.7. Labels are as follows: **Q**, Quelccaya Ice Cap, Andes, Peru (**SAIC**); **BG**, Blue Glacier, Olympic Mountains, Washington, USA; **D**, Dundee Ice Cap, Qinghai-Tibetan Plateau, China; **V**, Vatnajökull, Iceland; **Au**, Austfonna Ice Cap, Svalbard; **G**, Guliya Ice Cap, Qinghai-Tibetan Plateau, China; **B**, Barnes Ice Cap, Baffin Island, NWT, Canada; **Ag**, Agassiz Ice Cap, Ellesmere Island, NWT, Canada; **DI**, Devon Island Ice Cap, NWT, Canada; **LD**, Law Dome, Wilkes Land, East Antarctica; **WAIS**, Inland Divide of the West Antarctic Ice Sheet; **SD**, Siple Dome, Siple Coast, West Antarctica (**SWAR**); **GS**, Greenland Summit (GRIP/GISP2); **L(LGM)**, Laurentide Paleo-Ice Sheet at Last Glacial Maximum (LGM), North America; **TD**, Taylor Dome, Victoria Land, East Antarctica; **TD(LGM)**, Taylor Dome at LGM, Victoria Land, East Antarctica; **DA**, Dome A, East Antarctica; **VD**, Valkyrie Dome, site of Dome Fuji Station, Queen Maud Land, East Antarctica (**EAR**)

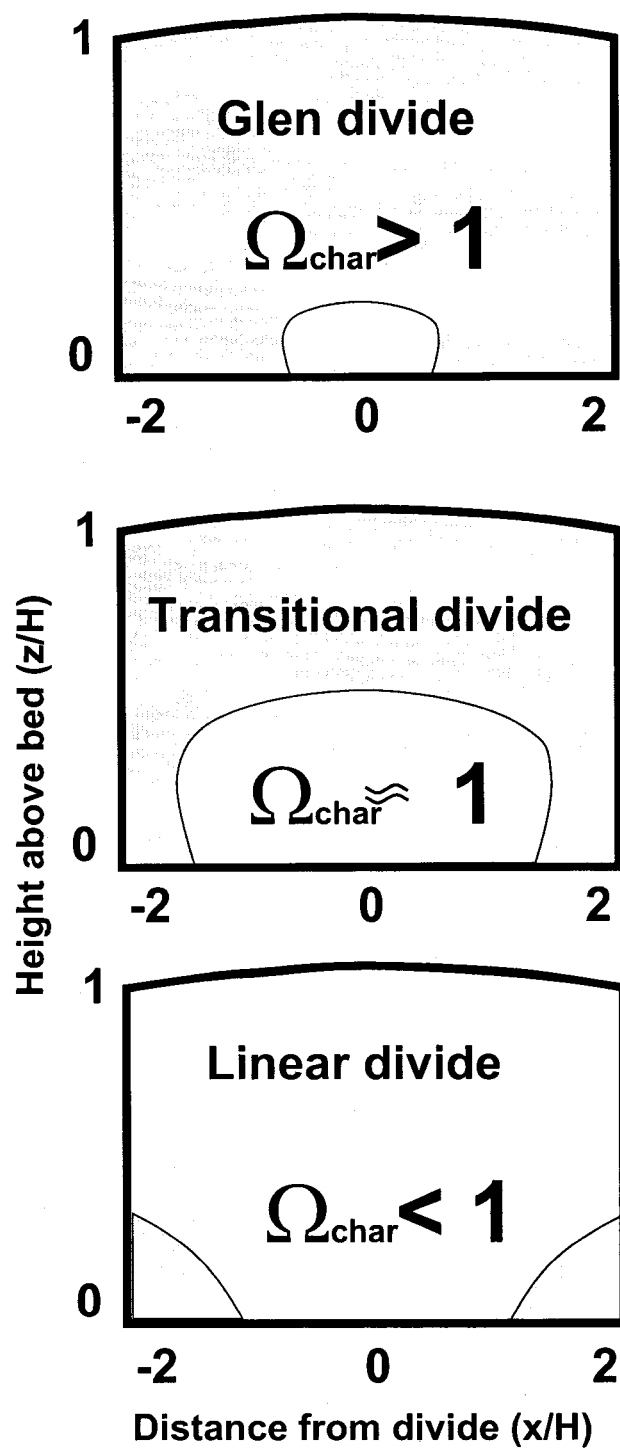


Figure 2.4: Characterization of ice divides based on magnitude of nondimensional stress, Ω . Where $\Omega = [\tau_{\text{eff}}^2/k^2]^{1/2}$ is greater than unity (shaded region), the Glen term in the flow law will dominate; where Ω is less than unity (unshaded region), the linear term will dominate.

2.7 Finite-Element Ice-Flow Model

Raymond [1983] developed a two-dimensional, plane-strain, finite-element model using all terms of the stress tensor to study divide behavior. We have modified this model to explore the impact of the linear term in the flow law on ice flow near a divide.

The model is structured around the following assumptions:

1. The ice deforms in plane strain; thus, the model best represents a ridge ice divide, such as Siple Dome [*Nereson et al.*, 1996] or Roosevelt Island [*Conway et al.*, 1999].
2. The ice sheet is in steady state.
3. Strain rate is a function of deviatoric stress according to Equation (2.11). We do not account for effects of fabric, impurities, or grain size in this model. This flow law is implemented by calculating an effective viscosity at each iteration based on the stress field of the previous iteration. These iterations continue until a convergence criterion is met.
4. Measured temperature profiles in the divide regions of ice sheets typically have a low gradient near the surface and a steeper gradient near the bed. To capture the qualitative features of this shape, we use a quarter of a cosine curve, specified by measured surface temperature and estimated geothermal gradient at the bed.
5. Total thickness of the ice and firn is reduced to ice-equivalent thickness.
6. The ice is frozen to the bed.
7. The ice surface is stress-free and is allowed to evolve until the topography reaches a steady state with the specified uniform accumulation rate. We terminate the evolution when the maximum change in surface-node elevations is $\leq 1 \text{ mm a}^{-1}$.
8. The horizontal-velocity profile on the flank boundary (at ~ 30 ice thicknesses from the divide) is based on laminar flow, and carries away the integrated mass balance from

the divide to the boundary, in order to satisfy mass conservation for a steady-state ice sheet. Because our boundary is more than 20 ice thicknesses from the divide, results for the region within ten ice thicknesses of the divide are insensitive to the details of the horizontal-velocity profile on the flank boundary [Raymond, 1983; Schøtt *et al.*, 1992].

9. We use finite-element grids with flat beds and 66×20 nodes. We choose initial ice thicknesses and accumulation rates to represent three ice divides that have very different characteristic stresses.

In order to isolate effects of the flow law from site-specific geometry, we model idealized ice sheets with flat beds and with the average accumulation rate, thickness, and deep-ice temperature characteristic of three divides that span a broad range of characteristic stress in Figure 2.3. The East Antarctic Ridge (EAR) end member, approximates Valkyrie Dome, the site of Dome Fuji Station, a thick, cold, low-accumulation region. Siple Dome is the model for our Small West Antarctic Ridge (SWAR), with moderate accumulation rate and thickness. The other end-member is a Small Alpine Ice Cap (SAIC); the thin, high-accumulation Quelccaya Ice Cap, Peru, is an example. Table 2.1 contains the model parameters that we use. In modelling each divide, we vary the crossover stress, k , from 0 (Glen flow) to 0.4 bars; this range spans all characteristic stresses in Figure 2.3.

2.8 Results

2.8.1 Vertical velocity and depth-age scale

Raymond [1983] used an earlier version of this model to determine the steady-state patterns of deviatoric stress and strain rate under an isothermal divide with Glen flow. His Figure 3 shows the depth profile of horizontal and vertical velocity at the divide and at various distances from the divide. There are two results to note in that figure: (1) the region affected by the presence of the divide extends horizontally several ice thicknesses, and (2) the vertical deformation rate is more concentrated in the upper two thirds of the ice sheet

Table 2.1: Model input parameters for the three divides. Data sources are as follows: ^a *Satow et al.* [1999]; ^b estimates based on heat flow assumptions; ^c *Nereson et al.* [1996]; and ^d *Mosley-Thompson et al.* [1993]

	$T_{\text{surf}}(^{\circ}\text{C})$	$dT/dz_{\text{bed}}(^{\circ}\text{C m}^{-1})$	\dot{b} (m a^{-1})	H (m)
East Antarctic Ridge (Valkyrie Dome, Dome Fuji Station)	-55^a	0.023^b	0.03^a	3500^a
Small West Antarctic Ridge (Siple Dome)	-26^c	0.030^b	0.1^c	1000^c
Small Alpine Ice Cap (Quelccaya Ice Cap, Peru)	-2^d	0.0^b	1.30^d	165^d

near the divide, when compared to the flank. This vertical-strain-rate pattern results from the presence of a region of low deviatoric stress near the bed at the divide, where Glen's Law predicts high viscosities. Because this region of stiff ice impedes downward flow, a particular isochrone moves down more quickly on the flank than at the divide, producing a local arch in the isochrone. These arches, called *Raymond bumps*, have been recognized in radio-echo-sounding images at Fletcher Promontory, West Antarctica [Vaughan et al., 1999], Siple Dome, West Antarctica [Nereson et al., 1998b], and Roosevelt Island, West Antarctica [Conway et al., 1999]. Interestingly, in radar transects of the divide in Greenland [Jacobel and Hodge, 1995] a Raymond bump is noticeably missing, most likely due to the peregrinations of the divide [Marshall and Cuffey, 2000; Hindmarsh, 1996].

In normal Glen flow, ice near the bed at a divide tends to be warmer due to reduced downward advection of cold ice relative to the flank [Paterson and Waddington, 1986]. This heat softens the ice, partially countering the increase in viscosity due to low deviatoric stress. Hvidberg [1996] predicted a smaller-amplitude Raymond bump due to this thermal softening.

Figure 2.5 shows our results for relative vertical-velocity profiles for the Small West Antarctic Ridge (SWAR) resulting from our calculations; the two other divides we modelled produce qualitatively similar results. When the linear term dominates at the divide ($\Omega \ll 1$), the shape of the relative vertical-velocity profile at the divide approaches the shape

found on the flanks, where the nonlinear term always dominates. The linear term allows the ice at the divide, where deviatoric stress is low, to maintain a viscosity comparable to that of the ice on the flank, which is under higher deviatoric stress. This causes both the differential thermal softening and the Raymond bump at the divide to disappear.

By impacting the shapes of isochrones near a divide, the value of k in a model's constitutive relation at low deviatoric stress also affects the calculated depth-age scale used to interpret ice cores. Since the age of ice at a given depth at the divide is equal to the integral of the inverse of the vertical-velocity field along the particle's flow path, the progression shown in Figure 2.5 affects the corresponding calculated depth-age scale. Inclusion of the linear term in a flow model results in younger ice at a given depth at a divide.

2.8.2 Isochrones and surface morphology

In Figure 2.6, we show the effect of the linear term on isochrones near a divide. Since k is unknown, we model the isochrone shapes near the three divides for four values of k .

For the lowest value of k , 0.01 bar, all three divides exhibit nonlinear behavior described by Glen's Law. For $k = 0.1$ bar, the East Antarctic Ridge (EAR) shows transitional behavior, since it has a characteristic τ_{char} of approximately 0.1 bar and $\Omega_{\text{char}} \sim 1$; the amplitude of the Raymond bump in the isochrone pattern is much-reduced. For the Small West Antarctic Ridge (SWAR), $\tau_{\text{char}} \sim 0.2$ bar and for the Small Alpine Ice Cap (SAIC), $\tau_{\text{char}} \sim 0.4$ bar; therefore, transitional behavior occurs only at values of k larger than 0.1 bar and 0.2 bar, respectively.

If Glen's Law works well for deviatoric stresses down to 0.3 bar, as *Budd and Jacka* [1989] suggest, it is unlikely that the crossover stress, k , is larger than 0.3 bar. The Small Alpine Ice Cap (SAIC), therefore, has deviatoric stresses large enough that nonlinear Glen flow should dominate, regardless of the value of k . Depending on the actual value of k , the Small West Antarctic Ridge (SWAR) and East Antarctic Ridge (EAR) could be transitional, linear, or Glen divides. The existence of a distinctive Raymond bump in the radar images of Siple Dome [*Nereson et al.*, 1998b], our model for a Small West Antarctic Ridge, suggests that it is a Glen or transitional divide and, therefore, $k < 0.2$ bar.

The relatively softer ice in the divide region of a linear or transitional ice sheet (com-

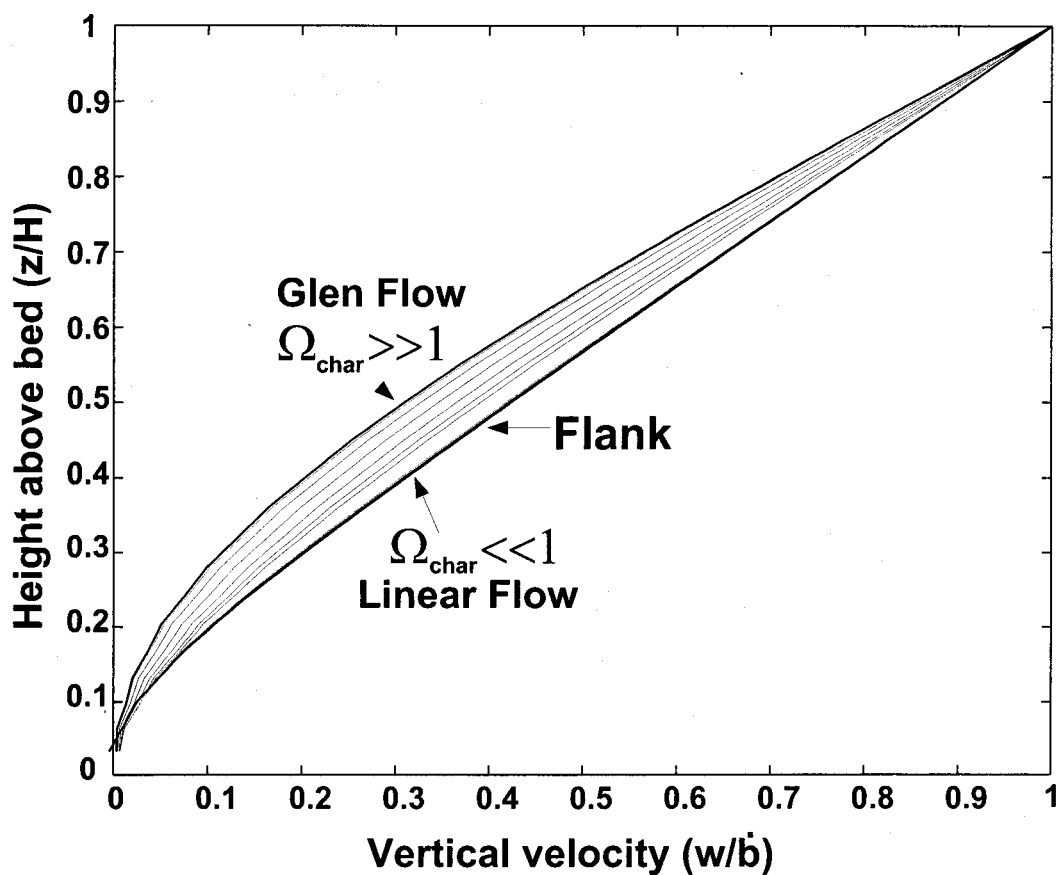


Figure 2.5: Modelled vertical-velocity profiles for divide flow (assuming a range of Ω_{char}) and for flank flow for the Small West Antarctic Ridge (SWAR). The SAIC and the EAR model results are qualitatively similar. Glen flow occurs when the nonlinear term dominates; there is a significant difference between the Glen profile and the flank profile where the nonlinear term always dominates. At a transitional divide, the linear term causes the divide profile to resemble the flank profile more closely. In the limit of $\Omega_{\text{char}} \rightarrow 0$, there is no difference between the divide profile and the flank profile.

pared to a Glen divide) also affects the surface geometry. Figure 2.7 shows the modelled surface shapes for the same three divides shown in Figure 2.6. The effect of the linear term is not only to reduce surface curvature near the divide, but if a large enough region of ice behaves linearly (i.e. $\Omega \gg 1$, see Figure 2.4) it may produce a slightly thinner divide. The overall thickness of an ice sheet, however, is ultimately limited by nonlinear (Glen) flow on the flanks, where shear stresses are high. The crossover stress, k , could have an impact on modelling of the Laurentide Ice Sheet, for example. Some models of the Laurentide Ice Sheet predict much thicker ice than can be accounted for by isostatic rebound and sea level changes [e.g. *Marshall et al.*, 2000]. Many scientists have ascribed this incompatibility to properties of the bed, but *Peltier et al.* [2000] noted that a different flow law could also contribute to a thinner ice sheet. In their model, *Peltier et al.* [2000] assumed a near-linear constitutive relation based on grain-boundary sliding for the entire ice sheet. Realistically, even an ice-sheet geometry based primarily on flow due to GBS is likely to be constrained by a higher-power constitutive relation on the flanks; thus, both terms are important for accurately modelling ice sheets.

2.9 Conclusions

Glen's Law, with a cubic relation between deviatoric stress and strain rate, was derived empirically, and it works well for modelling most ice sheets and glaciers. In the low-deviatoric-stress regimes found particularly near ice divides, Glen's Law may be inadequate, because the ice-flow mechanism may change. Our extended formulation for the constitutive relation for ice, Equation 2.5, is not mechanism-specific; it is intended to represent a range of microphysical processes (within their current experimental uncertainties), yet maintain simplicity for flow modelling at ice-sheet scales. Since empirical evidence shows that deviatoric stress and strain rate are related by exponents ranging from $n = 1$ to 4.2, our formulation uses a summation of three terms with exponents 1, 3, and 5. At low deviatoric stresses, the linear term dominates flow. At deviatoric stresses typical of most ice flow, the cubic term dominates. In high-deviatoric-stress situations, the fifth-power term may become important.

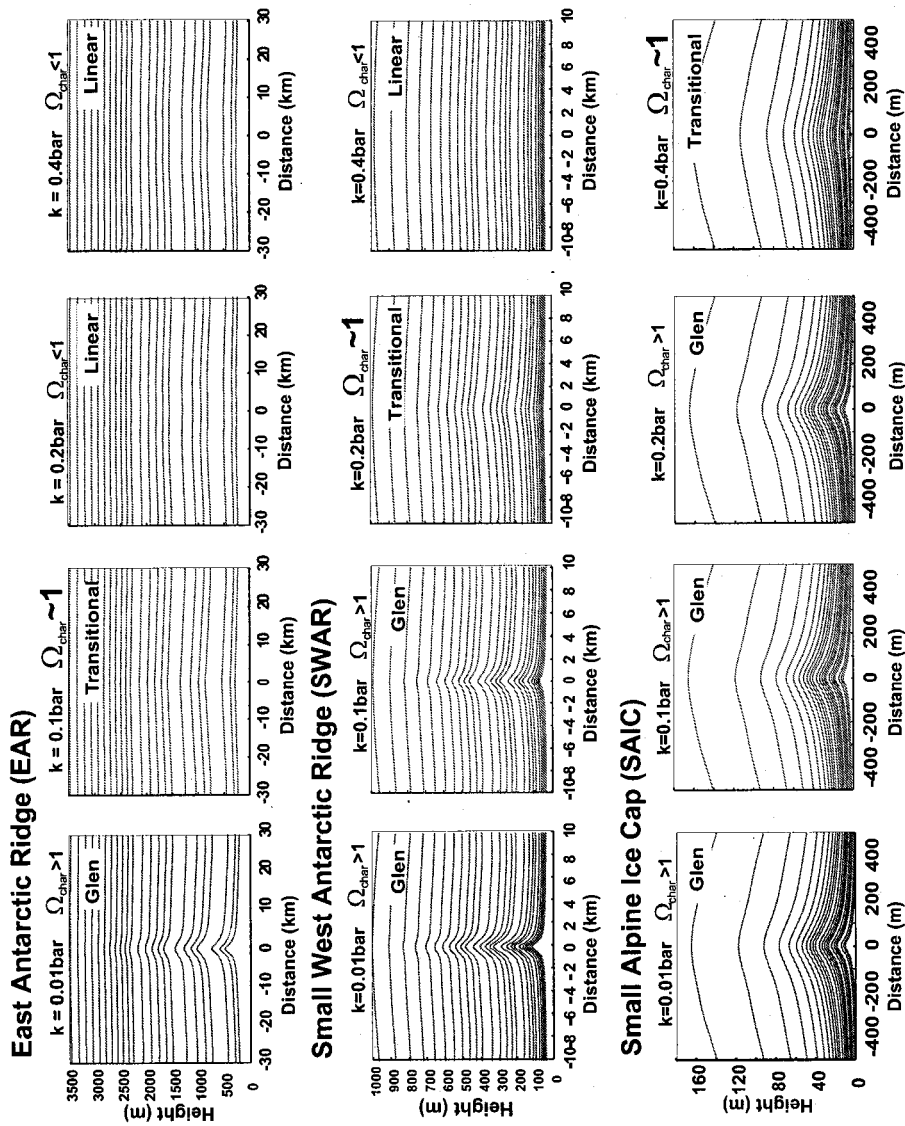


Figure 2.6: Modelled steady-state isochrones for three idealized ice divides, in order of increasing τ_{char} , assuming four different values for the unknown crossover stress, k . The EAR has the lowest τ_{char} and thus shows the largest effect from the linear term. The SAIC has the largest τ_{char} and, therefore, shows very little effect from the linear term.

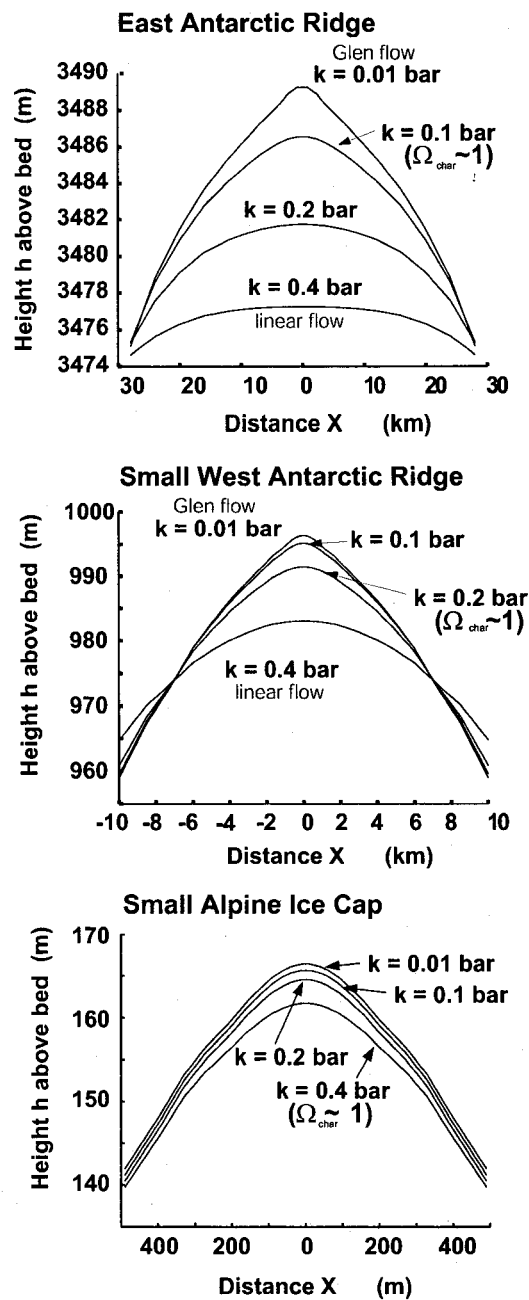


Figure 2.7: Modelled surface morphology for the three divides in Figure 2.6. The transition from Glen flow to linear flow causes a flattening of the surface in the divide region because of the change in the velocity field (see Figure 2.5.)

The importance of the linear term depends on the value of the unknown crossover stress, k , which is the deviatoric stress at which the linear and cubic terms contribute equally to the strain rate. A steady-state divide exhibiting *linear* flow has:

1. a vertical velocity profile that closely resembles the profile on the flanks (and, therefore, corresponding similarities in the shape of the horizontal velocity profile, and in vertical and horizontal strain rates),
2. a lack of a *Raymond bump* in isochrones or an arch in isotherms,
3. younger ice than a corresponding Glen divide at any given depth,
4. more-rounded topography at the ice divide.

The linear term of the flow law may also be important near the surfaces of ice sheets and glaciers, where shear stresses and τ_{eff} can be small. The impact of rheological properties of this near-surface region on large-scale ice-sheet models is minimal; it may, however, become important in flow of valley glaciers [Marshall *et al.*, 2002].

We must also consider whether the magnitude of this effect is large enough to be of concern to modelers, considering the variability in strain rates due to anisotropy, impurity content, and grain size. The model by Azuma [1994] predicts a maximum enhancement factor of 9 for anisotropic ice in simple shear; all other stress configurations produce less enhancement. Other anisotropy models give comparable results [e.g. Thorsteinsson *et al.*, 1999]. The theoretical basis for enhancement due to solid or chemical impurities or grain size is less well understood, but measurements from high-deviatoric-stress environments show maximum total enhancements (including anisotropy) of up to 10 relative to isotropic ice at the same temperature [Dahl-Jensen and Gundestrup, 1987; Cuffey *et al.*, 2000a]. In addition, laboratory tests on impurity-laden ice show enhancements up to 2 [Budd and Jacka, 1989]. From these data, we can conclude that the enhancement of the strain rate due to these effects is no more than one order of magnitude, and often less. On the other hand, transition to linear flow in the near-divide region is equivalent to applying an enhancement factor, E , of up to 10^5 to the $n = 3$ version of Glen's Law in regions where

$\Omega \ll 1$, such as near the bed at the divide. In other words, the uncertainties due to the unknown value of k will be negligible for much of the ice sheet, but in the near-divide regions, the assumption of an $n = 3$ flow law may result in large errors in models.

Before this constitutive law can be incorporated into current flow models, however, the value of the *crossover stress*, k , must be determined. This effort may involve re-analyzing existing laboratory and field data as well as designing future experiments to study the transition between linear and Glen constitutive behavior [e.g. *Morse, 1997; Zumberge et al., 2002*]. Although in this paper we modelled only isotropic ice, the issue of stress-dependent flow-law exponent also applies when modelling anisotropic ice, especially if the anisotropic model relies on an $n = 3$ relationship between deformation and resolved shear stress on the basal plane for an individual crystal.

Chapter 3

**EFFECTS OF BASAL SLIDING ON ISOCHRONES AND FLOW
NEAR AN ICE DIVIDE**

This chapter is in press under the same title in *Annals of Glaciology* 37, with co-authors H. P. Jacobson (who developed the finite-element model) and E. D. Waddington from Earth and Space Sciences Department, University of Washington. Helpful reviews were provided by A. Fowler, F. Ng, and T. Hulbe

3.1 Summary

If an ice sheet is frozen to its bed, deep ice directly under a divide experiences low deviatoric stress and is relatively hard, because the rheology of polar ice is described by a power-law constitutive relation. In steady state, stratigraphic layers tend to form an arch (“Raymond Bump”) in this region. However, when the basal ice can slide, the stresses are redistributed, and longitudinal extension due to sliding is associated with increased deviatoric stress in the deep ice under the divide. This increased deviatoric stress weakens the tendency to form a Raymond Bump. To find a realistic spatial distribution of sliding under an ice divide, we incorporate a thin layer of viscous till in a finite-element plane-strain flow model. The resulting basal “sliding” velocity varies approximately linearly with distance from the ice divide. By varying the till viscosity, we can adjust the amount of basal motion. We find that the Raymond Bump decays exponentially with the fraction of total ice flux carried by sliding: the arch is 50% smaller when the sliding flux is only 7% of the total ice flux. This implies that the possibility of a wet bed must be considered when inferring past ice-divide locations from radar internal layering.

3.2 Introduction

Ice-penetrating-radar images, ice-core records, and ice-deformation measurements hold clues to past and future behavior of ice sheets. The challenge is to infer paleoclimate and ice-flow history from these data. Rigorous solution of these inverse problems requires an

understanding of the subtleties of ice deformation and flow.

Ice cores are often drilled near ice divides, in order to minimize stratigraphic disturbance due to horizontal shearing of ice [e.g. *Waddington et al.*, 2001]. Therefore, a rigorous ice-flow model for the ice-divide region is required, particularly since, at ice divides, longitudinal stress gradients cannot be ignored [*Nye*, 1959; *Morland and Johnson*, 1980; *Raymond*, 1983]. Furthermore, at the low deviatoric-stress levels found under ice divides, the ice rheology may be near-linear, changing the pattern of ice flow [*Waddington et al.*, 1996; *Pettit and Waddington*, in press]. Ice flow can also be influenced by changing boundary conditions. For example, there is a significant feedback between the near-divide flow field and the surface temperature [*Hvidberg*, 1996]. Elevation changes of bounding ice streams [*Nereson et al.*, 1998a], or transient and spatially asymmetric accumulation-rate patterns [*Nereson et al.*, 1998b] can cause an ice divide to migrate.

Here, we explore the effects of basal motion on the ice-flow pattern and the internal stratigraphy under an ice divide. Some ice divides are presently frozen to their beds (e.g. Greenland Summit, *Johnsen et al.* [1995]; Devon Island, *Paterson and Clarke* [1978]; and Siple Dome, G. Clow, pers. comm.), while others such as Law Dome [*Budd et al.*, 1976] and parts of the West Antarctic Ross-Amundsen ice divide (*Morse and others*, in press) are at or near the pressure-melting temperature at the bed. At these divides, basal sliding, a deforming till layer, or both, may be present.

Because polar ice is described by a power-law constitutive relation, [e.g. *Paterson*, 1994, Chapter 5, *Glen's Law*], its “effective viscosity” increases with decreasing effective deviatoric stress. Where an ice sheet is frozen to its bed, the deep ice directly under a divide experiences low deviatoric stress, has a relatively high effective viscosity, and is relatively resistant to deformation. As a result, stratigraphic layers tend to move downward more slowly within a distance of one ice thickness of the ice divide, when compared to flank regions (at distances greater than about five ice thicknesses from the divide). In a steady state, these layers tend to form an arch (“Raymond Bump”) in the divide region [*Raymond*, 1983]. However, when the basal ice can slide, or when a deformable till layer exists, stresses are redistributed, and the deep ice undergoes more longitudinal extension. This extension increases longitudinal deviatoric stress in the deep ice under the divide, resulting in a lower

effective viscosity there and a weakened tendency to form a Raymond Bump.

In order to explore the effects of various levels of basal sliding on the flow pattern and the stratigraphy, we must first formulate a realistic spatial pattern of basal motion that might be expected under and near ice divides. This is not a trivial matter, because there is still no general agreement on the detailed form of a basal sliding relationship for ice sheets. Conventional sliding boundary conditions incorporate simplifications and assumptions that break down in the divide region. Many models incorporate a sliding law based on the theory by *Weertman* [1957], for which sliding velocity, u_b , is a function of local basal-shear stress [*Nye*, 1959; *Morland and Johnson*, 1980; *Payne*, 1995; *Tarasov and Peltier*, 2000; *Marshall et al.*, 2000]:

$$u_b = k\tau^m, \quad (3.1)$$

where τ is the local shear stress, and k is a function of several ice-flow and geometric parameters, potentially including effective water pressure (the difference between ice overburden pressure and basal water pressure).¹ As *Weertman* [1961] noted, this law includes the implicit assumption that longitudinal stresses are insignificant. Near an ice divide, however, longitudinal stresses cannot be neglected, because shear stresses approach zero. Because the driving shear stresses are small, we expect that longitudinal strain rates in the ice will control the allowable gradients in basal sliding velocity.

Here we use a two-dimensional plane-strain finite-element flow model, which automatically incorporates longitudinal-coupling effects. To parameterize sliding at the ice-bedrock interface, we use a layer of deformable, linearly-viscous till and allow the model to determine the pattern of basal motion under and near a divide. We then vary the till viscosity to examine the sensitivity of isochrone shape and the velocity field to varying amounts of basal “sliding”. From the perspective of the ice, varying the till-layer thickness has the same effect as varying the till viscosity. The choice to use a linear-viscous till, rather than a power-law till, will affect subtle details of the model results, but not the general features that we present here.

¹Appendix A is a table of the notation.

3.3 Finite-Element Ice-Flow Model

To calculate the velocity field and find the steady-state isochrone pattern, we use a thermomechanically coupled finite-element model (FEM). This model is similar to ice-divide models by *Raymond* [1983] and *Hvidberg* [1996]. Figure 3.1 shows the model geometry.

The model is structured around the following assumptions:

1. The ice deforms in plane strain; thus, the model best represents a ridge ice divide, such as Siple Dome [*Nereson et al.*, 1996] or Roosevelt Island [*Conway et al.*, 1999].
2. Strain rate is a power-law function of deviatoric stress according to Glen's flow law:

$$\dot{\epsilon}_{ij} = A(\tau_{\text{eff}}^2)^{\frac{n-1}{2}} \tau_{ij}, \quad (3.2)$$

where $\dot{\epsilon}_{ij}$ and τ_{ij} are the strain-rate and deviatoric stress tensors, respectively, τ_{eff} is the effective deviatoric stress [*Paterson*, 1994, p. 91] and we assume that A depends only on temperature through the Arrhenius relation $A = A_0 \exp(-Q/RT)$.

3. The ice is underlain by a layer of till of uniform thickness. There is no slip between the ice and the top of the till layer, and no slip between the bottom of the till and the bedrock. The viscosity of the till layer is a model input parameter which can be adjusted to model various levels of basal resistance.
4. The temperature calculation is based on the surface temperature and the geothermal gradient at the bottom of a thick layer of bedrock [*Waddington*, 1987]. In addition to conduction and advection, strain heating is included in the thermal model. The thermal conductivities and diffusivities of the ice, rock, and till are assumed to be equal and uniform (the values for ice fall within the range typical for sedimentary rocks, *Stein* [1995]).
5. The upper surface is stress-free and is allowed to evolve until a steady state is reached with a specified uniform accumulation rate. We define steady state as a maximum

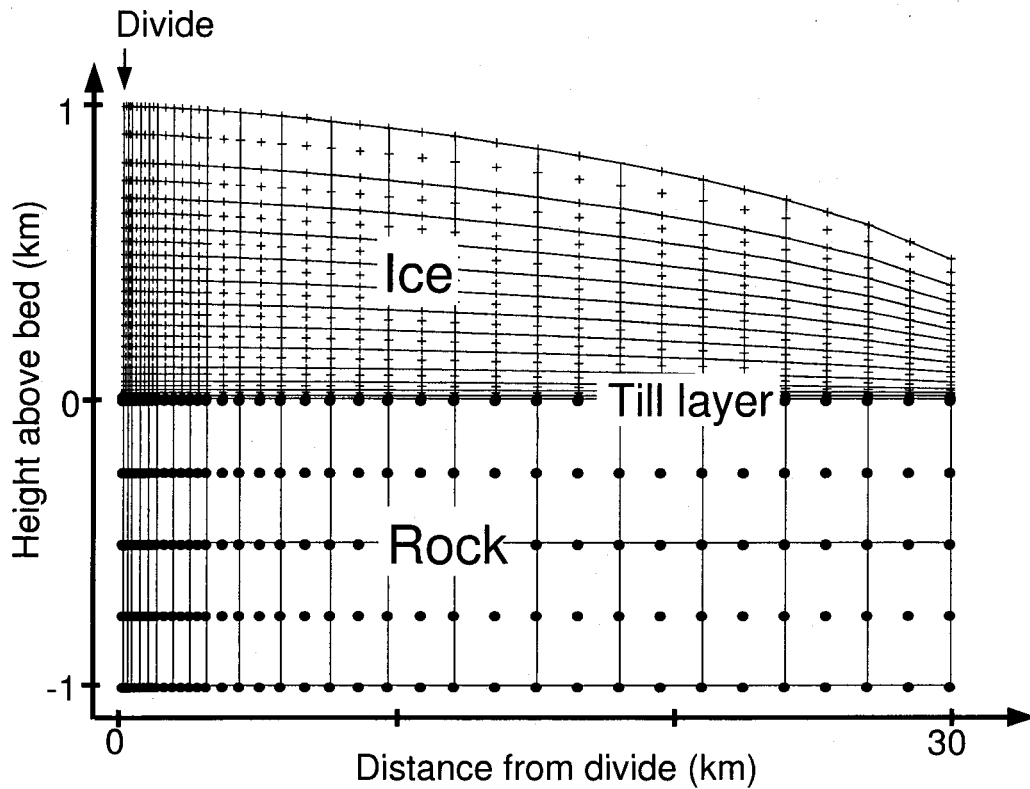


Figure 3.1: Finite-element model geometry. Solid lines are element (9-node quadrilaterals) boundaries. Plus signs mark nodes in the ice. Solid dots mark bedrock nodes. The ice is initially 1000m thick at the divide, with an initial surface profile is calculated using the shallow ice approximation. The ice at the divide can move only vertically. The velocity profile on the flank boundary ($\sim 30H_{\text{div}}$) exports ice flux equal to the surface accumulation integrated over the surface. The till layer is 10 meters thick (one element thick). The ice-till and the till-rock contact are no-slip boundaries. In each model run, the surface evolves until it reaches steady state with the uniform accumulation rate.

change in the surface elevation (excluding the 5 nodes nearest the flank boundary) over a year of less than a specified tolerance ϵ (typically <5 mm per year for a 1000 m thick ice sheet).

6. The divide is a line of symmetry where ice is constrained to move only vertically.
7. The horizontal-velocity profile on the flank boundary (at 30 ice thicknesses from the divide) carries away the integrated mass balance from the divide to the boundary, in order to satisfy mass conservation for a steady-state ice sheet. Because our boundary is more than 20 ice thicknesses from the divide, the results for the region within ten ice thicknesses of the divide are insensitive to the details of the horizontal-velocity profile on the flank boundary [*Raymond, 1983; Schøtt et al., 1992*].
8. Because our goal was to isolate the effect of sliding, the layer of till does not undergo the thinning that one would expect, given the export of till by shearing flow through the flank boundaries. We also do not allow for mass-loss due to melting from the base of the ice sheet or mass gain due to freeze-on of basal water.

Table 3.1 shows values of constants used in the model. We chose the surface temperature, geothermal flux, ice thickness, and accumulation rate characteristic of Siple Dome, West Antarctica.

As shown in Figure 3.1, we model an idealized symmetrical divide with a flat bed. We use a 39×31 -node grid of quadratic elements. Since we are most interested in the solution near the divide, the nodes are more closely spaced within the divide region. Horizontal ice velocity and horizontal temperature gradient are zero at the ice divide. The model solves for temperature, pressure, and velocity fields.

We varied the till viscosity from 10^6 to 10^{15} Pa.s, to capture the range of possible behaviors. For each till viscosity, the model reaches a steady state in which the accumulation rate and the flow due to gravity (a function of the model geometry) are balanced. In order to compare different model runs, we chose to keep the accumulation rate constant and to allow for differences in the final steady-state geometry. The alternative is to maintain

Table 3.1: Finite-Element model parameters.

Parameter	Value
n	flow-law exponent 3
A_o	flow-law constant ($T \leq -10^\circ \text{C}$) $1.3 \times 10^{-5} \text{ Pa}^{-3} \text{ a}^{-1}$
A_o	flow-law constant ($T > -10^\circ \text{C}$) $6.26 \times 10^{10} \text{ Pa}^{-3} \text{ a}^{-1}$
Q	activation energy ($T \leq -10^\circ \text{C}$) 60 kJmol $^{-1}$
Q	activation energy ($T > -10^\circ \text{C}$) 139 kJmol $^{-1}$
R	gas constant 8.314 Jmol $^{-1}$ K $^{-1}$
k	thermal conductivity 2.1 W m $^{-1}$ K $^{-1}$
c	heat capacity 2.11 kJK $^{-1}$ kg $^{-1}$
ρ	density 910 kg m $^{-3}$
T_{surf}	surface temperature -25 $^\circ \text{C}$
Q_{geo}	geothermal flux 65 W m $^{-2}$
H	ice thickness 1000 m
\dot{b}	accumulation rate 0.1 m a $^{-1}$
H_{till}	till thickness 10 m
η_{till}	till viscosity 10^6 to 10^{15} Pa s
η_{ice}	char. ice viscosity 10^{10} Pa s
H_{rock}	bedrock thickness 1000 m

constant ice sheet thickness at the divide, but adjust the accumulation rate for each set of boundary conditions. Our conclusions do not depend on this choice.

We present our results in non-dimensional form, indicated by a hat ($\hat{\cdot}$) over the variable. We use ice thickness at the divide, H_{div} , as the characteristic distance. The characteristic viscosity, η_{ice} , is defined by rearranging Equation (3.2) for $n = 3$ such that $\tau = 2\eta\dot{\epsilon}$ (the standard form for a linear fluid). This yields [Pettit and Waddington, in press]:

$$\eta_{\text{ice}} = (2A)^{-1/3} (\dot{\epsilon}_{\text{char}})^{-2/3}, \quad (3.3)$$

We use the value of A appropriate for average ice temperature. $\dot{\epsilon}_{\text{char}} = \dot{b}/H_{\text{div}}$, where \dot{b} is the accumulation rate. The characteristic time is $t_{\text{char}} = 1/\dot{\epsilon}_{\text{char}} = H_{\text{div}}/\dot{b}$. For Siple Dome, the characteristic viscosity is $\eta_{\text{ice}} = 10^{10}$ Pa s ($\hat{\eta}_{\text{ice}} = 1$) and the characteristic time is $t_{\text{char}} = 10^4$ years.

3.4 Results

Our first goal was to determine a realistic spatial distribution of basal-ice motion under an ice divide. To do this we used a layer of till with an adjustable but spatially uniform viscosity and thickness. When ice is frozen to its bed, the entire ice flux has to be transported through internal deformation in the ice. A very stiff till layer produces the same results. But as the viscosity of the till layer decreases, shear deformation in the till increases, decreasing the shear deformation required within the ice sheet to achieve equilibrium with the specified accumulation rate at the surface. Ultimately, when the till viscosity is low enough, virtually all of the shear deformation is concentrated in the till layer, shear stress at the base of the ice goes to zero, and the ice deforms only through longitudinal stretching (similar to an ice shelf). This trend is shown in Figures 3.2 and 3.3.

“Sliding velocity” is represented by the basal ice motion at the ice-till contact. Figure 3.2(a) shows the longitudinal profile of this basal ice motion for model runs with a range of non-dimensional till viscosities $\hat{\eta}_{\text{till}}$ from 10^{-4} to 10^5 . In the low-viscosity-till model run, the basal-ice motion increases linearly with distance from the divide. This result is not unexpected, since nearly all of the motion occurs through shearing of the till layer. In this case, longitudinal stress σ_{xx} in the overlying ice, which varies slowly with distance from the divide, controls the basal-velocity gradient. The ice near the divide moves away from the divide as “plug flow” (Figure 3.3a): the basal velocity in this region is equal to the surface velocity, which, from steady state mass continuity, is

$$u_s = u_b = \frac{\dot{b}}{H}x, \quad (3.4)$$

where x is the distance from the divide. In contrast, in the high-viscosity-till model run (Figure 3.3c), sliding velocity is zero everywhere, and the ice motion is accommodated largely through internal horizontal simple shear. In both of these cases, the details of the rheology of our till-layer do not affect the results.

To conserve mass, the plug-flow horizontal-velocity profile of the weak-till model run requires a near-linear vertical velocity profile at all distances from the divide, as shown on

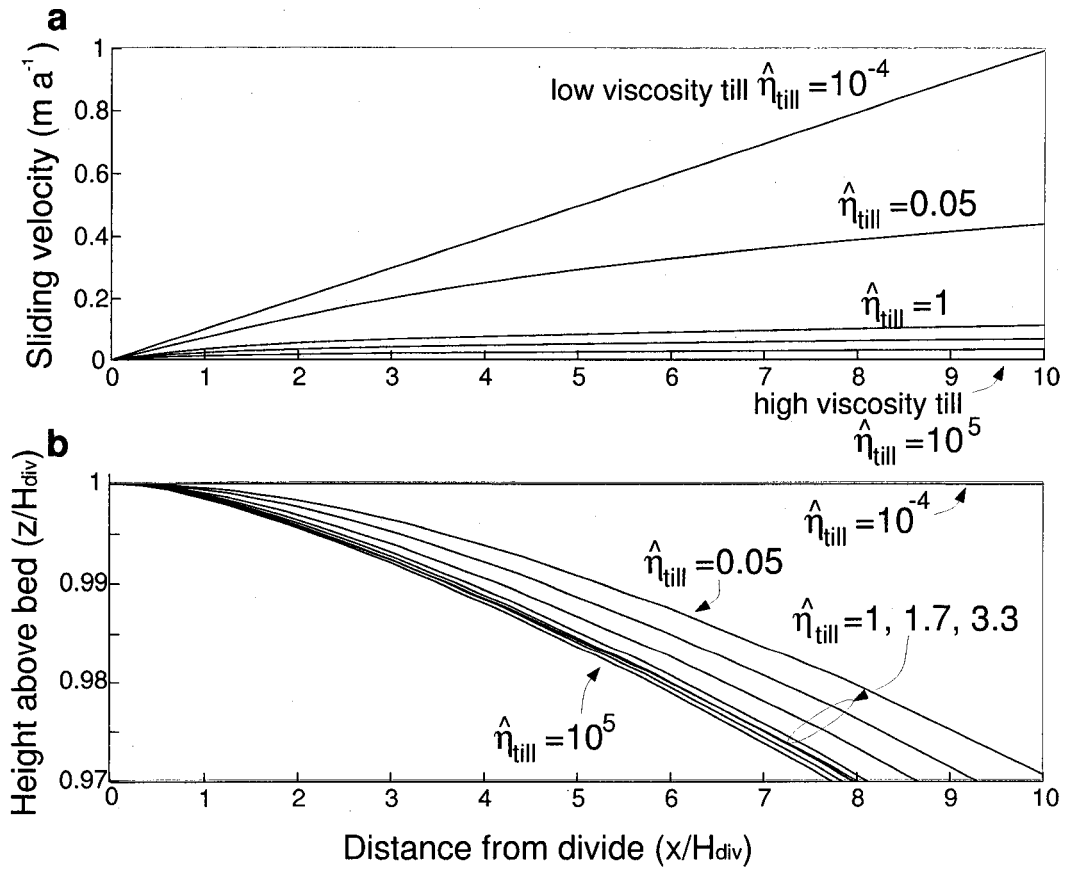


Figure 3.2: (a) Longitudinal profile of velocity at the till-ice contact and (b) the surface profile for a range of non-dimensional till viscosities. The non-dimensional viscosity of Siple Dome ice at -15°C is 1 (explained in the text).

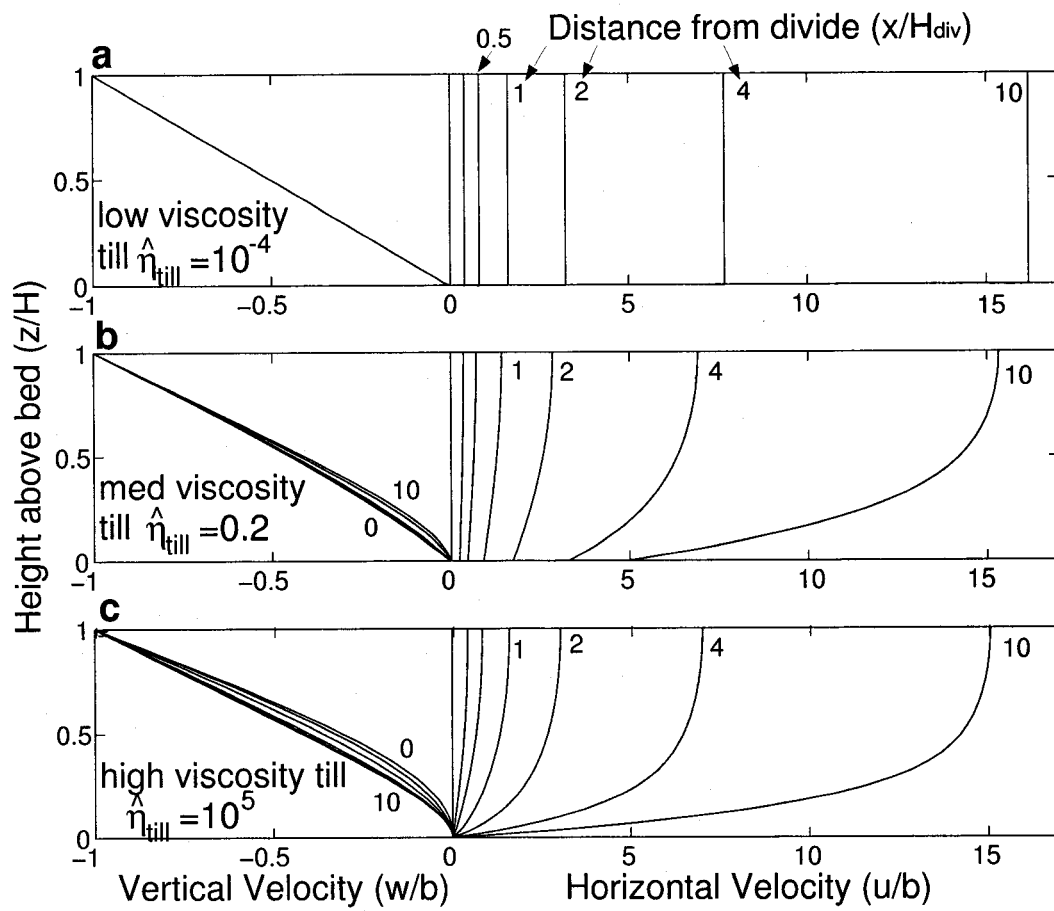


Figure 3.3: Vertical- and horizontal-velocity profiles at 0, 0.25H, 0.5H, 1H, 2H, 4H, and 10H from the divide (as indicated by the curve labels) for three model runs: (a) low-viscosity till, (b) medium-viscosity till, and (c) high-viscosity till.

the left side of Figure 3.3. The ice sheet necessarily reaches a different steady-state surface profile in plug flow compared to a steady state dominated by internal deformation in the ice (Figure 3.2b). In steady state, the ice flux at any position is equal to the integrated accumulation rate from the ice divide; this flux is the same regardless of the till viscosity. Therefore, as till viscosity decreases, increased basal sliding contributes more to the ice flux, and the internal deformation within the ice sheet must contribute less. Since internal deformation is driven by ice thickness and slope, a steady ice sheet with more sliding must be thinner and have a shallower slope.

We also explored the behavior of the flow and stratigraphy with basal-till viscosities intermediate between the stiff-till ($\hat{\eta}_{\text{till}} = 10^5$) and weak-till ($\hat{\eta}_{\text{till}} = 10^{-4}$) model runs. The velocity field and steady-state geometry of an ice sheet are most sensitive to the till viscosity when the till viscosity is within an order of magnitude of the characteristic ice viscosity ($\hat{\eta}_{\text{ice}} = 1$). For these transitional model runs, the total deformation is divided comparably between the till and the ice. The sliding velocities and surface profiles for these intermediate model runs are shown in Figure 3.2. Unlike the result in the weak-till model run, these velocity profiles are not linear (Figure 3.2a). The sliding velocity gradually increases with distance from the divide, with a steeper gradient within a few ice-thicknesses of the divide. The horizontal-velocity profile is more similar to plug flow near the divide; however, as surface slope and basal shear stress increase with increasing distance from the divide, internal deformation carries an increasing fraction of the ice flux (Figure 3.3b). The details of the model results for these transitional model runs depend on our choice of till rheology. A power-law till would slightly change the curvature of the sliding velocity and surface profile curves in Figure 3.2.

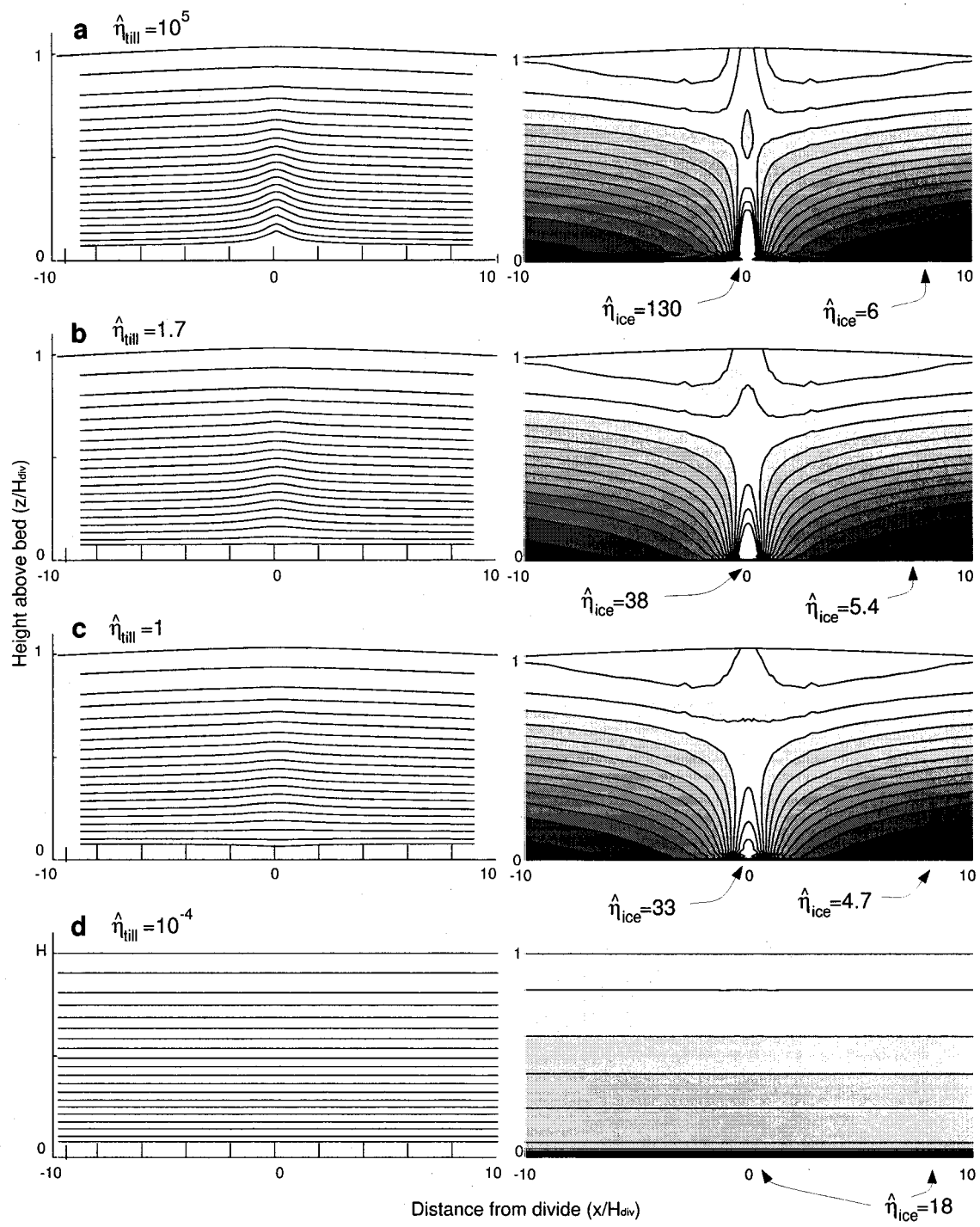
To maintain the plug flow characteristic of the low-viscosity-till model run (and the near divide zone of the transitional model runs), the longitudinal deviatoric stresses must be more evenly distributed with depth, compared with the pattern for an ice sheet frozen to its bed. This is particularly important near the base of the ice at the divide, where low deviatoric stresses and correspondingly high effective ice viscosity (due to the nonlinearity of Glen's flow law) contribute to the formation of the Raymond Bump in the isochrones. In Figure 3.4, we show results from four model runs with non-dimensional till viscosities

varying from 10^5 to 10^{-4} . The left column shows simulated steady-state isochrones and the right column shows the pattern of non-dimensional effective viscosity in the ice. Figure 3.4(a) shows the typical patterns for an ice sheet frozen to its bed. The arch in the isochrones on the left results from deformation around the “hard” zone deep under the divide, as seen in the effective-viscosity distribution on the right. All three of the high- to moderate-viscosity till model runs (a-c) show a zone of relatively hard ice deep under the divide. The extent of this zone and the magnitude of its peak effective viscosity relative to the viscosity on the flank determines the size of the Raymond Bump; as we increase basal sliding, the arch in the isochrones diminishes. The high longitudinal stresses near the bed of an ice sheet with basal sliding keep the effective viscosity low (Figure 3.4d), and hinder the formation of this zone, resulting in flatter isochrones.

By analyzing the decrease in prominence of the divide arch, we can quantify the effect of sliding on the flow field. We define the amplitude of the Raymond Bump for each isochrone as the maximum distance that the isochrone rises above an imaginary smooth curve that best fits the shape of the isochrone on both flanks of the dome. In Figure 3.5, this arch amplitude is plotted as a function of the fractional height of the isochrone at 10 ice thicknesses from the divide for each model run. The arch decreases in magnitude with increasing sliding. Also, the depth of its maximum amplitude decreases as sliding increases. This effect is due to a subtle change in the shape of the vertical velocity profile at the divide (see Figure 3.3). The depth of a layer is given by the temporal integral of its downward velocity along its particle path. The maximum arch amplitude occurs at a depth where the difference between these integrals is maximum for particle paths at the divide and on the flank. As the amount of basal sliding increases, the differences between flank and divide vertical-velocity profiles are pushed to shallower depths; this subtle shape change pushes the height of the maximum amplitude upwards.

In Figure 3.6 we take each curve from Figure 3.5, and plot the maximum bump amplitude against the flank flux ratio q_s , defined as the percentage of the total ice flux carried

Figure 3.4: Isochrones and effective viscosities for 4 model runs with decreasing till viscosity (dark shading represents low effective viscosities; light shading represents high viscosities). The size of the Raymond Bump is related to ice viscosity peak at the base of the ice at the divide relative to the flank (more than about 5 ice thicknesses away from the divide). (a) high till viscosity ($\hat{\eta}_{\text{till}} = 10^5$), (b) moderate till viscosity ($\hat{\eta}_{\text{till}} = 1.7$), (c) till viscosity ($\hat{\eta}_{\text{till}} = 1$) (d) low till viscosity ($\hat{\eta}_{\text{till}} = 10^{-4}$). (a) through (c) have similar flank viscosities, (d) has a slightly higher flank viscosity because the steady state ice sheet is somewhat thinner and therefore is colder. Note that (b) and (c) have similar till viscosities, yet measurably different viscosity peaks and Raymond Bump sizes; this is evidence that the transition from hard-till end member (a) to soft-till end member (d) occurs over a small range of till viscosities. The isochrones near the bed for the transitional model runs show a slight down-warping. This is a subtle effect of our choice of linear till rheology and is not likely to occur in a real ice sheet.



by sliding at about 5 ice thicknesses from the divide:

$$q_s = \frac{u_b H_5}{u_b H_5 + \int_0^{H_5} u_i(z) dz}, \quad (3.5)$$

where H_5 is the ice thickness at $5H_{\text{div}}$, u_b is the sliding velocity at $5H_{\text{div}}$, and u_i is the horizontal velocity due to internal deformation at $5H_{\text{div}}$. Figure 3.6 shows that the maximum arch amplitude decays exponentially with increasing sliding: it takes only 11% sliding flux to cause the arch to decrease to 36% ($1/e$) of its size in the stiff-till model run. Thus, a small amount of sliding can significantly alter ice flow and reduce the amplitude of the Raymond Bump.

3.5 Discussion

Previous attention to sliding has focused on fast-moving ice streams and on the central reaches of valley glaciers. The impact of sliding on the flow pattern near ice divides has received little attention. To our knowledge, only *Morland and Johnson* [1980] have looked in some detail at the effect of sliding on the flow field near an ice divide. They assumed a sliding velocity based on a modification of Equation (3.1), which we expect has difficulty in reflecting the important role of longitudinal stress gradients near a divide. Because the overlying ice resists dramatic inhomogeneities in longitudinal strain rate, the basal-ice velocity should also vary smoothly with position. *Weertman* [1961], realizing that Equation (3.1) may be inapplicable near a divide, added a longitudinal-stress term, and showed that, as a result, small ice caps such as the Barnes were predicted to have a flatter profile than the sliding law Equation (3.1) would suggest.

To investigate the effect of sliding at a divide more thoroughly, we have incorporated a layer of deformable till into our plane-strain finite-element ice-flow model. Our till layer is not intended to be a realistic basal substrate, but it is a simple method for representing sliding behavior that includes the strong longitudinal-stress coupling represented by extensional stresses in the ice. Indeed, for low-viscosity till, the sliding velocity near the divide is controlled by the longitudinal strain rate in the ice, not by the details of processes in the till. Furthermore, with a “slippery” ice-rock interface instead of a till layer,

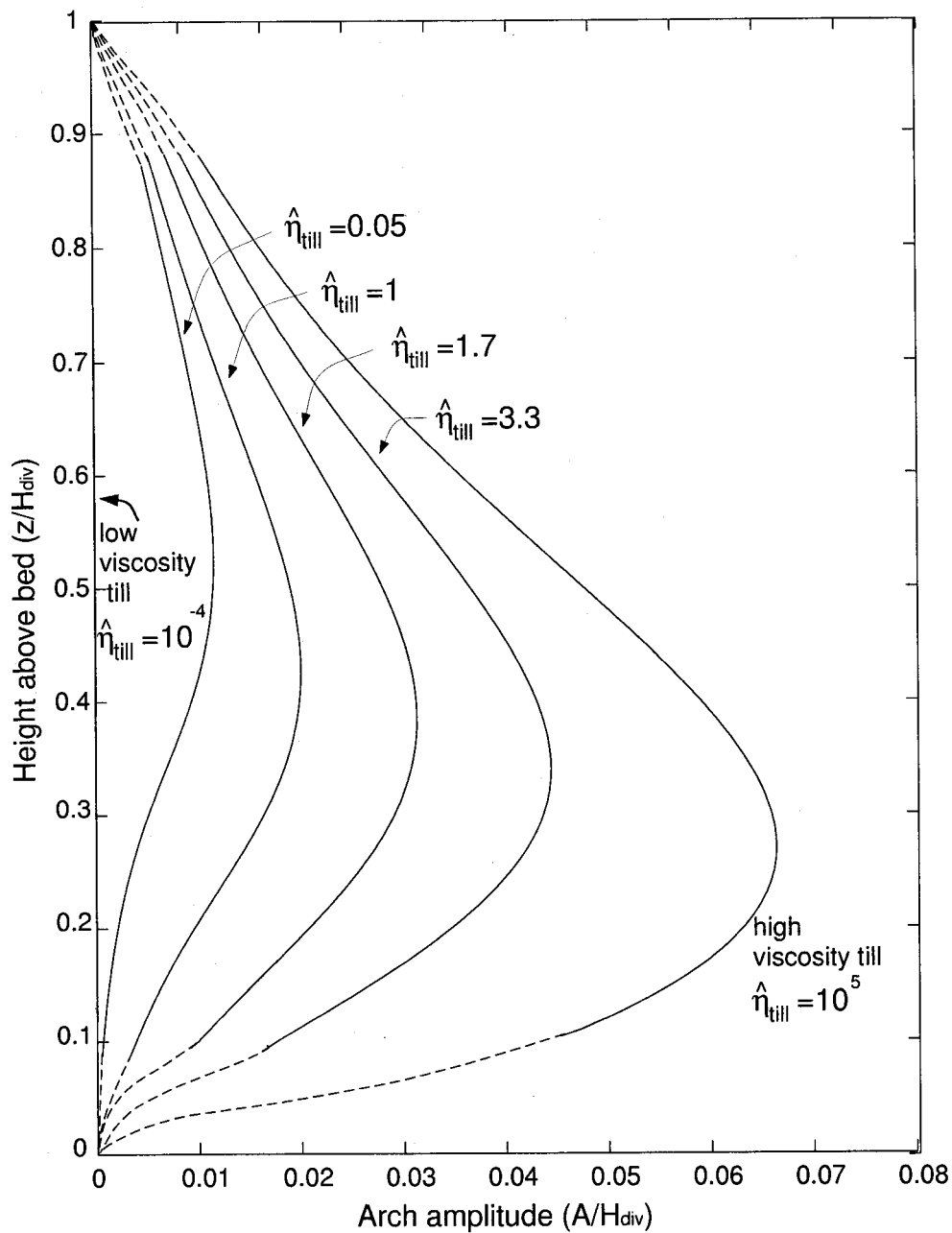


Figure 3.5: Variation in arch amplitude (relative to the ice sheet thickness) with height above bed for several model runs. The dashed part of the curves indicates a rough extrapolation to the surface and the bed (the curves should approach the surface and bed with infinite slope).

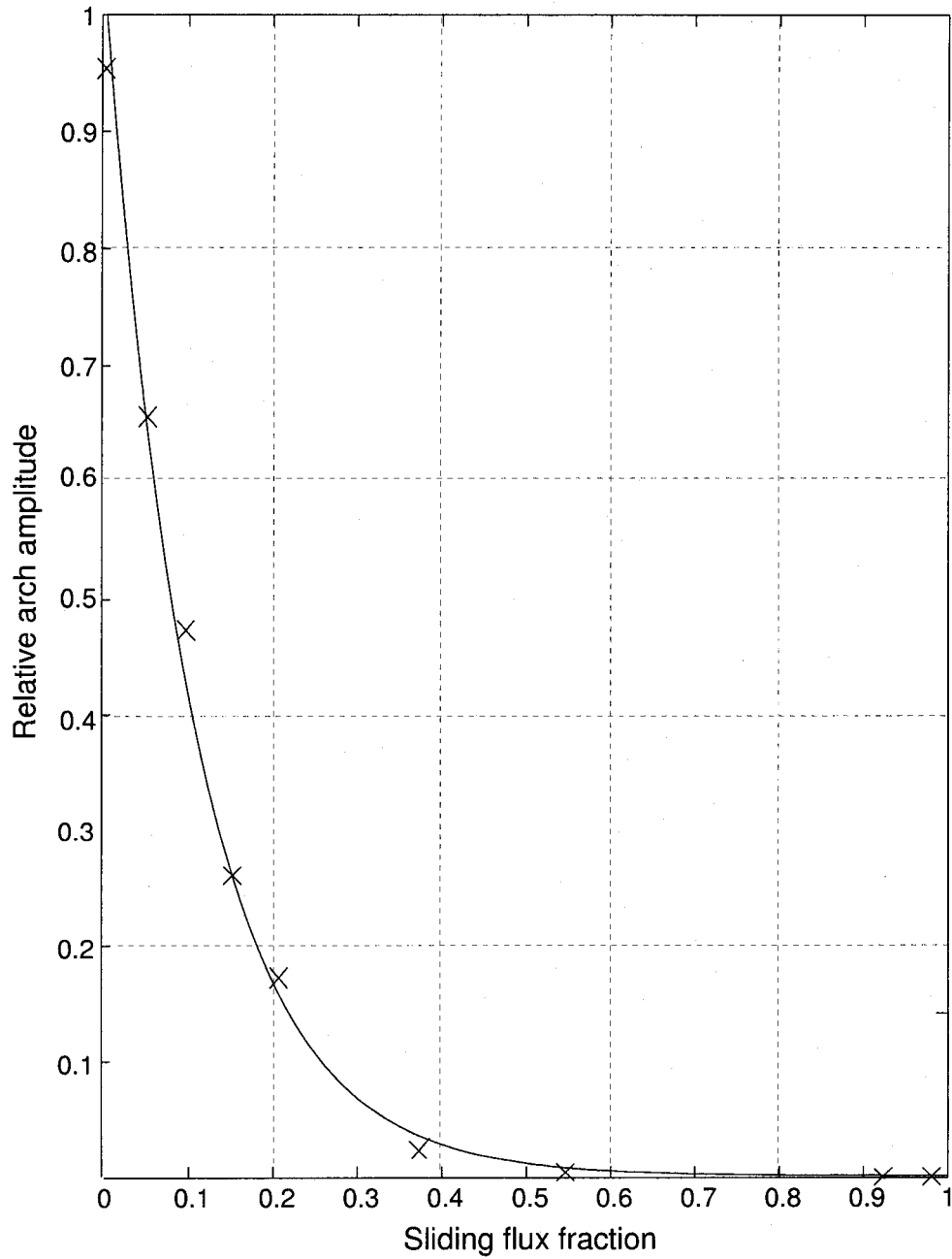


Figure 3.6: Relationship between the maximum Raymond Bump amplitude for each model run ('x'; plotted relative to the stiff-tilt model run) and the ratio of sliding to total flux at a distance of five ice thicknesses from the divide. The curve is an exponential fitted to the data points.

the results should be the same. Also, the longitudinal coupling in the ice will smooth out stress variations due to roughness or small topographic features.

Although we present results for a steady-state ice sheet, ice divides that are undergoing changes are probably never far from the steady-state stress and flow patterns that we derive [e.g. *Nereson and Waddington, 2002*]. This allows us to use our results to address changes in flow and stratigraphy as an ice sheet evolves. For example, *Conway et al. [1999]* used the stratigraphy observed by ice-penetrating radar in the vicinity of the divide on Roosevelt Island to infer that, prior to 3200 years ago, Roosevelt Island did not exhibit the special flow pattern that is characteristic of an ice divide frozen to its bed [*Raymond, 1983*]. They also went on to infer that Roosevelt Island was not an ice divide prior to 3200 B.P.; it may have been on the slope of a larger ice sheet. While the latter inference may be correct, our results suggest that an alternate interpretation is possible. Prior to 3200 B.P., Roosevelt Island could have supported an ice divide over a wet bed that allowed sliding; if, at 3200 B.P. the basal ice on Roosevelt Island then froze to the bedrock, then the special ice-divide flow pattern that is creating the observed transient Raymond Bump would have been initiated. The ice on Roosevelt Island appears to have thinned by several hundred meters since 3200 B.P. [*Conway et al., 1999*]. Comparable thinning prior to 3200 B.P. would have tended to cool the basal ice and, if it was thawed, could have lead to freezing.

3.6 Conclusion

In this modelling study, we find that basal-ice motion under a divide in plane strain is likely to exhibit a roughly linear increase with distance from the divide if the ice-bed interface is slippery. The basal motion is limited not by shearing in the till but by longitudinal stretching within the ice.

The shapes of the horizontal- and vertical-velocity profiles are more uniform with distance from the divide when the basal ice is allowed to slide; the unique divide flow described by *Raymond [1983]* disappears. This creates flatter isochrones and a younger depth-age scale. As the sliding contribution increases, the vertical-velocity pattern (Figure 3.3) and the depth-age distribution (Figure 3.7), approach their corresponding patterns on the

flank. In addition, as the flux fraction due to basal motion is increased, the longitudinal and vertical strain rates become more uniformly distributed over depth. As a result, the ice experiences greater downward flow at all intermediate depths, creating younger depth-age relationships as shown in Figure 3.7.

The history of basal sliding is an important factor in the interpretation of ice-penetrating radar layers and depth-age scales for ice-core records at ice divides.

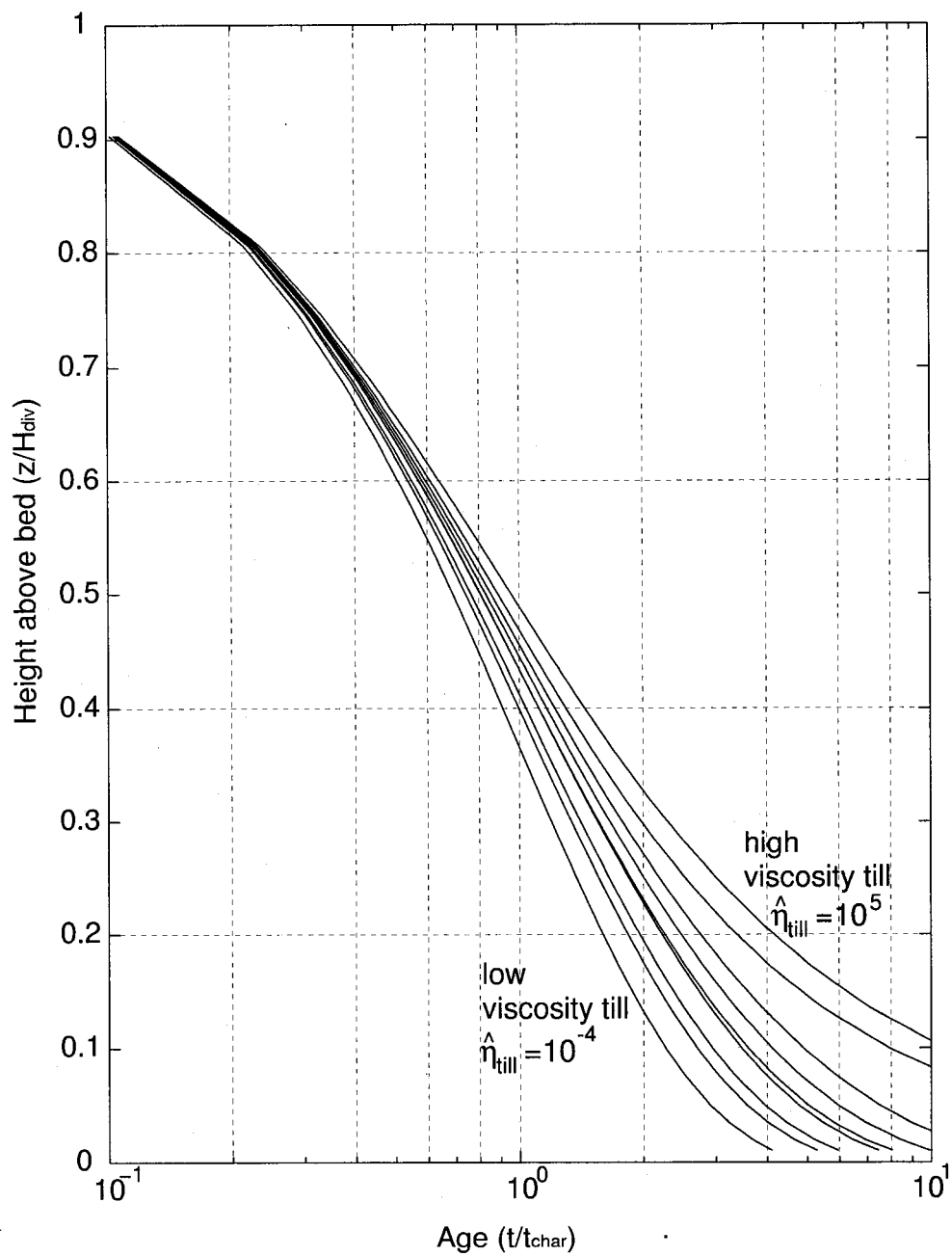


Figure 3.7: Depth-age scale at the ice divide for varying till viscosities. Since the final steady-state geometries are slightly different, we use non-dimensional time $t = \hat{t}/t_{\text{char}}$. The depth-age scales for all model runs at a location on the flank fall on the same curve as the low-viscosity till model run.

Chapter 4

THE ROLE OF ANISOTROPY IN FLOW NEAR AN ICE DIVIDE

This chapter is in preparation as a paper with co-authors Ed Waddington, Throstur Thorsteinsson, and Paul Jacobson.

4.1 Summary

Polycrystalline ice within an ice sheet shows a preferred crystal orientation that typically has a c-axes clustered vertically due to the dominant stress patterns. We explore the effect of this anisotropy on the large-scale flow pattern near an ice divide. We incorporate an analytical formulation for anisotropy into the nonlinear flow law within a finite-element ice-sheet flow model. With four different profiles of crystal fabric, we show that the effect of anisotropy depends on the vertical distribution of the crystal fabric and is consequential only when the fabric tightens to an effective cone angle of less than about 30 degrees. For a steady-state divide with a nonlinear flow law for ice, the shape and size of the isochrone arch reflects the details of the crystal fabric as well as the nonlinearity of ice flow. A vertically oriented fabric tends to increase the magnitude of the special divide flow pattern that is produced by the stress-dependent viscosity of a power-law fluid. Fabric has little effect on ice divide flow when ice is modelled as a constant viscosity fluid.

4.2 Introduction and Background

Deformation of single ice crystals in response to stress is strongly anisotropic. Crystals shear easily along their basal planes, much like a deck of cards, while shear on other planes is almost two orders of magnitude harder [Duval *et al.*, 1983]. Moreover, the bulk strain rate of a polycrystalline aggregate subjected to stress depends on the orientations of the crystals within it. The deformation of anisotropic ice has been studied extensively both in theory [Johnson, 1977; Budd and Jacka, 1989; Alley, 1992; Azuma, 1994; Azuma and

Goto-Azuma, 1996; *Castelnaud et al.*, 1996] and in the laboratory [*Duval*, 1981; *Duval and LeGac*, 1982; *Shoji and Langway*, 1985; *Pimienta et al.*, 1988; *Castelnaud et al.*, 1998]; it has been explored less so in observation and modelling of large-scale glacier flow [*Russell-Head and Budd*, 1979; *Paterson*, 1991; *Castelnaud et al.*, 1998; *Thorsteinsson et al.*, 1999].

As ice undergoes viscous deformation, the ice crystals rotate towards the most compressive stress [*Paterson*, 1994]. Thus, ice in glaciers and ice sheets typically has a non-random *crystal orientation fabric* (the statistical pattern of crystal orientations within the bulk) that exhibits preferred orientation depending on the state of stress [*Alley*, 1992, e.g.]. In valley glacier the fabric can vary widely because the stress tensor is variable on small spatial scales. In ice sheets, however, the stress tensor is more uniform, except near bedrock bumps and near the terminus.

Despite evidence that ice behaves anisotropically on large scales, most ice-sheet models treat ice as an isotropic material [*Marshall et al.*, 2000, e.g.]. This is a natural result of the complexity of describing an anisotropic stress-strain-rate relationship, and the large-scale effects of anisotropy can sometimes be incorporated through “enhancement factors” in the isotropic ice flow law known as Glen’s Law [*Glen*, 1958; *Nye*, 1953]. As ice sheet models are improved and our expectations for detailed predictions of ice flow increase, the effect of anisotropy on ice-sheet-scale ice flow may no longer be negligible. The need to incorporate measurements of crystal fabric into ice flow models is increasing, especially at ice divides where stratigraphy in ice cores may be affected in unanticipated ways [*Alley et al.*, 1997, e.g.].

We model two-dimensional plane-strain flow of the divide region of an ideal ice-sheet to examine the effects of anisotropy on the flow near ice divides. Divides are unique in terms of their flow behavior when compared to other regions of ice sheets. The low shear stress near the divide renders invalid the normal assumption that longitudinal stress and its gradients are negligible. Yet, accurate models of flow near ice divides contribute significantly to interpretation of ice-core and borehole measurements as well as to GPS surface motion and radar internal structure information [*Raymond*, 1983; *Nereson et al.*, 2000, e.g.] .

At the divide, the effective deviatoric stress is small and its spatial variability is dom-

inated by the longitudinal stress pattern. Because of the nonlinearity of Glen's Law, ice experiencing low stress has a high effective viscosity. In the central region of an ice sheet, the lowest deviatoric stresses are found near the bed and within one ice thickness of the divide (refer to Figure 2.1). Correspondingly, the ice there has a significantly higher effective viscosity than the surrounding ice. The flow field is warped around this "lump" of hard ice, producing a "special" divide flow pattern [Raymond, 1983]. Under the divide, older ice is closer to the surface than on the flanks; an arch appears in the isochrones, a feature often called a *Raymond bump*. We can observe the signature of this flow pattern in the internal structure observed by radio-echo sounding images [Vaughan *et al.*, 1999].

The divide signature, particularly as seen in radar images, has been used to infer past and present behavior of ice sheets [Nereson *et al.*, 1998b, a; Nereson and Waddington, 2002; Marshall and Cuffey, 2000]. Since ice-sheet ice typically exhibits a strong crystal fabric, we expect that anisotropic ice flow alters this special divide flow pattern. For example, when basal planes are aligned parallel to the direction of shear stress, flow is enhanced by up to nine times that predicted by Glen's Law [Budd and Jacka, 1989; Azuma, 1994; Azuma and Goto-Azuma, 1996; Castelnaud *et al.*, 1996; Thorsteinsson, 2002]. Characterizing the flow pattern resulting from combined nonlinear and anisotropic deformation will improve interpretation of the divide signature and predictions made by ice-sheet flow models.

As a first step, Mangeney *et al.* [1996] modelled the flow of anisotropic ice near an isothermal, plane-strain, two-dimensional divide using a linear stress-strain relationship for ice. In this chapter, we take the role of anisotropy to the next step by combining a description of anisotropic deformation based on linear flow at the crystal scale with a more realistic nonlinear constitutive relation for bulk flow of ice. We have developed an analytic description for anisotropy that is an extension of the work in Thorsteinsson [2001]. Although our model is not a full nonlinear anisotropic ice-sheet flow model, it captures the essential impact of anisotropy on deformation near a divide, and it is simple to implement in ice-sheet models.

4.3 An Anisotropic Constitutive Law for Ice

Empirically, ice behaves as a power-law fluid [Glen, 1955; Nye, 1953]. The simplest expression for Glen's Law (introduced in Chapter 2) is $\dot{\epsilon}_{\text{eff}} = A\tau_{\text{eff}}^3$, where $\dot{\epsilon}_{\text{eff}}$ is the effective strain rate and τ_{eff} is the effective stress.¹ In this form, all the variations due to properties of the ice are lumped into A , the *softness parameter*. As we discussed in Chapter 2, this form is limiting, for two primary reasons. First, ice flow results from a combination of micro-scale flow mechanisms, and as a result, the flow-law exponent may change as the dominant flow mechanism changes [Pettit and Waddington, in press, Chapter 2]. Second, polycrystalline ice in an ice sheet is strongly anisotropic; a vertically oriented fabric develops with depth driven by the stress regime [Alley, 1992]. In anisotropic ice flow, the components of the strain-rate tensor are no longer proportional to the corresponding stress component and, thus, a simple softness parameter is ineffective at describing ice flow.

The standard stress-strain-rate relationship used in ice flow models is

$$\dot{\epsilon}_{ij} = EA_0 e^{-Q/RT} \tau_{\text{eff}}^2 \tau_{ij}, \quad (4.1)$$

This formulation does not provide a means for incorporating the directional flow enhancements due to anisotropy, except cursorily through the scalar enhancement factor, E .

Many authors have presented anisotropic flow laws for ice [Castelnau *et al.*, 1996; Azuma, 1994; Thorsteinsson, 2001, e.g.]. Their approaches differ primarily in how they translate the large scale applied stress to the local deformation of a crystal within the aggregate. One end of the spectrum assumes that the strain of all crystals is the same, the *homogeneous-strain assumption*. In this case, crystals that are favorably oriented for deformation (under the given state of stress) deform and shift the stress burden onto neighboring unfavorably oriented crystals. The other end of the spectrum of anisotropic flow laws assumes that the applied stress is the same for all crystals, the *homogeneous-stress assumption* or the *Sachs model* [Sachs, 1928]. Each crystal deforms at a rate dependent on its orientation, and grain boundaries migrate to ensure no gaps between grains appear.

¹Appendix A is a table of the notation.

The real distribution of stress is probably somewhere in between. The homogeneous-stress assumption is likely closer to the real mechanism in ice since the homogeneous-strain assumption requires up to 5 active slip systems to accommodate deformation, while the homogeneous-stress assumption can be accommodated by grain-boundary processes [Thorsteinsson, 2000].

We use a model developed by Thorsteinsson [2001], based on homogeneous stress, in which the bulk deformation of the ice aggregate is assumed to be the average deformation of all the crystals within the aggregate. The resolved shear stress (RSS) on the basal plane of each crystal depends on its orientation relative to the applied stress. The RSS drives the deformation of the crystal. Thus, crystals with basal planes oriented parallel to the shear stress will have a larger RSS and will deform more readily than crystals with basal planes oriented perpendicular to the shear stress.

To build an ice flow law from this theory, Thorsteinsson [2001] used a distribution of crystal orientations within an aggregate to define the bulk deformation. The fabric within an ice sheet typically has a cluster of c-axes oriented vertically. This type of fabric can be approximated by defining a “cone angle” that is the half-apex angle of a cone within which all the crystals are uniformly distributed. Thorsteinsson derived analytical solutions to describe the deformation of the bulk material for a given cone angle. The advantage of the analytical solution is that it is relatively easy to incorporate into a flow model. Compared to other formulations, this formulation generally under-predicts anisotropic enhancement [Azuma, 1994; Castelnau *et al.*, 1996; Thorsteinsson, 2001]. But since the “real” enhancement is not known and the style of deformation is generally the same for all formulations, we assume the scalar enhancement factor, E , for the bulk material will adjust to account for this uncertainty. Thorsteinsson’s analytical formulation has two limitations; it does not allow for evolution of the fabric, and it does not include interactions between neighboring crystals [Thorsteinsson, 2002].

Under the assumption of plane strain with a stress state of combined pure shear and

simple shear, the deviatoric stress tensor has the form:

$$\tau_{ij} = \begin{bmatrix} \sigma & 0 & \tau \\ 0 & 0 & 0 \\ \tau & 0 & -\sigma \end{bmatrix}. \quad (4.2)$$

Based on *Thorsteinsson* [2001], using the homogeneous stress assumption (Sach's model) and a linear ice rheology, the strain rate can be described as a function of vertically oriented cone angle:

$$\dot{\epsilon}_{ij} = \frac{1}{\eta_{\text{eff}}} \begin{bmatrix} a\tau_{11} + c\tau_{22} + b\tau_{33} & d\tau_{12} & e\tau_{13} \\ d\tau_{12} & c\tau_{11} + a\tau_{22} + b\tau_{33} & e\tau_{23} \\ e\tau_{13} & e\tau_{23} & b(\tau_{11} + \tau_{22} - 2\tau_{33}) \end{bmatrix}, \quad (4.3)$$

where

$$\begin{aligned} a &= \frac{1}{48}(100 + 95 \cos \alpha + 36 \cos 2\alpha + 9 \cos 3\alpha) \sin^2 \left(\frac{\alpha}{2} \right), \\ b &= -\frac{1}{12}(20 + 25 \cos \alpha + 12 \cos 2\alpha + 3 \cos 3\alpha) \sin^2 \left(\frac{\alpha}{2} \right), \\ c &= \frac{1}{48}(-20 + 5 \cos \alpha + 12 \cos 2\alpha + 3 \cos 3\alpha) \sin^2 \left(\frac{\alpha}{2} \right), \\ d &= \frac{1}{8}(20 + 15 \cos \alpha + 4 \cos 2\alpha + \cos 3\alpha) \sin^2 \left(\frac{\alpha}{2} \right), \\ e &= \frac{1}{8}(10 + 4 \cos \alpha + 3 \cos 2\alpha + 2 \cos 3\alpha + \cos 4\alpha), \end{aligned} \quad (4.4)$$

α is the cone angle, and η_{eff} is an effective viscosity (from Glen's Law based on the isotropic softness parameter and enhancement factor). For the plane strain assumption (Equation 4.2), the stress balance and conservation of mass equations can be rewritten as partial differential equations²:

$$\eta_{\text{eff}} \left(\frac{-1}{3b} \frac{a-b}{2a+b} - \frac{1}{2e} \right) u_{xx} + \eta_{\text{eff}} \frac{1}{2e} u_{zz} - p_x = 0 \quad (4.5)$$

²A more complete derivation of these equations is in Appendix D

$$\eta_{\text{eff}} \frac{1}{2e} w_{xx} + \eta_{\text{eff}} \left(\frac{-1}{3b} - \frac{1}{2e} \right) w_{zz} - p_z = \rho g \quad (4.6)$$

$$u_x + w_z = 0. \quad (4.7)$$

This derivation assumes that A and a through e are spatially uniform; therefore, these PDE's apply to individual finite elements, and are not descriptive of the overall flow field.

4.4 Measurements of Anisotropy

Ice sheet fabric has traditionally been measured in two ways. In the laboratory, ice-core thin sections viewed through cross polarizing filters provide statistics of crystal orientation for tens to a few hundred crystals [Gow *et al.*, 1997; Thorsteinsson *et al.*, 1997, e.g.]. In the field, borehole sonic logging measures the speed of sound transmitted through through approximately 7 meters of ice (containing thousands of crystals) [Thorsteinsson *et al.*, 1999]. Sound speed reflects the elastic anisotropy, which is related to fabric in a straightforward way. Thorsteinsson [2000] relates this sonic velocity measurement to an effective cone angle, which is a convenient measure for vertically symmetric fabric such as ice found in ice sheets. Ice core fabric data can also be represented as an equivalent cone angle (such that it encloses 90% of the c-axes of the real fabric, for example) to compare with the sonic log. Thorsteinsson [2000] compared cone angles calculated from sonic velocity measurements to those calculated from thin section and concluded that the sonic velocity is the most useful and accurate and, additionally, has a high vertical spatial resolution. In this study, we take advantage of the sonic log measured at Siple Dome, West Antarctica (G. Lamorey, personal communication, 1999) and converted to cone angle using the method described by Thorsteinsson [2000].

4.5 Anisotropic Flow near an Ice Divide

Before studying anisotropic divide flow with the analytical finite element model, we estimate the expected effect of anisotropy in the divide region using results from the Thorsteinsson [2001] model for predicting anisotropic deformation (based on nonlinear ice rheology).

As we mentioned earlier, Mangeney *et al.* [1996] first examined the effect of a vertically

symmetric crystal fabric on linear, isothermal flow of a 2D plane-strain ice divide. Using a fabric that is isotropic near the surface and becomes progressively tighter with depth in the ice sheet, they showed that both the horizontal and vertical velocities increased by approximately 1.5 times. Shear was concentrated in the lower, tighter-fabric ice, causing the horizontal velocity profile to have slightly higher curvature. The key limitation in this model is that both the anisotropic deformation and the bulk ice flow are based on linear rheology; the shape of the velocity profiles does not vary with distance from the divide and no special divide flow pattern is produced.

The *Thorsteinsson* [2001] model is a more complex fully nonlinear version of Equations 4.3 through 4.7. Figure 4.1 shows results from his calculations for the increase in vertical strain rate due to anisotropic flow under a combined pure shear and simple shear stress state. Given a cone angle and a relative amount of shear stress, the contours show the flow enhancement of the vertical strain rate. (Enhancements for other strain rate components differ depending on the degree of anisotropy.) We focus on vertical strain rate because it is sensitive to ice rheology and the difference in shape of the vertical-velocity profile between the divide and flank profiles determines the size of the arch in the isochrones (see Chapter 2).

In Figure 4.1, note that the cone angle associated with peak enhancement of vertical strain rate varies from about 60 degrees to 35 degrees as the relative amount of shear stress increases. This is an expression of the differing direction of the maximum applied compressive stress (vertical on the left edge of the graph approaching 45 degrees on the right edge). The lower left region of the figure, where cone angles are less than 40 degrees, represents stiff ice in vertical compression relative to isotropic ice. Specifically, ice with cone angles between 20 and 40 degrees are stiff when compressed vertically, but softer than isotropic ice when undergoing shear. This is because an aggregate with a small vertical cone angle can easily shear parallel to the basal planes, yet vertical compression perpendicular to the basal planes is very difficult. If the crystals have a broader distribution of c-axes (spread over a cone larger than 45 degrees, for example) then the ice is soft when compressed vertically, because many of the crystals have basal planes tilted nearly parallel to the applied stress.

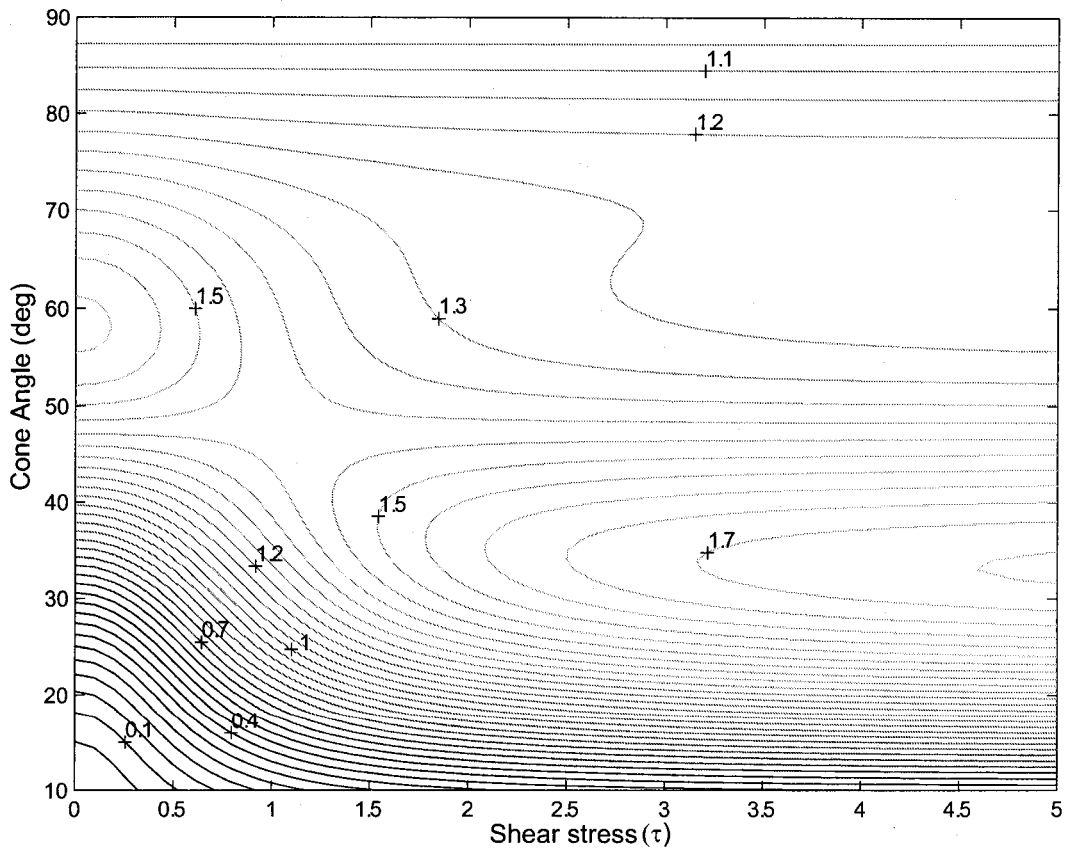


Figure 4.1: Enhancement in vertical strain rate due to anisotropy for combined simple and pure shear. The x-axis is the ratio of the magnitude of the simple shear stress to pure shear, such that the far left region of the figure represents flow dominated by pure shear (similar to ice divide flow) and the middle and right regions represent flow dominated by simple shear (similar to flank flow). On the vertical axis the cone angle varies from 0° (strongly anisotropic) to 90° (isotropic). Note that the cone angle associated with the peak enhancement varies as the relative amount of shear stress varies. (Adapted from *Thorsteinsson* [2001].)

We estimate the effect of this enhancement (or reduction) on flow near an ice divide by using a cone-angle profile derived from Siple Dome's sonic velocity log. To first order, the cone-angle profile at a site within ten ice-thicknesses of the divide will have the same character as the divide profile, since both areas have similar histories and particle paths for the deep ice begin near the divide. Therefore, in Figure 4.2 we apply the results shown in Figure 4.1 to Siple Dome's cone-angle profile for two stress fields: one similar to a divide (pure shear) and one similar to a flank site (dominated by simple shear).

Throughout most of the depth of the ice sheet, the ice is stiffer at the divide than on the flank. This difference in effective viscosity is similar in character to the viscosity difference described by *Raymond* [1983] due to the nonlinearity of the flow law, which produces an arch in the isochrones and affects the depth-age scale at an ice divide. Figure 4.2 suggests that anisotropy can produce an arch in the isochrones similar to the Raymond bump. This calculation is a first-order estimation of the effect of anisotropy on the divide flow pattern. There is no mechanism to redistribute the stresses within the ice sheet due to the feedback between the deviatoric stress distribution and the effective viscosity. A more realistic assessment of an anisotropy-induced arch in the isochrones ("Throstur's bump"?) requires a finite-element model.

4.6 Finite-Element Ice-Flow Model

We model an idealized divide with a thermomechanically coupled finite-element model. The geometry and approach are similar to *Raymond* [1983], *Mangeney et al.* [1996], and Chapters 2 and 3. The fundamental assumptions of the model include:

1. The ice deforms in plane strain; thus, the model best represents a ridge ice divide, such as Siple Dome [*Nereson et al.*, 1996] or Roosevelt Island [*Conway et al.*, 1999].
2. The temperature calculation is based on the surface temperature and the geothermal gradient. Conduction, advection, and strain heating are included in the thermal model. The temperature is updated once each time step after the iterative flow solution.

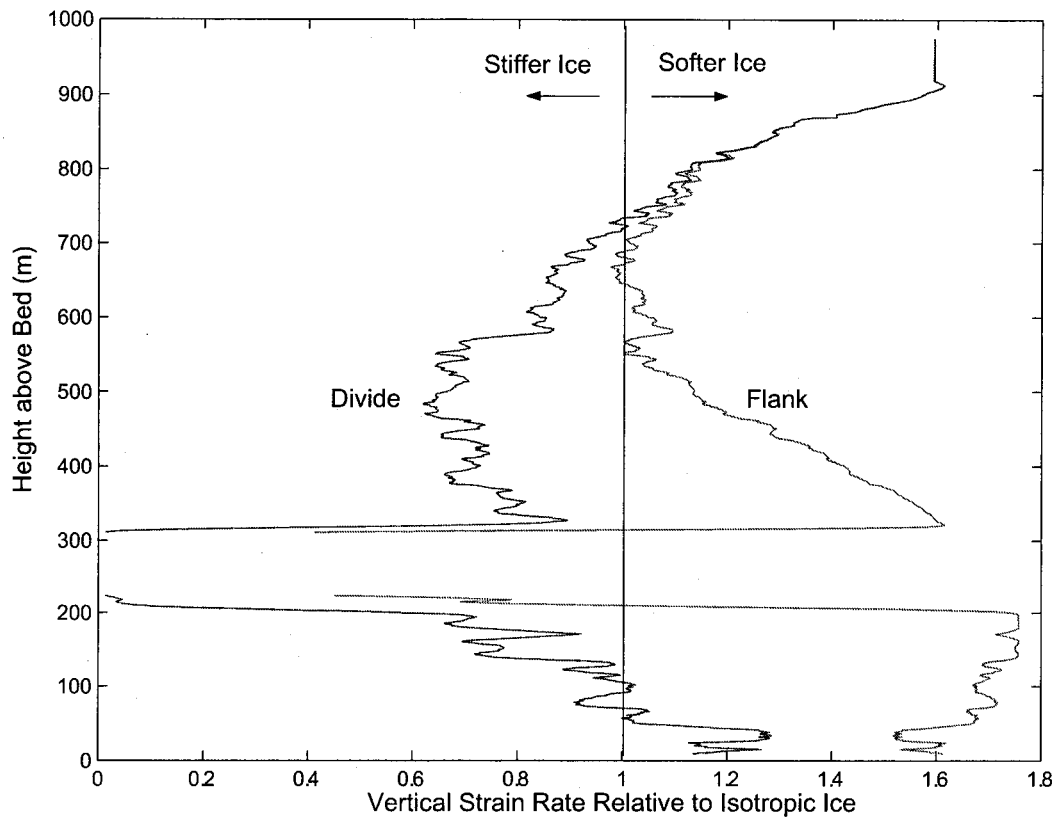


Figure 4.2: Enhancement in vertical strain rate (from Figure 4.1) at the divide and flank sites due to anisotropy for fabric measured by sonic velocity logging of the Siple Dome borehole.

3. The upper surface is stress-free.
4. The divide is a line of symmetry where ice is constrained to move only vertically.
5. The horizontal-velocity profile on the flank boundary (at 30 ice thicknesses from the divide) carries away the integrated mass balance from the divide to the boundary, in order to satisfy mass conservation for a steady-state ice sheet. Because our boundary is more than 20 ice thicknesses from the divide, the results for the region within ten ice thicknesses of the divide are insensitive to the details of the horizontal-velocity profile on the flank boundary [Raymond, 1983; Schøtt *et al.*, 1992]. In practice, we begin with a laminar flow profile at the boundary, but as velocities within the ice sheet are calculated, we update the shape of the horizontal-velocity profile at the boundary (while maintaining the flux) to account for the unique rheological properties of the anisotropic ice and the non-uniform temperature field.
6. The flow law with anisotropy is incorporated through a two steps calculation. First an isotropic effective viscosity (η_{eff}) is calculated for each element from the effective strain rate calculated during the previous iteration using Glen's cubic flow law for isotropic ice. Then this effective viscosity is substituted in Equations (4.5) to (4.7), which are solved for the new velocity gradients for the element, given the element's cone angle. This process is repeated for a specified number of iterations (typically 10) to achieve reasonable convergence within a timestep. This two-step process allows us to combine the nonlinear bulk flow of ice based on Glen's Law with a description of anisotropy (based on a linear rheology). Small uncertainties will be introduced where the ice properties (such as cone angle) of adjacent elements are vary.
7. In these models the cone angle at the divide is extrapolated to the flanks as a function of normalized depth ($z/H(x)$).
8. The model solves the flow equations on a grid of 9-node quadratic elements for temperature, pressure, and velocity fields.

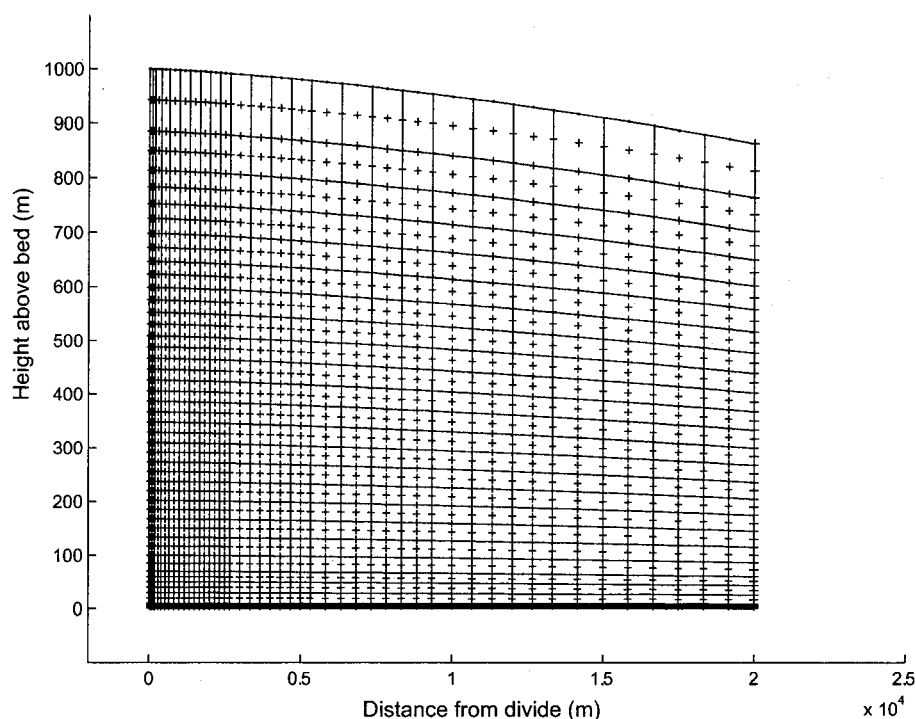


Figure 4.3: Finite element mesh of 9-node quadrilateral elements for a model of idealized divide. The divide is a plane of symmetry. Each plus marks the center of an element

The physical characteristics of the model are based on Siple Dome [Nereson *et al.*, 1996]: 1000 meter thick, with an accumulation rate of 0.12 m/a^{-1} , a surface temperature -25°C , and geothermal flux 65 W m^{-2} . We use a 55×51 node grid of elements with elements concentrated in the divide region and near the bed (Figure 4.3).

We initialize the surface profile from a simple isotropic model using the assumptions of the shallow ice approximation. The surface then evolves, forced by the ice flow and the prescribed accumulation rate, until it achieves a steady state. Steady state is reached when the root-mean-square of the change in the surface velocities within 10 ice-thicknesses of the divide does not exceed a specified tolerance, ϵ (typically $< 10^{-8} \text{ m a}^{-1}$ per year). The resulting solutions for different profiles of anisotropy, therefore, may not have the same ice thickness or surface profile. The alternative is to use the same ice-sheet thickness at the

divide for all models, but adjust the steady-state accumulation rate. The two alternatives produce similar conclusions; we chose to force each model with identical accumulation rates and allow ice thickness to vary because of simpler solution techniques. We therefore non-dimensionalized the results; velocities are expressed relative to the surface velocity (accumulation rate plus the small advection of ice from upstream) and thicknesses are relative to the ice thickness at the divide unless otherwise noted.

4.7 Model Results and Discussion

As discussed earlier, most measurements of crystal fabric in ice sheets show a similar pattern, with isotropic ice near the surface and a tightening of the fabric with depth. The details of the actual distribution of cone angle with depth can vary depending on each ice sheet's history. We chose four different cone-angle profiles for this study, shown in the left column of Figure 4.4. The isotropic profile used for comparison for all models has an equivalent cone-angle profile of 90 degrees at all depths. The middle column of Figure 4.4 shows the predicted vertical velocity profile at the divide and the flank for each model. The right column shows the horizontal velocity profiles at one, two, and ten ice-thicknesses from the divide. The solid lines represent the anisotropic-nonlinear solutions. For comparison, we include the solution for anisotropic-linear flow (dot-dash lines), isotropic-nonlinear flow (dashed lines), and isotropic-linear flow (dotted lines).

Models A and B have fabric that is consistently above about 35 degrees. Neither of these models show much effect from the anisotropy. The vertical-velocity profiles are nearly identical to the isotropic nonlinear model; this result is expected since the anisotropic model uses the isotropic nonlinear model as a foundation. Models C and D both have regions with extremely tight fabrics. Model C, which is based on the measured sonic log from Siple Dome, shows the significance of a distinct band of tight fabric. This band is a real feature in the sonic velocity log, possibly associated with the Holocene/Wisconsin boundary at about 700 meters depth and the onset of recrystallization at just over 800 meters depth. The results from this model are show larger in Figure 4.5.

Model D shows the effects of a broader band of tight fabric without the sharp discon-

tinuities in the Siple Dome fabric. Both of these fabrics show significant changes in the vertical-velocity profile when compared to the effects of model A and B. It seems fabric tighter than about 30 degrees is needed for the anisotropy to have a measurable effect on the divide flow pattern. Interestingly, for ice flow based on a linear rheology even strong anisotropy has small overall effect. This result agrees in part with the conclusion reached by *Mangoney et al.* [1996]. We see less of an increase in magnitude of the velocities than *Mangoney et al.* [1996], this may be because of the differences in the assumed cone angle profile. (Their profile is most similar in shape to our profile A, but with stronger fabric near the bed.)

The band of highly oriented crystals in the Siple Dome profile (C) concentrates the shear such that the band of oriented crystals behaves like a false-bed in the divide region. In the right plot in Figure 4.5, this shear zone is narrow near the divide and thickens with distance from the divide. The corresponding vertical velocity within the band of anomalously tight fabric is small; most of vertical strain occurs above the band.

In Figure 4.6, we assume the cone angle profiles and corresponding flow patterns have existed for all time and calculate the isochrone patterns produced from each flow field. This false-bottom effect in the Siple Dome profile produces a large arch in the isochrones, much bigger than can be produced by nonlinear isotropic ice flow. (The three sets of isochrones shown are anisotropic-nonlinear (largest bumps), isotropic-nonlinear (middle bumps), and isotropic-linear (flat isochrones). For all the anisotropy models, the isochrone arches vary in shape and size depending on the details of the profile of anisotropy in the ice.

To compare the arches produced from all four anisotropy models, we quantify the bump height as the distance above a curve that fits the isochrone along its flanks. In Figure 4.7, we plot this height (relative to the ice thickness) as a function of the relative height of the isochrone above the bed 10 km from the divide. This graphical method for examining the details of isochrone arches is similar to that used by *Nereson and Waddington* [2002] and *Conway et al.* [1999]. The general bump-height profile is the same, but there are slight variations in the magnitude and height of the peak bump amplitude.

Finally, as we see with the velocity profiles in Figure 4.4 and the bump height profile in Figure 4.7, anisotropy based on linear ice rheology has little effect on the special divide flow

pattern, producing no significant isochrone arch. The effective viscosity for ice with linear rheology is not a function of the magnitude of the effective deviatoric stress; the difference between the linear-anisotropic and linear-isotropic cases is that the effective viscosity is a constant tensor, rather than a constant scalar, respectively. In order to produce the special divide flow pattern, the effective viscosity (whether scalar or tensor) must be a function of distance from the divide, which occurs when the viscosity is a function of the deviatoric stress. In other words, an isochrone arch is formed when the vertical strain rate is different at the divide compared to the flank. The vertical compressive stress driving this strain rate is nearly uniform with distance from the divide, while the shear stress component increases. For linear rheology and vertically oriented fabric, this increasing shear stress component has minimal effect on the anisotropic viscosity tensor (in part because the shear stress does alter the fabric). The viscosity tensor, therefore, does not vary with distance from divide and no special divide flow pattern can appear.

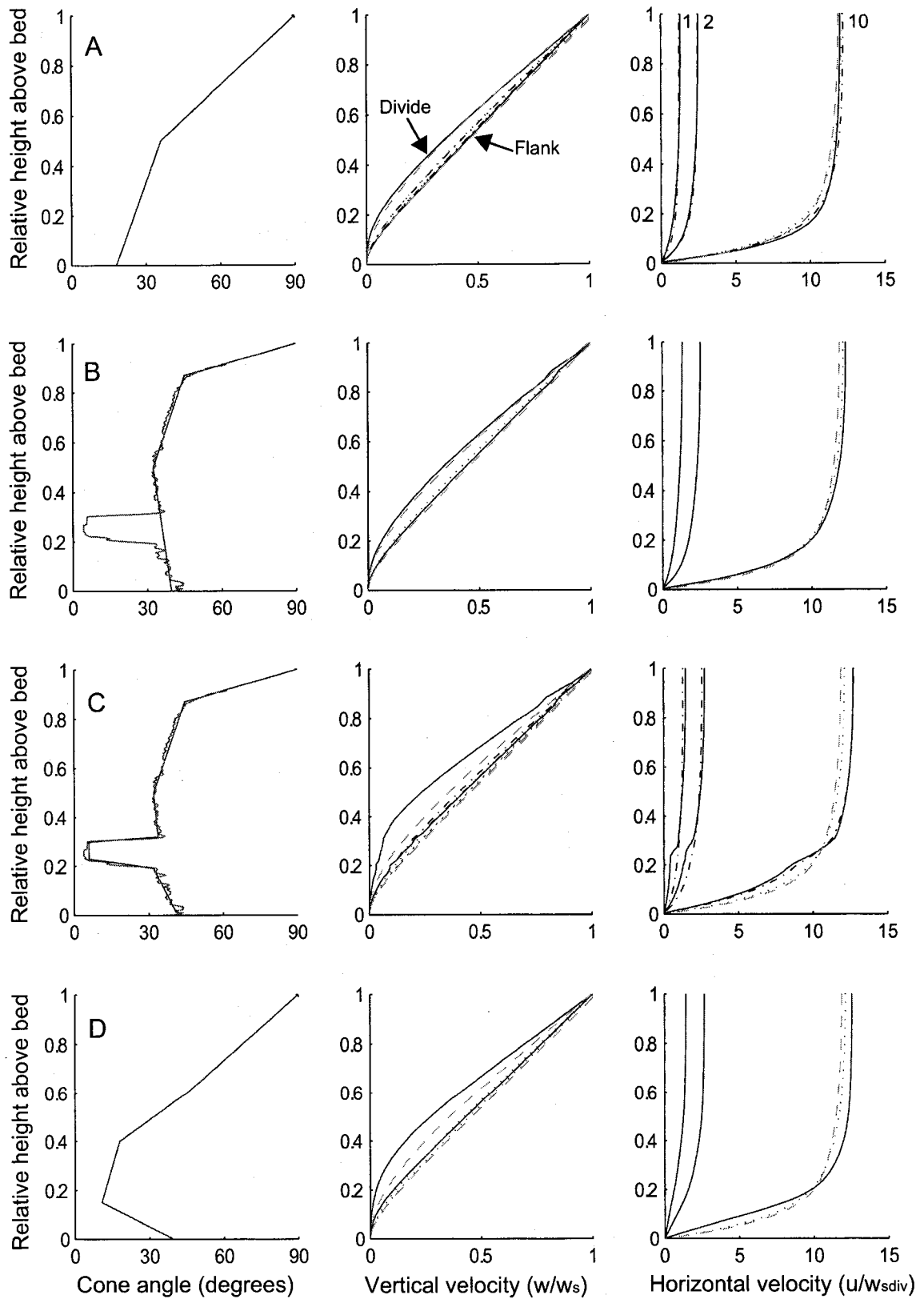
Also, with nonlinear rheology, there is a feedback between the deviatoric stress tensor and the effective viscosity. This feedback tends to redistribute the stresses within an ice sheet, such that stiff ice regions tend to support higher stresses (similar to ‘bridging’). These higher stresses then tend to decrease the stiffness, which, in turn, feeds back on the stress distribution. Linear rheology cuts off this feedback process. When anisotropy is included, the nonlinear feedback process is altered resulting in a large anisotropy effect on the divide flow pattern, while anisotropy has a negligible effect in the linear case without this feedback.

4.8 Conclusions and Implications

We combined a linear-based description for anisotropic ice flow with an isotropic nonlinear bulk ice constitutive law in a thermomechanical finite element model. Our goal was to assess the impact of crystal fabric on flow near a divide for nonlinearly behaving ice.

With four different profiles of crystal fabric, we show that the effect of anisotropy depends on the spatial distribution of the crystal fabric and is consequential only when the fabric tightens to an effective cone angle of less than about 30 degrees. For a steady-

Figure 4.4: The left plots are the four cone angle profiles we chose to model. Models B and C are based on the real sonic log for Siple Dome shown as the dotted line. The middle column shows the vertical velocity profiles at the divide and flank. The right column shows the horizontal profiles for 1, 2, and 10 ice thicknesses from the divide. On each plot, several models are shown for comparison. The solid lines are the anisotropic model with a nonlinear rheology. The dashed lines are isotropic and nonlinear. The dotted lines are isotropic linear flow. In models A and C, there is an additional dot-dash line that represents anisotropy combined with linear bulk ice rheology.



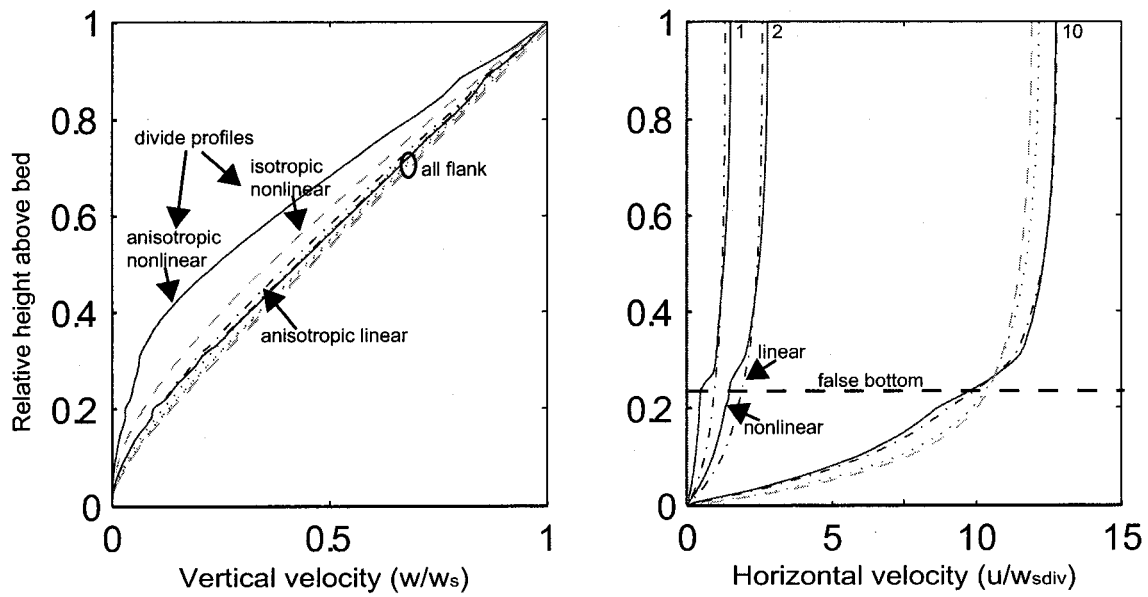


Figure 4.5: Vertical and horizontal velocities for an ice sheet with Siple Dome's cone-angle profile. The left figure shows the vertical velocity profiles at the divide and flank. The right figure shows the horizontal profiles for 1, 2, and 10 ice thicknesses from the divide. On each plot, several models are shown for comparison. The solid lines are the anisotropic profile from the left column with a nonlinear rheology. The dot-dash lines combine anisotropy with linear rheology (as labelled). The dashed lines are isotropic and nonlinear. And the dotted lines are isotropic linear flow.

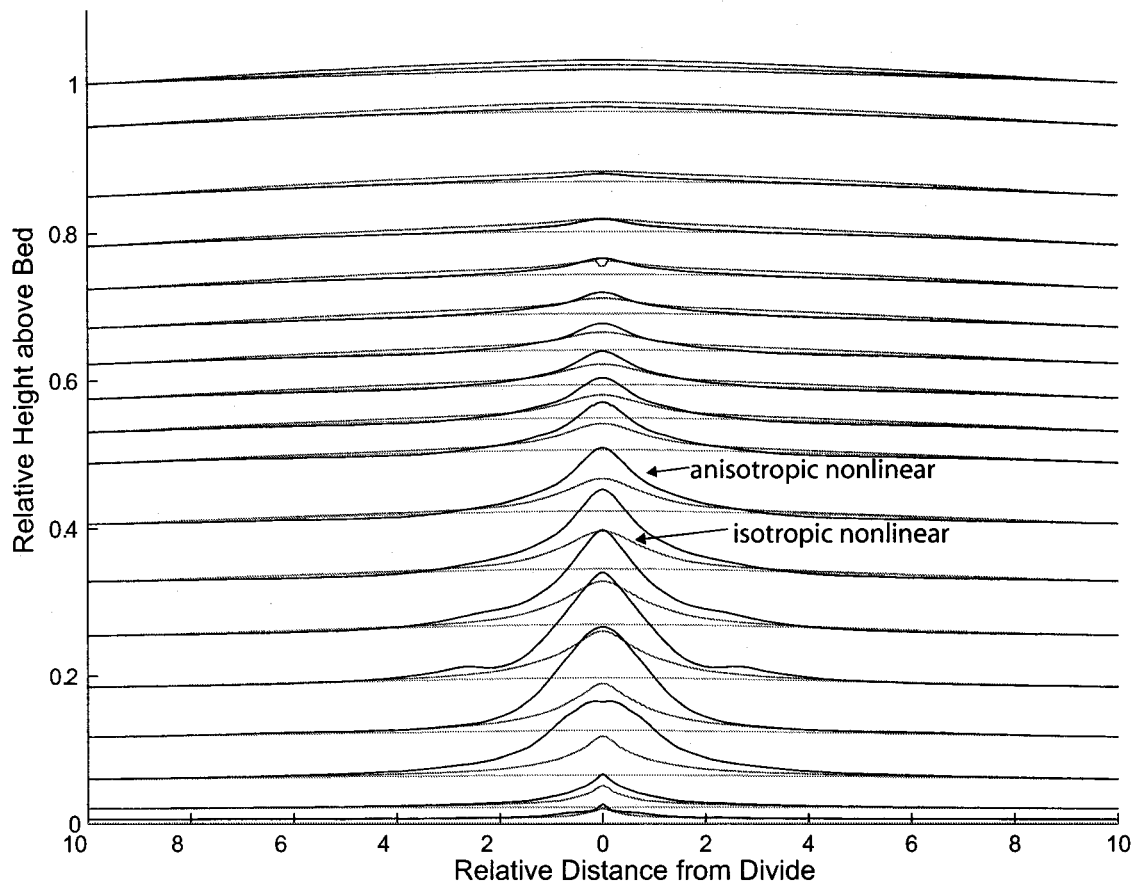


Figure 4.6: Isochrones in the divide region produced by anisotropic and isotropic flow for an ideal ice sheet. The largest isochrone arch is model D with nonlinear rheology, the second largest is model C, also nonlinear rheology. Models A and B are nearly indistinguishable from the isotropic nonlinear model. All linear models fail to produce an arch.

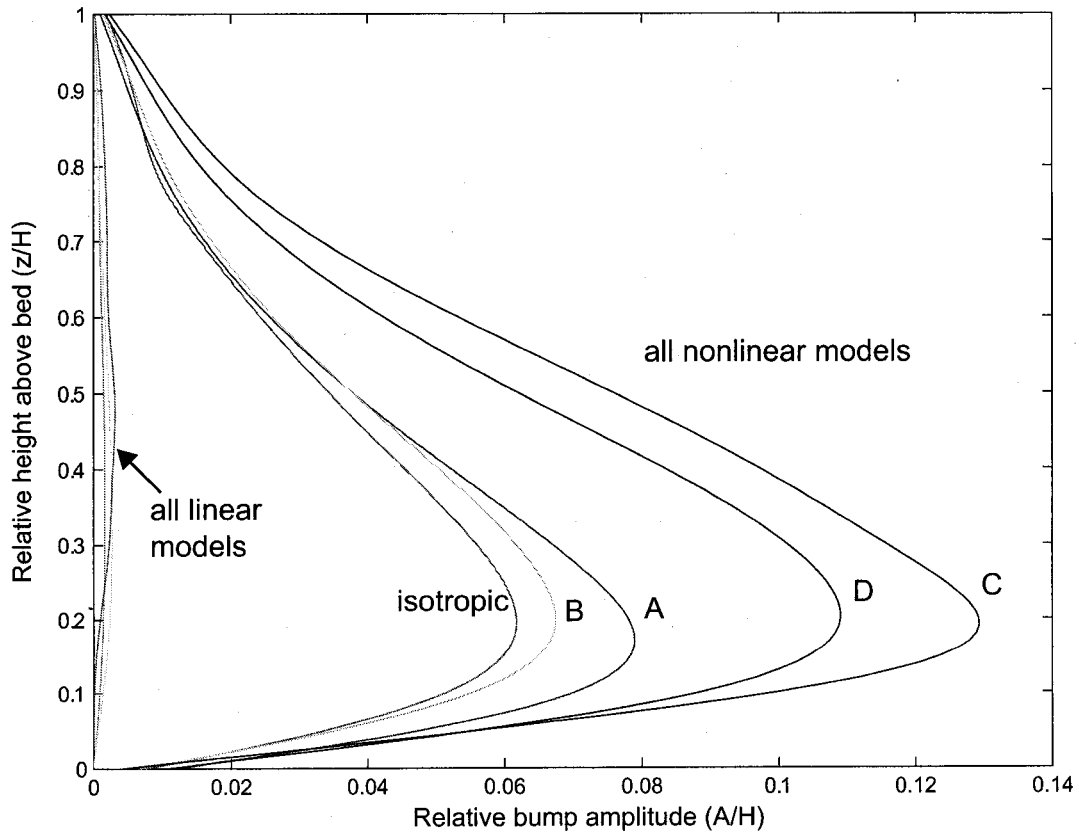


Figure 4.7: Height of the apex of the isochrone arch as a function of depth. Labels show models A-D, with the isotropic model for comparison. We quantify the bump height as the distance above a curve that fits an isochrone along its flanks. It is plotted as a function of the relative height of the isochrone 10 km from the divide.

state divide with a nonlinear flow law for ice, the shape and size of the isochrone arch reflects the details of the crystal fabric as well as the nonlinearity of ice flow.

An important conclusion is that anisotropic ice flow does not seem to produce an arch in the isochrones if the stress exponent in the flow law is equal to one. Only when the ice behaves nonlinearly (a stress exponent greater than unity), creating an isotropic Raymond bump, does crystal fabric work to enlarge and reshape the bump. With the vertically oriented crystal fabric typically found near ice divides, the effect of anisotropy is always to increase the size of the existing Raymond bump relative to the isotropic case.

The magnitude of the special divide flow pattern is a combination of several processes. *Pettit and Waddington* [in press] show that when flow near a divide is described by a flow law combining a linear term and a nonlinear (Glen) term, the size of the isochrone arch is a function of the relative importance of linear and nonlinear terms. The linear term dominates at low stresses, the nonlinear term at high stresses. When we expand this flow law to also describe flow of vertically-oriented anisotropic ice, the effect of the anisotropy is to modify the nonlinear term almost exclusively. Therefore we expect that a divide that has low enough stresses to be dominated by the linear term in the flow law will not be significantly affected by crystal anisotropy. But for divides that exhibit higher stresses, strongly anisotropic ice will significantly affect the ice flow pattern and the interpretation of ice core records, borehole logs, radar images, and deformation measurements.

Chapter 5

MASS BALANCE AND BEHAVIOR OF SIPLE DOME, WEST ANTARCTICA

This chapter was presented as a poster at the American Geophysical Union 2001 Fall Meeting with co-authors E.D. Waddington and N.A. Nereson (University of Washington), G. Hamilton (University of Maine), and M.A. Zumberge (UCSD Scripps Institute of Oceanography). One section (identified with footnotes) was published in *Zumberge et al.* [2002]. This chapter is also a draft of a paper for publication with the same co-authors.

5.1 Summary

We present three independent measurements of ice-thickness change in the divide region of Siple Dome: a GPS surface horizontal-strain network, fiber optic vertical-strain measurements at depth, and precision GPS measurements of vertical motion of near-surface ice (“coffee-can” method). From the horizontal strain network, we calculate the divergence of the horizontal velocity. This divergence is equal to the gradient of vertical velocity at the surface and, with some assumptions about the distribution of strain rates with depth, we can calculate the vertical velocity at the surface. For steady state, the vertical velocity must be balanced by the local accumulation rate. The fiber-optic instruments provide a profile of the relative vertical velocity with depth. We fit a theoretical vertical-velocity pattern to these data and extrapolate to find the surface vertical velocity. Our third method (coffee-can) directly measures the vertical motion of a marker 20 meters deep using precision GPS and compares it with the local long-term rate of snow accumulation to calculate the net rate of ice sheet thickness change.

All three methods reach the same conclusion: Siple Dome is currently very close to being in steady state. This result has three implications. First, ice dynamics models developed to interpret radar images or ice core data can assume steady state behavior in the present and recent past, simplifying the models. Second, our result suggests that the central part of the Ross Embayment may have had a low-elevation profile during the late

Holocene, even though other areas of the WAIS may have been thicker. Third, the steady state balance of Siple Dome constrains on the times scales for the behavior of its bounding ice streams.

5.2 Introduction

Siple Dome is a 1000 m thick ridge of slow-moving ice that sits between Ice Streams C and D, which are part of a system of ice streams that channel 90% of the ice flowing from the West Antarctic Ice Sheet into the Ross Ice Shelf [McIntyre, 1985] (Figure 5.1). The dynamics of these ice streams are a major factor affecting the rate of ice volume change in West Antarctica. As an inter-ice-stream ridge, Siple Dome's modern behavior in terms of its mass balance and geometric evolution provides constraints and clues to three glaciological puzzles related to the past and future of the West Antarctic Ice Sheet.

First, the Ross Sea Embayment has undergone significant thinning since the Last Glacial Maximum (LGM) [Denton and Hughes, 2000]. The pattern of deglaciation in the Ross Sea holds clues to the future of the marine-based West Antarctic Ice Sheet (WAIS). If Siple Dome is still undergoing thinning from deglaciation following the end of the LGM, measured accumulation rates should be smaller than the rate of surface lowering due to ice flow, as seems to be the case on Roosevelt Island [Conway *et al.*, 1999]. Second, as an inter-ice-stream ridge, Siple Dome's present geometry and internal structure are sensitive to changes in its bounding ice streams [Nereson *et al.*, 1998a; Nereson, 2000], thus it is possible to study recent ice dynamics of the Siple Coast through "reading" Siple Dome's present and past behavior. How has the shutdown of Kamb Ice Stream [Retzlaff and Bentley, 1993] affected Siple Dome? Can we "see" previous changes in the ice streams through Siple Dome? And third, Siple Dome is the location of the most recent U.S. Antarctic Program's deep drilling project for paleo-climate and paleo-ice-sheet studies. Successful interpretation of ice-core measurements requires knowledge of the local flow pattern and its history.

The mass balance of a polar ice sheet is a balance between snow accumulation and ice flow (characterized by the absolute vertical motion of the surface). A change in the

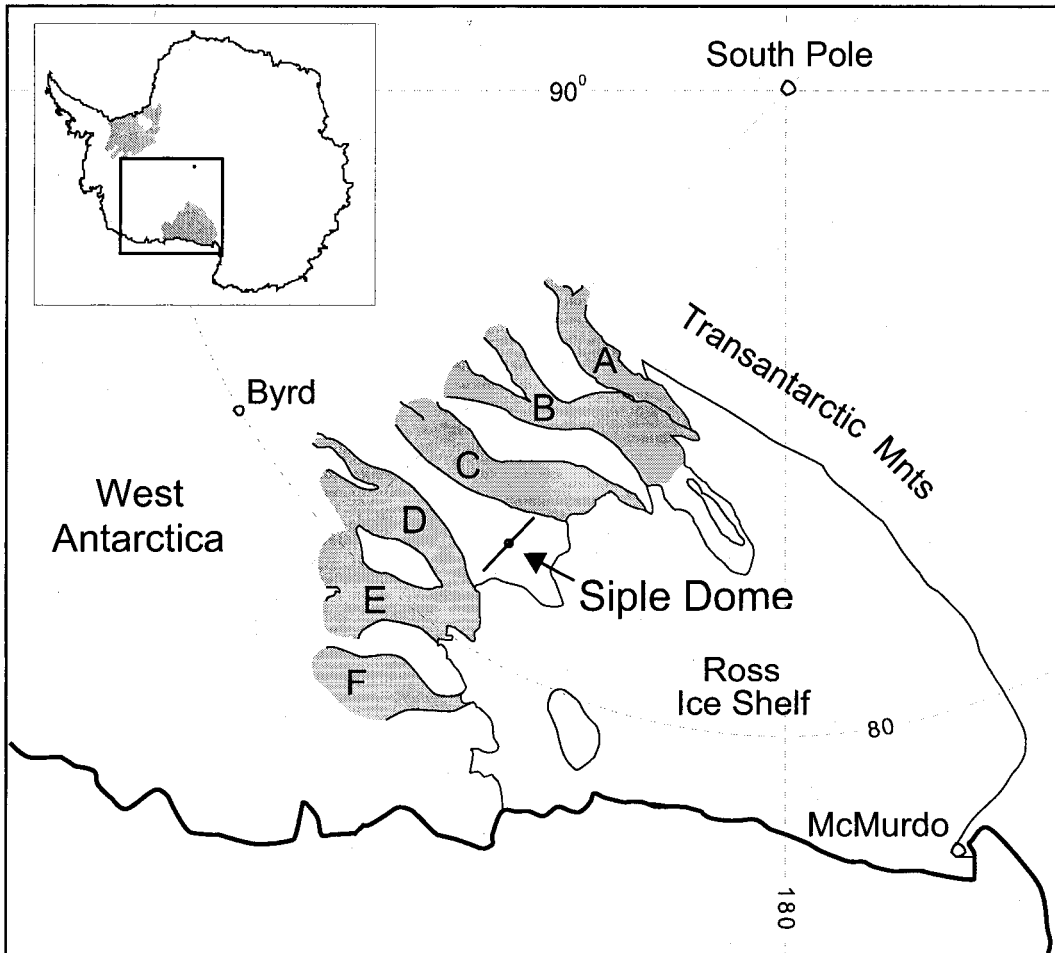


Figure 5.1: Map of Siple Coast and the Ross Sea Embayment, West Antarctica. Siple Dome is at 81.65° S and 148.81° W

accumulation rate or ice-sheet boundary conditions (e.g. temperature or flow of bounding ice streams) will alter the pattern of ice flow until the divide reaches a new steady-state geometry. These changes do not typically affect the ice sheet as a whole; it may be thickening in one region and in balance or thinning in another. Thus, it is the spatial pattern of mass balance that is important to understanding its present behavior. Neither the accumulation rate nor the surface vertical velocity is easy to measure, however. They are variable in both space and time, and the presence of the firn layer makes it difficult to measure absolute vertical motion of the surface or ice equivalent accumulation rate.

In this paper, we combine results from several independent studies of accumulation rate and ice flow to show that Siple Dome is in steady state: the central region (30 km on either side of the divide) is not significantly thinning or thickening. Then we discuss the implications of this result, in conjunction with conclusions from other studies, in terms of the local dynamics of the ice stream system and the larger-scale reconstruction of the evolution of the Ross Sea Embayment through the Holocene.

5.3 Mass Balance of a Polar Ice Sheet

5.3.1 Balance of processes

For a polar ice sheet to be in steady state, the total dynamic thinning due to flow must be balanced by ice-equivalent accumulation of snow on the surface. We calculate this dynamic thinning as the difference between the surface vertical velocity and the down-slope advection, which are both measurable quantities. The excess thinning (or thickening) rate is the imbalance between the mass lost to dynamic thinning and the mass gained through accumulation:

$$\underbrace{\dot{H}(x)}_{\substack{\text{excess} \\ \text{thinning rate} \\ (= 0 \text{ for} \\ \text{steady state})}} = \underbrace{\dot{b}(x)}_{\substack{\text{measured} \\ \text{accumulation} \\ \text{rate}}} + \underbrace{w_s(x)}_{\substack{\text{measured} \\ \text{surface} \\ \text{vertical} \\ \text{velocity}}} - \underbrace{u_s(x) \frac{dS(x)}{dx}}_{\substack{\text{calculated} \\ \text{slope} \\ \text{advection}}}, \quad (5.1)$$

equivalent to the total
dynamic thinning

where x is the distance from the divide along a flow line, \dot{b} is the ice-equivalent accumulation rate, w_s and u_s are the vertical and horizontal velocities at the surface, H is the ice thickness.¹ The terms in this equation are expressed as functions of distance along a flow line; in reality, they are also functions of time. Although we use this equation to determine the modern-day mass balance, we use the temporal nature of some of the measurement methods to infer constraints on the changes in mass balance with time.

We have measurements of the pattern of accumulation rate and surface vertical velocity using several different methods. The slope-advection term is small relative to the other two terms; we calculated it from the surface geometry and surface horizontal velocity, both measured using global position system (GPS).

5.3.2 Measurements of accumulation rate

The pattern of accumulation across Siple Dome was first described by *Zwally and Gloersen* [1977] through passive microwave satellite images. They observed a south-north gradient in accumulation across Siple Dome. This pattern has been attributed to orographic uplift of storms approaching from the north and depositing more moisture on the windward side of the dome [*Bromwich*, 1988, e.g.]. *Nereson et al.* [2000] confirmed that this pattern has existed through at least the last half of the Holocene through analysis of the structure of internal layers imaged by 3 MHz radio echo sounding (RES) (Figure 5.2), a system devel-

¹Appendix A is a table of the notation.

oped at the University of Washington [Gades, 1998]. *Nereson et al.* [2000] used a kinematic steady-state ice-flow model to predict internal-layer shapes as a function of a steady-state accumulation pattern across the dome. The pattern derived from the RES images gives relative accumulation rates, which are shown as the shaded regions in Figure 5.3. The darkest shading encompasses the accumulation rates that predict layers that best fit the observed internal layer pattern, with lighter shading showing less well-fitting patterns.

The accumulation pattern *Nereson et al.* [2000] deduced from the internal layer structure assumes that the asymmetry of the internal-layer structure seen in Figure 5.2 is not a result of asymmetrical thinning of bounding ice streams C and D. They discount this possibility because the presence of a distinct arch in the isochrones under the divide. This arch (often called a “Raymond bump”) is due to the nonlinearity of the ice-flow law [Raymond, 1983], and the development of a Raymond bump requires the divide to be in a stable position or slowly migrating for at least several thousand years. The asymmetric internal-layer pattern is visible as deep as 700 m; this suggests the accumulation pattern shown by the shaded regions in Figure 5.3 is an average over 5 to 10 ka.

We use two additional methods for determining the more recent accumulation across the dome. At 7 locations, *Hamilton* [2001] collected shallow cores for gross- β radioactivity measurements [Pourchet and Pinglot, 1979; Whillans and Bindshadler, 1988]. These provide a 42 year average accumulation rate at discrete points, and are plotted as relative accumulation in Figure 5.3 For all but the site 30 km south of the divide, there is not a significant difference between the modern day accumulation rates and the pattern determined by RES.

The final accumulation-rate data that we include in this study are 100MHz ground-penetrating radar (RAMAC System) collected in 1999-2000 season along a 13 km line across the divide. We converted the travel time to layer depth using a propagation velocity that is a function of the measured firn density (personal communication from G. Lamorey). The uncertainty in the absolute depth of the shallowest layer (at about 18 meters deep) is about 1 meter, with a relative uncertainty along a layer of 0.1 m. We used the measured firn density profile to determined the ice-equivalent depth to the shallowest continuous internal layer. Since the dynamic thinning due to ice flow is minimal in the top-most layer

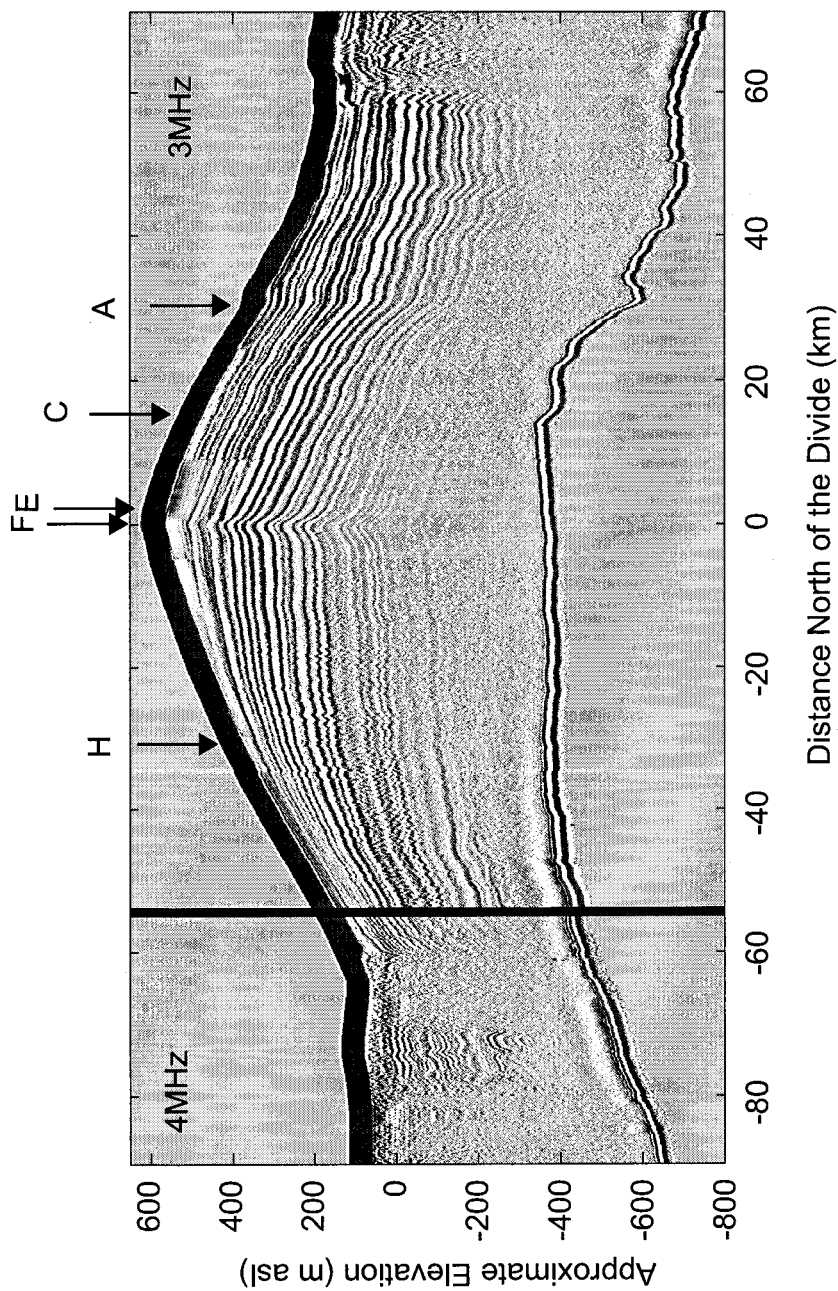


Figure 5.2: Composite radio echo sounding image of a cross section of Siple Dome using 2 (right of black line) and 4 MHz (left of black line) antennae. Data collected by Tony Gades, Bob Jacobel, and Charlie Raymond. We assume these layers follow the pattern of isochrones. Note the arch in the layers under the divide. This pattern is created by the special divide flow that is a result of the nonlinearity of the constitutive law for ice [Raymond, 1983]

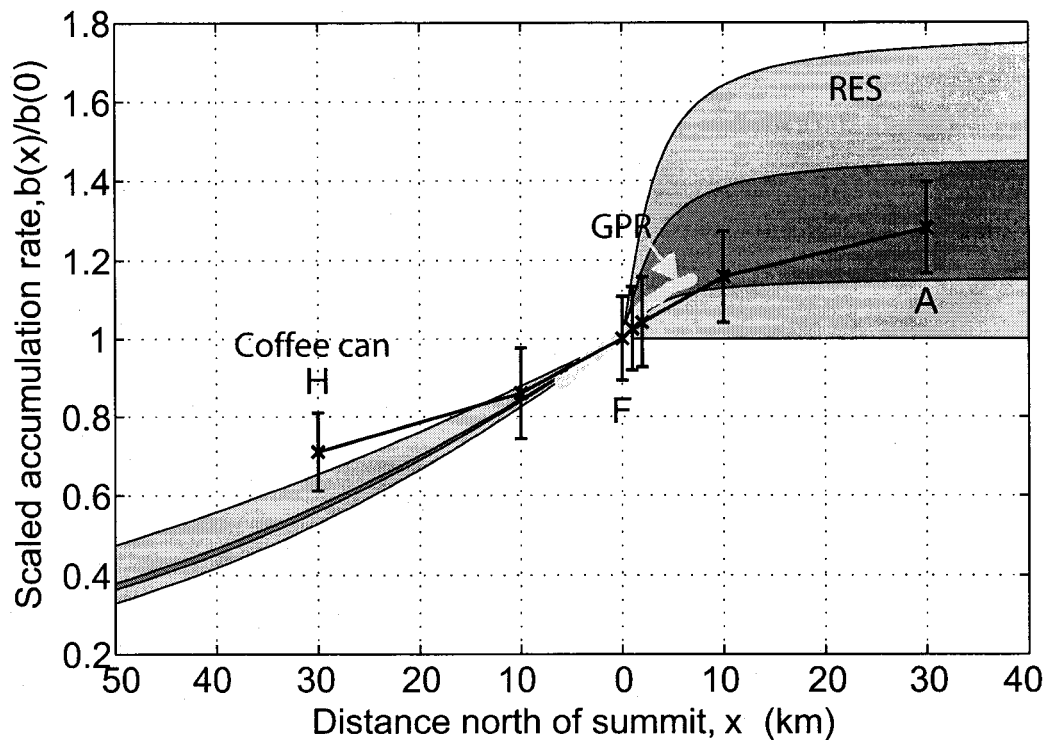


Figure 5.3: Accumulation rate pattern across Siple Dome. Shaded regions are the results from *Nereson et al.* [2000], dark represents accumulation rates that best model (within one standard deviation) the deep internal layer structure observed with radio echo sounding (Figure 5.2). This represents an average over 5-10 ka. Crosses with 1σ error bars, from *Hamilton* [2001], show average accumulation over 42 years based on shallow cores using Gross β identifying the radiation from the 1955 bomb layer. The light gray curve spanning approximately -6 km to 7 km is the ice-equivalent depth to a shallow layer observed by ground-penetrating radar, representing the average accumulation pattern over approximately 100 years. GPR data collected by Charlie Raymond and Nadine Nereson.

of the ice sheet, the relative accumulation rate is the ratio of the ice equivalent depth to the ice equivalent depth at the ice divide. This curve is shown as the heavy grey line in Figure 5.3. This accumulation pattern represents an average over approximately 100 years.

Since the absolute accumulation rate is only known for the shallow core 42 year average, we turn to the depth-age scale from layer-counting of the ice core [*Taylor et al.*, accepted] to estimate the absolute accumulation rate over a longer time-scale at the divide site to scale the RES and GPR patterns. At the divide, we can assume no horizontal advection of ice and that the vertical velocity pattern is time-independent. The age, A , of ice a certain depth, z , in a steady state divide is:

$$A(z) = \int_H^z \frac{1}{w(z')} dz', \quad (5.2)$$

where H is the ice thickness and $w(z')$ is defined by the shape function method of *Reeh* [1988]:

$$w(z') = -\dot{b}\psi(z'), \quad (5.3)$$

where \dot{b} is the accumulation rate, which we assume is constant with time for this estimation. For $\psi(z')$, we modified the analytical expression for vertical velocity shape function at a flow divide from *Reeh* [1988], (his Equation(32)), by including a steady-state temperature profile with vertical advection based on the *Robin* [1955] model as presented in *Paterson* [1994] using a surface temperature of -25°C , a bed temperature of -2°C , and a linear vertical velocity profile. This is a good approximation to the measured profile (personal communication from G.D. Clow, 2001). With the known depth-age scale, we solved for the average accumulation rate for several depths. These results are shown in Table 5.1. The These data are presented in table form in Table 5.2.

As Siple Dome is the site of the most recent U.S. Antarctic Program deep drilling project, many other data related to the modern accumulation rate exist. *Kreutz et al.* [1999] analyzed 2 m snow pits; *Kreutz et al.* [1997] counted annual layers in a 130 m core 5 km north of the divide; Richard Alley (personal communication, 2003) used layer counting from the deep ice core; and Bob Hawley inferred accumulation from strain rates in the

Table 5.1: Average accumulation rates based on measured depth-age scale from ice core

Ice Equiv. Height above Bed (m)	Age (a)	Accumulation Rate (cm a ⁻¹)
975.2	100	13.0
932.7	500	11.6
724.2	3000	12.1
616.5	5000	12.4

firn [*Hawley et al.*, in review]. For this study, we focus on the data relevant the pattern of accumulation across the divide both in recent times (but long enough to average out annual fluctuations) and over the longer term. The pattern of accumulation shown in Figure 5.3 are all similar, even though the the timescales of measurement are different (gross- β : 42 years; GPR: 100 years; RES: 1000 to 5000 years). The absolute magnitudes for the accumulation rate at the divide over different timescales shown in Table 5.1, reflects a slight increase in the accumulation rate in the recent past. Since our goal is to determine the modern-day thinning rate, we put more emphasis on the recent accumulation rates (also because fewer assumptions are involved in determining them). The RES and GPR accumulation patterns, however, provide important clues to Siple Dome’s past behavior.

5.3.3 Measurements of surface vertical velocity

The accumulation pattern shown in Figure 5.3 must be balanced by ice flow downward and outward from the divide to maintain a steady-state ice-sheet thickness (Equation 5.1). As a result the mass balance is not only sensitive to changes in the accumulation rate, but also to variations in the ice flow pattern induced by changes in the basal boundary conditions [*Pettit et al.*, 2002, and Chapter 3], surface temperature [*Hvidberg*, 1996], or the flow of bounding ice streams [*Nereson et al.*, 1998a; *Nereson*, 2000]. Measurement of the surface vertical velocity is key to determining if the ice sheet is in balance with the present-day accumulation rate. We combine the results from three independent methods for measuring vertical velocity, to ensure that the results are reproducible.

Table 5.2: Results of the three independent measurements of ice sheet thinning. All values are shown in ice-equivalent rates. Values in parentheses are uncertainties associated with the measurements (where available). The first thinning rates were calculated using the accumulation rates at each site from the gross- β 42 a average measurements, then recalculated for the 500 a average. The combined results from the coffee-can method and the optical-fiber sensors are shown in Figure 5.10.

Site Label	H 30 km South Flank	F 0 km Divide	E 1 km North Transitional	C 7 km North Flank	A 30 km North Flank
Distance from Divide					
Type of Flow					
Accumulation rates b (cm a^{-1})					
gross- β (42 yr)	9.4(1.3)	13.2(1.4)	13.5(1.4)	14.7(2.1)	16.9(1.5)
RES (1-5 kyr)	7.2	12.1	12.9	14.9	15.4
RES using 500 a average at summit	6.7	11.6	12.4	14.4	14.9
GPR (100 yr)	NA	13.0	13.5	15.0	NA
Slope Correction (cm a^{-1})	-0.7	-0.001	-0.03	-0.83	-8.0
Coffee-can method					
ρ_f ($\text{Mg m}^2 \text{a}^{-1}$)	0.609(0.013)	0.613(0.013)	0.625(0.013)	0.624(0.013)	0.616(0.013)
b_m/ρ_f (cm a^{-1})	15.4	21.5	21.6	23.6	27.4
w_f (cm a^{-1})	-16.8(1.2)	-18.8(1.1)	-20.4(1.2)	-24.8(1.3)	-37.4(1.2)
Thinning rate \dot{H} (cm a^{-1})	-2.1(2.6)	+1.0(2.5)	-0.6(2.5)	-2.6(3.6)	-4.7(2.8)
using 500 a average b	-6.5(2.4)	-1.6(2.3)	-2.4(2.3)	-3.0(3.3)	-7.9(2.6)
mean for site using 42 a average b	-2.3(2.6)	-1.7(2.5)	-1.5(2.5)	-2.3(3.6)	-5.1(2.8)
Optical-fiber method					
w_s (cm a^{-1})	NA	-11.9(0.5)	NA	-17.8(1)	NA
Thinning rate \dot{H} (cm a^{-1})	NA	+1.3(1.6)	NA	-2.3(2.5)	NA
using 500 a average b	NA	-0.3(1.6)	NA	-2.6(2.5)	NA
Horizontal Flux Divergence					
w_s (cm a^{-1})	NA	-14(5)	NA	-21.4(5.7)	NA
Thinning rate \dot{H} (cm a^{-1})	NA	-0.8(5.2)	NA	-5.9(6.1)	NA
using 500 a average b	NA	-2.4(5.2)	NA	-6.2(6.1)	NA

Precision GPS “Coffee-Can” method

Hamilton et al. [1998] and *Hamilton and Whillans* [2000] developed a method for directly measuring the vertical velocity at the surface of an ice sheet using a suite of three to five markers at 5 to 20 m below the surface. They have used this method in West Antarctica (Byrd Station, near Whillans Ice Stream, and as part of the US ITASE expedition) and western Greenland. *Hamilton* [2001] originally published the application of this method to Siple Dome; we use these results.

Each marker is a piece of steel stock frozen into the firn at the bottom of a shallow borehole. A non-stretchable wire attached to the marker comes up the borehole and is encased in a 2.5 m steel pipe that extends above the surface (Figure 5.4). A marker’s movement is measured using precision GPS on the steel pipe combined with accurate measurement of the non-stretchable wire relative to the top of the steel pipe. A suite of three to five markers at varying depths 5 to 20 m below the surface is used at each site to test for repeatability. One pole at each site is defined as the long-term tracking pole, and 12 to 24 hour static GPS measurements define the absolute motion of this pole. The other markers are measured using repeated local surveys using GPS and optical leveling to connect them to the long-term tracking pole.

Because this measurement of vertical motion takes place within the firn column, we compare it to the “firn-equivalent” accumulation rate, or \dot{b}_m/ρ_f , where \dot{b}_m is the accumulation rate measured in mass units and ρ_f is the density of the firn at the depth of the marker. The ice-equivalent rate of thickness change is then:

$$\dot{H} = \frac{\dot{b}_m}{\rho_f} + w_f - u_s \left(\frac{dS}{dx} \right), \quad (5.4)$$

where w_f is the velocity of the marker in the firn, u_s is the horizontal velocity, and S is the surface elevation. The derivation of firn-equivalent accumulation relies on the assumption of Sorge’s Law: the density profile remains constant with time. The density for this calculation is measured from the same shallow core that also provided the samples for the gross- β accumulation measurements shown in Figure 5.3. The densities, firn-equivalent accumulation rates, and the measured marker velocities are shown in Table 5.2.

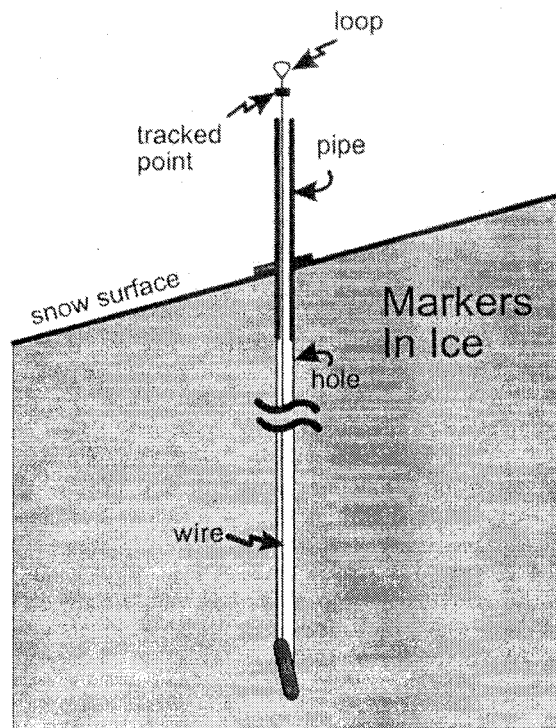


Figure 5.4: Diagram of experimental setup for the Coffee-Can method of determining surface vertical velocity. At each site a suite of 3 to 5 markers are frozen in at varying depths from 5 to 20 meters below the surface. From *Hamilton and Whillans* [2000]

*Fiber-optic vertical-strain network*²

Because of the uncertainties associated with firn densification and direct surface velocity measurements, this method aims to measure the vertical-velocity profile throughout the depth of the ice using embedded instruments and to determine the vertical velocity at the surface by extrapolating this curve from the bed to the surface using an ice-flow model. *Zumberge* [1997] originally developed this method of measuring motion for determining seafloor spreading. The application to ice at Siple Dome is described in *Zumberge et al.* [2002] and we initially installed the instruments to study the rheology of ice near ice divides [*Pettit and Waddington*, in press, Chapter 2, and Chapter 6].

Figure 5.5 shows the instrument design for these optical-fiber strain sensors. A complete description of the instrument design is in *Zumberge et al.* [2002]; here, we summarize the important aspects. Similar to the coffee-can method, these sensors work by anchoring the end of an optical-fiber cable (“the marker”) to the ice by lowering it under tension (prestrain is 0.1% to 0.2%) into a water filled borehole and which subsequently freezes. The fiber is encased in an aluminum sheath such that only the anchored end of the fiber is frozen to the ice, to protect the fiber from breakage and to ensure that it is strained uniformly over its length. The optical-fiber cable consists of two fibers spliced at the anchored end: a transmit fiber and a return fiber. The fibers were installed in pairs, a short fiber 80 m in length and a long fiber 235 to 985 m in length (ice depth is 1000 m), such that each pair provides the vertical compression of the ice over the depth interval between the short and long fiber. We installed an array of five fiber pairs at each of two sites on Siple Dome: the divide site (site F in the coffee-can experiment) and a flank site, 7 km north of the divide (site C in the coffee-can experiment)

The optical length of each fiber was measured using a modified electronic distance meter (EDM) and converted to physical length by the fiber’s index of refraction (which is a function of the amount of strain). The system also has to be corrected for temperature effects, both within the fiber and in the EDM. Repeat measurements were made within each field season and over the four years the instruments were active. The uncertainties

²Part of this section was published in *Zumberge et al.* [2002]

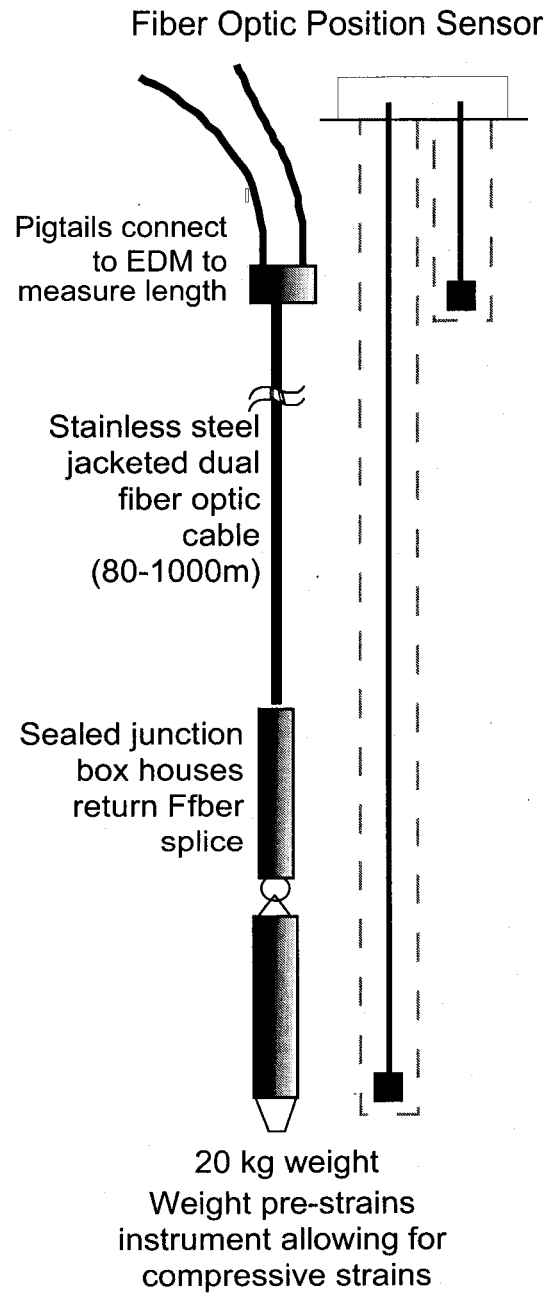


Figure 5.5: Diagram of optical-fiber instrument for measuring vertical strain rates. See text or *Zumberge et al.* [2002] for further details.

for these measurements are a combination of the uncertainty for a single measurement of displacement (thermally induced error in the EDM, uncompensated temperature effects, and differencing two adjacent measurements) and the rms residuals from fitting a straight line to the measurements taken over time.

The differential shortening of the optical-fiber cables provides average strain over the interval between a shallow fiber anchor and a deep fiber anchors (intervals of 174 m to 905 m). To extract a surface vertical velocity from these data, we fit our measurements of vertical strain rate to a flow model. We approximate Siple Dome as a linear ridge and model it in cross-section as two-dimensional plane flow. Using the shape function method of *Reeh* [1988], the vertical velocity is expressed by

$$w(x, z') = -[\dot{b}(x) - \dot{H}(x)]\psi(z') + u_s(x)\phi(z') \left(\frac{dB}{dx} + z' \frac{dH}{dx} \right), \quad (5.5)$$

where x is horizontal position, $\dot{b}(x)$ is the accumulation rate, $B(x)$ is the bed elevation, $H(x)$ is the thickness in ice-equivalent units (as if the firn had been compacted to an ice layer, reducing Siple Dome's thickness by about 16 m), $\dot{H}(x)$ is the excess thinning rate, $u_s(x)$ is the horizontal velocity at the surface, z' is the height above the bed scaled to the local ice thickness $H(x)$, and $\phi(z')$ and $\psi(z')$ are the shapes of the horizontal and vertical velocity profiles, respectively. For $\phi(z')$ and $\psi(z')$, a Dansgaard-Johnsen velocity model [*Dansgaard and Johnsen*, 1969] is applicable at the flank site. The horizontal velocity shape $\phi(z')$ is constant in the upper part of the ice sheet (above height h above the bed) and decreases linearly to zero between height h and the bed. Using the value of $h = 227$ m recommended by *Nereson et al.* [1996], with their measured values of $B(x)$, $H(x)$, and $u_s(x)$, we found the value of the vertical velocity at the surface, $w_s = \dot{b}(x) - \dot{H}(x)$ necessary to best fit the slope of the vertical velocity (Equation (5.5)) to our vertical strain-rate data in a least-squares sense.

At the divide, however, the Dansgaard-Johnsen model does not satisfy the boundary condition that $du/dz = 0$ at the bed [*Raymond*, 1983; *Reeh*, 1988]. The horizontal velocity profile, $\phi(z')$, at the divide must have an inflection point such that it is concave downward near the bed. This curvature results in a vertical velocity profile, $\psi(z')$, that

is steeper in the lower part of the ice sheet than the Dansgaard-Johnsen model permits. We modified the analytical expression for vertical velocity shape function at a flow divide from *Reeh* [1988], (his Equation(32)), by including a steady-state temperature profile with vertical advection based on the *Robin* [1955] model as presented in *Paterson* [1994] using a surface temperature of -25°C , a bed temperature of -2°C , and a linear vertical velocity profile. This is a good approximation to the measured profile (personal communication from G.D. Clow, 2001). We then used this shape function to find the best-fitting value of w_s . Because $u_s(x) = 0$ at the divide, we did not need to derive the corresponding temperature-dependent forms of $\phi(z')$ in Equation (5.5).

At the divide, the best-fitting model predicts $w_s = 11.9 \pm 0.5 \text{ cm a}^{-1}$. At the flank, $w_s = 17.8 \pm 1 \text{ cm a}^{-1}$ (refer to Table 5.2). These uncertainties are calculated from the measurement uncertainties propagated through the model and the fit of the model to the data; they do not include uncertainties resulting from model assumptions. The solid curves in Figure 5.6 and 5.7 are these best-fitting models for the divide and flank, respectively (Equation (5.5) using these values of w_s).

These models rely solely on the measured velocity difference of pairs of anchors (each consisting of an 80 m anchor and a deep anchor), not absolute motion of the anchors. To plot these data for comparison with the model results, we needed to assign an absolute velocity to each pair of anchors. We did this by minimizing the mismatch between the absolute velocity of each pair and the model curves in Figures 5.6 and 5.7.

The coffee-can method for measuring vertical velocity at the surface has a significant advantage over the optical-fiber method because of the simplicity of the installation and data collection. Because the fiber-optic method involves measurements from the entire depth of the ice sheet, it provides a better picture of the dynamic behavior of the ice sheet on a large scale (of one ice-thickness or more).

GPS horizontal strain network

This method for calculating the downward vertical velocity of the surface relies on the conservation of ice mass at the surface. *Nereson* [1998] originally applied this method to the divide region of Siple Dome (sites F and E), here we complete the analysis by applying

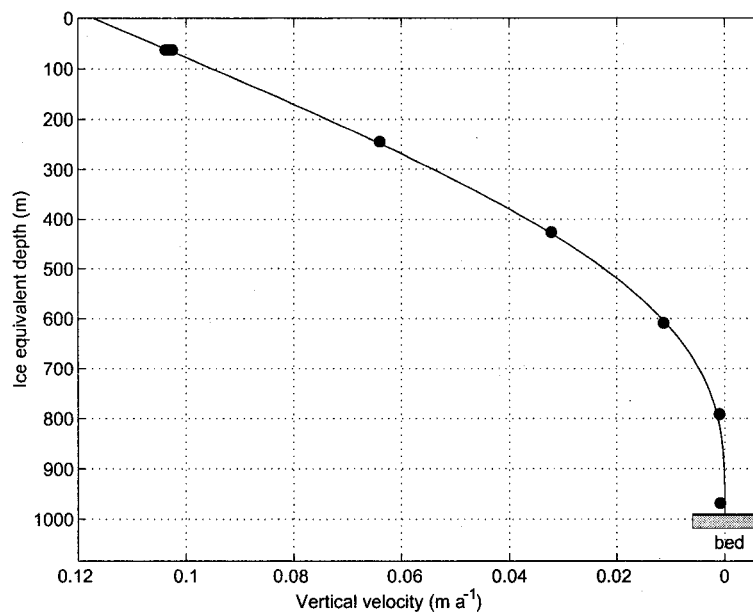


Figure 5.6: Vertical velocity profile at the divide site. Dots represent velocities measured by the optical-fiber strain sensors (measurement errors are less than the width of the dot). Solid line is best-fitting steady-state model (Equation (5.5)) using the Reeh velocity profile.

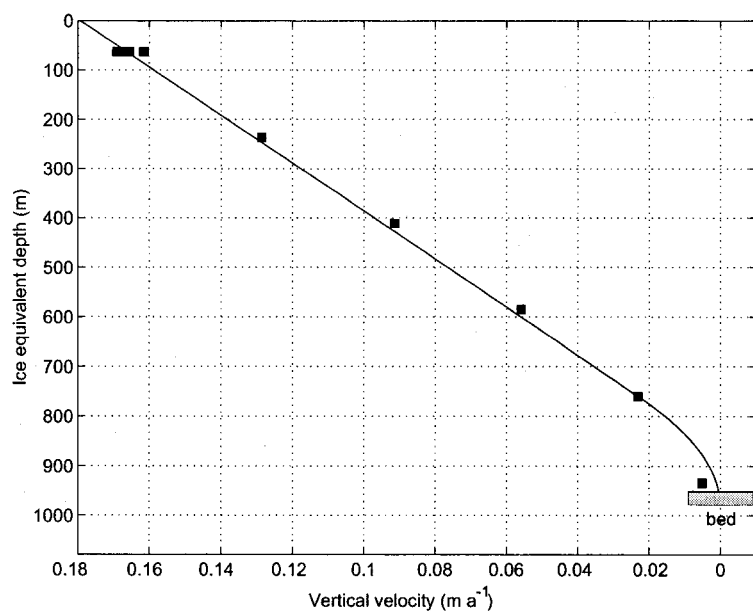


Figure 5.7: Vertical velocity profile at the flank site. Squares represent velocities measured by the optical-fiber strain sensors (measurement errors are less than the width of the square). Solid line is best-fitting steady-state model (Equation (5.5)) using the Dansgaard-Johnsen velocity profile.

it to the flank (site C) as well.

The continuity equation requires that the divergence of the horizontal ice flux out of a volume of ice be balanced by vertical thinning of the ice volume and accumulation added to the volume. For a column of ice:

$$\dot{H} = \dot{b} - \left(\frac{\partial q_x}{\partial x} + \frac{\partial q_y}{\partial y} \right), \quad (5.6)$$

where \dot{H} is the time rate of change of ice thickness, \dot{b} is the accumulation rate, q_x and q_y are components of the horizontal ice flux. The divergence of the horizontal ice flux can be determined from measurements of surface horizontal velocity gradients:

$$\left(\frac{\partial q_x}{\partial x} + \frac{\partial q_y}{\partial y} \right) = \gamma H \left(\frac{\partial u_s}{\partial x} + \frac{\partial v_s}{\partial y} \right), \quad (5.7)$$

where γ is the ratio of the depth-averaged horizontal velocity to the surface horizontal velocity (\bar{u}/u_s). It can range from 0.8 for isothermal, laminar flow with a nonlinear ($n=3$) flow law to 0.85, empirically determined from finite-element modelling of Siple Dome. We use 0.8, but include this range of values in our uncertainty analysis.

In December 1994, a survey grid was set up around the summit site, in anticipation of the deep drilling program; the details of the data collection are described in *Nereson* [1998]. *Nereson* [1998] resurveyed the grid in December 1996 and determined the pole velocities (Figure 5.8). This extensive survey produced relative pole positions with residuals less than 0.01 m. That same year, additional poles were installed around the flank site. We resurveyed these poles in January of 1999. Because the grid contains fewer poles and did not contain redundant measurements, the uncertainties for these pole positions are up to 0.2 m in the horizontal. The velocity vectors for this grid are shown in Figure 5.9.

We used these velocity measurements in Equation (5.7) to determine the horizontal flux divergence. Then we calculated w_s ($= \dot{H} - \dot{b}$) from continuity, Equation (5.6). The results are shown in the bottom row of Table 5.2. The uncertainty for the divide horizontal divergence is 0.05 m a^{-1} , found from the range of results obtained when various pole configurations are used in the calculation, combined with the uncertainty in the value of

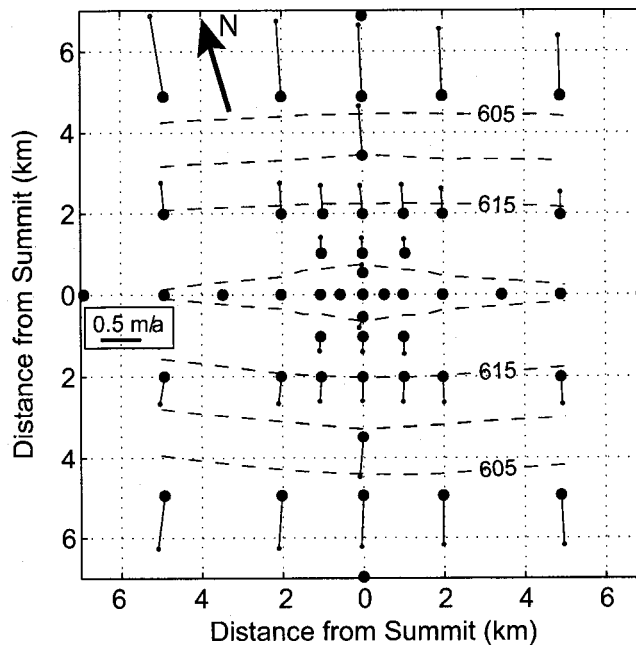


Figure 5.8: Map view of GPS survey network at the summit site (site F) including velocity vectors and elevation contours. Zero on the x-axis is the ridge; zero on the y-axis is the peak along the ridge. The large arrow points to true north. The data span the austral summer 1994/95 to austral summer 1996/97. Adapted from *Nereson* [1998].

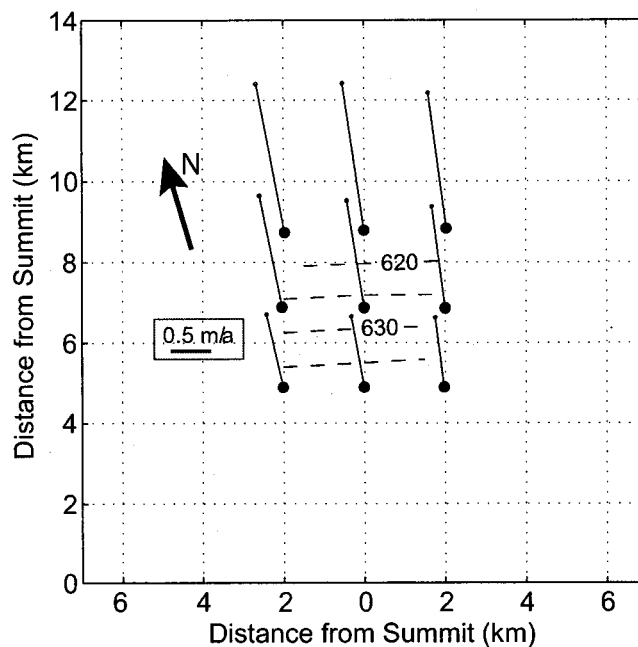


Figure 5.9: Map view of GPS survey network at the flank site (site C), showing velocity vectors and elevation contours. Zero on the x-axis is the ridge; zero on the y-axis is the peak along the ridge. The large arrow points to true north. The two sites are shown at the same scale; note that the survey grid is less extensive at this site. The data for these velocity calculations span the austral summer 1996/97 to austral summer 1998/99.

γ . The uncertainty at the flank is higher because of the higher uncertainties in the GPS residuals.

5.3.4 Slope correction term

To complete this mass-balance analysis, we calculate the slope correction term for each site. The horizontal velocity at each site was measured during the same GPS occupations as the coffee-can vertical motion measurements and confirmed at sites F and C by the GPS survey network. The region extending 1 to 2 km from each site was surveyed for surface topography using kinematic GPS. A spatial scale of several ice thicknesses is used to determine the slope important for large-scale ice flow; this slope is assumed to be time invariant. The correction term for each of the five sites is shown in Table 5.2.

5.3.5 Net ice-sheet thinning rate

Table 5.2 shows the results for each of the three methods. We calculated the thinning rates using both the 42 a average gross- β measurements and the 500 a average calculation from Table 5.1. Since the coffee-can method and the optical-fiber method have the lowest uncertainties, we have plotted the average of these results (using the 42 a average accumulation rate) as arrows in Figure 5.10, a diagram showing the geometry of Siple Dome. The errors are shown as thin bars behind the arrows. For the three sites nearest the summit, our calculations show neither thinning nor thickening within our uncertainties. Only one of the five sites shows significant thinning: site A, on the side of Siple Dome nearest Bind-schadler Ice Stream. We calculate thinning at both sites A and H when vertical velocities are compared to the 500 a average accumulation rate.

5.4 Implications for Siple Dome

The conclusion that Siple Dome is in balance with its modern accumulation rate provides an important constraint on the region. We present the implications of this result on three spatial scales: the dome itself, the dome and its neighboring ice streams, and the Ross Sea Embayment.

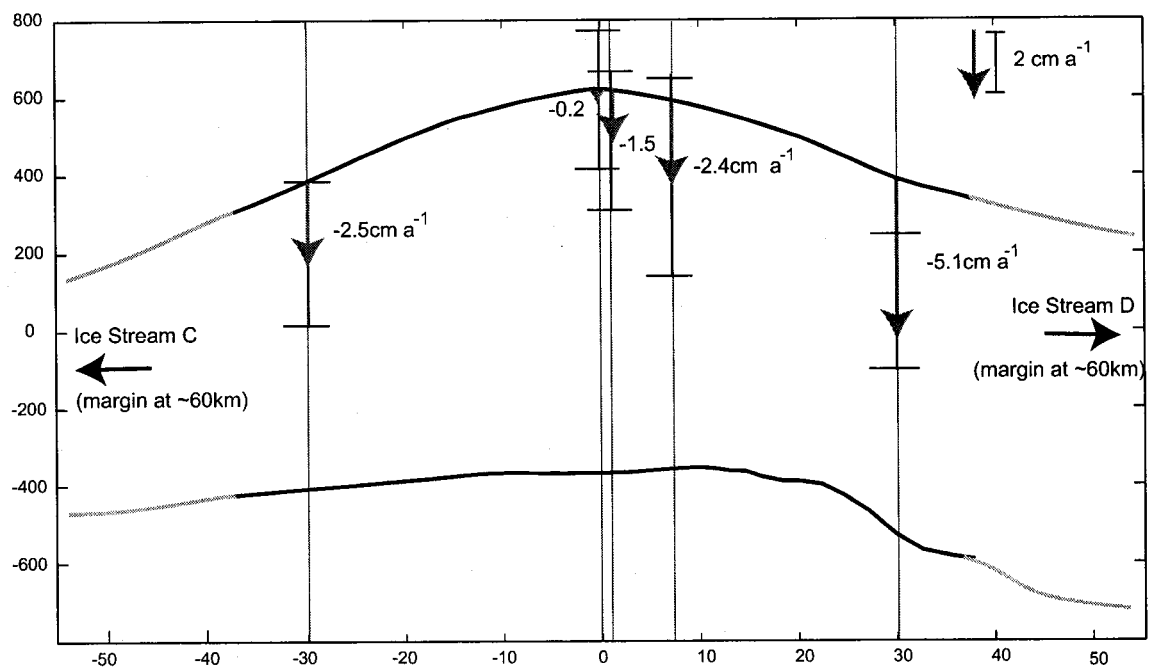


Figure 5.10: Calculated thinning rates plotted on a cross section of Siple Dome. The arrow and error bar scale is shown in the upper right of the figure. The surface profile is from kinematic GPS; the bed profile is from RES data (Figure 5.2; the grey lines indicate approximate extensions of the surface and bed profiles). The region within 10 km of the divide is in steady state within our measurement uncertainty; at larger distances, only Site A, on the north slope shows significant thinning.

5.4.1 History of Siple Dome

A summary of key conclusions from this study and from others (as cited) for the Dome as a whole:

1. Siple Dome is 1000 m thick and has an average accumulation rate of approximately 0.12 to 0.13 m a⁻¹. This implies that it has a fundamental response time to perturbations in its boundary conditions of $H/\dot{b} = 8,000$ years. This is the timescale over which perturbations are felt throughout the depth of the ice sheet; therefore, it is the response time for the shape of the internal layers.
2. *Nereson et al.* [1998a] showed that it has a *volume* response time of about 700 years. This timescale reflects the adjustment of the surface geometry to a step change in boundary conditions.
3. The RES data in Figure 5.2 show asymmetry in the internal layer structure to the deepest observable layers. This asymmetry is a result of an orographic precipitation pattern [*Nereson et al.*, 2000].
4. At the divide there is a distinct arch in the isochrones (see Figure 5.2). [*Nereson et al.*, 1998b] showed that this feature is most likely a Raymond bump, a result of the special divide flow that results from the nonlinearity of the ice-flow law. To produce a Raymond bump, the divide must be frozen to its bed [*Pettit et al.*, 2002] and cannot have moved more than a few ice-thicknesses from its present position [*Nereson et al.*, 1998b], otherwise the bump would have been “smeared out” by a migrating divide [*Nereson and Waddington*, 2002].
5. The three sites nearest the summit (within 7 ice-thicknesses) in this study show no significant thinning (the resolution of these methods is on the order of 2.5 cm a⁻¹).
6. The north flank site (at 30 km from the divide) shows significant thinning. The south flank site (also 30 km from the divide) is also thinning according to our estimate using the longer-term accumulation rate measured from the RES study.

These six observations imply that Siple Dome has been a ridge-like elevated feature (driving orographic precipitation patterns), exhibiting stable or slowly migrating divide-flow, surrounded by lower-lying ice streams, for much of the Holocene (since its fundamental response time is 8,000 years). It is probable, although we cannot say for sure, that it was a dome surrounded by ice streams during the glacial maximum (about 20 ka BP).

Since the volume response time is much shorter than the fundamental timescale, our conclusion that it has no net thinning at present only constrains the behavior for the past few thousand years. If Siple Dome was more than 40 m higher 2000 a BP, our techniques would detect thinning (assuming a constant thinning rate over the last 2000 years). Therefore, we can only say that any significant thinning from the deglaciation must have occurred earlier in the Holocene, and Siple Dome reached its present thickness by 1000-2000 a BP.

That at least one, and perhaps both sites 30 km from the divide (about half-way to the ice-stream margin), may be thinning, yet the summit is in steady state, suggests that the elevation difference between the summit and the ice streams was smaller in the recent past, but still enough to drive orographic precipitation. This may imply that the flanks have not reached steady state after deglaciation, while the divide has; although since the surface adjustment timescale is short relative to the length of the Holocene, it is more likely that the flanks are responding to more recent forcings, such as thinning of the ice streams.

5.4.2 Siple Coast dynamics

The system of ice streams and inter-ice-stream ridges along the Siple Coast of West Antarctica has proven to be very dynamic. Adjacent to Siple Dome (Figure 5.11), the Siple Ice Stream and the Duckfoot both seem to be relic ice streams that ceased fast flow within the last 500 years [Jacobel *et al.*, 2000; Nereson, 2000, and unpublished work by Ben E. Smith]. Also, Kamb Ice Stream stagnated about 130 years ago [Retzlaff and Bentley, 1993]. Whillans and Bindshadler [1988] observed a modern thinning rate of Whillans Ice Stream of 6 cm a^{-1} . Bindshadler *et al.* [2002] calculate a thinning of Bindshadler Ice Stream in its middle and lower reaches of 1 to 30 cm a^{-1} and a thickening of Ice Stream E. Also, Conway *et al.* [2002] found evidence suggesting that Ice Stream C-0 has switched

flow directions less than 250 years BP. All of these observations imply that the Siple Coast is an active region of constantly changing flow.

The most stable parts of this region are the inter-ice-stream ridges, yet they are affected (although more subtly) by changes in the ice streams on their boundaries. Changes in the bounding ice streams leave an imprint in the glaciological record recorded in the slow moving ridge ice. *Nereson and Raymond* [2001] compared Ridges DE and BC with Siple Dome and found that Siple Dome is the most steady of the three ridges. The most significant clue to its stability is the presence of a Raymond Bump in the internal layer structure (see the radar image in Figure 5.2). The relative stability of Siple Dome is intriguing since Siple Dome is bounded by Kamb Ice Stream which has shown the most dramatic change in recent history. The clues we have to the history of Siple Dome and its bounding ice streams are:

1. Siple Dome has been an elevated feature for much of the Holocene and has not undergone large volume changes in the last few thousand years.
2. *Nereson et al.* [1998b] found that Siple Dome has been migrating toward Bindschadler Ice Stream at a rate of up to 0.5 m a^{-1} for several thousand years, at least until 1000 years ago from analysis of the Raymond bump in the Siple Dome radar stratigraphy. (The bump is too subtle in the near surface layers to extend this analysis to the most recent 1000 years.
3. Kamb Ice Stream stopped approximately 130 years ago [*Retzlaff and Bentley*, 1993] and is currently thickening in its upper reaches [*Price et al.*, 2001].
4. Bindschadler Ice Stream is thinning in its middle and lower reaches at a rate of up to 30 cm a^{-1} [*Bindschadler et al.*, 2002].
5. The grounding line for the Siple Coast has been retreating [*Bindschadler and Vornberger*, 1998]

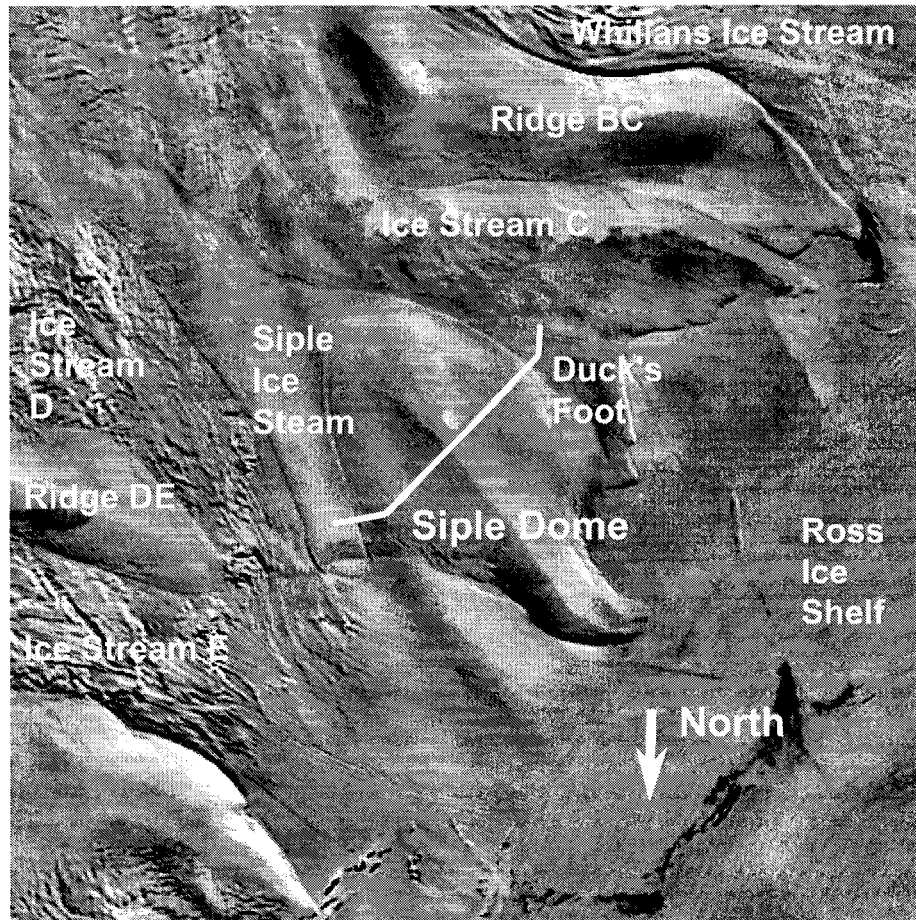


Figure 5.11: Satellite image of Siple Dome and surrounding ice streams. White line indicates the location of the RES cross-section shown in Figure 5.2.

These observations present some puzzles. The most likely driving force for migration of the Siple Dome divide is changes in the relative elevations of the ice streams. Yet, if the divide is presently migrating toward Bindschadler Ice Stream, we would expect a thickening of the ice at sites C and A in this study and a thickening of the boundary with Bindschadler Ice Stream.

The divide has been migrating to the north for a minimum of about 2000 years (the time it would take to move the divide the 700 meters (the observed displacement of the peak of the deepest visible internal layer to the modern divide position) at the maximum rate determined by *Nereson et al.* [1998b]). A thinning of Kamb Ice Stream relative to Bindschadler Ice Stream would be required to drive the migration northward. This may be possible if Kamb Ice Stream underwent a steady thinning over thousands of years until it reached a threshold thickness that caused it to stop flowing. At present, Kamb Ice Stream is thickening in its upper reaches [*Price et al.*, 2001], and, thus, should drive the divide migration in the opposite direction. *Nereson et al.* [1998a] predicted that a perturbation in the ice streams take 200 to 350 years to affect the divide position. Therefore it is most likely that the divide has not yet “felt” the thickening due to the shut down of Kamb Ice Stream. Site H, however, is much closer to the boundary with Kamb Ice Stream and should feel the effects of the shutdown as a thickening (or reduced thinning rate) in a much shorter amount of time. We do not observe a thickening at this site, either because the thickening of Kamb Ice Stream is occurring only much farther upstream; because it is a small effect, below the resolution of our technique; or because it is balanced by a longer-term thinning process (perhaps associated with the northward divide migration).

On the other hand, the northward migration may be caused by thickening of Bindschadler Ice Stream. One possibility is the stoppage of the Siple Ice Stream about 450 a BP [*Conway et al.*, 2002, and unpublished work by Ben E. Smith], a tributary of Bindschadler Ice Stream. But evidence suggests this is too recent to cause the migration we observe [*Nereson*, 2000].

Because the migration happened over at least 2000 years [*Nereson et al.*, 1998b] it is not likely that abrupt changes in the ice streams, such as the stoppage of Kamb Ice Stream or the Siple Ice Stream, have caused the northward migration. Indeed the presence of a

strong arch in the isochrones [*Nereson and Raymond, 2001*, cf. Ridge BC or DE], coupled with the steady-state behavior that we measure, suggests that Ice Streams C and D have not undergone dramatic changes in the past several thousand years. The only ice-stream fluctuations consistent with the evidence are long-term gradual changes or very short-term changes. Since the propagation time for changes in the margins to reach the divide is less than 300 years [*Nereson et al., 1998a*], the effects of rapid fluctuations in ice stream behavior (on the scale of 100 to 200) years would be averaged out before perturbing the divide significantly.

The other possible driver for northward migration is changes in the accumulation rate. In 5.3.2, we show that there is a general increase in accumulation from the south side of the dome to the north side. [*Nereson et al., 1998a*] showed that a change in this accumulation-rate gradient can cause divide migration. In particular, a strengthening (increase) in the gradient can drive the divide northward. *Nereson et al. [2000]* used the layers in Figure 5.3a to deduce the change in accumulation rate over the Holocene from the layer dips. They found that the accumulation rate gradient has possibly decreased in time during the last 10 ka, a change that would drive the divide southward instead of northward (if not accompanied by a compensating change in the flow). Therefore this is not a likely candidate for the observed behavior.

5.4.3 *Deglaciation of the Ross Sea Embayment*

On a larger scale, the present steady state behavior of Siple Dome provides a constraint on the deglaciation of the Ross Sea Embayment. The results presented here along with results from other studies constrain aspects of the deglaciation process. These important results are:

1. This study showed that Siple Dome has been stable for the last several thousand years and has been an elevated feature with respect to the surrounding ice streams for over ten thousand years. The ice streams bounding Siple Dome have been a persistent and relatively stable feature of the Ross Ice Drainage since the LGM.

2. *Denton and Hughes* [2000] and *Conway et al.* [1999] present results from several studies of radiocarbon dating of ice-age glacial drifts along the Transantarctic mountains. This evidence suggests the ice did not retreat past McMurdo Sound until after 7600 yr BP.
3. Roosevelt Island, a grounded ridge of ice within the floating Ross Ice Shelf, also has a Raymond bump in its internal structure, as imaged by radar. *Conway et al.* [1999] analyzed the shape of this bump to conclude that before 3200 a BP, the dome did not exhibit the special nonlinear divide-flow pattern seen now. In the early Holocene, Roosevelt Island possibly was overrun by faster moving ice, then as the ice around it thinned and the grounding line retreated, it became an elevated feature with a slippery bed, and ultimately 3200 a BP, it froze to its bed and began exhibiting the divide-flow pattern. They also show that the dome is currently still thinning by $0.09 \pm 0.03 \text{ m a}^{-1}$.
4. Among the mountains to the east of the Ross Ice Shelf are the Ford Ranges. The ice in this region feeds into the Sulzberger Ice Shelf. *Stone et al.* [2003] have analyzed samples of glacial deposits from various elevations using cosmogenic isotopes to determine exposure ages. These data show that the ice has thinned by more than 700 meters during the Holocene and this thinning may still be occurring.

Each of these points is highlighted in Figure 5.12, along with dashed lines indicating the most likely evolution of the grounding line during deglaciation [adapted from *Conway et al.*, 1999].

The most recent reconstruction of the Ross Ice Drainage during the LGM is from *Denton and Hughes* [2000], who incorporate past ice elevations (from total gas content and stable isotope studies from Byrd Station and Taylor Dome ice cores and ice-flow modelling) with the elevations of glacial deposits along the Transantarctics (Point 2 above) and the suspected elevation history of Roosevelt Island [Point 3, *Conway et al.*, 1999]. This reconstruction is consistent with the minimum LGM elevations required by the evidence from *Stone et al.* [2003]. In the Siple Dome region, however, the *Denton and Hughes* [2000]

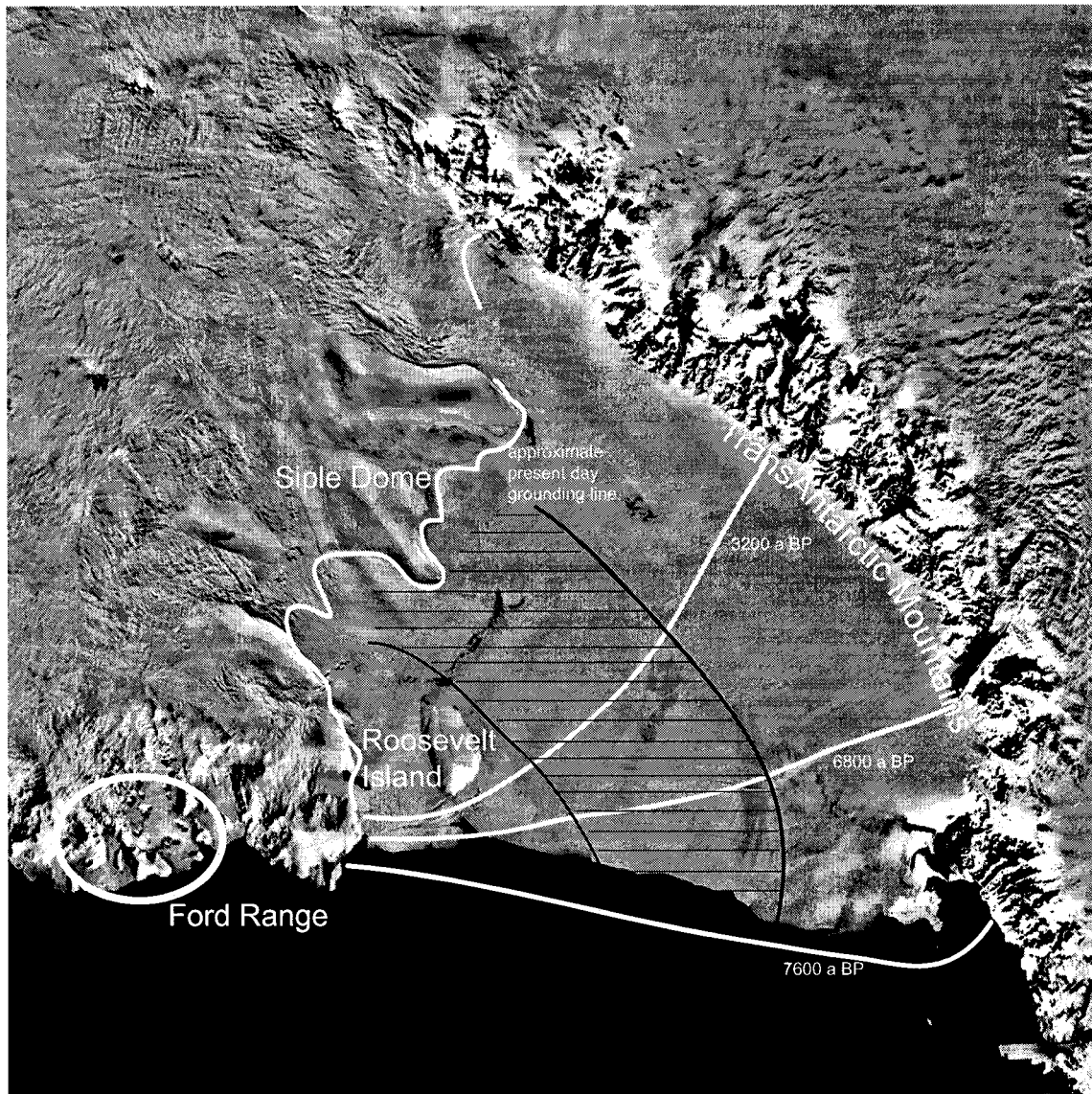


Figure 5.12: Satellite image of the Ross Ice Shelf. Key evidence for the reconstruction of the Ross Ice Drainage at LGM and deglaciation during the Holocene are highlighted: Siple Dome (this study), the Ford Ranges [Stone *et al.*, 2003], Roosevelt Island [Conway *et al.*, 1999], and sites along the Transantarctic Mountains [Denton and Hughes, 2000; Conway *et al.*, 1999]. The white lines show possible grounding line positions as the ice sheet retreated (adapted from Conway *et al.* [1999]. This retreat has been coined the “swinging gate theory” [Denton and Hughes, 2000; Conway *et al.*, 1999]. The hatched black region is downstream from Siple Dome and Ice Streams C and D and may have had a low profile through much of the Holocene, in contrast to the other parts of the Ross Embayment.

reconstruction predicts ice elevations over 700 m thicker than the dome is today. The results of this study restrict Siple Dome to at most 40 m thicker 2000 a BP, and with lower-lying ice streams on either side through much of the Holocene. To make the reconstruction consistent with our results, we suggest that in the early Holocene, the central region of the Siple Coast (Ice Streams C and D with Siple Dome in between, the black hatched region in Figure 5.12), was thin with active ice streams, while the region around Roosevelt Island may have been much thicker.

There are two histories that can produce this difference across the Ross Sea. First, Siple Dome and the flow downstream may have always been low and thin, even during the glacial maximum. Or Siple Dome was much thicker during the LGM. Then the grounding line retreated in the central Ross Sea much earlier in the Holocene than on the sides, thinning Siple Dome and Ice Streams Kamb and Bindschadler well before Roosevelt Island. With the thin interior ice near and downstream from Siple Dome and thicker ice to the north and east, an ice cap possibly existed over the Ford Ranges that fed the region around Ice Stream E and Roosevelt Island.

5.5 Conclusions

In this paper we have brought together results of multiple studies related to the mass balance of Siple Dome to show that its geometry is in balance its present accumulation rate.

We examine the pattern of accumulation across the dome over three timescales. A 42 year average was determined by detecting the 1955 bomb layer using gross- β at seven points across the divide. We used the shallowest layer imaged by ground penetrating radar to estimate a 100 year average. We use the average pattern over several thousand year from the pattern of internal layers in 3 MHz radio echo sounding. And we estimated longer-term accumulation rates from the depth-age scale from the ice core. All reflect an orographically driven pattern of high accumulation on the north (upwind) side and low accumulation on the south side.

We determined the surface vertical velocity necessary to balance this accumulation

pattern using three independent methods: high-resolution GPS firn-motion measurements, deep ice vertical strain rates, and surface horizontal strain rates.

Our results show that the surface within about 10 km of the divide is in steady state to within the uncertainties of the measurements. The north side of the dome, halfway between the summit and the Bindschadler Ice Stream margin, appears to be thinning a small amount. The south side of the dome may also be thinning, but at a rate that is just above the detection level of our methods. This has several implications for the local and regional ice sheet history.

Siple Dome cannot have been more than 40 meters thicker 2000 a BP, otherwise it would show measurable thinning. This result is in contrast to Roosevelt Island, which shows a $9(\pm 6) \text{ cm a}^{-1}$ thinning rate [Conway *et al.*, 1999]. Siple Dome has been a fairly stable, elevated topographic feature bounded by ice streams through much of the Holocene and probably as early as the LGM. The divide has a distinctive Raymond bump, an arch in the isochrones characteristic of a stable divide. Since the ice divide is sensitive to changes in its bounding ice streams, Siple Dome's stability puts constraints on the behavior of Ice Streams C and D. The ice streams cannot have fluctuated greatly in their thicknesses and speeds over timescales greater than about 300 years (the propagation timescale for a step change in ice stream thickness to affect the summit [Nereson *et al.*, 1998a]). We conclude that the stoppage of Kamb Ice Stream, therefore, is either a gradual event occurring over thousands of years (possibly due to the overall ice sheet thinning since LGM) or part of "rapid" (less than 300 year) fluctuations in streaming flow.

Finally, evidence of present steady state behavior and the existence of a Raymond bump in the isochrones at the divide suggests that Siple Dome and Ice Streams C and D have been stable feature of the West Antarctic Ice Sheet throughout the Holocene. We surmise that the central part of the Siple Coast maintained a low profile with fast flowing ice, while there was much thicker ice along the Transantarctic Mountains and between the Ford Ranges and Roosevelt Island along the coast.

Chapter 6

**THE CROSSOVER STRESS, ANISOTROPY, AND THE FLOW LAW
AT SIPLE DOME**

This chapter is a draft of a paper with possible co-authors Ed Waddington, Throstur Thorsteinsson, Paul Jacobson, Will Harrison, Dan Elsberg, Mark Zumberge, Eric Hussman, John Morack, and Gregg Lamorey.

6.1 Summary

The flow pattern near an ice divide is the result of a combination of processes. The nonlinear rheology of ice flow causes ice near the bed at a divide to have a high viscosity. The ice particle paths refract and velocities decrease as they move through this region; over time this produces an arch in the isochrones. The shape and size of this arch is modified by the action of crystal anisotropy, the temperature field, and a shift in the flow-law exponent that occurs at low stresses. We use Siple Dome, a nearly steady-state ridge with a frozen bed, to study the relative importance of these processes in a realistic setting constrained by measurements of ice-flow, temperature, and ice properties.

We find that the linear term in the flow law and crystal anisotropy both contribute significantly to deformation. The crossover stress that best fits our data, assuming the divide is still migrating, is $k = 0.22$ bar. It is larger if the divide is no longer migrating. The band of strong crystal fabric around 750 m depth causes an increase in the difference between the flank and divide vertical-velocity profiles. The isotropic enhancement factors for the three layer ice sheet that best fit our data are: Holocene Ice, $E_1 = 1.3$; Ice-Age Ice, $E_2 = 0.06$; Recrystallized Ice, $E = 0.2$. The Ice-Age Ice and Recrystallized Ice layers are stiffer relative to clean, isotropic Holocene Ice. Finally, on the flank, the strong crystal fabric at depth concentrates the shear strain such that the recrystallized ice near the bed undergoes minimal deformation, creating a “false-bed” effect.

6.2 Introduction and Background

Ice divides separate the drainage basins of ice sheets. As the locations where the surface slopes and shear stresses approach zero, ice divides maintain a unique stress regime: ice is essentially in pure shear with lower effective deviatoric stresses than elsewhere on the ice sheet (see Figure 2.1). This stress regime poses an interesting challenge for ice dynamics modelling, since the low shear stress near the divide renders invalid the normal shallow-ice-approximation assumption that longitudinal stresses are negligible. Yet, modelling the flow of ice in this region is crucial to interpreting ice cores and examining the histories and possible futures of all ice sheets.

The ways in which the ice-divide stress regime alters the ice flow pattern depend on the ice-sheet boundary conditions and the details of the constitutive law for ice. Near a divide, the effective deviatoric stress is dominated by the longitudinal-stress rather than the bed-parallel shear-stress. Also, the magnitudes of the deviatoric stresses (both longitudinal and shear) are small relative to the shear stresses on the flanks of the ice sheet. According to Glen's flow law for ice, effective viscosity is inversely proportional to the square of the stress [Nye, 1953; Glen, 1958]. Thus, the region with the lowest stress (near the bed at the divide), is more resistant to deformation than surrounding areas. Deformation is concentrated in the softer ice nearer the surface; the ice flow trajectories are deflected near this hard "lump" of ice producing a unique flow pattern. Raymond [1983] first described the details of this special divide flow pattern and noted that the internal stratigraphy at a steady-state divide would reflect this flow pattern, causing ice of a particular age to appear higher in the stratigraphic column at the divide than at the flank. Since the special divide flow pattern has a limited horizontal extent, blending into flank flow within one to two ice thicknesses from the divide, this theory leads to an arch in the isochrones, commonly called a "Raymond bump".

Since Raymond's initial analysis, several authors have expanded on this theory of divide flow by looking at the perturbations to the flow field caused by variations in the boundary conditions. Nereson *et al.* [1998a] explored the effects of changes in elevation of bounding ice streams (which can cause the divide to migrate). Hvidberg [1996] included realistic

thermal boundary conditions and *Nereson and Waddington* [2002] characterized isotherms more fully under migrating divides. Finally, in Chapter 3 [also published as *Pettit et al.*, 2002], we modelled the effects of a sliding boundary condition at the base of the ice.

In addition to boundary conditions, crystal anisotropy can play a significant role in ice deformation and may modify the special divide flow pattern. *Mangeney et al.* [1996] modelled the flow of anisotropic ice near an isothermal divide with a linear ice-flow law and found little change in the overall flow pattern. In Chapter 4, however, we combined the characteristics of anisotropic flow with a more realistic nonlinear constitutive relation and found that strong anisotropy perturbs and enhances the special divide flow pattern.

Finally, the degree to which ice behaves as a nonlinear fluid in the low-stress divide region is still under debate. Conventionally, glaciologists have used Glen's Law, which describes ice as a power-law fluid with an $n = 3$ relation between stress and strain rate (where n is the exponent in the power law). It is probable that at low stresses the micro-scale mechanism driving ice flow shifts to a more linear flow mechanism [*Langdon*, 1996; *Goldsby and Kohlstedt*, 2001, e.g.]. In Chapter 2 [also published as *Pettit and Waddington*, in press], we summarize the theory behind this possible shift in flow mechanism, reformulate the flow law as a two-term law, and define the *crossover stress* as the stress at which the linear mechanism and the traditional Glen's Law ($n = 3$) mechanism contribute equally to the strain rate. We then model the flow patterns resulting from different combinations of linear and Glen flow laws.

In this chapter, we compare the impact of the constitutive law's stress exponent with that of deformational anisotropy (introduced in Chapter 4) for a real divide: Siple Dome, West Antarctica. We chose Siple Dome because it has been studied extensively over the last decade, and it is the site of the U.S. Antarctic Program's most recent deep drilling project. In this study, we take advantage of the plethora of available ice core, surface flow, mass balance, and *in situ* vertical-strain data. The vertical-strain data are unique and essential to this study; the instruments were developed as part of a collaboration with the University of Washington to study the details of ice flow at an ice divide [*Zumberge et al.*, 2002; *Elsberg et al.*, in review]. We use two high-resolution custom instruments: fiber-optic position sensors developed by the University of California, San Diego [*Zumberge et al.*,

2002], and wire strain meters developed by the University of Alaska, Fairbanks [Elsberg *et al.*, in review]. The existence of these data allows us to use the known geometry and ice properties of Siple Dome to invert for realistic flow-law parameters based on vertical-strain rates measured at depth and horizontal velocities measured on the surface.

6.3 Case Study of Siple Dome

Siple Dome is a 1000 m thick ridge of slow-moving ice between Ice Streams C and D on the Siple Coast of West Antarctica (Figure 6.1). The summit region has been in steady state for several thousand years (Chapter 5) and it has been an elevated dome-like feature for much of the Holocene and possibly since the last glacial maximum [Nereson *et al.*, 2000]. The internal structure, as imaged by low-frequency ice-penetrating radar, shows a distinctive Raymond bump (Figure 6.2). The characteristic deviatoric stress [as defined by Waddington *et al.*, 1996; Pettit and Waddington, in press, and Chapter 2] is 0.2 bar, low enough that linear and near-linear flow mechanisms may contribute measurably to the deformation. These characteristics make Siple Dome ideal for a case study of the effects of rheological processes on divide flow.

If we assume that the radar stratigraphy in Figure 6.2 represent isochrones [Paren and Robin, 1975], the pattern existing in the ice sheet today reflects the integrated flow field over tens of thousands of years. Some authors have used these layers to study the present and past dynamics of ice divides [Vaughan *et al.*, 1999; Nereson and Raymond, 2001]. Our focus, however, is on the rheological properties and the flow law of the ice; therefore, we prefer to use a more direct measurement of the modern strain-rate field in the divide region. Our analysis is based on *in situ* vertical-strain-rate measurements, which depends only on the modern geometry of the ice sheet and on the present rheological properties of the ice, not on the divide's history.

As introduced above, many processes can modify the vertical velocity profile and thus, over time, the arch in the isochrones. These include the effects of boundary conditions, deformation due to anisotropy, near-linear flow mechanisms, and the temperature regime. Here, we narrow our focus to anisotropy and the activation of linear and near-linear flow

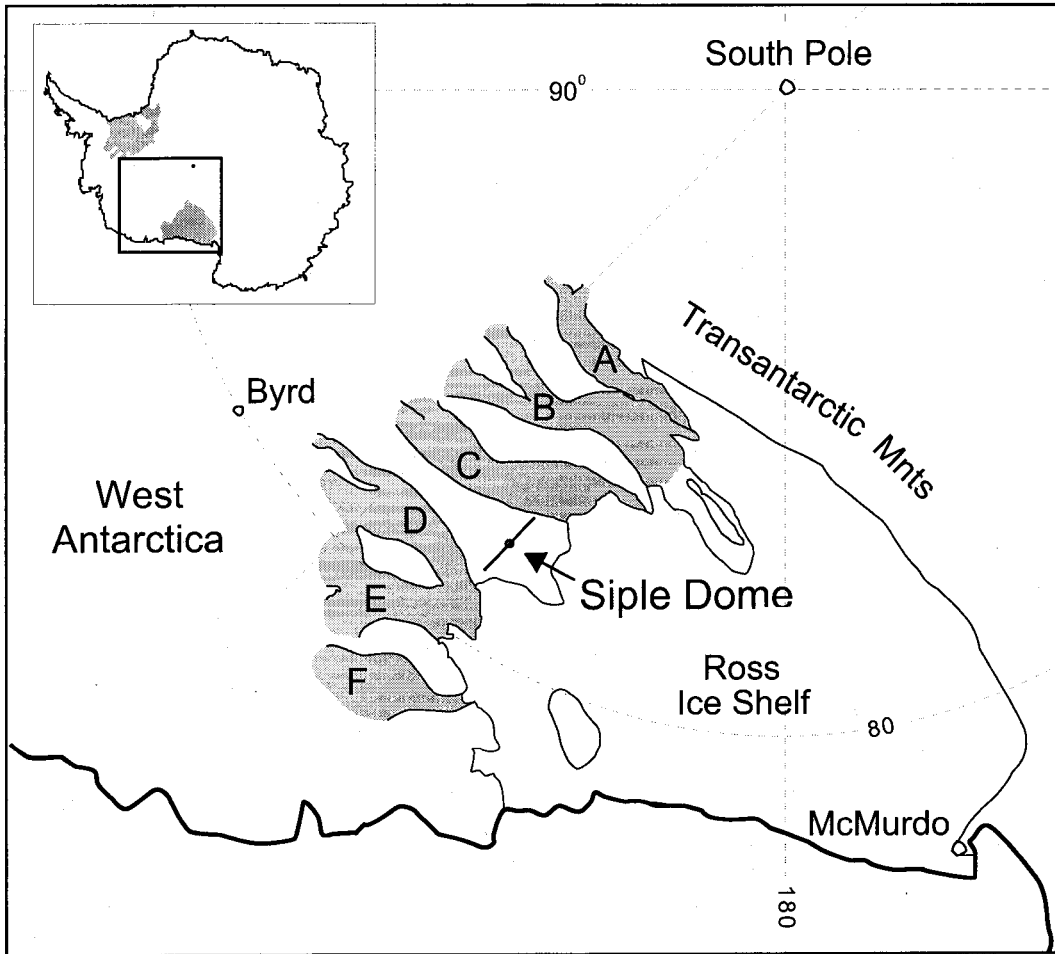


Figure 6.1: The Siple Coast and the Ross Sea Embayment, West Antarctica. Siple Dome (81.65° S and 148.81° W) is an inter-ice stream ridge on the Siple Coast of West Antarctica. Shaded regions represent fast flow ice, including ice streams A (Mercer Ice Stream), B (Whillans Ice Stream), C (Kamb Ice Stream), D (Bindschadler Ice Stream), E (MacAyeal Ice Stream), and F (Echelmeyer Ice Stream). The dot on Siple Dome approximately identifies the summit location, and the adjacent line represents the cross section modelled here.

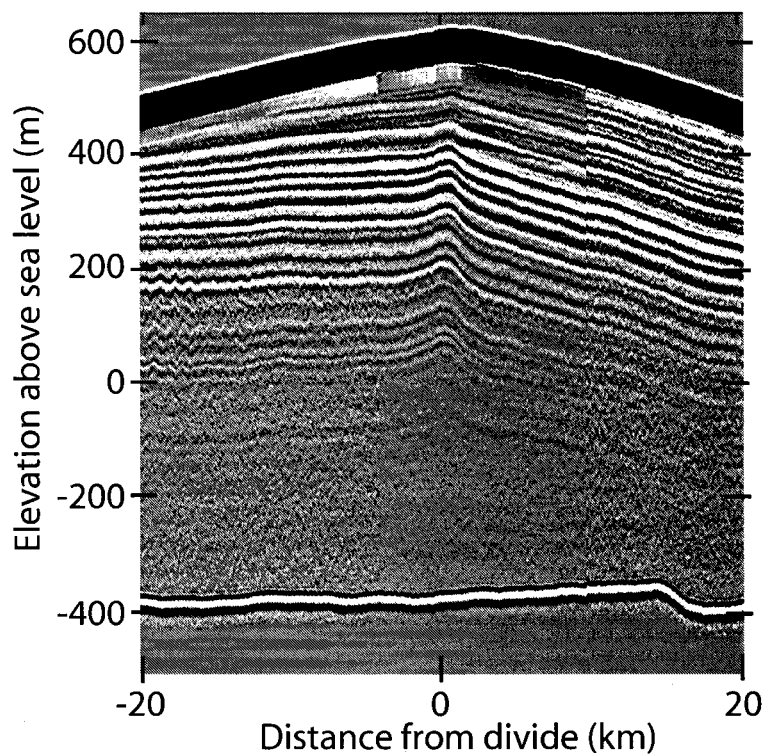


Figure 6.2: Ground-based 3 MHz ice-penetrating radar image of the divide region of Siple Dome [Raymond *et al.*, 1995; Scambos and Nereson, 1995; Jacobel *et al.*, 1996]. The image corresponds to the central section of the black line across Siple Dome in Figure 6.1. Bindshadler Ice Stream is to the right and Kamb Ice Stream is to the left. Note the concave-downward arch in the isochrones at the divide that is driven by the nonlinear stress-strain-rate relationship and a vertically-oriented crystal fabric.

mechanisms.

The tendency of crystals to align vertically with depth in an ice sheet causes stiffening of the ice undergoing vertical compression at the divide and softening of the ice shearing on the flanks (Chapter 4). This contrast in effective viscosity alters the vertical-strain-rate profile and enlarges the isochrone arch. On the other hand, we showed in Chapter 2 that the introduction of a linear term into Glen's Law diminishes the divide-flank flow difference and attenuates the arch. It is important to note that these effects modify an existing Raymond bump; where no bump exists (because of a sliding bed or a wandering

divide, for example), anisotropic deformation cannot create one.

Our question is:

Given a crystal fabric field (based on the measured sonic velocity in the borehole) and a temperature field (also based on measurements in the borehole) what is the relative importance of the three Raymond bump “modifiers” (anisotropy, linear flow mechanisms, and temperature) at Siple Dome?

6.4 The Constitutive Law for Ice

In general, empirical analyses have shown that ice behaves as a power-law fluid [Glen, 1955; Nye, 1953]. The simplest expression for Glen’s Law (introduced in Chapter 2) is $\dot{\epsilon}_{ij} = A\tau_{\text{eff}}^2\tau_{ij}$, where $\dot{\epsilon}_{ij}$ and τ_{ij} are the strain-rate and stress tensors and τ_{eff} is the second invariant of the stress tensor.¹ In this form, all the variations due to properties of the ice are lumped into A , the *softness parameter*. As we discussed in Chapters 2 and 4, this form is limiting, for two primary reasons. First, ice flow results from a combination of micro-scale flow mechanisms, and as a result, the exponent may change as the dominant flow mechanism changes. Second, polycrystalline ice in an ice sheet can be strongly anisotropic. The stress regime in an ice sheet tends to drive development of a vertically oriented fabric [Alley, 1992]. The simple form of Glen’s Law with a scalar softness parameter is ineffective at describing ice flow with crystal anisotropy.

6.4.1 A two-term isotropic flow law

In Chapter 2, we develop a two-term flow law for isotropic ice that is simple to incorporate into ice-flow models, but can encompass a range of deformation behaviors, specifically the low-stress behavior seen near ice divides. This flow law is:

$$\dot{\epsilon}_{ij} = \Gamma[k^2 + \tau_{\text{eff}}^2]\tau_{ij}, \quad (6.1)$$

¹Appendix A is a table of the notation.

where $\dot{\epsilon}_{ij}$ and τ_{ij} are the strain-rate and deviatoric-stress tensors,

$$\Gamma = \frac{E_{nl}A_{o_{nl}}}{d^{p_{nl}}} e^{-\frac{Q_{nl}}{RT}}, \quad (6.2)$$

and

$$k = \left[\frac{E_l A_{o_l}}{E_{nl} A_{o_{nl}}} \frac{d^{p_{nl}}}{d^{p_l}} e^{-\frac{Q_l - Q_{nl}}{RT}} \right]^{1/2}. \quad (6.3)$$

In these expressions, E is an enhancement factor, A_o is the softness parameter, Q is the activation energy, T is the temperature, R is the gas constant, d is the average grain size (if $p = 0$, there is no crystal-size dependency), and the subscripts refer to the linear and nonlinear creep mechanisms. In this formulation, k , the *crossover stress*, is the effective deviatoric stress at which the linear and cubic terms contribute equally to the total strain rate and, when $p_{nl} = 0$, Γ is the coefficient for “normal” Glen flow (for a derivation of this flow law see Chapter 2).

6.4.2 An anisotropic modification to flow

This formulation still does not provide a means for incorporating the directional flow enhancements due to anisotropy. Ice crystals only two active slip systems (similar, in many ways, to a deck of cards), with deformation on other slip systems being more than 60 times harder [Duval *et al.*, 1983]. As a result, an ice aggregate with crystals aligned in the same direction is much softer in simple shear than an isotropic aggregate. Since grains within an ice sheet are known to develop a preferred orientation as the ice sheet evolves [Alley, 1992], incorporating anisotropy into a flow law may improve our ability to realistically model ice-sheet deformation.

We use an anisotropic flow model originally developed by Thorsteinsson [2001] based on the Sachs [1928] homogeneous-stress assumption. In Sachs’ description of anisotropy, the bulk deformation of the ice aggregate is assumed to be the average deformation of all the crystals within the aggregate. The resolved shear stress (RSS) on the basal plane of each crystal depends on its orientation to the applied stress. The RSS drives the deformation within the crystal. Thus, crystals with basal planes oriented parallel to the shear stress

have a larger RSS and deform at a faster rate than crystals with basal planes oriented perpendicular to the shear stress.

To build a law from this theory, *Thorsteinsson* [2001] used a statistical distribution of crystal orientations within an aggregate to define the bulk deformation. The fabric near an ice divide typically has a cluster of c-axes oriented vertically. This type of fabric can be described by a “cone angle”, the half-apex angle of a cone within which all crystals in an ideal block of ice are uniformly distributed. (In real ice, the distribution is not uniform and there are outliers; its cone angle is that of the ideal block of ice which produces the same strain rate.) *Thorsteinsson* derived analytical solutions to describe the deformation of the bulk material for a given cone angle with a linear RSS-strain-rate relationship on the basal plane (Chapter 4). The conservations of momentum and mass are (a more complete derivation of these equations is in Appendix D):

$$\frac{1}{\Gamma} \left(\frac{-1}{3b} \frac{a-b}{2a+b} - \frac{1}{2e} \right) u_{xx} + \frac{1}{\Gamma} \frac{1}{2e} u_{zz} - p_x = 0 \quad (6.4)$$

$$\frac{1}{\Gamma} \frac{1}{2e} w_{xx} + \frac{1}{\Gamma} \left(\frac{-1}{3b} - \frac{1}{2e} \right) w_{zz} - p_z = \rho g \quad (6.5)$$

$$u_x + w_z = 0. \quad (6.6)$$

where $1/\Gamma$ is the isotropic effective viscosity (with Γ as defined in Equation 6.2) and a through e are functions of the cone angle based on the the Sach’s model (Appendix D contains the definition of a through e). This derivation assumes that Γ and a through e are spatially uniform; therefore, these PDE’s apply to individual finite elements in the model, and are not descriptive of the overall flow field. This analytical solution is relatively easy to incorporate into a flow model.

Compared to other anisotropic flow laws, this formulation generally under-predicts anisotropic enhancement [*Azuma*, 1994; *Castelnau et al.*, 1996; *Thorsteinsson*, 2001]. Since the “real” magnitude of enhancement is not known, yet the style of deformation is generally the same for all formulations, we allow the scalar enhancement factors (E_n and E_1) for the bulk material to adjust to account for this uncertainty.

Thorsteinsson’s analytical formulation has three limitations. It is based on linear de-

formation on the basal plane, it does not allow for evolution of the fabric, and it does not include interactions between neighboring crystals [Thorsteinsson, 2002]. We assume that the effects of these limitations are small compared to the magnitude of the anisotropic deformation. First, the use of a linear stress-strain-rate relationship to determine anisotropic deformation for single crystals is combined with nonlinear bulk deformation of the ice; this method approximates the pattern of behavior of the fully nonlinear system without the mathematical complexity. Second, crystal fabric is continually evolving in an ice sheet. In this model, however, we are not analyzing time-dependent behavior. We relate the modern stress field (imposed by the present geometry) the measured strain-rate field, and measured crystal orientation (cone angle) through the ice flow law. And third, Thorsteinsson showed that interactions between neighboring crystals generally speeds the rate of fabric development, but maintains the general pattern of ice flow. Again, we assume slight variations in the flow due to neighboring crystals as included in the enhancement factors.

6.5 Finite-Element Ice-Flow Model

To study the flow at Siple Dome, we use a finite-element model (FEM), similar to the ice-divide models developed by *Raymond* [1983] and *Hvidberg* [1996]. The fundamental assumptions include:

1. The ice deforms in plane strain; thus, the model best represents a ridge ice divide, such as Siple Dome [*Nereson et al.*, 1996] or Roosevelt Island [*Conway et al.*, 1999].
2. The temperature field is specified.
3. The present geometry is specified.
4. The upper surface is stress free.
5. The horizontal-velocity profile on the flank boundary (at 30 ice thicknesses from the divide) carries away the integrated mass balance from the divide to the boundary, in order to satisfy mass conservation for a steady-state ice sheet. Because our boundary

is more than 20 ice thicknesses from the divide, the results for the region within ten ice thicknesses of the divide are insensitive to the details of the horizontal-velocity profile on the flank boundary [Raymond, 1983; Schøtt *et al.*, 1992]. In practice, we begin with a laminar flow profile at the boundary, but as velocities within the ice sheet are calculated, we update the shape of the horizontal-velocity profile at the boundary (while maintaining the flux) to account for the unique rheological properties of the anisotropic ice and the non-uniform temperature field.

6. Ice rheology is described by the two-term isotropic flow law shown in Equation 6.1 incorporated with the anisotropy description. The A_0 parameters is taken from Paterson, 1994, Chapter 5, while variation from this standard softness is expressed in enhancement factors, E_i . The model is solved iteratively. First, an isotropic effective viscosity ($1/\Gamma$) is calculated for each element from the effective strain rate calculated during the previous iteration using Equation 6.1. Then this effective viscosity is substituted in Equations (6.4) to (6.6), which are solved for the new velocity gradients for the element, given the element's cone angle. This process is repeated for a specified number of iterations (typically 10) to achieve reasonable convergence within a timestep. This two-step process allows us to combine the nonlinear bulk flow of ice based on Glen's Law with a description of anisotropy (based on a linear rheology). Small uncertainties will be introduced where the ice properties (such as cone angle) of adjacent elements are vary.
7. In these models the cone angle at the divide is extrapolated to the flanks as a function of normalized depth ($z/H(x)$).
8. The model solves the flow equations on a grid of 9-node quadratic elements for temperature, pressure, and velocity fields.

6.6 Field Site: Siple Dome, West Antarctica (81.65° S and 148.81° W).

Siple Dome is the site of the most recent deep ice core drilled by the United States National Science Foundation Office of Polar Program's WAISCORES Initiative. The ice-core drilling was completed in January of 1999 and collaborating scientists are now completing a comprehensive analysis of the ice-core and borehole data to reconstruct climate history. In addition to the ice core, an extensive strain network provides surface flow; snow pits, shallow cores, and radar provide spatial and temporal accumulation rate patterns, and instruments buried in the ice provide vertical motion measurements.

Where pertinent, we have incorporated the available measurements in this study. The measured divide geometry, borehole temperatures, and sonic log (a proxy for crystal fabric [Thorsteinsson, 2000]) provide inputs to the model, while the surface and depth strain data, accumulation rates, and grain size provide constraints on possible solutions.

6.6.1 Model inputs

Geometry

The surface topography along the cross section that we study (the line across the dome in Figure 6.1) was measured using Global Positioning System (GPS) data [Raymond *et al.*, 1995; Scambos and Nereson, 1995; Nereson *et al.*, 1996]. The bed topography come from low-frequency ice-penetrating radar [Raymond *et al.*, 1995; Jacobel *et al.*, 1996]. Near the divide, there is no evidence for significant flow perpendicular to the cross section [Nereson, 1998]; therefore we assume two-dimensional plane-strain flow.

Figure 6.3 shows the model geometry and the finite-element mesh. We placed more elements near the divide and in regions of strong vertical gradients in ice properties.

Accumulation rate

The pattern of accumulation rate at Siple Dome is driven by the topography. Storms generally approach from the north, ocean-ward, side of the divide, and deposit more of their moisture on the north side, leaving the south side significantly dryer [Bromwich,

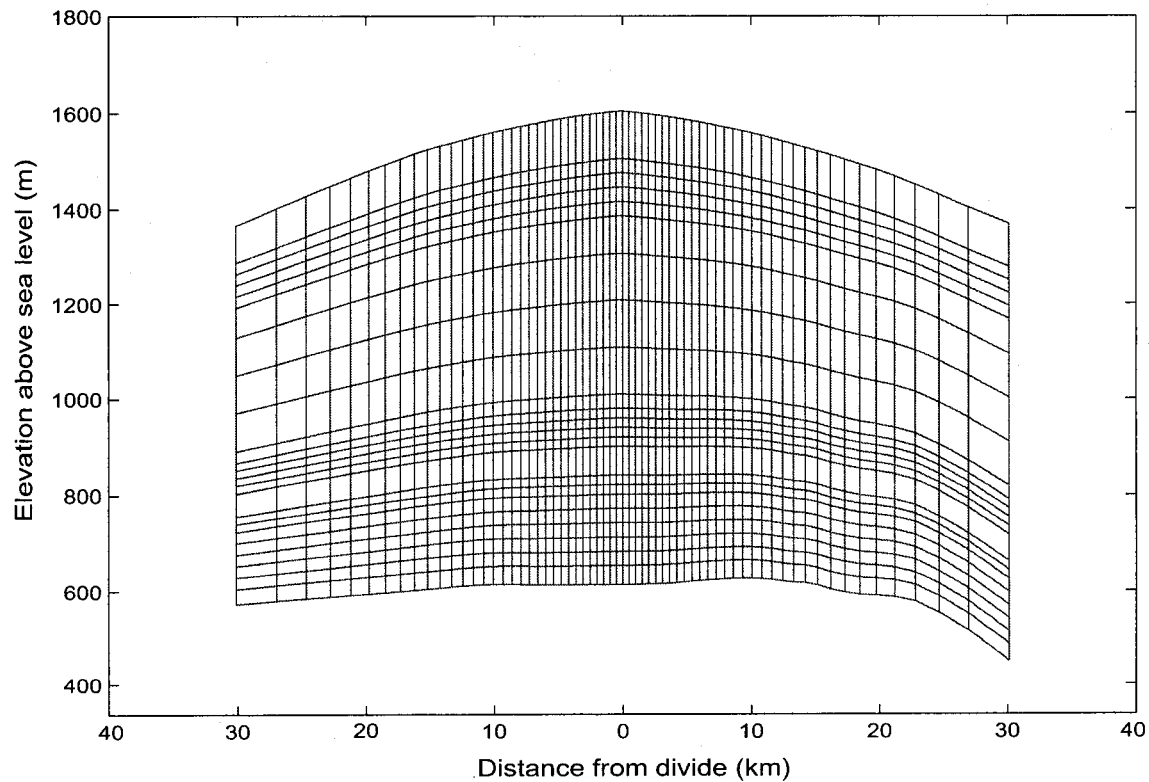


Figure 6.3: Geometry for Siple Dome. Surface profile is from GPS measurements [Raymond *et al.*, 1995; Scambos and Nereson, 1995; Nereson *et al.*, 1996] and bed topography is from ice-penetrating radar [Raymond *et al.*, 1995; Jacobel *et al.*, 1996]. Bindshadler Ice Stream is to the right and Kamb Ice Stream is to the left. The crosses are nodes, lines represent element boundaries. The grid is finer where we expect the largest gradients in velocities (due either to proximity to the divide or to gradients in the physical characteristics of the ice).

1988]. *Nereson et al.* [2000] observed this trend in the pattern of radar-detected internal layers. They used a kinematic steady-state ice-flow model to predict internal-layer shapes as a function of a steady-state accumulation pattern across the dome. The accumulation pattern derived from the RES images provides only relative accumulation rates, since the layers in the image are not dated (a depth-age scale for the ice core is just recently available to complete this analysis *Taylor et al.* [accepted]). In our analysis of ice flow at Siple Dome, we use this pattern, scaled to a point measurement of the modern accumulation rate (42 a average) at the divide (0.132 m a^{-1}) determined by *Hamilton* [2001] using gross- β analysis on a shallow core.

Temperature

The temperature profile at Siple Dome was measured both in the deep borehole 500 meters South of the summit by the University of Washington and in a hot-water-drilled borehole at the summit by the California Institute of Technology [*Hermann Englehardt*, personally communication, 2003]. *Englehardt* also measured a shorter profile to about 300 meters depth at the flank strain-gauge instrumentation site approximately 7 km North-east (81.60°S , 148.69°W).

In a steady-state ice sheet, both advection and diffusion can contribute significantly to the temperature field if the Peclet number is large. As we introduced above, near a divide the vertical velocity field is altered by low-stress behavior such that an arch appears in the isochrones. The process that produces this arch in the isochrones also produces an arch in isotherms by affecting the advection term in the heat equation. We determine the temperature for our entire model cross section by adapting the 2-D steady-state advection-diffusion kinematic model from *Nereson and Waddington* [2002] constrained by the measured temperature profile at the divide.

The *Nereson-Waddington* model uses a kinematic velocity field based on the shape-function method of *Reeh* [1988]. Here, we apply this model using surface velocities derived from the local accumulation rate. For a real divide, the temperature field is also dependent on the history of surface temperature and ice flow. To account for Siple Dome's history, we adjust the bulk values of thermal conductivity, specific heat, and geothermal flux to

best fit the measured temperature profile at the divide. We, then, apply these values to the entire ice-sheet cross section. We ultimately used $2.1 \text{ W m}^{-1}\text{K}^{-1}$ for conductivity, $1700 \text{ J kg}^{-1}\text{K}^{-1}$ for specific heat and 70 mW m^{-2} for the geothermal flux. (The generally accepted values of the conductivity and specific heat for pure ice range from $2.1 \text{ W m}^{-1}\text{K}^{-1}$ and $1741 \text{ J kg}^{-1}\text{K}^{-1}$ for -50° C to $2.76 \text{ W m}^{-1}\text{K}^{-1}$ and $2097 \text{ J kg}^{-1}\text{K}^{-1}$ for ice at 0° C .)

Although Siple Dome has been neither thickening nor thinning in the late Holocene (see Chapter 5), there is evidence of slow divide migration in the recent past [*Nereson et al.*, 1998b]. The range of possible migration speeds found by *Nereson et al.* [1998b] is $0.05\text{--}0.50 \text{ ma}^{-1}$. We include a migration rate in the middle of this range (0.26 ma^{-1}) in this calculation. Figure 6.4 shows the temperature field we used in our model. The range of possible migration rates introduces some uncertainty in the temperature field.

The additional temperature measurements on the flank made by Englehardt provide one location with which to check our temperature calculation. All of our calculated temperatures in that location are less than 0.5° C from the measured values. We estimate, using the Arrhenius temperature model, that this difference would result in at most a 5% error in our strain-rate calculations.

Crystal size and orientation

Preferred crystal orientation can alter local strain-rate patterns by up to an order of magnitude. Chemical and physical impurities also affect the flow [*Cuffey et al.*, 2000a; *Paterson*, 1991, e.g.], but the relationships are complicated and difficult to predict. Grain size is suspected to be important where the grains are small [*Goldsby and Kohlstedt*, 2001; *Cuffey et al.*, 2000b]; however, it is unclear whether grain size is an independent factor or whether it is driven by impurity content and the strain-rate field [*de Bresser et al.*, 2001]. Here, we focus on crystal orientation. Flow enhancement due to grain size and impurity content are smaller-scale effects that we incorporate through an enhancement factor.

Since we have coupled an anisotropic flow description with the finite-element model, crystal orientation is an important input. We use results from borehole sonic logging (completed by the Desert Research Institute), which measures the speed of sound transmitted through approximately 7 meters of ice (thousands to millions of crystals). Sound

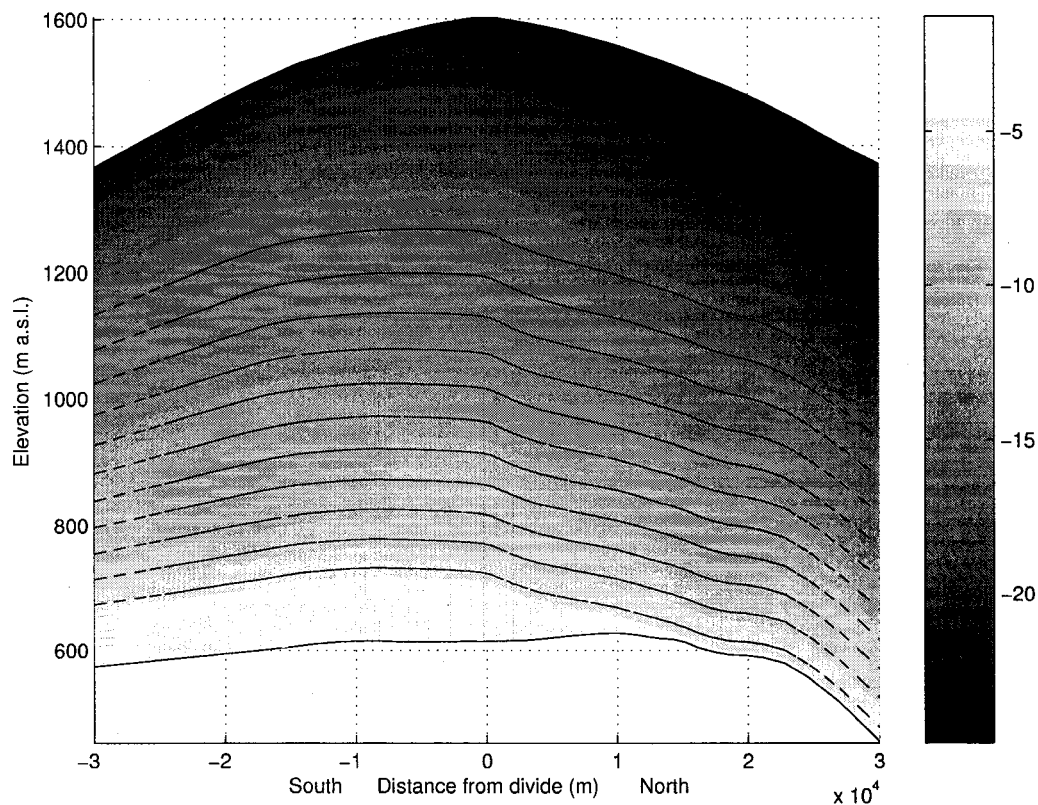


Figure 6.4: Temperature field used as model input for the finite-element model. Bindschadler Ice Stream is to the right and Kamb Ice Stream is to the left. The temperature field is derived from measured temperatures at the divide and a kinematic flow model based on *Nereson and Waddington* [2002]. The isotherms are elevated on the South side because low accumulation there reduces advection.

speed varies with the elastic anisotropy, which is related to the deformational anisotropy of a crystal in a straightforward way. We use the method of *Thorsteinsson* [2000] to convert the sonic log into effective cone angle.

The cone angle profile is shown in Figure 6.5, along with preliminary grain radius data (Larry Wilen, personal communication, 2003) and temperature (Hermann Englehardt, personal communication, 2003) as a function of depth and age (Kendrick Taylor, personal

communication, 2003). We include grain size and temperature to highlight the structural difference in the ice at different depths. The sonic log shows a distinct layer of extremely tight vertical fabric, with large gradients in cone angle above and below. The upper transition begins at 680 m and occurs over 16 m. This transition occurs between 17.4 ka BP and 20 ka BP and it corresponds with a decrease in the grain size. A shift in grain size is typical of the boundary between Holocene ice and deeper ice-age ice [e.g. *Paterson*, 1994, p. 193], since ice-age crystals grow more slowly [*Lipenkov et al.*, 1989]. This transition is slightly deeper than the transition to a warmer climate expressed by the stable isotopes [*Taylor et al.*, in prep]. This offset might arise because warmer temperatures of the early Holocene we expect to affect the last 10 to 20 m of ice age ice during its time within the firn and normal grain-growth regions. With the low accumulation rates expected during the ice age and early Holocene, the timescale for advection is several times longer than the timescale for diffusion.

We estimate that the cone-angle transition between 756 m (-10°C) and about 805 m (-8°C), marks the upper bound of dynamic recrystallization, which occurs as the ice warms near the bed.

In our model, we divide the ice into these three layers (Holocene, Ice Age, and Recrystallized Ice) since they will likely have distinct deformation characteristics. For each layer, we define the flow law coefficient Γ_o (see Equation (6.2)) as:

$$\Gamma_o = \frac{E_{nl}A_{o,nl}}{d^{p_{nl}}}. \quad (6.7)$$

We use the value of A_o that is recommended by *Paterson* [1994], based on data from multiple studies. It represent an average for clean Holocene ice. We define E_i as $E_{nl}/d^{p_{nl}}$ for each of the three layers shown in Figure 6.5 (E_1 for Holocene Ice, E_2 for Ice Age Ice, and E_3 for Recrystallized Ice). These three coefficients, along with the crossover stress, k , are the unknown parameters in the flow law. We expect the E_1 for Holocene ice at Siple Dome to be near 1, if it is similar to the *Paterson's* average value, but we do not assume that $E_1 = 1$.

In using the crystal fabric and other ice-core data in our analysis, we make one impor-

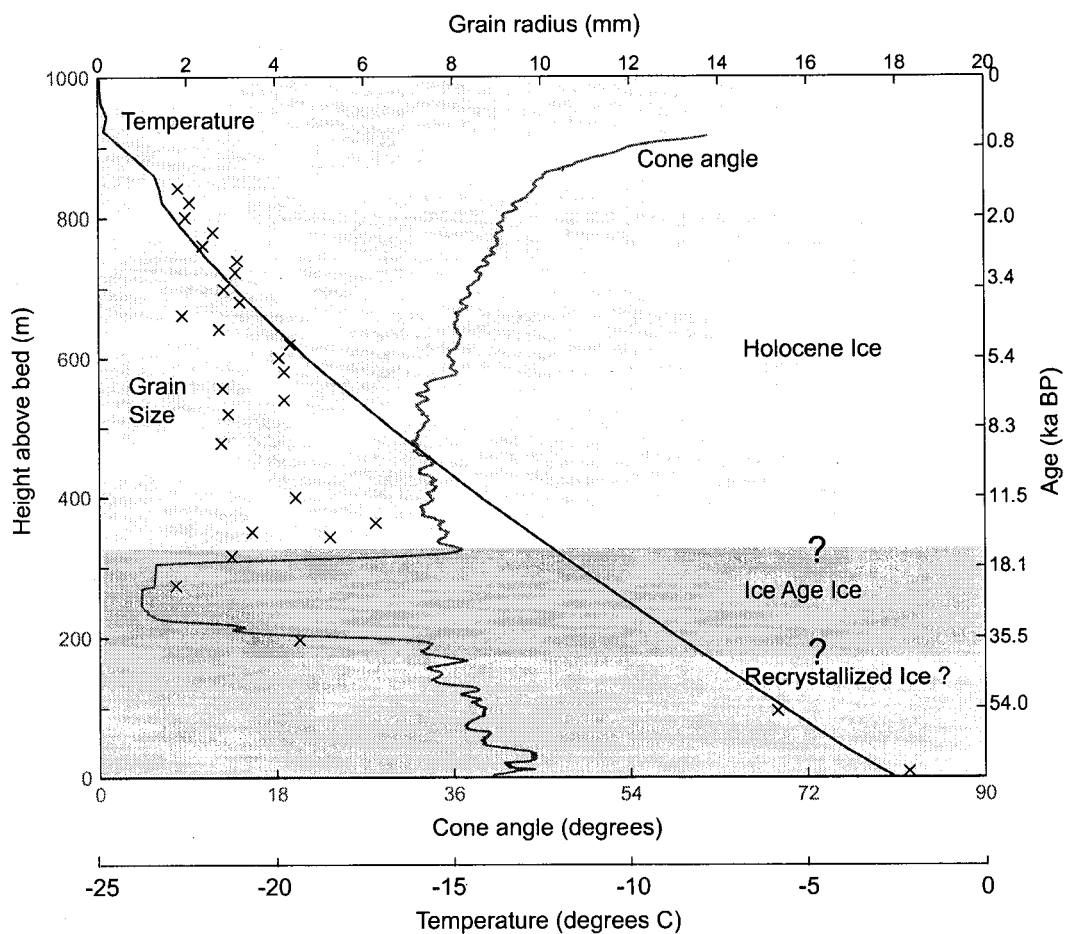


Figure 6.5: Cone angle is from the sonic log of the borehole, transformed to cone angle using the method of *Thorsteinsson* [2002]. Grain size is from thin sections of the ice core (Richard Alley, Matt Spencer, Carlos DiPrinzio, and Larry Wilen, personal communication, 2003). Temperature is from a hot-water-drilled borehole at the summit (Hermann Englehardt, personal communication). The approximate ages are given on the right vertical axis based on the combined timescale [*Taylor et al.*, accepted]. Note the correspondence of the band of tight fabric with small grains between 700 and 800 meters depth. Our assignment of Holocene, Wisconsin, and Recrystallized Ice regions is an estimate based on ice properties. See text for complete explanation.

tant assumption, that the ice properties are uniform horizontally. Realistically, there will be some variation in ice structure with distance from the divide, since ice properties are advected along particle paths, but we assume that it is small compared to the vertical variations in the ice. The preferred crystal orientation for vertical compression at the divide is similar to that for simple shear at the flank (a single maximum cluster of c-axes oriented vertically). As ice flows from the divide to the flank, the shearing would tend to strengthen the fabric and decrease the effective cone angle. Also, the particle paths are deeper with distance from the divide. We estimate that this fabric variation would enhance the effect of anisotropy that we are modelling, so our model at present may slightly underestimate the role of anisotropy.

6.6.2 Data used to constrain model outputs

Horizontal velocities at the surface

Horizontal velocities at the surface of Siple Dome have been measured most accurately using GPS to survey a network of stakes [Chapter 5 and *Nereson, 1998*]. Although there are numerous horizontal velocity measurements at points across the divide, we focus on those within 9 km of the divide. Figure 6.6 shows the stake velocities as solid dots. The thin solid line shows theoretical surface velocities predicted from the accumulation rate and ice thickness using conservation of mass (the balance velocity): $u_s = \frac{1}{\gamma} \frac{b\alpha}{H}$. γ is the ratio of the average velocity to the surface velocity and depends on the velocity profile; we assume $\gamma = 0.85$ based on velocity profiles from an isotropic finite-element model. North of the divide, the predicted velocities match well with the measured velocities. Among other things, this implies that our assumption of 2D plane strain flow is valid. On the south side, however, the balance velocities are too large. *Nereson [1998]* observed a similar imbalance in calculating the flux divergence along the southward flow line. This imbalance could be rectified by including ice-sheet thickening, flow-line divergence, or both. On the other hand, the mass balance study presented in Chapter 5 suggests the ice is in balance. Since our data and model results focus on the north side of the divide, this discrepancy is of minor concern.

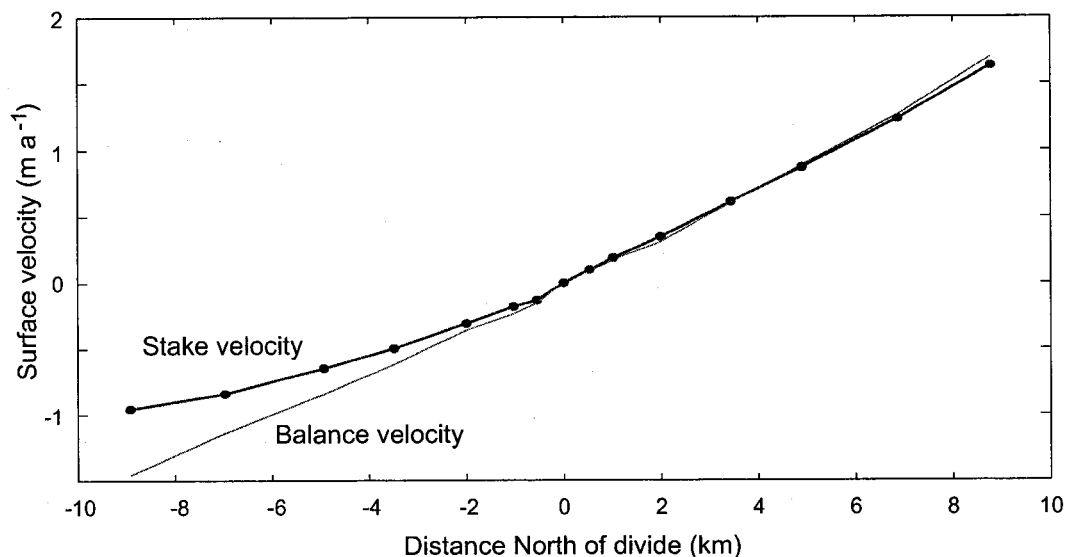


Figure 6.6: Horizontal surface velocities from GPS stake surveys (solid line, dots represent stakes). Bindschadler Ice Stream is to the right and Kamb Ice Stream is to the left. Thin solid line is the predicted surface velocities assuming continuity in 2 dimensions given the accumulation rate, ice thickness, and velocity profile: $u_s = \frac{1}{\gamma} \frac{bx}{H}$.

Vertical-strain rate data

The unique ingredient in our analysis is measurements of the vertical-strain-rate profile at the divide (81.65°S and 148.81°W) and at a flank site (81.60°S , 148.69°W) 7 km to the northeast of the divide. We used two types of instruments, wire-resistance strain gauges (gauge length 1 meter) and optical-fiber position sensors (effective gauge lengths 174 and 178 meters).

The optical-fiber instrument, developed by *Zumberge et al.* [2002] of the University of California, San Diego uses a pair of dual fiber optic cables, one short and one long, to measure the total strain between the fiber endpoints. Each dual fiber cable consists of two fibers spliced together at the bottom: a transmit fiber and a return fiber. It is anchored at the surface and at depth, and the length between anchors is measured using an electronic distance meter. Each fiber is housed in a stainless steel sheath, so that the fiber can move

and deform freely along the borehole, except at the anchors.

At each of the two sites (divide and flank), ten fibers were lowered into water-filled boreholes and frozen into the ice. Five 80 m fibers were paired with five longer fibers, whose lower anchors were spaced evenly throughout the ice-sheet thickness. The fibers were pre-stretched with a 20 kg mass, allowing us to measure subsequent vertical compression within the ice. We monitored the length of each fiber using a specially adapted electronic distance meter during a few weeks each summer for four years. Subsequently, the data were corrected for temperature, optical-physical length ratio [Zumberge *et al.*, 2002], and horizontal shearing of the boreholes (see Appendix C). From these data [published in Zumberge *et al.*, 2002; Elsberg *et al.*, in review], we determined the average annual strain rate over an effective gauge length of 178 meters at the divide and 174 meters at the flank. The average strain rate over 4 years data are shown as open (flank) and closed (divide) circles in Figure 6.7; the vertical bars represent the effective gauge length. The uncertainties in these data are about 3 to $9 \times 10^{-6} \text{ a}^{-1}$.

The fiber-optic sensors measure strain over large depth intervals. We paired these instruments with one-meter-long wire resistance gauges developed by Elsberg *et al.* [in review]. These instruments use a Wheatstone bridge configuration with one “active” wire that is one meter long and frozen into the ice, a return wire, and the three other wires in the bridge coiled up inside the gauge housing. Similar to the fibers, the active wire was installed under tension to allow us to measure subsequent vertical compressive strains. A data logger on the surface recorded the voltage balance of the bridge every 30 to 90 minutes almost continuously for four years. Thus, as the fiber instruments measure average strain rates over time and space intervals, the wire strain gauges are essentially point measurements of strain rate logged continuously. Although they exhibit some intriguing small-scale time-dependent fluctuations [Elsberg *et al.*, in review], in this analysis we use the average strain rate over 4 years (after initial transients have dissipated), shown as squares in Figures 6.7. The instrument uncertainties in these data are between 5 and $10 \times 10^{-6} \text{ a}^{-1}$.

Because these instruments measure strain over a short distance, they are sensitive to inhomogeneities in the ice on scales of decimeters to 10 meters. These instruments may measure small-scale flow unrepresentative of larger ice volumes, particularly where there

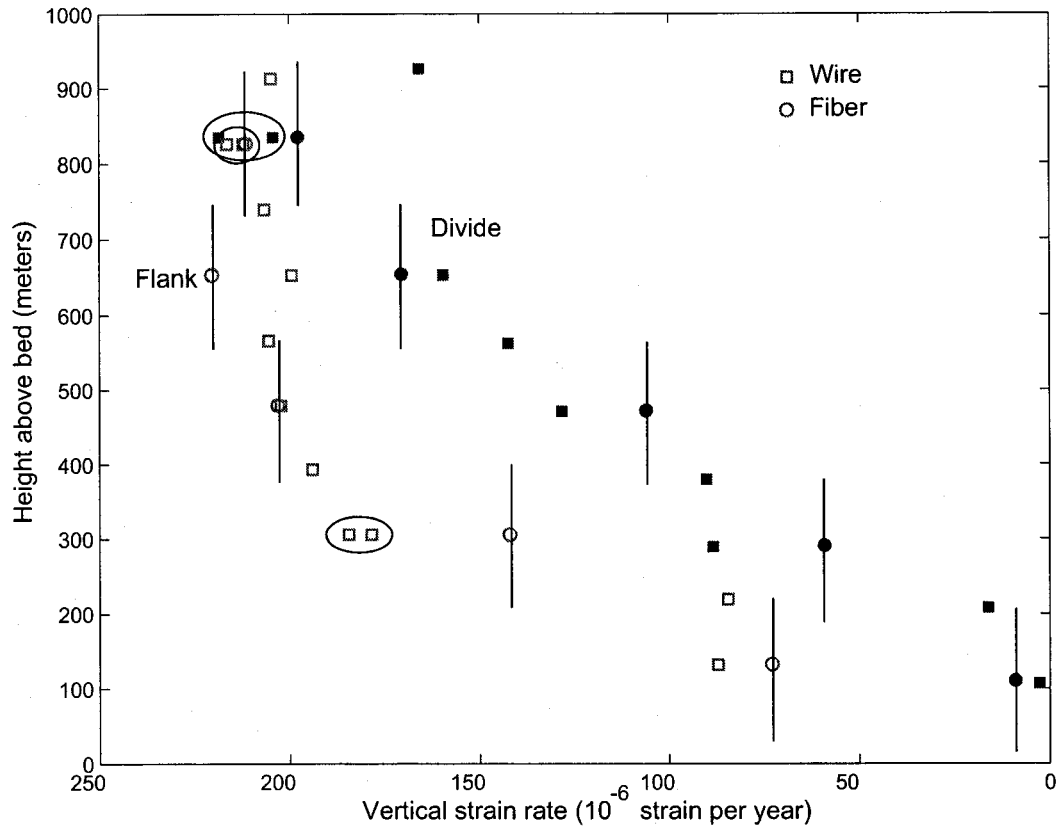


Figure 6.7: Data from the wire-resistance and fiber-optic strain gauges. Circles identify fiber data, squares identify wire data. The open symbols are flank site measurements, while the closed symbols are from the divide. The vertical bars represent the effective strain-gauge length for the fiber-optic instruments. The $1-\sigma$ errors for each gauges are less than $10 \times 10^{-6} \text{ a}^{-1}$; for most instruments, the error is smaller than the size of the symbol. The three pairs of circles data points are redundant wire gauges. The spread of these data represent the possible inhomogeneities in the ice on a scale of less than 10 meters.

are large spatial gradients in ice properties. At three points, we installed two gauges within 10 meters of each other to observe this variability in the data. The results for both gauges are shown in Figure 6.7; each pair of redundant gauges is circled. Observations from thin sections suggest that structural variability exists (Richard Alley and Larry Wilen, personal communication, 2003), but it is difficult to quantify with the available data, and the effect on the flow is not well understood.

There are three corrections applied to the wire data. First, the correction for horizontal shear (Appendix C) applies to the wires as well as the fibers; it is larger for the wires than for the fibers. It applies primarily to the deepest 4 wire instruments.

Second, compared to the fiber strain-rate data, the raw wire strain-rate data show a systematic offset of about 12% at the divide and 16% at the flank. According to *Elsberg et al.* [in review], this is a result of unexpected coupling between the wire anchor and the bridge casing during the freeze-in process, that may increase the effective gauge length by 5 to 25%. Here, we report the adjusted data. We assume a random error in this correction factor of 2% and add it (in quadrature) to the overall uncertainty for the instruments.

The final correction involves only the uppermost wire and fiber instruments. Near the surface, the firn undergoes densification. Most, but not all, of this densification happens in the upper 80 meters. Therefore, the wire gauge installed at 80 meters deep recorded some measurable vertical strain rate due to densification of the ice. Densification also affected the uppermost fiber gauge, but the error introduced is much smaller.

We calculate the rate of densification from the measured density profile (Joan Fitzpatrick, personal communication, 2003) and the measured depth-age scale [*Taylor et al.*, accepted]:

$$\dot{\epsilon}_{\text{dens}}(z) = \frac{1}{\rho(z)} \frac{d\rho}{dz} \frac{dz}{dt}. \quad (6.8)$$

where ρ is the density at depth z and dz/dt is derived from the depth-age scale. The two types of instruments have finite gauge lengths. To find the correction factor for each instrument, we average the strain rate due to densification over the gauge length (1 m for the wire instruments and about 180 m for the fiber instruments). This correction factor has a stronger gradient at 80 meters depth than deeper in the ice column. At that depth it

is sensitive to errors in the density profile, the depth–age scale, and the depth and effective gauge length of the wire instruments. In Figure 6.7 we present the corrected data. It appears, however, that this calculation has over-corrected the 80 m wire gauge at the divide by 20 to $30 \times 10^{-6} \text{ } \epsilon \text{ a}^{-1}$, and it may have over-corrected the flank 80 m instrument by a smaller amount. Because of the large uncertainty associated with this correction factor, we have given less weight to these data points in our model assessment.

6.7 The Inverse Problem

Our goal in this case study is to determine the relative importance of deformation due to anisotropy and deformation associated with a transition to a more-linear viscosity at low stress. We model the stress field and strain-rate field in a cross section across Siple Dome, using measured geometry, accumulation rate, temperature field, and ice properties as inputs. The ice flow law used in the model has an isotropic component and an anisotropic component. The isotropic flow law includes a linear term and a nonlinear term. The anisotropic component describes the effect of vertically oriented crystal fabric.

There are four unknown flow-law parameters. The crossover stress, k defines the relative importance of the linear term. If $k = 0$, nonlinear flow mechanisms dominate deformation. We assume k is spatially constant; although, as defined in Equation 6.3, it can vary with temperature and other ice properties [see *Pettit and Waddington*, in press, and Chapter 2 for more details]. The other three unknowns are the three enhancement factors (E_1 , E_2 , and E_3) for the three layers shown in Figure 6.5 (Holocene, ice-age, and recrystallized ice, respectively). This factor includes enhancements due to grain size and impurities, as well as the overall magnitude (but not the spatial pattern) of the anisotropic deformation. An enhancement factor equal to unity defines clean, isotropic, Holocene ice, as recommended by *Paterson* [1994]; as such, we expect our E_1 to be close to 1.

We determine the best model parameters such that the strain-rate field calculated by from the model matches the strain rates measured by the fiber-optic and wire-resistance strain meters. The forward model is finite element model that requires significant computer time. This precludes the use of formal inverse theory techniques. Instead, we explored the

4-D parameter space systematically. We start with a coarse grid spanning the maximum expected extent of parameter values, and narrow the grid spacing with successive series of model runs.

The model calculates horizontal- and vertical-velocity fields. For the divide and flank positions, we determined the vertical strain-rate profiles by taking the derivative with respect to depth of the vertical-velocity profile ($\dot{\epsilon} = dw/dz$). To determine the best models, we selected the strain-rate profiles that were the smoothest, yet still maintain the structure reflected by the gradients in ice properties. We choose a smooth model because in a real ice sheet, strong gradients in the strain rate would be moderated by redistribution of the stress.

We defined a misfit function to determine which models fit the data to within the uncertainties:

$$J = \frac{1}{T - p} \sum_{j=1}^T w_j \frac{(s_j^m - s_j^d)^2}{\epsilon_j^2}. \quad (6.9)$$

s_j^d and s_j^m are the measured data and the corresponding model outputs, respectively. ϵ_j are the uncertainties in the data. w_j is a weighting function designed to give more weight to important data. (Although we tested several weighting functions, we ultimately used $w_j = 1$ for all but the uppermost wire strain gauges, where $w_j = 0$.) T is the number of data points, and p is one less than the degrees of freedom. In this formulation a misfit index less than unity fits the data within one standard deviation, and a misfit of $J = 2$ fits the data within two standard deviations.

The primary data are the measured strain rates from both the wire-resistance and the fiber-optic strain gauges, but we also include in our misfit index the difference between the gauges installed at the divide and those installed at the flank because that difference is sensitive to the linear term in the flow law [Waddington *et al.*, 1996; Pettit and Waddington, in press]. The calculated horizontal velocities at the surface are much less sensitive to the deformation at depth in the ice sheet than is the strain rate profile. We included velocity measurements in some misfit calculations, but not in these presented here; their impact on the choice of best models was negligible.

6.8 Results and Discussion

Figure 6.8 shows the misfit index for the four-dimensional parameter space in the region with the best solution. Each row of plots has a different crossover stress; each column has a different Holocene enhancement factor. Each small plot is $J(E_2, E_3)$. Dark areas show regions where the misfit index is $J < 3$. The thin black curve outlines the region within which the misfit index is $J < 2$ (none of the models has a misfit index $J < 1$). White areas reflect larger misfit indices (in most cases) or non-existent data.

The pattern of dark areas shows the resolution of our model. All of the models that produce misfit indices less than two are valid models, and without more data we cannot choose a best model among them. We chose a model that is in the center of the cluster of valid models on which to focus our discussion:

$$\text{Crossover Stress } k = 0.22(\pm 0.1)\text{bar} \quad (6.10)$$

$$\text{Holocene Ice } E_1 = 1.3(\pm 0.2) \quad (6.11)$$

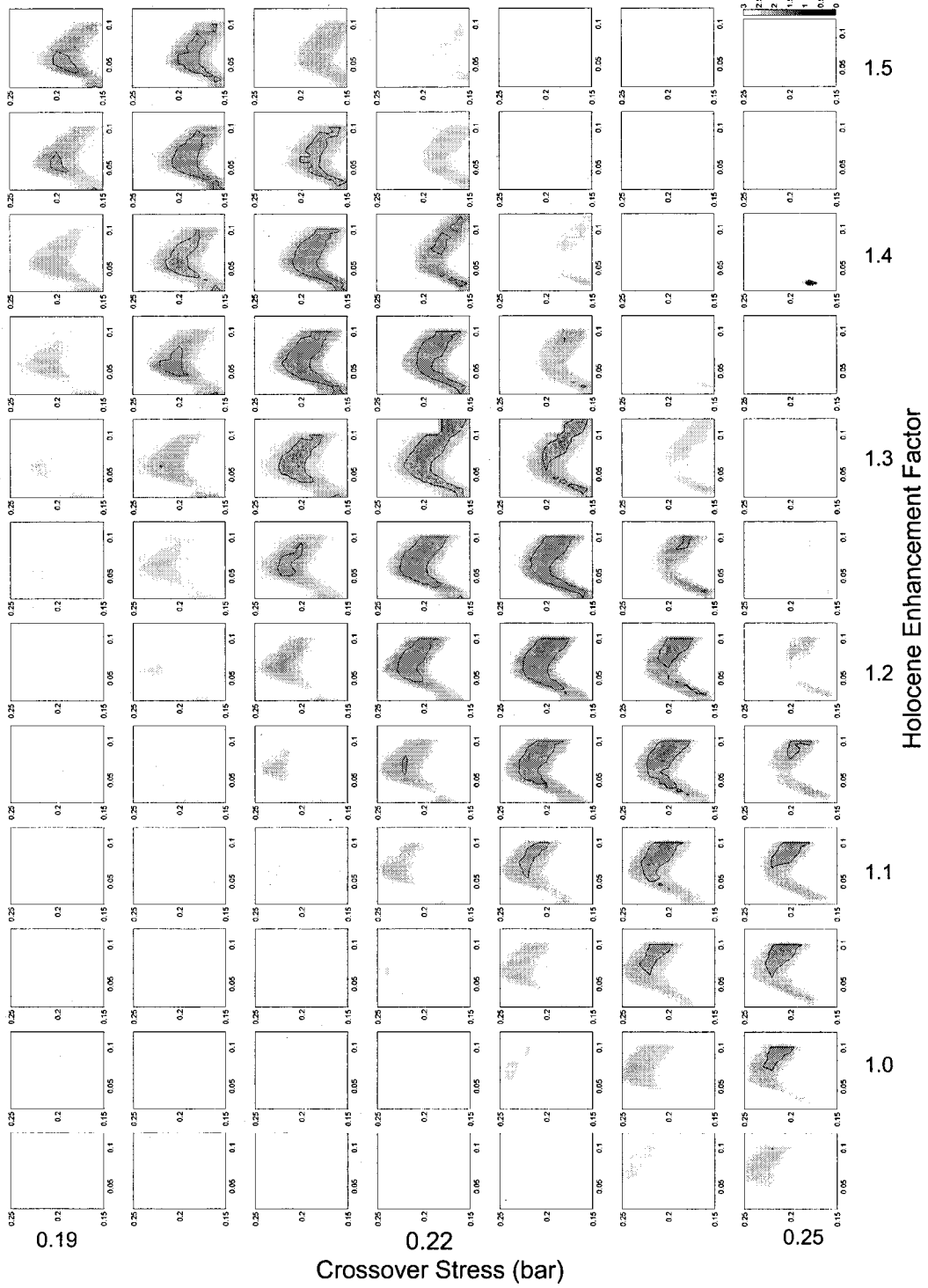
$$\text{Ice - Age Ice } E_2 = 0.06(\pm 0.03) \quad (6.12)$$

$$\text{Recrystallized Ice } E_3 = 0.20(\pm 0.04) \quad (6.13)$$

where the values in parentheses are the approximate resolution of our solution. It is important to reiterate here that this model accounts for anisotropy explicitly through the cone angle, so these enhancement factors reflect softening or stiffening due to impurities, grain size, or other related effects, but not softening or stiffening due to anisotropy.

The flank and divide strain-rate profiles for this model are shown in Figure 6.9. They are generally smooth, but maintain structure in the regions where there are large gradients in the ice properties. The profiles follow the pattern expressed by the fiber data (vertical bars) throughout most of the depth of the ice sheet. Only the divide profile fails to capture the deformation measured by the lowermost fiber data. The modelled profiles fit the wire data less well, most likely due to small-scale (<10 m) inhomogeneities in the ice. This is supported by the observation that the largest disagreements between the model and the

Figure 6.8: Misfit index describing the model results for the four-dimensional parameter space. Although we have explored the parameter space outside the range shown here, we show only the region near the best solution. Each row of plots has a different crossover stress (from 0.19 to 0.25 bar). Each column has a different Holocene enhancement factor (0.95 to 1.5). Each small plot has E_2 on the x-axis and E_3 on the y axis. The scale for shading is 0 black to 3 white. Most of the white areas have a misfit index much larger than 3; in a few places the white is missing data.



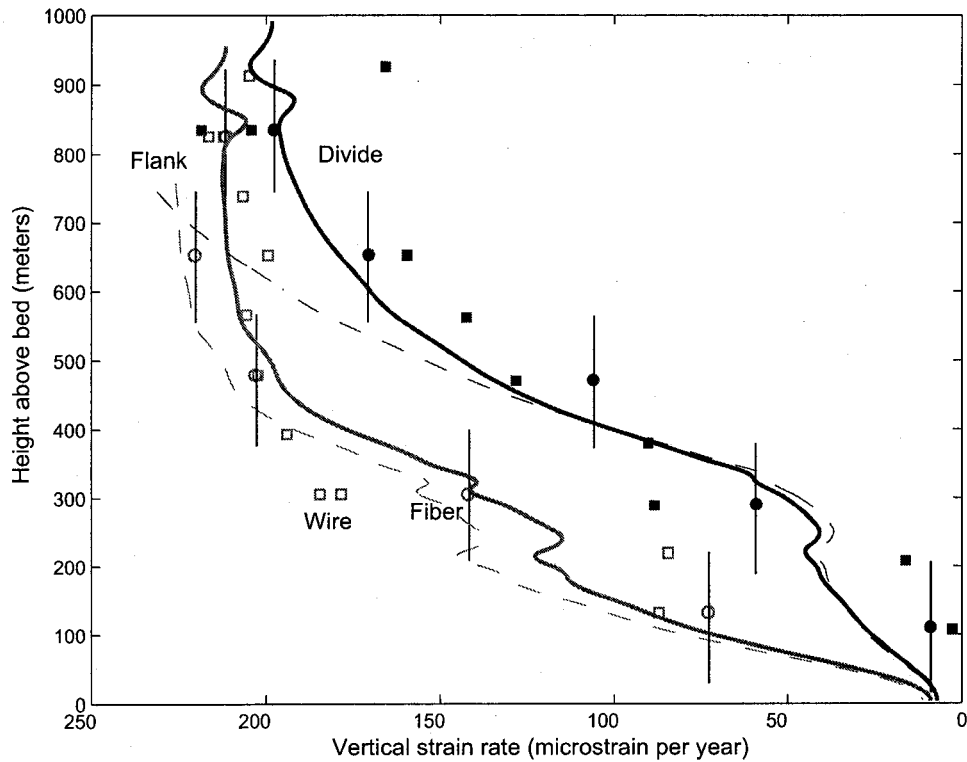


Figure 6.9: Flank and divide strain-rate profiles for solution shown in Equation 6.13. The data are from Figure 6.7. The thick solid lines are the best-fitting model results. The thin dashed lines result from the same model parameters but a surface profile that is in balance with the accumulation rate derived from the radar internal layers (see discussion in text).

wire data occur in and near the band of tight fabric.

Near the bed at the divide the model predicts much larger deformation rates than the instruments measure. Decreasing the enhancement factor for the recrystallized ice layer (E_3) results in stiffer ice and smaller deformation rates in that region, better fitting those data, but the model then fails to fit the data in the upper layers. What may be required for the model to fit all the data is an increase in the effect of anisotropy. This could be driven by horizontal variation in the cone angle profile. As the ice undergoes deformation, the fabric should tighten with distance from the divide. This would increase the flank-divide difference in the lowest layers and possibly result in a better fitting model.

In Figure 6.10 we show qualitatively the sensitivity of the model to each input parameter, providing a sense for the influence of each parameter on the flow. In each graph, the dashed curves are the best fitting model result (Equations (6.10) through (6.13)). The solid line is the same model except for a change in one input parameter. Figure 6.10a show that the crossover stress controls the separation between the flank and the divide profiles. This difference is key to the special divide flow pattern that causes a Raymond bump to evolve over time. A divide dominated by the linear term in the flow law ($k \gg 1$ bar) has no Raymond bump and little difference between the divide and flank vertical strain-rate profiles [Pettit and Waddington, in press, and Chapter 2]. Anisotropy also plays a role in the difference between the divide and flank profiles. If our model were isotropic, a different value of the crossover stress would best fit the data.

The three enhancement factors control the isotropic bulk softness of each layer of ice (but not the directionally dependent anisotropic softness pattern). These are shown in Figure 6.10. Since ice flow in the upper part of the ice sheet depends on the shear deformation lower in the ice sheet, and, conversely, the deformation of the lower part of the ice sheet depends on the softness in the upper part of the ice sheet (through longitudinal stresses), a change in any one of the three enhancement factors affects flow throughout the depth of the ice.

The enhancement factors that we find in this analysis have physical implications for the ice flow. The Holocene enhancement factor, $E_1 = 1.3$, implies that the upper part of the ice sheet is about 30% softer than the softness parameter suggested by Paterson [1994]. The lower two layers have much smaller enhancements, implying that the ice at depth is much stiffer than Holocene ice. Thorsteinsson *et al.* [1999] found a similar result for the deformation of the Dye 3 borehole in Greenland (they separated the softness due to anisotropy from the overall enhancement factor). It is unclear why this deeper ice may be stiffer, but there are several possible reasons. The deepest ice has large interlocking crystals. During deformation, grain boundary migration allows these interlocked grains to move with respect to each other, but the migration process may be slow, so as to create “drag” in the flow. Ice-age ice also has a different level of impurities, which may act to hinder flow, but since impurities typically enhance flow, the stiffness of this ice remains a

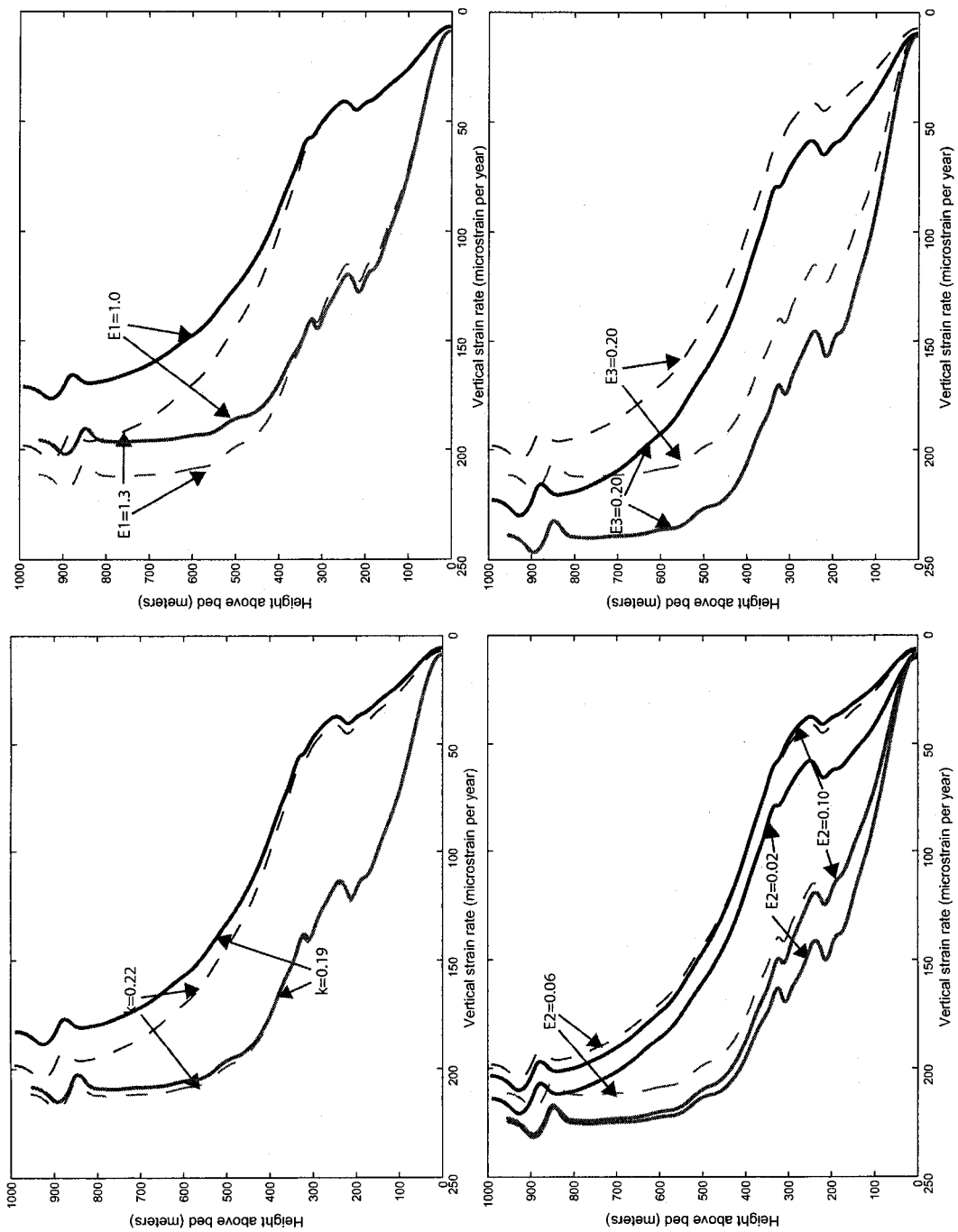


Figure 6.10: Sensitivity of the models to the four model parameters. The model is nonlinear; therefore, these are local sensitivities in the region near the best solution. In the lower left figure, the enhancement of the band of tight fabric produces a nonlinear response in the strain rate; therefore, we show curves from both above and below the best fitting model.

puzzle.

With only four adjustable parameters in our model, we are limited in how much detail about the flow we can deduce. A more complete analysis would allow k and E to be functions of depth, and E would be further split into a linear-term enhancement factor and a nonlinear-term enhancement factor. Resolving these functions, however, would not only require much more intense computing, but also a more comprehensive data set.

In this analysis, the finite-element model calculates the modern deformation rates based on the present geometry and the measured ice properties. This calculation does not involve time evolution. Nor does it explicitly rely on an assumption of steady state. It is useful, however, to run the model using the best-fitting parameters (Equation (6.13)) through time and allow the surface to evolve until the flow is in balance with the accumulation rate pattern. In Chapter 5, our measurements show that Siple Dome has been in steady state for several thousand years. The thin dashed curves in Figure 6.9 show these model results, and Figure 6.11 shows the horizontal and vertical velocity fields. Although close, there is a measurable difference between the modelled vertical strain rates (Figure 6.9), particularly in the upper part of the ice sheet. There is some error, therefore, in our assumptions that the dome is not thinning or thickening, that our accumulation pattern is realistic, and that the divide flows primarily in 2D plane strain (the first two assumptions apply to the time-evolved version of the model, the third applies to both versions of the model). Without further data we cannot determine the dominant source of imbalance in our model.

The horizontal velocity field (Figure 6.11) has an interesting kink in it about 300 above the bed. This kink is a result of the strong vertical fabric of the ice-age ice. Because this layer is soft in horizontal shearing, shear strain is concentrated within this layer instead of near the base of the ice sheet. Although not stagnant, the ice below this layer supports less shear stress and, therefore, deforms less than it would in a normal ice sheet. We call this the false-bed effect, it was first suggested in analyses of flow properties and crystal fabric in the ice core at Law Dome [*Russell-Head and Budd, 1979*].

It is also interesting to compare these results with the internal structure imaged by radar shown in Figure 6.2. The inferred isochrones from the model (Figure 6.12) assume

that Siple Dome has been in steady state since the deepest layer was deposited. In reality, the history of Siple Dome is reflected in its internal-layer structure. *Nereson et al.* [1998b] used these radar layers to show that Siple Dome migrated slowly at least 700 m towards Bindschadler Ice Stream over the last several thousand years. It may still be migrating. Also, the dome probably had lower accumulation rates during the ice age. It is valuable, however, to compare the isochrones predicted by the steady-state model with those observed. For the top half of the ice sheet, the arch in the predicted isochrones is generally broader, but does not have a significantly larger amplitude than the observed layers. The radar-image layers are steeper on the northward side than the modelled steady-state layers. *Nereson and Waddington* [2002] predict this in their study of migrating divides. The deeper layers, which show the greatest effect of anisotropy in the ice in the model, were not detected by radar, and therefore, are not available for comparison.

6.9 Conclusions and Implications for Other Ice Divides

The results of this analysis provide insight into the deformation of ice near an ice divide. Our initial goals in this study were twofold. First, we wanted to determine the importance of a linear term introduced into the nonlinear Glen's flow law. Second, we wanted to explore the effect of the unique pattern of crystal orientations at Siple Dome.

6.9.1 Linear creep mechanisms

In Chapter 4, we showed theoretically that a crystal fabric similar to that seen at Siple Dome can have a dramatic effect on divide flow and can produce a much larger Raymond bump than the isotropic, nonlinear Glen's flow law alone. The amplitude of the Raymond bump imaged by ice-penetrating radar (Figure 6.2) for Siple Dome is smaller than predicted when using an anisotropic nonlinear flow law, implying that the effects of anisotropy must be moderated by other processes. One such process is the increased activity of linear or near-linear creep mechanisms at low stresses relative to the non-linear creep mechanisms (all deformation slows at low stress, it's the relative activity of the mechanisms that is important). In the models presented here, we used a two-term flow law, with a crossover

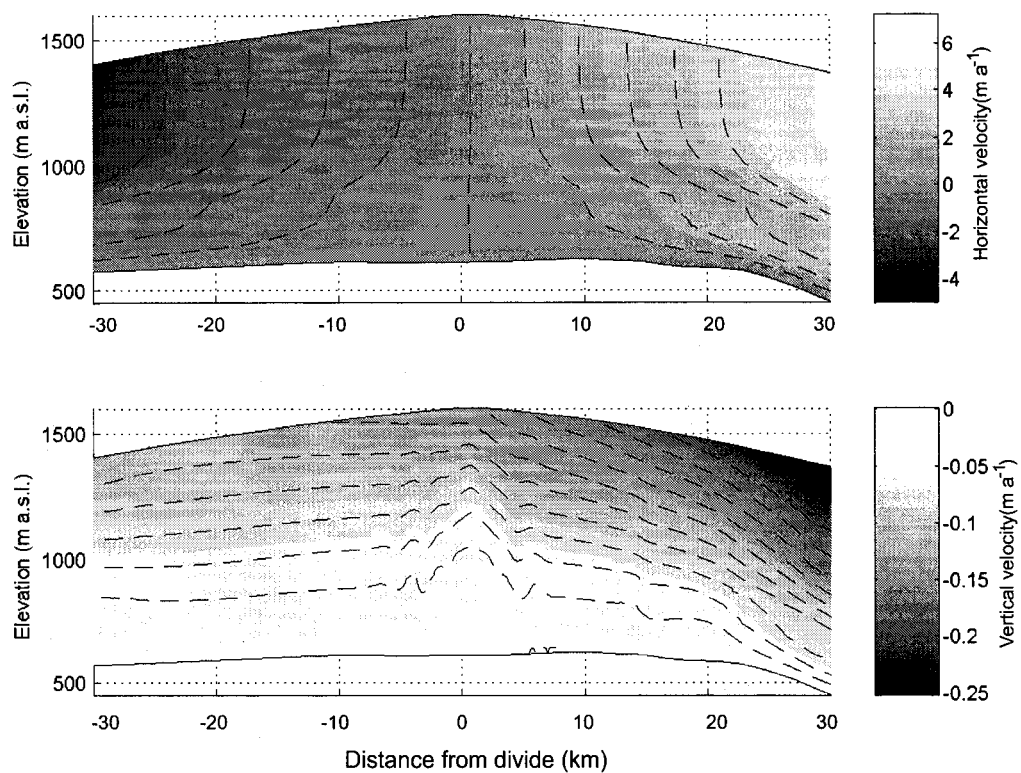


Figure 6.11: Velocity fields from the best fitting model using a surface profile that is in balance with the accumulation rate derived from the radar internal layers. Bindschadler Ice Stream is to the right and Kamb Ice Stream is to the left. The dashed lines are velocity contours. Note the kink in the horizontal velocity contours which results from the false-bed effect (see text).

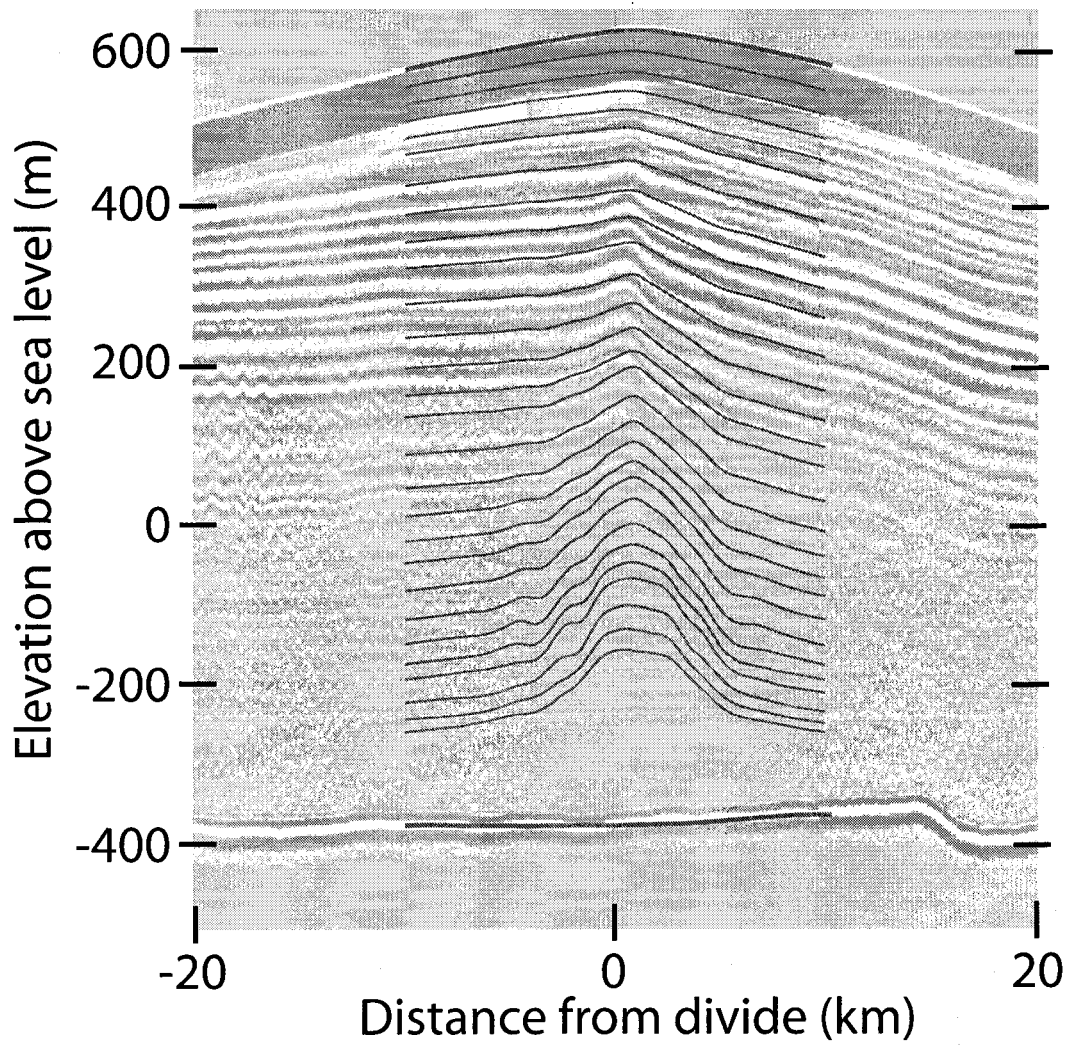


Figure 6.12: Isochrones inferred from the best-fitting model (Figure 6.9) overlaid on the ice-penetrating radar data shown in Figure 6.2.

stress, k , defined as the stress at which the linear and Glen terms contribute equally to the strain rate.

The form of the flow law reflects the nature of ice, not the geometry of the ice sheet in which the ice flows. The crossover stress is, in a sense, an intrinsic property of ice, which may depend on temperature, grain size, and impurity content, as defined in Equation 6.3, but not on geometry or boundary conditions of the ice sheet. In general, however, the value we determined as best-fitting for Siple Dome, $k = 0.22$ bar is applicable to other divides as well. This result agrees with a study on Taylor Dome [Morse, 1997] that used velocities measured on an extended surface strain network as the primary data set. Our best-fitting value for the crossover stress is dependent on the divide migration rate that we used in modelling the temperature field (Figure 6.4). A smaller migration rate would require a larger crossover stress to fit the data (more active linear creep mechanisms).

A first step in modelling the divide region of an ice sheet more accurately would be to use the flow law suggested here (Equation 6.1 with $k = 0.22$). An important point that we show in this study, however, is the large effect of anisotropy on the flow, that modifies the effect of the linear creep mechanisms in the divide region.

6.9.2 *Crystal fabric*

Compared to other divides, the crystal fabric at Siple Dome appears to have stronger vertical gradients. The sharp vertical transition in the fabric from a cone angle of over 30° to under 5° occurs within 16 meters of ice and creates a “false bed” effect (described in more detail in Chapter 4). Shear strain on the flank of the ice sheet is concentrated in this band of ice, since its crystals are aligned for easy deformation in shear. It follows that the vertical compressive stresses reflect this false bed by concentrating the vertical strain higher in the ice column than in an isotropic ice sheet (Figure 6.9). This will affect accumulation-rate histories derived from depth-age scales.

Strong crystal fabrics, such as that at Siple Dome, are not uncommon in ice sheets. The sonic logs for both GRIP and GISP2 boreholes in Greenland, also show fabric with less than 5° cone angles (Throstur Thorsteinsson, personal communication, 2003), but there are no sharp transitions in cone angle in those profiles. In Chapter 4, we show that fabrics

with cone angles greater than 30° do not measurably impact modelled ice flow compared to the isotropic case, whereas fabrics tighter than 20° have significant effect on ice flow. To accurately model ice flow, therefore, a sonic log or other measure of anisotropy is essential.

6.9.3 Other divides

None of the analysis presented here hints at the reason that a dome such as Siple Dome should have such a crystal fabric. Indeed, it is intriguing and many other puzzling results are coming from analysis of the Siple Dome ice core [*Taylor et al.*, in prep] hint that Siple Dome may have an uncommon history. It is possible, that Siple Dome is representative of small ice sheets. There are no other small ice sheets for which we have such extensive data. Radar cross sections exist for Roosevelt Island *Conway et al.* [1999] and Fletcher Promontory *Vaughan et al.* [1999], for example, but no accompanying sonic logs. The larger divides where radar data exist (Greenland [*Jacobel and Hodge*, 1995], Inland WAIS [*Conway et al.*, 2003], Dome Fuji [*Fujita et al.*, 1999], for example), do not show evidence of a Raymond bump in the radar profile.

There are several reasons why a divide may not form a Raymond bump. First, it may have wandered over its history, smoothing out the divide flow pattern [*Marshall and Cuffey*, 2000]. Second, the stresses within the ice may be low enough that the linear term dominates flow [*Pettit and Waddington*, in press]. Third the base of the ice sheet may be sliding [*Pettit et al.*, 2002]. And fourth, in Chapter 4 we showed that strong anisotropy coupled with a nonlinear flow law produces the largest bumps. The amplitude of Raymond bumps under divides without strong anisotropy will generally be smaller than those with strong anisotropy.

For large ice sheets, such as Greenland, another factor may play a role. The divide-flow pattern does not scale directly with ice-sheet thickness. Greenland and Siple Dome have similar characteristic response times ($\tau = H/\dot{b}$, for Greenland $\tau = 3000/0.3 = 9 \text{ k a}^{-1}$ and for Siple Dome $\tau = 1000/0.12 = 8 \text{ k a}^{-1}$). Continuity requires that the ice flux past a point must equal the accumulated snow upstream:

$$\bar{u}H = \dot{b}x \tag{6.14}$$

. At one ice thickness from the divide, $x = H$, the average velocity equals the accumulation rate. Thus, for equal response times the ice flux at one ice thickness is $\dot{b}H$, a much large flux for a larger ice sheet. In a larger ice sheet, the ice moves more quickly through the "divide zone" (within about two ice-thicknesses of the divide). This implies that a thicker divide is more sensitive to perturbations in boundary conditions than a smaller divide; therefore, it may wander more easily, dampening the Raymond bump.

Chapter 7

CONCLUSION

This study of ice divide dynamics is part of the larger question of how ice sheets respond to changing climate. Past environmental boundary conditions (from temperature to accumulation of snow on its surface to fluctuations of a nearby ice stream) leave an imprint on the structure and properties of ice within an ice sheet. For example, the temperature field reflects past flow as well as temperature, the grain size and crystal orientation reflect past deformation, and the annual layering reflects past flow patterns and accumulation rates. Understanding the process by which these histories are recorded in the ice permits the inversion of modern structure and behavior for historical environmental patterns.

In this dissertation, I used the dynamic behavior of ice divides, both modelled and measured, to investigate the constitutive relationship between applied stress and deformation rate of the ice, given the ice properties and the modern boundary conditions. Chapters 2 through 4 are numerical modelling studies of ideal ice divides, focusing on the effect of low deviatoric stress, basal sliding, and crystal anisotropy on the special divide flow pattern. Ultimately, I bring these theoretical findings together with observations and inferences from other studies in a study of Siple Dome. The results not only impact the local and regional history of Siple Dome and the interpretation of the Siple Dome ice core, but also constrain the parameters of a flow law for ice that is applicable to other ice sheets. My conclusions and questions for future research fall into three categories: the constitutive relation for ice, sliding or deformable till as a basal boundary condition under an ice divide, and the local and regional history of Siple Dome.

7.1 A Flow Law for Ice

Ice deformation is inherently a small-scale process. Each grain deforms according to the stresses it experiences in its immediate surroundings. Large-scale ice deformation is the accumulation of many grain-scale deformations, with feedback processes that distribute the stress and deformation in order to minimize internal energy stored as flaws in the crystal structure. Many researchers have measured or modelled the deformation of small blocks of ice in the laboratory and inferred small-scale flow laws. Many others have measured flow of ice sheets and inferred large-scale flow laws.

In Chapter 2, I extrapolate knowledge of small-scale flow to ice-sheet scale flow in a way that is useful for ice flow modelling. This reformulated flow law (Equation (2.7)) contains a linear term that dominates at low deviatoric stress. The inclusion of the linear term is necessary because at low deviatoric stresses, the dominant micro-scale mechanism for ice deformation most likely changes to one that is more linear. The crossover stress is the stress at which the linear and Glen terms contribute equally to the strain rate; it is a function of ice properties, independent of the geometry of the ice sheet. This linear term will be important for ice sheet modelling only for ice sheets with effective deviatoric stresses smaller than or equal to the crossover stress ($\Omega \leq 1$).

I present a series of models for three idealized ice divides with different characteristic stresses. These show that when the linear term dominates, the special divide flow pattern disappears and no Raymond bump forms in the isochrones. This flow pattern results in a different depth-age scale, with younger ice deeper in the ice column, when compared to a more conventional Glen divide.

In order to move from modelling ideal divides to investigating the flow of real divides, I needed to assess the effect of anisotropy on the ice-divide flow pattern. Based on *Thorsteinsson* [2001], in Chapter 4, I used an isotropic finite-element model coupled with an analytic representation of anisotropic ice flow of an ideal ice sheet. I showed that a vertically symmetric preferred crystal orientation interacts with the divide stress pattern (dominated by pure shear at the divide and by simple shear on the flanks), to produce a flow pattern similar to that produced by nonlinear isotropic constitutive relation. When

nonlinear rheological properties are coupled with a strongly anisotropic fabric, the Raymond bump is enlarged. Interestingly, the effect of anisotropy is limited to situations where the nonlinear term in the flow law is dominant. Crystal fabric has little effect when the linear term dominates deformation rate.

After exploring theoretically in Chapters 2 and 4 the effect of a two-term anisotropic flow law on flow near an ice divide, in Chapter 6, I use measured deformation data from Siple Dome to determine the relative importance of these two processes. I find that both are important to flow at Siple Dome. The crystal fabric is strong enough to induce a large increase in the Raymond bump as compared to the isotropic flow pattern. To fit the measured strain-rate data, the linear term must be active to effectively soften the ice that is stiffened by the alignment of crystals. We found that a crossover stress of 0.22 bar is necessary to fit the measurements at Siple Dome, and that may be an underestimate if the divide is not migrating as fast as we assumed.

7.2 Basal Boundary Conditions

In Chapter 3 I took a step away from the details of the constitutive law for ice to look at the effect of a sliding boundary condition on the pattern of flow at an ice divide. Although Siple Dome is presently frozen to its bed, it is possible that it had a wet bed and was sliding in the past (if it were significantly thicker during the last ice age, for example). Other divides may have a wet bed presently.

I modelled basal sliding for ideal divides with a layer of linearly-viscous till at the ice-rock interface in the finite-element model. The amount of sliding is controlled by the effective viscosity of the till layer. The details of this constitutive relation for till in most cases are not significant because the motion is limited by longitudinal stretching of the ice rather than by shearing of the till layer.

Model results show that basal sliding tends to redistribute the longitudinal stresses within the ice. A small amount of sliding can have a significant effect on the stress pattern. When all of the ice flux is carried by sliding, the longitudinal stresses are uniformly distributed with depth and the ice near the divide behaves more like a spreading ice shelf

with a horizontal velocity that is uniform over the depth. Isochrones are flat and the ice at a given depth is younger compared to the frozen bed model.

This model relies on the assumption that the till layer (or thin water layer) beneath a sliding divide will always have an effective viscosity that is less than the viscosity of the ice at all horizontal positions. This assumption leaves out the case where the till/water layer is highly nonlinear. A plastic till layer defined with a yield stress could be more stiff than the ice (mimicking a frozen divide) for a finite distance from the divide, then be much softer than the ice on the flanks. The resulting flow pattern within the ice would depend on the yield stress in the till layer.

A major conclusion from this study of sliding under ice divides is that the history of basal sliding is an important factor in the interpretation of deformation measurements and radar images near an ice divide. A divide that was sliding, then froze will reflect this in its Raymond bump pattern; similar in character to the isochrones produced when a 'new' divide appears as an ice sheet thins. For example, the isochrone pattern is not sufficient to say that Roosevelt Island is a new divide or an older divide that froze to its bed [*Conway et al.*, 1999]

7.3 Siple Dome, West Antarctica

The goal of Chapter 5 was to answer the question: "Is Siple Dome in Steady State?" and to examine the constraints the answer puts on the local dynamics and regional deglaciation history.

The answer is Yes, at least within about 10 ice-thicknesses from the divide. I compared results from three independent methods of measuring the vertical surface motion. None of the three could detect significant surface imbalance within 10 km of the divide; to within the uncertainties of the methods, the surface is lowering at the same rate as snow is accumulating. The uncertainties in these methods restrict the resolution to thinning rates greater than about 2.5 cm a^{-1} . Assuming a maximum modern thinning of 2.5 cm a^{-1} , the dome could not have been more than about 40 meters thicker 2 to 3 ka BP. At 30 km from the divide there is some measurable thinning.

This result has two main implications. First, if Siple Dome has been a dome for 10 ka and in steady state for two to three thousand years, then the ice streams that flank it, Kamb and the Bindshadler Ice Streams, must change their behavior on timescales either longer than 1 to 2 ka or shorter than about 300 a, the time it takes the divide to notice and record a change in the boundary conditions. Also, the apparent stability of the divide implies that the ice streams are somewhat coherent in their behavior (if one ice stream thickened and the other thinned, then the divide would move one way or the other more quickly than is evident in the radar images). This is an intriguing result considering that Kamb Ice Stream stopped flowing fast less than 200 years ago. Either events like these occur rarely so that memory of older ice stream stoppage events has been lost or they exhibit short-period fluctuations that are not recorded in the slower-responding divide.

In Chapter 6, I explored the pattern of flow in the divide zone. The profile of sonic velocity from the borehole reveals a band of ice between 680 and 810 m depth that has very strong vertically symmetric fabric. My flow models and the vertical strain-rate measurements show that this band of ice acts as a false bed, with much of the deformation happening within and above this band of ice, instead of in the warmer ice below it. The observed and predicted isochrones (Figure 6.12) match reasonably well in the upper layers, but the large arch in the isochrones predicted by my model are not seen in the real divide. This is most likely because the layer of tight fabric was thicker and higher up in the ice column (if it is ice-age ice), and its effect on the flow field had a distinctly different character.

This effect of this layer on the flow pattern is intriguing enough, but it leads to the questions: How did it form with such distinct upper and lower transitions in the first place? How does the transition compare with transitions in other properties of the ice? How has it evolved over time? Do other small ice caps have a similar layer? Do any large ice sheets exhibit similar crystal fabrics?

BIBLIOGRAPHY

- Alley, R., A. Gow, D. Meese, J. Fitzpatrick, E. Waddington, and J. Bolzan, Grain-scale processes, folding, and stratigraphic disturbance in the gisp2 ice core, *Journal of Geophysical Research*, 102(C12), 26818–26830, 1997.
- Alley, R. B., Flow-law hypotheses for ice-sheet modeling, *Journal of Glaciology*, 38(129), 245–256, 1992.
- Alley, R. B., and R. A. Bindschadler, eds., *The West Antarctic Ice Sheet: Behavior and Environment*, American Geophysical Union, 2001.
- Anandakrishnan, S., and R. B. Alley, Stagnation of Ice Stream C, West Antarctica by water piracy, *Geophysical Research Letters*, 24(3), 265–268, 1997.
- Azuma, N., A flow law for anisotropic ice and its application to ice sheets, *Earth and Planetary Science Letters*, 128(3–4), 601–614, 1994.
- Azuma, N., and K. Goto-Azuma, An anisotropic flow law for ice-sheet ice and its implications, *Annals of Glaciology*, 23, 202–208, 1996.
- Bindschadler, R., and P. Vornberger, Changes in the West Antarctic Ice Sheet since 1963 from declassified satellite photography, *Science*, 279, 689–692, 1998.
- Bindschadler, R., P. Vornberger, D. Blankenship, T. Scambos, and R. Jacobel, Surface velocity and mass balance of Ice Streams D and E, West Antarctica, *Journal of Glaciology*, 42(142), 461–475, 2002.
- Bromwich, D. H., Snowfall in high southern latitudes, *Reviews of Geophysics*, 26(1), 149–168, 1988.
- Budd, W. F., and T. H. Jacka, A review of ice rheology for ice sheet modeling, *Cold Regions Science and Technology*, 16, 107–144, 1989.
- Budd, W. F., N. W. Young, and C. R. Austin, Measured and computed temperature distributions in the Law Dome ice cap, Antarctica, *Journal of Glaciology*, 16(74), 99–110, 1976.
- Castelnaud, O., P. Duval, R. A. Lebensohn, and G. R. Canova, Viscoplastic modeling of texture development in polycrystalline ice with a self-consistent approach: comparison with bound estimates, *Journal of Geophysical Research*, 101(B6), 13851–13868, 1996.

- Castelnau, O., H. Shoji, A. Mangeney, H. Milsch, P. Duval, A. Miyamoto, K. Kawada, and O. Watanabe, Anisotropic behavior of GRIP icers and flow in Central Greenland, *Earth and Planetary Science Letters*, 154(1–4), 307–322, 1998.
- Colbeck, S. C., and R. J. Evans, Flow law of temperate glacier ice, *Journal of Glaciology*, 12(64), 71–86, 1973.
- Conway, H., B. L. Hall, G. H. Denton, A. M. Gades, and E. D. Waddington, Past and future grounding-line retreat of the West Antarctic Ice Sheet, *Science*, 286(5438), 280–283, 1999.
- Conway, H., G. Catania, C. F. Raymond, A. M. Gades, T. A. Scambos, and H. Engelhardt, Switch of flow direction in an antarctic ice stream, *Nature*, 419, 465–467, 2002.
- Conway, H., T. Neumann, E. Waddington, G. Catania, E. Pettit, F. Ng, and D. Morse., Climate and thickness history near the divide between the Ross and Amundsen Seas, *10th Annual West Antarctic Ice Sheet Workshop*, 2003, abstract.
- Cuffey, K. M., Glaciological investigations beneath an active polar glacier, Ph.D. thesis, University of Washington, 1999.
- Cuffey, K. M., H. Conway, A. Gades, B. Hallet, C. F. Raymond, and S. Whitlow, Deformation properties of subfreezing glacier ice: role of crystal size, chemical impurities, and rock particles inferred from in situ measurements, *Journal of Geophysical Research*, 105(B12), 27895–27915, 2000a.
- Cuffey, K. M., T. Thorsteinsson, and E. D. Waddington, A renewed argument for crystal size control of ice sheet strain rates, *Journal of Geophysical Research*, 105(B12), 27889–27894, 2000b.
- Dahl-Jensen, D., and N. S. Gundestrup, Constitutive properties of ice at Dye 3, Greenland, in *International Association of Hydrological Sciences Publication 170* (Symposium at Vancouver 1987 – *The Physical Basis of Ice Sheet Modelling*), pp. 31–43, 1987.
- Dansgaard, W., and S. J. Johnsen, A flow model and a time scale for the ice core from Camp Century, Greenland, *Journal of Glaciology*, 8(53), 215–223, 1969.
- de Bresser, J. H. P., J. H. ter Heege, and C. J. Spiers, Grain size reduction by dynamic recrystallization: can it result in major tectological weakening?, *International Journal of Earth Sciences*, 90(1), 28–45, 2001.
- Denton, G. H., and T. J. Hughes, Reconstruction of the Ross ice drainage system, Antarctica, at the Last Glacial Maximum, *Geografiska Annaler*, 82A(2–3), 143–166, 2000.
- Durham, W. B., and L. A. Stern, Rheological properties of water ice – applications to satellites of the outer planets, *Annual Review of Earth and Planetary Science*, 29, 295–330, 2001.

- Durham, W. B., L. A. Stern, and S. H. Kirby, Rheology of ice I at low stress and elevated confining pressure, *Journal of Geophysical Research*, 106(B6), 11031–11042, 2001.
- Duval, P., Creep and fabrics of polycrystalline ice under shear and compression, *Journal of Glaciology*, 27(95), 129–140, 1981.
- Duval, P., and H. LeGac, Mechanical behavior of antarctic ice, *Annals of Glaciology*, 3, 92–96, 1982.
- Duval, P., and L. Lliboutry, Superplasticity owing to grain growth in polar ices, *Journal of Glaciology*, 31(107), 60–62, 1985.
- Duval, P., M. F. Ashby, and I. Anderman, Rate-controlling processes in the creep of polycrystalline ice, *Journal of Physical Chemistry*, 87(21), 4066–4074, 1983.
- Duval, P., L. Arnaud, O. Brissaud, M. Montagnat, and S. de la Chapelle, Deformation and recrystallization processes of ice from polar ice sheets, *Annals of Glaciology*, 30, 83–87, 2000.
- Elsberg, D. H., W. D. Harrison, E. Husmann, J. L. Morack, E. C. Pettit, E. D. Waddington, and M. A. Zumberge, Strain rates and short term strain events measured at Siple Dome, Antarctica, *Journal of Glaciology*, in review.
- Fujita, S., H. Maeno, S. Uratsuka, T. Furukawa, S. Mae, Y. Fujii, and O. Watanabe, Nature of radio echo layering in the Antarctic ice sheet detected by a two-frequency experiment, *Journal of Geophysical Research*, 104(B6), 13013–13024, 1999.
- Gades, A. M., Spatial and temporal variations of basal conditions beneath glaciers and ice sheets inferred from radio echo-sounding measurements, Ph.D. thesis, University of Washington, 1998.
- Glen, J. W., The creep of polycrystalline ice, *Proceedings of the Royal Society of London, Ser A*, 228(1175), 519–538, 1955.
- Glen, J. W., The flow law of ice. A discussion of the assumptions made in glacier theory, their experimental foundations and consequences, in *International Association of Hydrological Sciences Publication 47* (Symposium at Chamonix 1958 – *Physics of the Movement of the Ice*), pp. 171–183, 1958.
- Goldsby, D. L., and D. L. Kohlstedt, Grain boundary sliding in fine-grained Ice I, *Scripta Materialia*, 37, 1399–1406, 1997.
- Goldsby, D. L., and D. L. Kohlstedt, Superplastic deformation of ice: Experimental observations, *Journal of Geophysical Research*, 106(B6), 11017–11030, 2001.

- Gow, A. J., D. A. Meese, R. B. Alley, J. J. Fitzpatrick, S. Anandakrishnan, G. A. Woods, and B. C. Elder, Physical and structural properties of the Greenland Ice Sheet Project 2 ice core: A review, *Journal of Geophysical Research*, 102(C12), 26559–26575, 1997.
- Greve, R., Large-scale ice-sheet modelling as a means of dating deep ice cores in Greenland, *Journal of Glaciology*, 43(144), 307–310, 1997.
- Hamilton, G. S., Mass balance and accumulation rate across Siple Dome, West Antarctica, *Annals of Glaciology*, 35, in press, 2001.
- Hamilton, G. S., and I. M. Whillans, Point measurements of mass balance of the Greenland Ice Sheet using precision vertical Global Positioning System surveys, *Journal of Geophysical Research*, 105(B7), 16295–16301, 2000.
- Hamilton, G. S., I. M. Whillans, and P. J. Morgan, First point measurements of ice-sheet thickness change in Antarctica, *Annals of Glaciology*, 27, 125–129, 1998.
- Hawley, R. L., E. D. Waddington, G. W. Lamorey, and K. C. Taylor, Vertical-strain measurements in firn at Siple Dome, Antarctica, *Journal of Glaciology*, in review.
- Hindmarsh, R. C. A., Stochastic perturbation of divide position, *Annals of Glaciology*, 23, 94–104, 1996.
- Hutter, K., F. Legerer, and U. Spring, First-order stresses and deformations in glaciers and ice sheets, *Journal of Glaciology*, 27(96), 227–270, 1981.
- Hvidberg, C. S., Steady-state thermomechanical modelling of ice flow near the centre of large ice sheets with the finite element technique, *Annals of Glaciology*, 23, 116–123, 1996.
- Hvidberg, C. S., D. Dahl-Jensen, and E. D. Waddington, Ice flow between the Greenland Ice Core Project and Greenland Ice Sheet Project 2 boreholes in central Greenland, *Journal of Geophysical Research*, 102(C12), 26851–26859, 1997.
- Jacobel, R. W., and S. M. Hodge, Radar internal layers from the Greenland summit, *Geophysical Research Letters*, 22(5), 587–590, 1995.
- Jacobel, R. W., A. J. Fisher, and N. M. Sundell, Internal stratigraphy from ground-based radar studies at Siple Dome summit, *Antarct. J. U. S.*, 1996 Review, 31(5), 55–56, 1996.
- Jacobel, R. W., T. A. Scambos, N. A. Nereson, and C. F. Raymond, Changes in the margin of Ice Stream C, Antarctica, *Journal of Glaciology*, 46(152), 102–110, 2000.
- Jacobson, H. P., Folding of stratigraphic layers in ice domes, Ph.D. thesis, University of Washington, 2001.

- Johnsen, S., D. Dahl-Jensen, W. Dansgaard, and N. Gundestrup, Greenland palaeotemperatures derived from GRIP bore hole temperature and ice core isotope profiles, *Tellus*, *47B*, 624–629, 1995.
- Johnson, A. F., Creep characterization of transversely isotropic metallic materials, *Journal of Mechanical and Physical Solids*, *25*, 117–126, 1977.
- Kreutz, K. J., P. A. Mayewski, L. D. Meeker, M. S. Twickler, S. I. Whitlow, and I. I. Pittalwala, Bipolar changes in atmospheric circulation during the Little Ice Age, *Science*, *277*, 1294–1296, 1997.
- Kreutz, K. J., P. A. Mayewski, M. S. Twickler, S. I. Whitlow, J. W. C. White, C. A. Shuman, C. F. Raymond, H. Conway, and J. R. McConnell, Seasonal variations of glaciochemical, isotopic and stratigraphic properties in Siple Dome (Antarctica) surface snow, *Annals of Glaciology*, *29*, 38–44, 1999.
- Langdon, T. G., Creep mechanisms in ice, in *Physics and Chemistry of Ice*, edited by E. Whalley, S. Jones, and L. Gold, Royal Society of Canada, 1973.
- Langdon, T. G., The physics of superplastic deformation, *Materials Science and Engineering*, *A137*, 1–11, 1991.
- Langdon, T. G., A unified approach to grain boundary sliding in creep and superplasticity, *Acta Metallurgica et Materialia*, *42*, 2437–2443, 1994.
- Langdon, T. G., Transitions in creep behavior, *Materials Transactions JIM*, *37*(3), 359–362, 1996.
- Langdon, T. G., and F. A. Mohamed, The characteristics of independent and sequential creep processes, *The Journal of the Australian Institute of Metals*, *22*(3-4), 189–199, 1977.
- Lipenkov, V. Y., N. I. Barkov, P. Duval, and P. Pimienta, Crystalline texture of the 2083m ice core at Vostok Station, Antarctica, *Journal of Glaciology*, *35*(121), 392–398, 1989.
- Lliboutry, L., The dynamics of temperate glaciers from the detailed viewpoint, *Journal of Glaciology*, *8*(53), 185–205, 1969.
- Lliboutry, L., *Very slow flows of solids; basics of modeling in geodynamics and glaciology*, Martinus Nijhoff Publishers, 1987.
- Lliboutry, L., Anisotropic, transversely isotropic nonlinear viscosity of rock ice and rheological parameters inferred from homogenization, *International Journal of Plasticity*, *9*, 619–632, 1993.

- Mangeny, A., F. Califano, and O. Castelnau, Isothermal flow of an anisotropic ice sheet in the vicinity of an ice divide, *Journal of Geophysical Research*, 101(B12), 28189–28204, 1996.
- Marshall, H. P., J. T. Harper, W. T. Pfeffer, and N. F. Humphrey, Depth-varying constitutive properties observed in an isothermal glacier, *Geophysical Research Letters*, 29(23), 61–1:61–4, 2002, doi:10.1029/2002GL015412.
- Marshall, S. J., and K. M. Cuffey, Peregrinations of the Greenland Ice Sheet divide in the last glacial cycle: implications for central Greenland ice cores, *Earth and Planetary Science Letters*, 179, 73–79, 2000.
- Marshall, S. J., L. Tarasov, G. K. C. Clarke, and W. R. Peltier, Glaciological reconstruction of the Laurentide Ice Sheet: physical processes and modelling challenges, *Canadian Journal of Earth Science*, 37, 769–793, 2000.
- McIntyre, N., The dynamics of ice-sheet outlets, *Journal of Glaciology*, 31(108), 99–107, 1985.
- Meier, M. F., Vertical profiles of velocity and the flow law of glacier ice, in *International Association of Hydrological Sciences Publication 47* (Symposium at Chamonix 1958 – *Physics of the Movement of the Ice*), pp. 169–170, 1958.
- Montagnat, M., and P. Duval, Rate controlling processes in the creep of polar ice, influence of grain boundary migration associated with recrystallization, *Earth and Planetary Science Letters*, 183, 179–186, 2000.
- Morland, L. W., and I. R. Johnson, Steady motion of ice sheets, *Journal of Glaciology*, 25(92), 229–246, 1980.
- Morse, D., Glacier geophysics at Taylor Dome, Antarctica, Ph.D. thesis, University of Washington, 1997.
- Morse, D. L., D. D. Blankenship, E. D. Waddington, and T. A. Neumann, A site for deep ice coring in west antarctica: Results from aerogeophysical surveys and thermo-kinematic modeling, *Annals of Glaciology*, 35, in press, 2001.
- Mosley-Thompson, E., L. G. Thompson, J. Dai, M. Davis, and P. N. Lin, Climate of the last 500 years: high resolution ice core records, *Quaternary Science Reviews*, 12, 419–430, 1993.
- Nereson, N. A., The flow history of Siple Dome and Ice Streams C and D, West Antarctica: Inferences from geophysical measurements and ice flow models, Ph.D. thesis, University of Washington, 1998.

- Nereson, N. A., Elevation of ice-stream margin scars after stagnation, *Journal of Glaciology*, 46(152), 111–118, 2000.
- Nereson, N. A., and C. F. Raymond, The elevation history of ice streams and the spatial accumulation pattern along the Siple Coast of West Antarctica inferred from ground-based radar data from three inter-ice-stream ridges, *Journal of Glaciology*, 47(157), 303–313, 2001.
- Nereson, N. A., and E. D. Waddington, Isochrones and isotherms beneath migrating ice divides, *Journal of Glaciology*, 160(48), 95–108, 2002.
- Nereson, N. A., E. D. Waddington, C. F. Raymond, and H. P. Jacobson, Predicted age-depth scales for Siple Dome and inland WAIS ice cores in West Antarctica, *Geophysical Research Letters*, 23(22), 3163–3166, 1996.
- Nereson, N. A., R. C. A. Hindmarsh, and C. F. Raymond, Sensitivity of the divide position at Siple Dome, West Antarctica, to boundary forcing, *Annals of Glaciology*, 27, 207–214, 1998a.
- Nereson, N. A., C. F. Raymond, E. D. Waddington, and R. W. Jacobel, Migration of the Siple Dome ice divide, West Antarctica, *Journal of Glaciology*, 44(148), 643–652, 1998b.
- Nereson, N. A., C. F. Raymond, R. W. Jacobel, and E. D. Waddington, The accumulation pattern across Siple Dome, West Antarctica, inferred from radar-detected internal layers, *Journal of Glaciology*, 46(152), 75–87, 2000.
- Nye, J. F., The flow law of ice from measurements in glacier tunnels, laboratory experiments and the Jungfraufirn borehole experiment, *Proceedings of the Royal Society of London, Ser A*, 219(1193), 477–489, 1953.
- Nye, J. F., The distribution of stress and velocity in glaciers and ice-sheets, *Proceedings of the Royal Society of London, Ser A*, 239(1216), 113–133, 1957.
- Nye, J. F., The motion of ice sheets and glaciers, *Journal of Glaciology*, 3(26), 493–507, 1959.
- Paren, J., and G. Robin, Internal reflections in polar ice sheets, *Journal of Glaciology*, 21(85), 251–259, 1975.
- Paterson, W. S. B., Why ice-age ice is sometimes "soft", *Cold Regions Science and Technology*, 20(1), 75–98, 1991.
- Paterson, W. S. B., *The physics of glaciers*, Pergamon Press, Oxford, 3rd edn., 1994.

- Paterson, W. S. B., and G. K. C. Clarke, Comparison of theoretical and observed temperature profiles in Devon Island ice cap, Canada, *Geophys. J. R. Astr. Soc.*, 55, 615–632, 1978.
- Paterson, W. S. B., and E. D. Waddington, Past precipitation rates derived from ice core measurements: methods and data analysis, *Reviews of Geophysics and Space Physics*, 22(2), 123–130, 1984.
- Paterson, W. S. B., and E. D. Waddington, Estimated basal temperatures at Crête Greenland, throughout a glacial cycle, *Cold Regions Science and Technology*, 12, 99–102, 1986.
- Payne, A., Limit cycles in the basal thermal regime of ice sheets, *Journal of Geophysical Research*, 100(B3), 4249–4263, 1995.
- Peltier, W. R., D. L. Goldsby, D. L. Kohlstedt, and L. Tarasov, Ice-age ice-sheet rheology: constraints from the last glacial maximum form of the Laurentide Ice Sheet, *Annals of Glaciology*, 30, 163–176, 2000.
- Pettit, E. C., and E. D. Waddington, Ice flow at low deviatoric stress, *Journal of Glaciology*, in press.
- Pettit, E. C., H. P. Jacobson, and E. D. Waddington, Effects of basal sliding on isochrons and flow near an ice divide, *Annals of Glaciology*, 37, in press, 2002.
- Pimienta, P., P. Duval, and V. Y. Lipenkov, Mechanical behaviour of ice along the 2040 m Vostok core, Antarctica, *Annals of Glaciology*, 10, 137–140, 1988.
- Pourchet, M., and F. Pinglot, Determination of the stratospheric residence time from the total β activity of Antarctica and Greenland snows, *Geophysical Research Letters*, 6(5), 365–367, 1979.
- Price, S. F., R. A. Bindschadler, C. L. Hulbe, and I. R. Joughin, Post-stagnation behavior in the upstream regions of Ice Stream C, West Antarctica, *Journal of Glaciology*, 47(157), 283–2894, 2001.
- Raymond, C., N. Nereson, A. Gades, H. Conway, R. Jacobel, and T. Scambos, Geometry and stratigraphy of Siple Dome, Antarctica, *Antarct. J. U.S.*, 1995 Review, 30(5), 91–93, 1995.
- Raymond, C. F., Deformation in the vicinity of ice divides, *Journal of Glaciology*, 29(103), 357–373, 1983.
- Reeh, N., A flow line model for calculating the surface profile and the velocity, strain rate, and stress field in an ice sheet, *Journal of Glaciology*, 34(127), 46–54, 1988.

- Retzlaff, R., and C. R. Bentley, Timing of stagnation of Ice Stream C, West Antarctica, from short-pulse radar studies of buried surface crevasses, *Journal of Glaciology*, 39(133), 553–561, 1993.
- Robin, G., Ice movement and temperature distribution in glaciers and ice sheets, *Journal of Glaciology*, 2(18), 523–532, 1955.
- Russell-Head, D., and W. Budd, Ice-sheet flow properties derived from bore-hole shear measurements combined with ice-core studies, *Journal of Glaciology*, 24(90), 117–130, 1979.
- Sachs, G., Zur Ableitung einer Fließbedingung, *Zeitschrift des Vereines Deutscher Ingenieure*, 72(22), 734–736, 1928.
- Satow, K., O. Watanabe, H. Shoji, and H. Motoyama, The relationship among accumulation rate, stable isotope ratio and surface temperature on the plateau of East Dronning Maud Land, Antarctica, *Polar Meteorology and Glaciology*, 13, 43–52, 1999.
- Scambos, T., and N. Nereson, Satellite image and GPS study of the morphology of Siple Dome, Antarctica, *Antarct. J. U.S., 1995 Review*, 30(5), 87–89, 1995.
- Schøtt, C., E. D. Waddington, and C. F. Raymond, Predicted time-scales for GISP2 and GRIP boreholes at Summit, Greenland, *Journal of Glaciology*, 38(128), 162–168, 1992.
- Shoji, H., and C. C. Langway, Mechanical properties of fresh ice core from Dye 3, Greenland, in *Greenland Ice Core: Geophysics, Geochemistry and the Environment*, vol. 33 of *Geophysical Monograph*, pp. 39–48, American Geophysical Union, 1985.
- Smith, G. D., and L. W. Morland, Viscous relations for the steady creep of polycrystalline ice, *Cold Regions Science and Technology*, 5, 141–150, 1981.
- Stein, C. A., Heat flow of the earth, in *Global Earth Physics: a Handbook of Physical Constants*, edited by T. Ahrens, pp. 144–158, AGU, Washington, D.C., 1995, vol. 1 of AGU Ref. Shelf.
- Stone, J. O., G. A. Balco, D. E. Sugden, M. W. Caffee, L. C. Sass, S. G. Cowderly, and C. Siddoway, Holocene deglaciation of Marie Byrd Land, West Antarctica, *Science*, 299, 99–102, 2003.
- Tarasov, L., and W. R. Peltier, Laurentide Ice Sheet aspect ratio in models based on Glen's flow law, *Annals of Glaciology*, 30, 177–186, 2000.
- Taylor, K., et al., Abrupt late glacial climate change on the Siple Coast of Antarctica, accepted.
- Taylor, K. C., et al., Abrupt late glacial climate change on the Siple Coast of Antarctica, in prep.

- Thorsteinsson, T., Anisotropy of ice I_h : development of fabric and effects of anisotropy on deformation, Ph.D. thesis, University of Washington, 2000.
- Thorsteinsson, T., An analytical approach to deformation of anisotropic ice crystal aggregates, *Journal of Glaciology*, 47(158), 507–516, 2001.
- Thorsteinsson, T., Fabric development with nearest-neighbor interaction and dynamic recrystallization, *Journal of Geophysical Research*, 107(B1), 1–13, 2002.
- Thorsteinsson, T., J. Kipfstuhl, and H. Miller, Texture and fabric in the GRIP ice core, *Journal of Geophysical Research*, 102(C12), 26583–26599, 1997.
- Thorsteinsson, T., E. D. Waddington, K. C. Taylor, R. B. Alley, and D. D. Blankenship, Strain-rate enhancement at Dye 3, Greenland, *Journal of Glaciology*, 45(150), 338–345, 1999.
- van der Veen, C. J., and I. M. Whillans, Development of fabric in ice, *Cold Regions Science and Technology*, 22, 171–195, 1994.
- Vaughan, D. G., H. F. J. Corr, C. S. M. Doake, and E. D. Waddington, Distortion of isochronous layers in ice revealed by ground-penetrating radar, *Nature*, 398, 323–326, 1999.
- Waddington, E. D., Geothermal heat flux beneath ice sheets, 1987, *International Association of Hydrological Sciences Publication 170* (Symposium at Vancouver 1987 – *The Physical Basis for Ice Sheet Modelling*), 217–226.
- Waddington, E. D., C. F. Raymond, D. L. Morse, and W. D. Harrison, Flow law for ice at low deviatoric stress, and implications for ice divide and ice core studies, *Eos*, 77(46), F196, 1996, Fall Meeting Supplement.
- Waddington, E. D., J. F. Bolzan, and R. B. Alley, Potential for stratigraphic folding near ice-sheet centers, *Journal of Glaciology*, 47(159), 639–648, 2001.
- Weertman, J., On the sliding of glaciers, *Journal of Glaciology*, 3(21), 33–38, 1957.
- Weertman, J., Equilibrium profile of ice caps, *Journal of Glaciology*, 3(30), 953–964, 1961.
- Weertman, J., Creep of ice, in *Physics and Chemistry of Ice*, edited by E. Whalley, S. Jones, and L. Gold, pp. 320–337, Royal Society of Canada, 1973.
- Whillans, I., and R. Bindschadler, Mass balance of Ice Stream B, West Antarctica, *Annals of Glaciology*, 11, 187–193, 1988.
- Wolff, E., and C. Doake, Implications of the form of the flow law for vertical velocity and age depth profiles in polar ice, *Journal of Glaciology*, 32(112), 366–370, 1986.

- Zumberge, M. A., Precise optical path length measurements through an optical fiber: application to seafloor strain monitoring, *Ocean Engineering*, 24(6), 531–542, 1997.
- Zumberge, M. A., D. H. Elsberg, W. D. Harrison, E. Husmann, J. L. Morack, E. C. Pettit, and E. D. Waddington, Measurement of vertical velocity and strain at Siple Dome by optical sensors, *Journal of Glaciology*, 46(161), 217–225, 2002.
- Zwally, H. J., and P. Gloersen, Passive microwave images of the polar regions and research applications, *Polar Record*, 18(16), 421–450, 1977.

Appendix A

NOTATION

A	Flow-law softness parameter ($\text{Pa}^{-n}\text{s}^{-1}$)
A_0	Temperature-independent softness parameter for clean, isotropic, Holocene ice ($\text{Pa}^{-n}\text{s}^{-1}$)
B	Elevation of ice sheet bed (m)
E	Enhancement factor relative to Holocene ice
H	Ice-equivalent ice-sheet thickness (m)
J	Misfit
N	Number of data points
\dot{H}	Rate of excess thinning/thickening (m a^{-1})
Q	Thermal activation energy for creep (J mol^{-1})
R	Gas constant ($8.314 \text{ J mol}^{-1} \text{ K}^{-1}$)
S	Elevation of ice sheet surface (m)
T	Temperature (K)
T_s	Surface temperature ($^{\circ}\text{C}$)
\dot{b}	Ice-equivalent accumulation rate (m a^{-1})
\dot{b}_m	Accumulation rate expressed in mass units ($\text{Mg m}^2 \text{ a}^{-1}$)
$a-e$	Coefficients in anisotropic flow description (functions of cone angle)
d	Average grain diameter (m)
g	Acceleration due to gravity (m s^{-2})
h	Dansgaard-Johnsen model parameter (m)
k	Crossover stress (Pa)
n	Stress exponent in flow law
p	Grain-size exponent in flow law
p	Pressure
p	One less than the degrees of freedom
q	horizontal ice flux (m^3a^{-1})
\mathbf{u}	Velocity vector (m a^{-1})
u	Horizontal velocity along flow line (function of depth, m a^{-1})
\bar{u}	Horizontal velocity along flow line averaged over depth (m a^{-1})
u_s	Horizontal velocity at the surface, along flow line (m a^{-1})
v	Horizontal velocity perpendicular to the flow line (function of depth, (m a^{-1}))

v_s	Horizontal velocity at the surface, perpendicular to the flow line (m a^{-1})
w	Vertical velocity along flow line (function of depth, (m a^{-1}))
w_j	Weighting function in the misfit function
w_s	Vertical velocity at the surface, along flow line (m a^{-1})
x	Horizontal position along flow line (m)
x	As subscript, identifies partial derivative with respect to x
y	Horizontal position perpendicular to the flow line (m)
z	Height above bed (m)
z'	Height above bed relative to local ice thickness (m)
z	As subscript, identifies partial derivative with respect to z
Γ	Coefficient of Glen term in flow law (equal to coefficient for “normal” Glen flow when $p = 0$)
Ω	Non-dimensional effective deviatoric stress
Ω_{char}	Characteristic Ω for a particular divide
α	Cone angle (degrees)
γ	Ratio of \bar{u} to the surface velocity u_s
δ	Length scale for deformation of 10% strain (m)
$\dot{\epsilon}_{ij}$	Strain-rate tensor (s^{-1})
$\dot{\epsilon}_{\text{char}}$	Characteristic strain rate (s^{-1} , equals \dot{b}/H)
$\dot{\epsilon}_{\text{eff}}$	Effective strain rate (s^{-1} , second invariant of $\dot{\epsilon}_{ij}$)
η	Scaled height above bed
η_{eff}	Effective viscosity (Pa.s)
$\hat{\eta}$	Effective viscosity relative to 10^{10} Pa.s
σ_{ij}	Stress tensor (Pa)
ϕ	Horizontal velocity shape function
ψ	Vertical velocity shape function
ρ	Ice density (Mg m^{-3})
ρ_f	Density of the firn at a particular depth (Mg m^{-3})
τ	Characteristic H/\dot{b} timescale
τ_{ij}	Deviatoric stress tensor (Pa)
τ_{char}	Characteristic stress for a particular divide (Pa)
τ_{eff}	Effective shear stress (Pa, second invariant of τ_{ij})

Appendix B

DERIVATION OF THE GLEN FLOW LAW

The constitutive relation for any isotropic material is a physical property of the material and cannot change with the coordinate system. Therefore the most general form for an isotropic flow law is [Glen, 1958]

$$\dot{\epsilon}_{ij} = A(\Sigma_1, \Sigma_2, \Sigma_3)\delta_{ij} + B(\Sigma_1, \Sigma_2, \Sigma_3)\sigma_{ij} + C(\Sigma_1, \Sigma_2, \Sigma_3)\sigma_{ik}\sigma_{kj}, \quad (\text{B.1})$$

where $\dot{\epsilon}$ is the strain rate tensor and σ is the stress tensor. A , B , and C are functions of the three invariants of the stress tensor:

$$\begin{aligned} \Sigma_1 &= \sigma_1 + \sigma_2 + \sigma_3 = \sigma_{ii}, \\ \Sigma_2 &= -(\sigma_1\sigma_2 + \sigma_2\sigma_3 + \sigma_3\sigma_1) = \frac{1}{2}\sigma_{ij}\sigma_{ij}, \\ \Sigma_3 &= \sigma_1\sigma_2\sigma_3 = \frac{1}{3}\sigma_{ij}\sigma_{jk}\sigma_{ki}, \end{aligned} \quad (\text{B.2})$$

where σ_1 , σ_2 , and σ_3 are the three principal stresses.

This flow law can be simplified by making four assumptions:

1. **Strain rate is independent of hydrostatic pressure.** As long as the temperature is measured relative to the pressure melting temperature, any effect of hydrostatic pressure is small enough to be ignored [Paterson, 1994]. With this assumption, we define a deviatoric stress tensor as $\tau_{ij} = \sigma_{ij} - \frac{1}{3}\Sigma_1\delta_{ij}$ and the corresponding invariants in Equation (B.2) are T_1 , T_2 , and T_3 . Equation (B.1) can be rewritten with these invariants in place of Σ_i and, since $T_1 = 0$, it no longer dependent on the first invariant.
2. **Ice is incompressible.** The first invariant of the strain rate tensor, $\dot{\epsilon}_{ii}$, describes a change in volume, which must be zero for incompressibility to be true. This allows A , in Equation (B.1) to be a function of C . (Refer to Glen [1958] for details.)

3. **Components of the strain rate tensor are proportional to the respective components of the deviatoric stress tensor.** The function C describes uncommon behavior such a dilation of a material under shear stress. Most studies on ice show no evidence of this type of behavior, so there is no reason to make a flow law more complicated than it needs to be. Therefore, $C = 0$, as was first suggested by *Nye* [1953].
4. **The second invariant of the strain rate tensor is a function of the second invariant of the stress tensor only.** Thus, the flow is independent of T_3 , which describes the anisotropy of the stress tensor. This assumption may break down for anisotropic ice [*Budd and Jacka*, 1989].

As a result of these assumptions, Equation (B.1) becomes

$$\dot{\epsilon}_{ij} = B(\tau_{\text{eff}}^2)\tau_{ij}, \quad (\text{B.3})$$

where τ_{eff} is the 'effective shear stress' and $\tau_{\text{eff}} = T_2^{1/2} = (\frac{1}{2}\tau_{ij}\tau_{ij})^{1/2}$.

For the past several decades, most authors have assumed $B(\tau_{\text{eff}}^2)$ for isotropic glacier ice has the form of a power law, similar to many polycrystalline metals [*Glen*, 1955; *Nye*, 1953]:

$$B(\tau_{\text{eff}}^2) = EA(T)(\tau_{\text{eff}}^2)^{\frac{n-1}{2}} \quad (\text{B.4})$$

Including the *Arrhenius relation* for temperature dependence, the full expression for *Glen's Law* that most researchers now use is

$$\dot{\epsilon}_{ij} = EA_0 e^{-\frac{Q}{RT}} (\tau_{\text{eff}}^2)^{\frac{n-1}{2}} \tau_{ij}. \quad (\text{B.5})$$

n is a constant (usually equal to 3). A_0 is typically considered a constant that describes clean, isotropic, Holocene glacier ice (it is often called the *softness parameter* and has units of $\text{kPa}^{-n}\text{s}^{-1}$). E is the *enhancement factor*. It is a non-dimensional multiplier describing the increase in flow caused by variations crystal size, impurity content, and crystal orientation; it is typically a function of depth.

Appendix C

BOREHOLE DEFORMATION CORRECTION

Both the optical-fiber and wire-resistance strain gauges measure along-borehole strain, which is a combination of vertical compression and the horizontal shear strain due to horizontal flow of the ice. The horizontal flow is only significant at the flank site. Therefore, the flank data must be corrected for strain due to horizontal deformation of the borehole.

We model the deformation of the borehole and calculate a correction factor using two different horizontal velocity profiles extracted from finite-element model runs: isotropic nonlinear steady-state flow and a more complex profile based on preliminary modelling of flow with anisotropy.

C.1 Isotropic Flow Correction

Figure C.1 shows the evolution of an initially straight borehole at 1 year intervals driven by a horizontal velocity profile from a finite-element model of isotropic nonlinear steady-state ice flow for Siple Dome.

Because the boreholes were drilled vertically rather than bed-normal, the borehole initially shortens in length until it rotates past the bed-normal orientation, then it lengthens with increased deformation. This makes the correction factor not only depth dependent but time dependent.

Figure C.3 shows the measured strain rates due to horizontal shearing expected at each depth for the 1 meter wire-resistance gauges. Figure C.2 shows the results for the optical-fiber instruments and Figure C.3. The instruments near the bed have the largest correction because that is where the shear strain is concentrated. Also, the fiber instruments have smaller total correction factors because the gauge length of the instruments is longer than the length scale of the shear zone; the peak strains are distributed over the long gauge length.

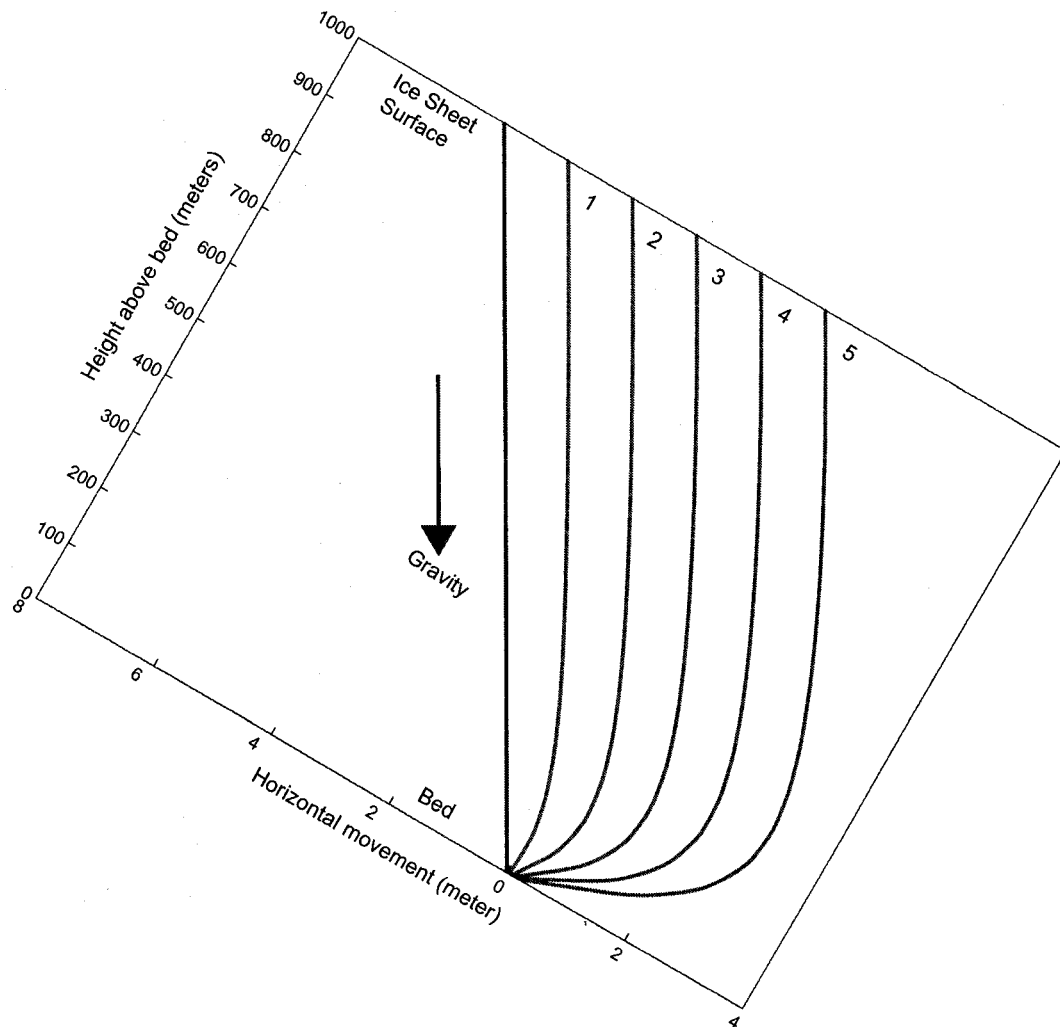


Figure C.1: Evolution of borehole with time. Plot is tilted to make gravity vertical on the page.

C.2 Anisotropic Flow Correction

The above calculation of the correction factor assumes the simplest horizontal velocity profile. The deformation of the borehole, however, is sensitive to the details of the horizontal velocity profile. *Elsberg et al.* [in review] noticed a temporal trend in the optical-fiber data

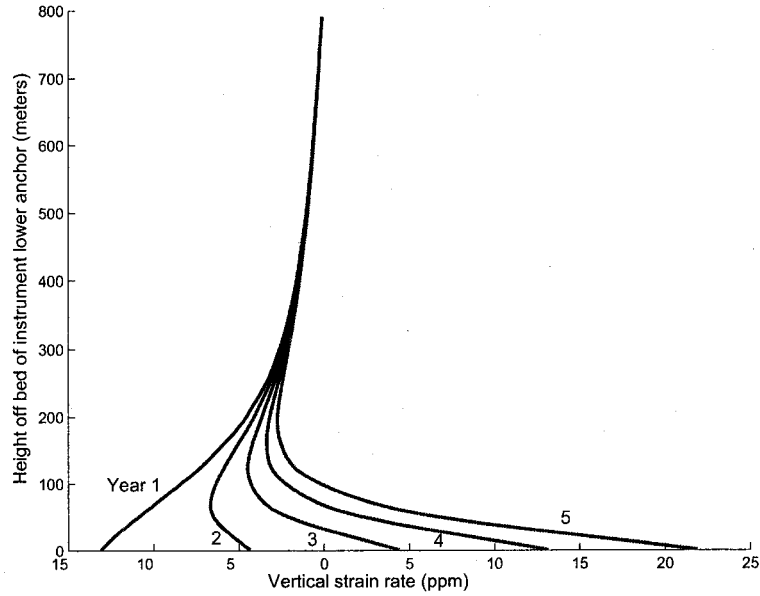


Figure C.2: Vertical strain rate correction due to horizontal shearing of the borehole for the optical-fiber gauges (gauge length is 174 meter) after 1 to 5 years of deformation. Note that the height on the vertical axis is to the bottom of the instrument.

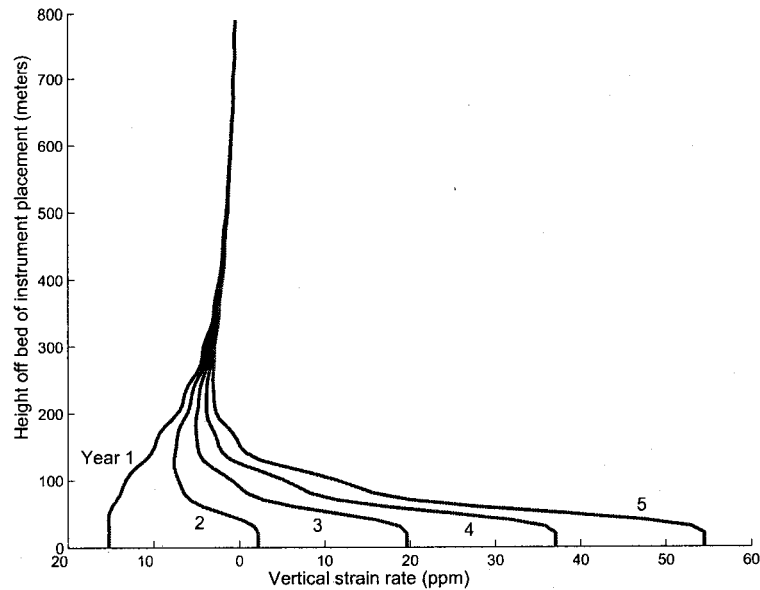


Figure C.3: Vertical strain rate correction due to horizontal shearing of the borehole for the wire-resistance gauges (gauge length is 1 meter) after 1 to 5 years of deformation.

for the two deepest gauges at the flank site that could not be explained by instrumentation artifact or expected deformation of the ice. It is possible that this temporal trend is the results of a real process occurring within the ice; however, the more likely cause is the horizontal shearing. Figures C.2 and C.3 do show a temporal trend for instruments close to the bed. If our correction factor calculation is in error, then that temporal trend may be measurable higher up in the ice column as well.

The properties of the ice at Siple Dome are not homogeneous. Preliminary results from the ice core show unexpected jumps in profiles of oxygen isotopes and gases [*Taylor et al.*, in prep]. And, more important for this study, the borehole sonic log shows two discontinuities in the crystal fabric, such that there is a band approximately 100 meters thick of fabric whose crystals are so tightly aligned vertically that one could interpret it as a single crystal of ice. Clearly, Siple Dome has an interesting pre-history (before the Holocene history presented in Chapter 5), but for this analysis, it is the effect of a band of nearly-single crystal ice on the horizontal velocity profile that we focus on.

As we discussed in Chapter 4, a tight vertical fabric is hard to compress vertically but soft to horizontal shearing. Using the model developed in Chapter 4 we calculated the horizontal velocity profile based on estimates of the ice properties. Figure C.4 shows the profile on the right, and the corresponding profile of cone angle versus depth derived from the sonic log. For now this profile is just an approximation to show what we can learn from a more detailed analysis of this type. We assume that this profile applies at all distances from the divide; in reality, the ice on the flank may have even tighter fabric than the divide, as the horizontal shearing process tends to rotate crystals to the vertical [*Paterson*, 1994].

The band of tight fabric (from 700 m to about 820 m) behaves somewhat like a false bed. As compared to the isotropic horizontal velocity profile, the shear in this profile is concentrated in this band of unusual ice. Using this velocity profile, Figure C.5 shows how the borehole will deform over time.

With this borehole evolution, the corrections for the optical-fiber and wire gauges are presented in Figures C.6 and C.7. The largest corrections are now shown higher off the bed, within the band of tight fabric, as expected.

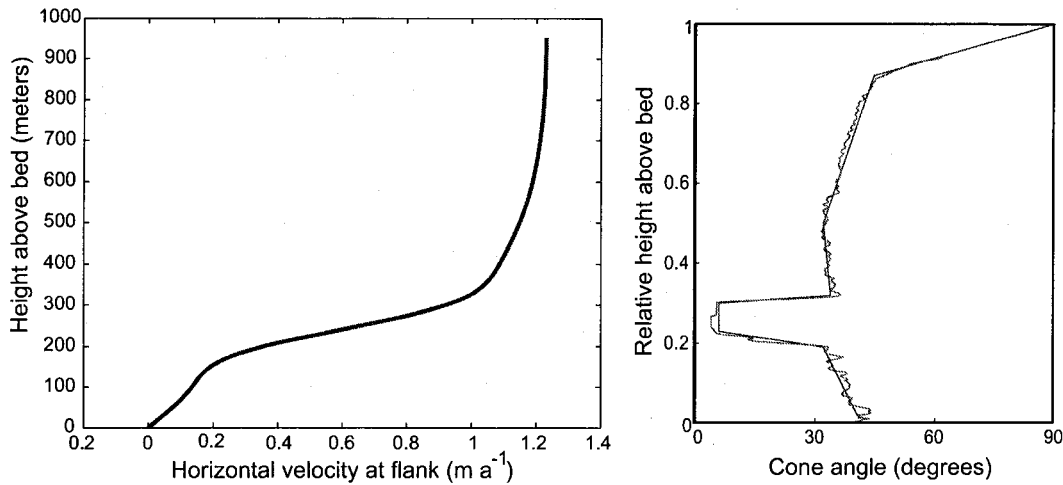


Figure C.4: Horizontal velocity profile at flank including the effect of the measured anisotropy. Cone angle profile measure with sonic logging from Siple Dome (from Greg Lamorey and Throstur Thorsteinsson)

C.3 Synthesis

For the present work, we continue to use the correction factor based on the simple horizontal velocity profile, while we acknowledge the uncertainties in those strain rates for the lower instruments. It may be difficult to determine an accurate correction factor without a measurement of the borehole deformation. The anisotropic model for borehole deformation depends on many assumptions about the properties of the ice and the effect of anisotropy on ice flow, some of which we have approached in Chapters 4 and 6, which rely on these vertical strain rate data, making the argument somewhat circular.

Interestingly, this more advanced model for borehole deformation may lead to more direct assessment of the flow properties of the band of tight fabric. If we assume the temporal trends in the optical-fiber data is due solely to the deformation of the borehole, then we can estimate the shear deformation necessary to cause the temporal trends. With known shear strain rates at depth, we can infer the flow properties of the ice.

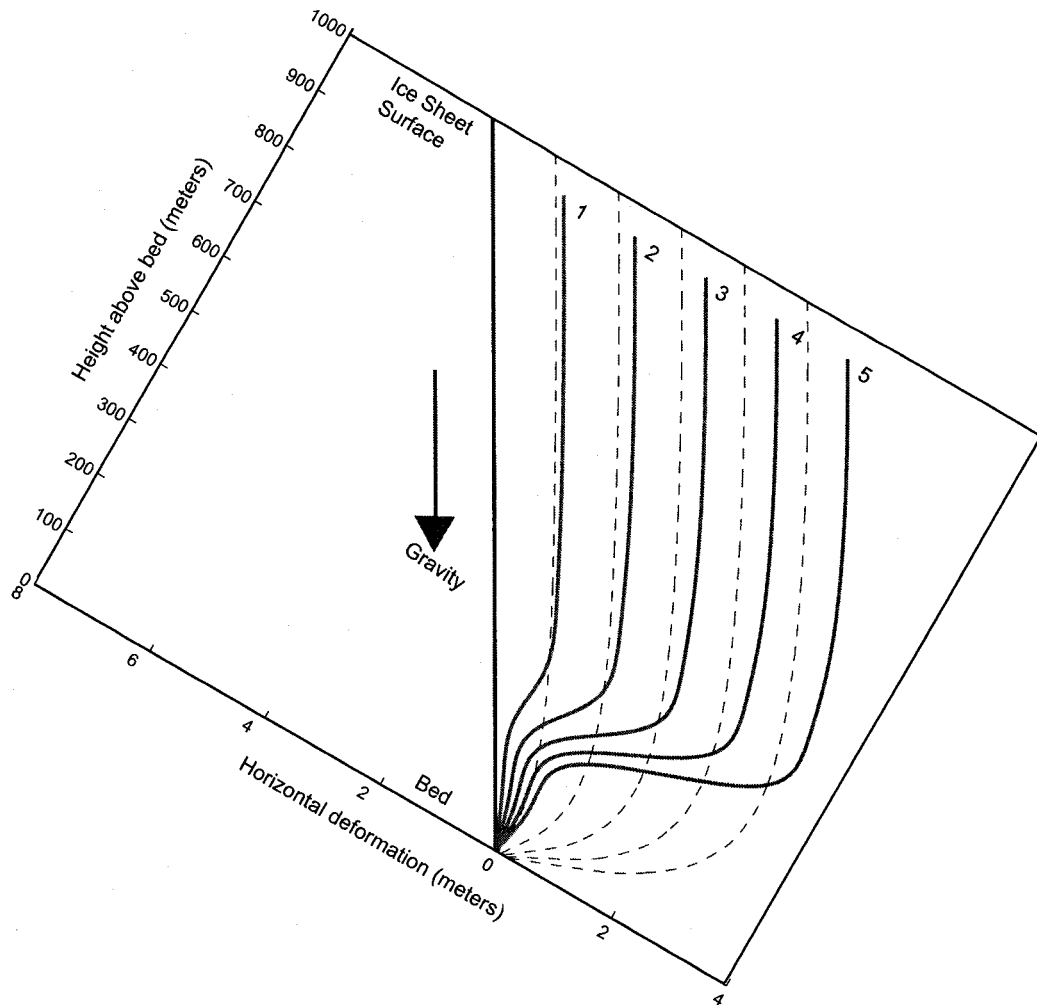


Figure C.5: Deformation of the borehole due to horizontal motion for the first 5 years.

It may be possible, as well, to learn more about the properties of the ice on an even smaller scale by comparing the wire-resistance gauge data, which was collected up to 48

times a day throughout the year, with the total strain predicted by the ice flow model at the gauge depth. Figure C.8 shows the predicted total strain accumulated as a function of time for each of the gauges. The upper gauges all show the expected linear trend that *Elsberg et al.* [in review] assumed in determining the vertical strain rates from these gauges. The bottom two gauges, however, show a very different trend.

In a future analysis, we will examine the raw data from the instruments more closely with the modelled horizontal shearing of the borehole to study the ice flow properties at depth under Siple Dome.

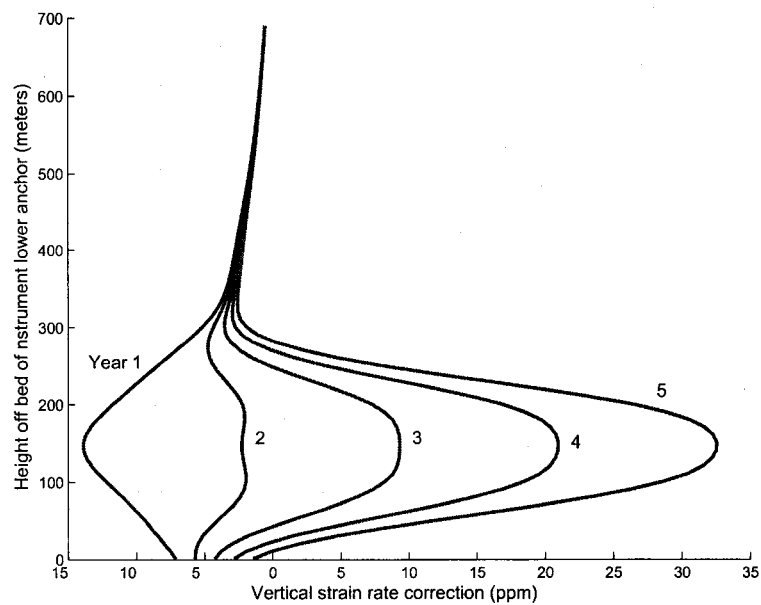


Figure C.6: Correction for the fiber instruments, calculated with a 174 meter “effective gauge length”.

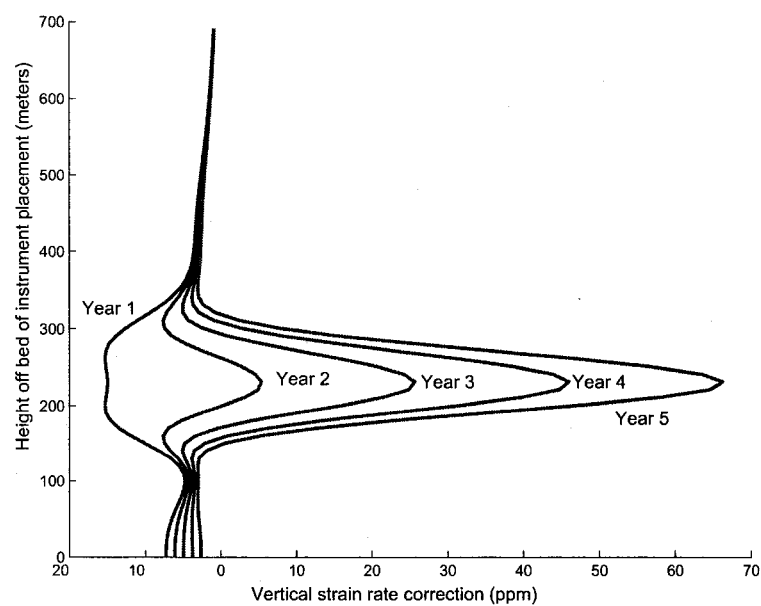


Figure C.7: Correction for the wire instruments, calculated with a 1 meter “effective gauge length”.

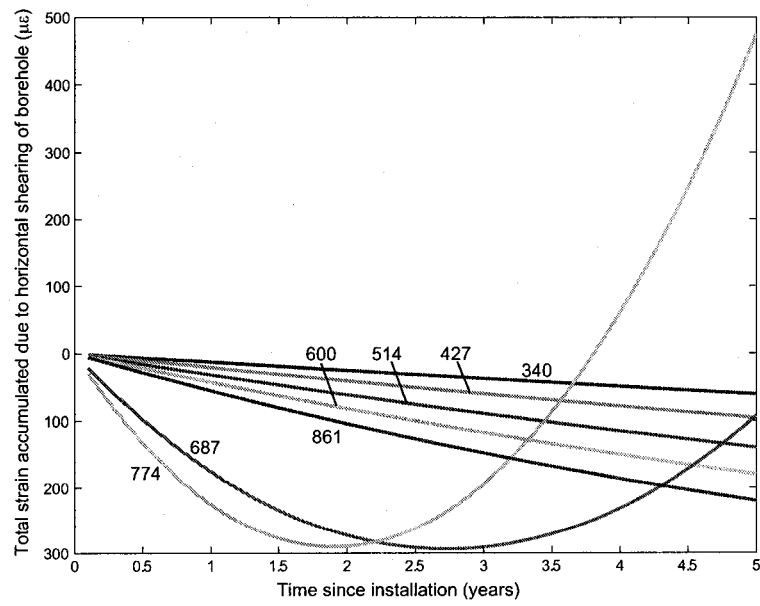


Figure C.8: Total strain accumulated over time in the wire-resistance gauges due to horizontal shearing of the borehole.

Appendix D

ANISOTROPIC ICE FLOW

This appendix is unpublished work by Throstur Thorsteinsson and H. Paul Jacobson. It is included here with their permission because this material is necessary to fully describe the finite-element ice-flow model that I use in Chapters 4 and 6. I have added some text for flow and clarification only.

D.1 Background

This analytical description of anisotropy described is based on the *Sachs* [1928] assumption of homogeneous stress, with deformation occurring as slip on the basal planes. Under this assumption, the applied stress is the same on all crystals within the aggregate. The deformation is determined by the crystal orientation through the resolved shear stress, the component of the applied stress acting on the three slip systems of the basal plane (the three a-axes of the hexagonal ice crystal).

According to *Thorsteinsson* [2001], for a single crystal, the strain rate based on these assumptions is:

$$\dot{\epsilon}^c = \beta A(T) \sum_s \mathbf{R}^{(s)} \tau_{(s)}^n, \quad (\text{D.1})$$

where β is a constant, $A(T)$ is the temperature dependent coefficient of Glen's Law for isotropic ice, and n is the power-law exponent. $\mathbf{R}^{(s)} = (\mathbf{S} + \mathbf{S}^T)/2$ is the symmetric part of the Schmid tensor ($\mathbf{S} = \mathbf{b} \otimes \mathbf{n}$) for each slip system, s , where \mathbf{n} is the normal to the basal plane and \mathbf{b} is the Burgers vector. $\tau_{(s)}$, the resolved shear stress for a particular slip system, has the general form:

$$\tau(s) = n_1 b_1^{(s)} \sigma_{11} + n_2 b_2^{(s)} \sigma_{22} + n_3 b_3^{(s)} \sigma_{33} + (n_1 b_2^{(s)} + n_2 b_1^{(s)}) \sigma_{12} + (n_1 b_3^{(s)} \quad (\text{D.2})$$

$$+ n_3 b_1^{(s)}) \sigma_{13} + (n_2 b_3^{(s)} + n_3 b_2^{(s)}) \sigma_{23}. \quad (\text{D.3})$$

The bulk strain rate for the material results from the integral:

$$\dot{\epsilon} = \int \int \dot{\epsilon}^c(\theta, \phi) F(\theta, \phi) d\theta d\phi, \quad (\text{D.4})$$

where $F(\theta, \phi)$ is the c-axis-orientation distribution function. ($\int \int F(\theta, \phi) d\theta d\phi = 1$).

D.2 Analytical Derivation

From this point, we make the assumptions that $n = 1$ and the fabric can be described by a vertical cone angle (α). We incorporate the nonlinearity of the isotropic Glen flow law through η_{eff} , which is the effective viscosity from Glen's Law (Equation (2.3)):

$$\eta_{\text{eff}} = [2EA_0 e^{-\frac{Q}{RT}} (\tau_{\text{eff}}^2)^{\frac{n-1}{2}}]^{-1}. \quad (\text{D.5})$$

We assume that η_{eff} is constant over a finite-element for each timestep. When $\beta = 30$ (this parameter becomes part of the enhancement factor when it is incorporated into the finite-element model; its value is not important for this derivation), Sach's law can be written:

$$\dot{\epsilon}_{ij}^S = \frac{1}{\eta_{\text{eff}}} \begin{bmatrix} a\sigma_{11} + c\sigma_{22} + b\sigma_{33} & d\sigma_{12} & e\sigma_{13} \\ d\sigma_{12} & c\sigma_{11} + a\sigma_{22} + b\sigma_{33} & e\sigma_{23} \\ e\sigma_{13} & e\sigma_{23} & b(\sigma_{11} + \sigma_{22} - 2\sigma_{33}) \end{bmatrix}, \quad (\text{D.6})$$

where

$$\begin{aligned} a &= \frac{1}{48} (100 + 95 \cos \alpha + 36 \cos 2\alpha + 9 \cos 3\alpha) \sin^2 \left(\frac{\alpha}{2} \right), \\ b &= -\frac{1}{12} (20 + 25 \cos \alpha + 12 \cos 2\alpha + 3 \cos 3\alpha) \sin^2 \left(\frac{\alpha}{2} \right), \\ c &= -\frac{1}{12} (19 + 18 \cos \alpha + 3 \cos 2\alpha) \sin^4 \left(\frac{\alpha}{2} \right), \\ c &= \frac{1}{48} (-20 + 5 \cos \alpha + 12 \cos 2\alpha + 3 \cos 3\alpha) \sin^2 \left(\frac{\alpha}{2} \right), \\ d &= \frac{1}{8} (20 + 15 \cos \alpha + 4 \cos 2\alpha + \cos 3\alpha) \sin^2 \left(\frac{\alpha}{2} \right), \\ e &= \frac{1}{8} (10 + 4 \cos \alpha + 3 \cos 2\alpha + 2 \cos 3\alpha + \cos 4\alpha). \end{aligned} \quad (\text{D.7})$$

These coefficients are plotted as a function of cone angle in Figure D.1. Note that c can be written in two forms ($c = -a - b$). In the limit of isotropy ($\lim_{\alpha \rightarrow 90^\circ}$), $a = \frac{2}{3\eta_{\text{eff}}}$,

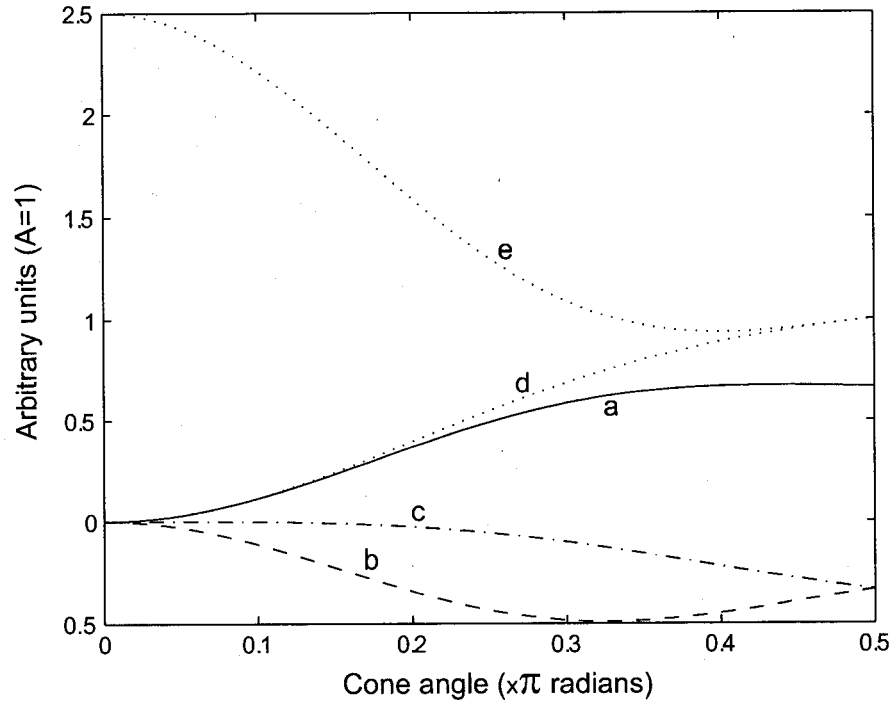


Figure D.1: a (solid), b (dash), c (dot dash), d, e (dotted)

$$b = c = -\frac{1}{3\eta_{\text{eff}}}, \text{ and } d = e = \frac{1}{\eta_{\text{eff}}}.$$

This matrix can also be written as vectors:

$$\begin{bmatrix} \dot{\epsilon}_{11}^S \\ \dot{\epsilon}_{22}^S \\ \dot{\epsilon}_{33}^S \\ \dot{\epsilon}_{13}^S \\ \dot{\epsilon}_{23}^S \\ \dot{\epsilon}_{12}^S \end{bmatrix} = \frac{1}{\eta_{\text{eff}}} \begin{bmatrix} a & c & b & 0 & 0 & 0 \\ c & a & b & 0 & 0 & 0 \\ b & b & -2b & 0 & 0 & 0 \\ 0 & 0 & 0 & e & 0 & 0 \\ 0 & 0 & 0 & 0 & e & 0 \\ 0 & 0 & 0 & 0 & 0 & d \end{bmatrix} \begin{bmatrix} \sigma_{11} \\ \sigma_{22} \\ \sigma_{33} \\ \sigma_{13} \\ \sigma_{23} \\ \sigma_{12} \end{bmatrix}, \quad (\text{D.8})$$

with the inverse:

$$\begin{bmatrix} \sigma_{11} \\ \sigma_{22} \\ \sigma_{33} \\ \sigma_{13} \\ \sigma_{23} \\ \sigma_{12} \end{bmatrix} = \frac{1}{\eta_{\text{eff}}} \begin{bmatrix} \frac{2a+b}{2(a-c)(a+b+c)} & \frac{b+2c}{2(c-a)(a+b+c)} & \frac{1}{2(a+b+c)} & 0 & 0 & 0 \\ \frac{b+2c}{2(c-a)(a+b+c)} & \frac{2a+b}{2(a-c)(a+b+c)} & \frac{1}{2(a+b+c)} & 0 & 0 & 0 \\ \frac{1}{2(a+b+c)} & \frac{1}{2(a+b+c)} & -\frac{a+c}{2b(a+b+c)} & 0 & 0 & 0 \\ 0 & 0 & 0 & \frac{1}{e} & 0 & 0 \\ 0 & 0 & 0 & 0 & \frac{1}{e} & 0 \\ 0 & 0 & 0 & 0 & 0 & \frac{1}{d} \end{bmatrix} \begin{bmatrix} \dot{\epsilon}_{11}^S \\ \dot{\epsilon}_{22}^S \\ \dot{\epsilon}_{33}^S \\ \dot{\epsilon}_{13}^S \\ \dot{\epsilon}_{23}^S \\ \dot{\epsilon}_{12}^S \end{bmatrix}. \quad (\text{D.9})$$

This inverse is impossible, however, since for all angles, $a + b + c = 0$.

When we substitute the deviatoric stress in Equation (D.8), the pressure (the trace of the stress tensor) drops out:

$$\tau_{ij} = \sigma_{ij} + \delta_{ij}p \quad p = -1/3\sigma_{jj} \quad (\text{D.10})$$

$$\begin{bmatrix} \dot{\epsilon}_{11}^S \\ \dot{\epsilon}_{22}^S \\ \dot{\epsilon}_{33}^S \\ \dot{\epsilon}_{13}^S \\ \dot{\epsilon}_{23}^S \\ \dot{\epsilon}_{12}^S \end{bmatrix} = \frac{1}{\eta_{\text{eff}}} \begin{bmatrix} a & c & b & 0 & 0 & 0 \\ c & a & b & 0 & 0 & 0 \\ b & b & -2b & 0 & 0 & 0 \\ 0 & 0 & 0 & e & 0 & 0 \\ 0 & 0 & 0 & 0 & e & 0 \\ 0 & 0 & 0 & 0 & 0 & d \end{bmatrix} \begin{bmatrix} \tau_{11} - p \\ \tau_{22} - p \\ \tau_{33} - p \\ \tau_{13} \\ \tau_{23} \\ \tau_{12} \end{bmatrix} \quad (\text{D.11})$$

$$= \frac{1}{\eta_{\text{eff}}} \begin{bmatrix} a & c & b & 0 & 0 & 0 \\ c & a & b & 0 & 0 & 0 \\ b & b & -2b & 0 & 0 & 0 \\ 0 & 0 & 0 & e & 0 & 0 \\ 0 & 0 & 0 & 0 & e & 0 \\ 0 & 0 & 0 & 0 & 0 & d \end{bmatrix} \begin{bmatrix} \tau_{11} \\ \tau_{22} \\ \tau_{33} \\ \tau_{13} \\ \tau_{23} \\ \tau_{12} \end{bmatrix} - \frac{1}{\eta_{\text{eff}}} \begin{bmatrix} a + c + b \\ c + a + b \\ b + b - 2b \\ 0 \\ 0 \\ 0 \end{bmatrix} p. \quad (\text{D.12})$$

Since the trace of the deviatoric stress tensor is zero, this version of the constitutive equation can be inverted if we multiply the trace by a constant, which makes the inversion

possible. First, multiply the trace by g :

$$\begin{bmatrix} \dot{\epsilon}_{11}^S \\ \dot{\epsilon}_{22}^S \\ \dot{\epsilon}_{33}^S \\ \dot{\epsilon}_{13}^S \\ \dot{\epsilon}_{23}^S \\ \dot{\epsilon}_{12}^S \end{bmatrix} = \frac{1}{\eta_{\text{eff}}} \begin{bmatrix} a & c & b & 0 & 0 & 0 \\ c & a & b & 0 & 0 & 0 \\ b & b & -2b & 0 & 0 & 0 \\ 0 & 0 & 0 & e & 0 & 0 \\ 0 & 0 & 0 & 0 & e & 0 \\ 0 & 0 & 0 & 0 & 0 & d \end{bmatrix} \begin{bmatrix} \tau_{11} \\ \tau_{22} \\ \tau_{33} \\ \tau_{13} \\ \tau_{23} \\ \tau_{12} \end{bmatrix} + g \frac{1}{\eta_{\text{eff}}} \begin{bmatrix} 1 \\ 1 \\ 1 \\ 0 \\ 0 \\ 0 \end{bmatrix} (\tau_{11} + \tau_{22} + \tau_{33}) \quad (\text{D.13})$$

$$= \frac{1}{\eta_{\text{eff}}} \begin{bmatrix} a+g & c+g & b+g & 0 & 0 & 0 \\ c+g & a+g & b+g & 0 & 0 & 0 \\ b+g & b+g & -2b+g & 0 & 0 & 0 \\ 0 & 0 & 0 & e & 0 & 0 \\ 0 & 0 & 0 & 0 & e & 0 \\ 0 & 0 & 0 & 0 & 0 & d \end{bmatrix} \begin{bmatrix} \tau_{11} \\ \tau_{22} \\ \tau_{33} \\ \tau_{13} \\ \tau_{23} \\ \tau_{12} \end{bmatrix} \quad (\text{D.14})$$

When $g = 1/3$ and $\alpha = 90^\circ$ (isotropic), this matrix reduces to the identity matrix (the tensor components are shown in Figure D.2):

$$\begin{bmatrix} \dot{\epsilon}_{11}^S \\ \dot{\epsilon}_{22}^S \\ \dot{\epsilon}_{33}^S \\ \dot{\epsilon}_{13}^S \\ \dot{\epsilon}_{23}^S \\ \dot{\epsilon}_{12}^S \end{bmatrix} = \frac{1}{\eta_{\text{eff}}} \begin{bmatrix} \frac{2}{3} + \frac{1}{3} & -\frac{1}{3} + \frac{1}{3} & -\frac{1}{3} + \frac{1}{3} & 0 & 0 & 0 \\ -\frac{1}{3} + \frac{1}{3} & \frac{2}{3} + \frac{1}{3} & -\frac{1}{3} + \frac{1}{3} & 0 & 0 & 0 \\ -\frac{1}{3} + \frac{1}{3} & -\frac{1}{3} + \frac{1}{3} & \frac{2}{3} + \frac{1}{3} & 0 & 0 & 0 \\ 0 & 0 & 0 & e & 0 & 0 \\ 0 & 0 & 0 & 0 & e & 0 \\ 0 & 0 & 0 & 0 & 0 & d \end{bmatrix} \begin{bmatrix} \tau_{11} \\ \tau_{22} \\ \tau_{33} \\ \tau_{13} \\ \tau_{23} \\ \tau_{12} \end{bmatrix} = \frac{1}{\eta_{\text{eff}}} \begin{bmatrix} \tau_{11} \\ \tau_{22} \\ \tau_{33} \\ \tau_{13} \\ \tau_{23} \\ \tau_{12} \end{bmatrix} \quad (\text{D.15})$$

For angles other than $\alpha = 0$ (where only e is non zero), the matrix in Equation D.14 is invertible. First, we can make $a + b + c = 0$ explicit by rewriting the matrix (from

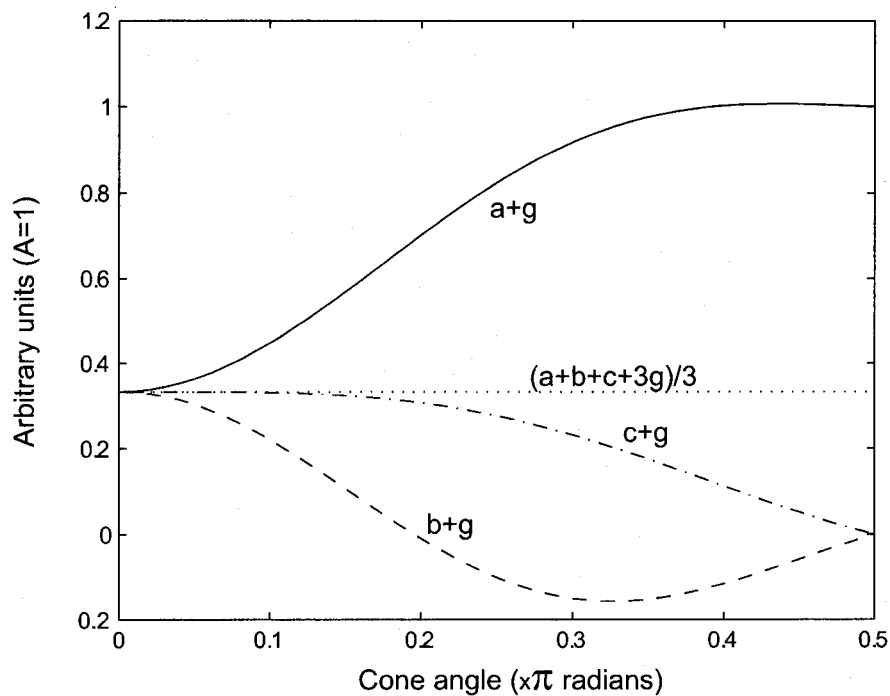


Figure D.2: $g = 1/3$. $a + g$ (solid), $b + g$ (dash), $c + g$ (dot dash), $(a + b + c + 3g)/3 = g$ (dotted)

Equation (D.14), omitting the shear terms):

$$M2 = \begin{bmatrix} a & -b - a & b \\ -b - a & a & b \\ b & b & -2b \end{bmatrix} \quad (\text{D.16})$$

Its eigenvalues are $[0, b + 2a, -3b]$. The eigenvalues for the corresponding $M2 + g$ are $[3g, b + 2a, -3b]$.

The inverse of $M2 + g$ is:

$$\begin{aligned}
& \begin{bmatrix} \frac{(4b-a)g + b^2 + 2ab}{(9b^2 + 18ab)g} & -\frac{(5b+a)g - b^2 - 2ab}{(9b^2 + 18ab)g} & \frac{g+b}{9bg} \\ \frac{(5b+a)g - b^2 - 2ab}{(9b^2 + 18ab)g} & \frac{(4b-a)g + b^2 + 2ab}{(9b^2 + 18ab)g} & \frac{g+b}{9bg} \\ \frac{g+b}{9bg} & \frac{g+b}{9bg} & \frac{2g-b}{9bg} \end{bmatrix} \\
&= \frac{1}{9bg} \begin{bmatrix} \frac{(4b-a)g + b^2 + 2ab}{b+2a} & -\frac{(5b+a)g - b^2 - 2ab}{b+2a} & g+b \\ \frac{(5b+a)g - b^2 - 2ab}{b+2a} & \frac{(4b-a)g + b^2 + 2ab}{b+2a} & g+b \\ g+b & g+b & b-2g \end{bmatrix} \\
&= \frac{1}{9bg} \begin{bmatrix} \frac{(4b-a)g}{b+2a} + b & -\frac{(5b+a)g}{b+2a} + b & g+b \\ \frac{(5b+a)g}{b+2a} + b & \frac{(4b-a)g}{b+2a} + b & g+b \\ g+b & g+b & -2g+b \end{bmatrix} = \frac{-1}{9b} \begin{bmatrix} \frac{a-4b}{2a+b} & \frac{a+5b}{2a+b} & -1 \\ \frac{a+5b}{2a+b} & \frac{a-4b}{2a+b} & -1 \\ -1 & -1 & 2 \end{bmatrix} + \frac{1}{9g} \\
& \tag{D.17}
\end{aligned}$$

Finally, the vertical-cone anisotropic constitutive equation is:

$$\begin{bmatrix} \tau_{11} \\ \tau_{22} \\ \tau_{33} \\ \tau_{13} \\ \tau_{23} \\ \tau_{12} \end{bmatrix} = \frac{1}{\eta_{\text{eff}}} \begin{bmatrix} a_{11} & a_{12} & a_{13} & 0 & 0 & 0 \\ a_{12} & a_{11} & a_{13} & 0 & 0 & 0 \\ a_{13} & a_{13} & a_{33} & 0 & 0 & 0 \\ 0 & 0 & 0 & \frac{1}{e} & 0 & 0 \\ 0 & 0 & 0 & 0 & \frac{1}{e} & 0 \\ 0 & 0 & 0 & 0 & 0 & \frac{1}{d} \end{bmatrix} \begin{bmatrix} \dot{\epsilon}_{11} \\ \dot{\epsilon}_{22} \\ \dot{\epsilon}_{33} \\ \dot{\epsilon}_{13} \\ \dot{\epsilon}_{23} \\ \dot{\epsilon}_{12} \end{bmatrix} \tag{D.18}$$

$$a_{11} = \frac{-1}{9b} \frac{a-4b}{2a+b} + \frac{1}{9g} \quad a_{12} = \frac{-1}{9b} \frac{a+5b}{2a+b} + \frac{1}{9g} \tag{D.19}$$

$$a_{13} = \frac{1}{9b} + \frac{1}{9g} \quad a_{33} = \frac{-2}{9b} + \frac{1}{9g} \tag{D.20}$$

Now we assume plane strain, $\dot{\epsilon}_{22} = \dot{\epsilon}_{12} = \dot{\epsilon}_{23} = 0$, and Equation (D.18) reduces to:

$$\begin{bmatrix} \tau_{11} \\ \tau_{22} \\ \tau_{33} \\ \tau_{13} \\ \tau_{23} \\ \tau_{12} \end{bmatrix} = \eta_{\text{eff}} \begin{bmatrix} a_{11} & a_{13} & 0 \\ a_{12} & a_{13} & 0 \\ a_{13} & a_{33} & 0 \\ 0 & 0 & \frac{1}{e} \\ 0 & 0 & 0 \\ 0 & 0 & 0 \end{bmatrix} \begin{bmatrix} \dot{\epsilon}_{11} \\ \dot{\epsilon}_{33} \\ \dot{\epsilon}_{13} \end{bmatrix}, \quad (\text{D.21})$$

which can also be written

$$\begin{bmatrix} \tau_{11} \\ \tau_{33} \\ \tau_{13} \end{bmatrix} = \eta_{\text{eff}} \begin{bmatrix} a_{11} & a_{13} & 0 \\ a_{13} & a_{33} & 0 \\ 0 & 0 & \frac{1}{e} \end{bmatrix} \begin{bmatrix} \dot{\epsilon}_{11} \\ \dot{\epsilon}_{33} \\ \dot{\epsilon}_{13} \end{bmatrix} \quad (\text{D.22})$$

$$\tau_{12} = \tau_{23} = 0 \quad \tau_{22} = a_{12} \dot{\epsilon}_{11} + a_{13} \dot{\epsilon}_{33}. \quad (\text{D.23})$$

Using $\dot{\epsilon}_{11} = -\dot{\epsilon}_{33}$ the transverse stress term can be written

$$\tau_{22} = \frac{-1}{3b} \frac{a+2b}{2a+b} \dot{\epsilon}_{11} \quad (\text{D.24})$$

For isotropic ice $\tau_{22} = 0$; for general anisotropic ice it is not. The main implication of this, is that $\tau_{11} \neq -\tau_{33}$. For an anisotropic material, different (deviatoric) stresses may be required in all three directions to keep the flow constrained within the plane.

For incompressible plane strain ($\dot{\epsilon}_{11} = -\dot{\epsilon}_{33}$) the 2D matrix in Equation D.22 can be diagonalized by subtracting a_{13} from 4 of the terms (because $\dot{\epsilon}_{11} = -\dot{\epsilon}_{33}$ this subtraction does not change the value of the deviatoric stress tensor):

$$\begin{bmatrix} a_{11} - a_{13} & 0 & 0 \\ 0 & a_{33} - a_{13} & 0 \\ 0 & 0 & \frac{1}{e} \end{bmatrix} = \begin{bmatrix} a_{11} & a_{13} & 0 \\ a_{13} & a_{33} & 0 \\ 0 & 0 & \frac{1}{e} \end{bmatrix} - \begin{bmatrix} a_{13} & a_{13} & 0 \\ a_{13} & a_{13} & 0 \\ 0 & 0 & 0 \end{bmatrix} \quad (\text{D.25})$$

$$\begin{bmatrix} \tau_{11} \\ \tau_{33} \\ \tau_{13} \end{bmatrix} = \eta_{\text{eff}} \begin{bmatrix} a_{11} - a_{13} & 0 & 0 \\ 0 & a_{33} - a_{13} & 0 \\ 0 & 0 & \frac{1}{e} \end{bmatrix} \begin{bmatrix} \dot{\epsilon}_{11} \\ \dot{\epsilon}_{33} \\ \dot{\epsilon}_{13} \end{bmatrix} \quad (\text{D.26})$$

$$a_{11} - a_{13} = \frac{-1}{3b} \frac{a-b}{2a+b} \quad a_{33} - a_{13} = \frac{-1}{3b} \quad (\text{D.27})$$

When we substitute velocity gradients for the strain rates, the constitutive equation is:

$$u_x = \dot{\epsilon}_{11} \quad w_z = \dot{\epsilon}_{33} \quad (u_z + w_x)/2 = \dot{\epsilon}_{13} \quad (\text{D.28})$$

$$\begin{bmatrix} \tau_{11} \\ \tau_{33} \\ \tau_{13} \end{bmatrix} = \eta_{\text{eff}} \begin{bmatrix} \frac{-1}{3b} \frac{a-b}{2a+b} & 0 & 0 \\ 0 & \frac{-1}{3b} & 0 \\ 0 & 0 & \frac{1}{e} \end{bmatrix} \begin{bmatrix} u_x \\ w_z \\ (u_z + w_x)/2 \end{bmatrix} \quad (\text{D.29})$$

The final step in this derivation is to incorporate this constitutive equation into the stress-balance equations for the ice sheet. The stress-balance equations are:

$$\frac{\partial \tau_{11}}{\partial x} + \frac{\partial \tau_{13}}{\partial z} - \frac{\partial p}{\partial x} = f_1 \quad \frac{\partial \tau_{13}}{\partial x} + \frac{\partial \tau_{33}}{\partial z} - \frac{\partial p}{\partial z} = f_2. \quad (\text{D.30})$$

Substituting the constitutive relation for the deviatoric stresses leads to:

$$\eta_{\text{eff}} \left(\frac{\partial \left[\frac{-1}{3b} \frac{a-b}{2a+b} u_x \right]}{\partial x} + \frac{\partial \left[\frac{1}{e} (u_z + w_x) / 2 \right]}{\partial z} \right) - \frac{\partial p}{\partial x} = f_1 \quad (\text{D.31})$$

$$\eta_{\text{eff}} \left(\frac{-1}{3b} \frac{a-b}{2a+b} u_{xx} + \frac{1}{2e} (u_{zz} + w_{xz}) \right) - p_x = f_1 \quad (\text{D.32})$$

$$\eta_{\text{eff}} \left(\frac{-1}{3b} \frac{a-b}{2a+b} u_{xx} + \frac{1}{2e} (u_{zz} - u_{xx}) \right) - p_x = f_1 \quad (\text{D.33})$$

$$(\text{D.34})$$

for the first stress-balance equation and for the second:

$$\eta_{\text{eff}} \left(\frac{\partial \left[\frac{1}{e} (u_z + w_x) / 2 \right]}{\partial x} + \frac{\partial \left[\frac{-1}{3b} w_z \right]}{\partial z} \right) - \frac{\partial p}{\partial z} = f_2 \quad (\text{D.35})$$

$$\eta_{\text{eff}} \left(\frac{1}{2e} (u_{zx} + w_{xx}) + \frac{-1}{3b} w_{zz} \right) - p_z = f_2 \quad (\text{D.36})$$

$$\eta_{\text{eff}} \left(\frac{1}{2e} (-w_{zz} + w_{xx}) + \frac{-1}{3b} w_{zz} \right) - p_z = f_2 \quad (\text{D.37})$$

The resulting 2-dimensional partial differential equations are

$$\eta_{\text{eff}} \left(\frac{-1}{3b} \frac{a-b}{2a+b} - \frac{1}{2e} \right) u_{xx} + \eta_{\text{eff}} \frac{1}{2e} u_{zz} - p_x = 0 \quad (\text{D.38})$$

$$\eta_{\text{eff}} \frac{1}{2e} w_{xx} + \eta_{\text{eff}} \left(\frac{-1}{3b} - \frac{1}{2e} \right) w_{zz} - p_z = \rho g \quad (\text{D.39})$$

$$u_x + w_z = 0 \quad (\text{D.40})$$

Figure D.3 shows the coefficients for each of the terms as a function of cone angle.

These equations reduce to a Laplacian for isotropic ice, $a = 2/3$, $b = -1/3$, and $e = 1$,

$$\frac{\eta_{\text{eff}}}{2} u_{xx} + \frac{\eta_{\text{eff}}}{2} u_{zz} - p_x = 0 \quad \frac{\eta_{\text{eff}}}{2} w_{xx} + \frac{\eta_{\text{eff}}}{2} w_{zz} - p_z = \rho g. \quad (\text{D.41})$$

This derivation for Equations (D.38) to (D.40) assumes spatially uniform cone angle functions (a through e) and a constant η_{eff} . This assumption applies to an individual element, not to the flow field as a whole. Errors may be introduced when adjacent elements

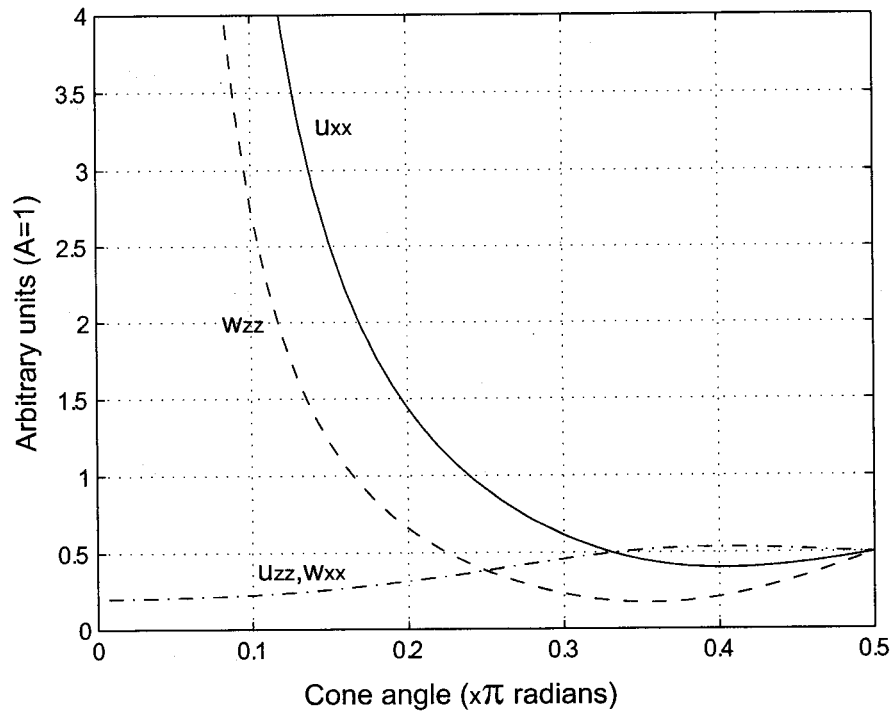


Figure D.3: Coefficients for u_{xx} (solid), w_{zz} (dash), u_{zz}, w_{xx} (dot dash)

have different cone angles or enhancement factors; we assume that these are negligible compared to the overall uncertainties accompanying our other model assumptions.

VITA

Erin C. Pettit
December 5, 2003

EDUCATION

Ph.D. University of Washington, Geophysics	2003
NSF Graduate Research Fellow	
Advisor: Edwin D. Waddington	
Dissertation: <i>Unique Dynamic Behaviors of Ice Divides: Siple Dome and the Rheological Properties of Ice</i>	
Sc.B. Brown University, Mechanical Engineering, with Honors	1994
Thesis: <i>Effects of Excited State Emission of Erbium Doped Fiber Pumped at 820 nm</i>	
St. Aloysius Instituut St. Triuden, Belgium, Exchange Student	1989–90

RESEARCH EXPERIENCE

Research Assistant, UW GEOPHYSICS PROGRAM	1997–2003
Mechanical and Systems Engineer, AEROVIRONMENT	1994–97
Research Assistant LAB. FOR LIGHTWAVE TECH., Brown Univ.	1992–94
Summer Research Program, AT&T BELL LABS	1993

TEACHING EXPERIENCE

Instructor, NORTH CASCADES INSTITUTE	2001–Present
Girls on Ice: Scientific Research and Wilderness Travel for Young Women	
A River's Journey: The Skagit Watershed from Headwaters to Delta	
Scientist-Instructor, SEATTLE PARTNERSHIP FOR INQUIRY-BASED SCIENCE	2000–01
Land and Water: Science Content for Elementary Teachers	
Teaching Assistant, U. OF WASHINGTON	2000–01
Glaciers and Global Change	
Introduction to Geologic Sciences	
Instructor, UW EDUCATIONAL OUTREACH FOR YOUTH	1999
The Ice, An Exploration of Antarctica	
The Glacier Climate Connection, A Field Course in Glaciology	

PUBLICATIONS

- Elsberg, D.H., W.D. Harrison, E. Husmann, J.L. Morack, **E.C. Pettit**, E.D. Waddington, M.A. Zumberge. in review. Strain rates and short term strain events measured at Siple Dome, Antarctica. *Journal of Glaciology*.
- Pettit, E.C.** and E.D. Waddington. in press. Ice flow at low deviatoric stress. *Journal of Glaciology*.
- Kay, J.E., A.R. Gillespie, G.B. Hansen, and **E.C. Pettit**. 2003. Spatial relationships between snow contaminant content, grain size, and surface temperature from multispectral images of Mt. Rainier, Washington (USA). *Remote Sensing of the Environment*. 86. 216-231.
- Pettit, E.C.**, H.P. Jacobson, and E.D. Waddington. 2002. Effects of basal sliding on isochrones and flow near an ice divide. *Annals of Glaciology*. 37.
- Zumberge, M.A., D.H. Elsberg, W.D. Harrison, E. Husmann, J.L. Morack, **E.C. Pettit**, and E.D. Waddington. 2002. Measurement of vertical strain and velocity at Siple Dome with optical sensors. *Journal of Glaciology*. 48(161). 217-225.
- Pettit, E.C.**, J.R. Simpson, K. Oh, and T.F. Morse. 1999. Thermal effects on the excited state absorption and upconversion process of erbium ions in germanosilicate optical fiber. *Journal of Non-Crystalline Solids*. 259. 51-56.
- Oh, K, **E.C. Pettit**, A. Kilian, and T.F. Morse. 1999. Analysis of spectroscopic properties of erbium doped $Ta_2O_5 - Al_2O_3 - SiO_2$ optical fiber. *Journal of Non-Crystalline Solids*. 259. 10-15.
- Anderson, C.A. and **E.C. Pettit**. 1995. The effects of APU characteristics on the design of hybrid control strategies for hybrid electric vehicles. SAE Technical Paper Series 950493. In *Design Innovations in Electric and Hybrid Electric Vehicles*. SAE SP-1089. Bates, B. and F. Stodolsky (eds.). Society of Automotive Engineers, Inc. Warrendale, PA.

ABSTRACTS AND PRESENTATIONS

- Conway, H., T.A. Neumann, E.D. Waddington, G. Catania, **E.C. Pettit**, F. Ng, and D.L. Morse. 2003. Climate and thickness history near the divide between the Ross and Amundsen Seas. 10th Annual West Antarctic Ice Sheet Workshop. Washington, D.C.
- Pettit, E.C.**, E.D. Waddington, N.A. Nereson, M.A. Zumberge, G.S. Hamilton. 2001. Siple Dome: is it in steady state? *EOS*. 82(47). IP21A-0662. F527. AGU Fall Meeting Supplement.
- Pettit, E.C.** and M. N. Koppes. 2001. Girls on ice: an inquiry-based wilderness science education program. *EOS*. 82(47). ED42B-0177. F246. AGU Fall Meeting Supplement.

- Kay, J.E., E.C. Pettit, A. Gillespie. 2001. Characterization of melting snowpack properties on Mt. Rainier using MASTER multispectral data. *EOS*. 82(47). V41A-979. F1361. AGU Fall Meeting Supplement.
- Pettit, E.C. 2000. Radar Studies of Mount Rainier's Summit Crater. Northwest Glaciology Meeting. Portland.
- Pettit, E.C. 2000. Stability of the West Antarctic Ice Sheet. Rotary International Meeting, Seattle.
- Pettit, E.C., E.D. Waddington, W.D. Harrison, J.L. Morack, M.A. Zumberge, E.H. Elsberg, E. Husmann, and C.F. Raymond. 1999. Ice flow at low deviatoric stress: Siple Dome vertical strain experiment. *EOS*. 80(46). F334. AGU Fall Meeting Supplement.
- Pettit, E.C., E.D. Waddington, W.D. Harrison, J.L. Morack, M.A. Zumberge, E.H. Elsberg, E. Husmann, and C.F. Raymond. 1999. Ice Flow at Low Deviatoric Stress: Siple Dome Ice Divide Vertical Strain Experiment. Deformation of Glacial Materials Conference. London, UK.
- Pettit, E.C., E.D. Waddington, C.F. Raymond, W.D. Harrison, J.L. Morack, E.H. Elsberg, M.A. Zumberge, and E. Husmann. 1998. A strategy for determining ice flow parameters from vertical strain measurements. *EOS*. 79(45). F274. Fall Meeting Supplement.